REACTIVE TRACERS FOR CHARACTERIZING FRACTURED GEOTHERMAL RESERVOIRS

A Dissertation

Presented to the Faculty of the Graduate School

of Cornell University

In Partial Fulfillment of the Requirements for the Degree of

Doctor of Philosophy

by

Adam J. Hawkins

May 2017

© 2017 Adam J. Hawkins

REACTIVE TRACERS FOR CHARACTERIZING FRACTURED GEOTHERMAL RESERVOIRS

Adam J. Hawkins, Ph. D.
Cornell University 2017

Multi-component tracer tests were conducted at a 10 x 10 m well field located in the Altona Flat Rocks of northern New York. Temperature advancement between two wells separated by 14 m was monitored throughout the well field during progressive heating of the reservoir over 6 d. Multiple approaches to predicting heat transport were applied to field data and compared to temperature rise recorded during reservoir heat-up.

Tracer analysis incorporated both an analytical one-dimensional model and a two-dimensional numerical model for non-uniform fractures experiencing “flow-channeling.” Modeling efforts demonstrated that estimating heat transfer surface area using a combined inert/adsorbing tracer (cesium-iodide) could provide accurate forecasting of premature thermal breakthrough. In addition, thermally degrading tracer tests were used to monitor inter-well temperature during progressive reservoir heating.

Inert tracers alone were, in general, inadequate in forecasting thermal performance. In fact, moment analysis shows that, mathematically, thermal breakthrough is independent of parameters that primarily influence inert

tracers. The most accurate prediction of thermal breakthrough using inert tracer alone was produced by treating hydrodynamic dispersion as a truly Fickian process with known and accurate mathematical models. Under this assumption, inert tracer data was matched by solving an inverse problem for non-uniform fracture aperture. Early arrival of the thermal front was predicted at the production, but was less accurate than using a combined inert/adsorbing tracer test.

The spatial distribution of fluid flow paths in the plane of the fracture were identified using computational models, Fiber-Optic Distributed Temperature Sensing (FO-DTS), and Ground Penetrating Radar (GPR) imaging of saline tracer flow paths in the target fracture. Without exception, fluid flow was found to be concentrated in a roughly 1 m wide flow channel directly between the two wells.

The following key findings summarize the results of this study: (1) flow channeling resulted in rapid thermal breakthrough; (2) advection-dispersion models for inert tracers cannot calibrate forward-models of thermal performance; (3) adsorption tracers accurately estimated heat transfer surface area; (4) thermally degrading tracer tests identified the migration of a thermal front; and (5) Principal Component Analysis can be used to simplify fracture aperture fields and subsequently aid in solving an inverse problem for non-uniform aperture. In addition, two significant fluid/rock interactions were found: (1) adsorption was rate-limited over the timespan of tracer tests at

Altona; and (2) the target fracture catalyzed thermal degradation leading to substantial over-estimates of inter-well temperature.

BIOGRAPHICAL SKETCH

In 1986, Adam Hawkins was born in Pittsburg, California to parents Joseph and Maureen Hawkins. He graduated from Freedom High School in Oakley, California as a member of the class of 2005. In 2009, he obtained a Bachelor's of Science degree in Geology from the University of California, Davis. After spending a year working in the environmental consulting industry, he began a Master's of Science program in Geology with Professor Matthew Becker at California State University, Long Beach. After graduating in 2013, he spent another year in the environmental consulting industry. From 2013 to 2017, he worked towards his Doctorate of Philosophy in Geological Sciences at Cornell University.

This dissertation is dedicated to a kid who could not decide if he wanted to be a geologist or a plumber.

ACKNOWLEDGMENTS

I owe tremendous gratitude to family, friends, co-authors, academic advisors, and my graduate student colleagues. In fact, the entire length of this dissertation could be filled with nothing but my gratitude. I hope the abbreviated acknowledgement that follows will suffice.

First, I would like to thank my supervisor, Professor Jefferson Tester, and my other committee members, Professors Lawrence Cathles and Donald Koch. Each of these individuals possess incredible expertise in their field and I have benefited greatly from their mentorship and areas of expertise, which were both unique and complimentary to one another. Professor Tester, I am grateful for the numerous opportunities you have provided. Your mentorship has given me an invaluable platform for beginning my academic career.

Other faculty and staff members at Cornell, California State University, Long Beach, the University of Kansas, and SUNY Plattsburgh deserve my thanks. Professor Matthew Becker, I cannot thank you enough for your guidance and support during my time as your graduate student at California State University, Long Beach. I would also like to thank Georgios Tsoflias, Dave Franzi, Teresa Jordan, Richard Allmendinger, Lou Derry, Bill White, John Thompson, Frank Horowitz, and many more.

My fellow graduate students at Cornell University, thank you for sharing your expertise, your willingness to aid my field efforts, and your friendship.

Don Fox, thank you for your mentorship and an exceptional computational framework. To all of you that made my field experiments possible, I am truly grateful. These individuals include Sean Hillson, Ivan Beentjes, Russell Zhao, Koenraad Beckers, Maciek Lukawski, Don Fox, Caryl Mansing, Akshaya Nambiar, and numerous others. Others who deserve my thanks include Arna Pálsdóttir, Chris Siron, Casey Root, Andres Aguirre, Gregg McElwee, and so many others who are part of Earth & Atmospheric Science and Chemical Engineering.

TABLE OF CONTENTS

LIST OF FIGURES

LIST OF TABLES

LIST OF ABBREVIATIONS

CEC	Cation Exchange Capacity
CFS	Channeled Flow Scenario
DFN	Discrete Fracture Network
EGS	Engineered (or “Enhanced”) Geothermal System
ESFL	Ecosystems Studies Field Laboratory
FEM	Finite Element Method
FFT	Fast Fourier Transforms
FID	Flame Ionization Detector
FO-DTS	Fiber-Optic Distributed temperature Sensing
FWA	Flow-Wetted Area
GA	Genetic Algorithm
GC	Gas Chromatograph
GPR	Ground Penetrating Radar
HDR	Hot Dry Rock
ICP-MS	Inductively Coupled Plasma Mass Spectrometry
ICP-OES	Inductively Coupled Plasma Optical Emission Spectroscopy
IDFS	Ideal Dipole-Flow Scenario
ISO	Independent System Operator
NDS	Napthalene Disulfonate
NLCG	Non-Linear Conjugate Gradient Method
PCA	Principal Component Analysis
PTS	Pyrene-1,3,6,8-tetra sulphonic acid (PTS)
QD	Quantum Dots
RTD	Residence Time Distribution
SPME	Solid Phase MicroExtraction
SSE	Sum of Square Errors
SUNY	State University of New York

LIST OF SYMBOLS

Roman Letters

A	Pre-exponential factor for the Arrhenius Equation
A_f	fracture surface area
c	Concentration
C	covariance matrix for Principal Component Analysis (PCA)
C_p	specific heat capacity
D^*	mass diffusion coefficient
D_f	hydrodynamic dispersion
D_m	effective thermal diffusivity
E_a	activation energy
f	reservoir volume fraction
F_T	transfer function
G	Green's function
h	local fracture aperture fluctuation
K	thermal conductivity
k_{ads}	adsorption rate constant
k	reaction rate constant
k_{eff}	effective reaction rate constant
L	fracture spacing interval
M	tracer mass recovered
$\dot{m}$	mass flow rate
M_1	first moment
M_2	second moment
M_{inj}	tracer mass injected
P	pressure / adsorption partition coefficient
Pe	Peclet number
Q	volumetric flow rate
q_s	surface heat flux

$\mathbf{r}$	position vector
R_c	circle radius
s	Laplace transform variable
t	Time
T	Temperature
T_{eff}	effective reservoir temperature
V	volume
υ	mean fluid velocity
ω	fracture aperture
X_{ij}	data set for Principal Component Analysis (PCA)

Greek Letters

a	PCA coefficient
a_L	longitudinal dispersivity
Γ	surface concentration
γ	variogram function
ζ	Hurst roughness coefficient
Θ	non-dimensional temperature
κ	adsorption parameter grouping
μ	dynamic fluid viscosity
ρ	density
τ	mean tracer residence time
φ	rock matrix porosity
$\mathbf{\Phi}$	PCA modes

Subscripts

f	fracture
inj	injection well
m	matrix

r	rock
s	fracture surface
$prod$	production well
w	water

CHAPTER 1: INTRODUCTION

The field experiments and computational models presented in the following dissertation focus on the use of inert and reactive tracers for characterizing fluid flow in fractured rock. These studies are relevant both in terms of their significance to the field of hydrogeology and in industrial applications, including geothermal energy, oil and gas production, environmental remediation, water resources, and carbon storage. The main motivation, however, is in the practical application of these tracers for characterizing geothermal reservoirs. In particular, the emphasis is on the use of inert, adsorbing, and thermally degrading tracers in the development of low-grade geothermal systems which require sufficient connectivity of their subsurface reservoir to sustain injected and produced fluid rates at commercial levels.

These systems, commonly referred to as “Engineered” or “Enhanced” Geothermal Systems (EGS), lack one or more of the following: (1) fluid conductivity; (2) fluid saturation; and/or (3) a high geothermal gradient. Since the 1970s, this geothermal resource has been investigated in the field as a potentially scalable and sustainable source of both heat and electricity. As of 2017, however, there is no active commercial EGS in any country.

Tracer tests are an invaluable tool for determining the Residence Time Distribution (RTD) of fluids circulating between injection and production wells. In addition, inverse models combined with tracer return measurements can be

used to infer relevant subsurface characteristics, such as the surface area available for heat exchange (i.e., “Flow-Wetted Area,” FWA), reservoir fluid volume, and the width of the fracture opening water flows through (i.e., fracture aperture).

Of particular interest is using tracer testing in forecasting how long commercial levels of heat production can be maintained before thermal breakthrough occurs where produced fluid temperatures fall below plant operating and/or design set points (i.e., “thermal performance” or “thermal lifetime”). When produced fluid temperatures drop below a specified temperature earlier than the planned project lifetime, “premature thermal breakthrough” has occurred which reduces performance and, if uncorrected, can be financially disastrous for a commercial operation.

1.1 Motivation

Since 1950, global population has grown by a factor of three (United Nations, 2015). As a result of world-wide industrialization, global consumption of primary energy has outpaced population growth with roughly a factor of five growth since 1950 (Smil, 2010). As early as 2050, world-wide population is projected to grow to roughly 10 billion (United Nations, 2015). In the United States and other developed nations, relatively high levels of energy consumption have provided a high quality of life. For ten billion people to enjoy comparable levels of energy consumption, global primary energy consumption would reach nearly 2000 EJ based on energy consumption per capita in 2013 (United Nations, 2013). To meet this demand before population reaches ten

billion, there would be an increase of more than a factor of five compared to 2013 global primary energy consumption levels.

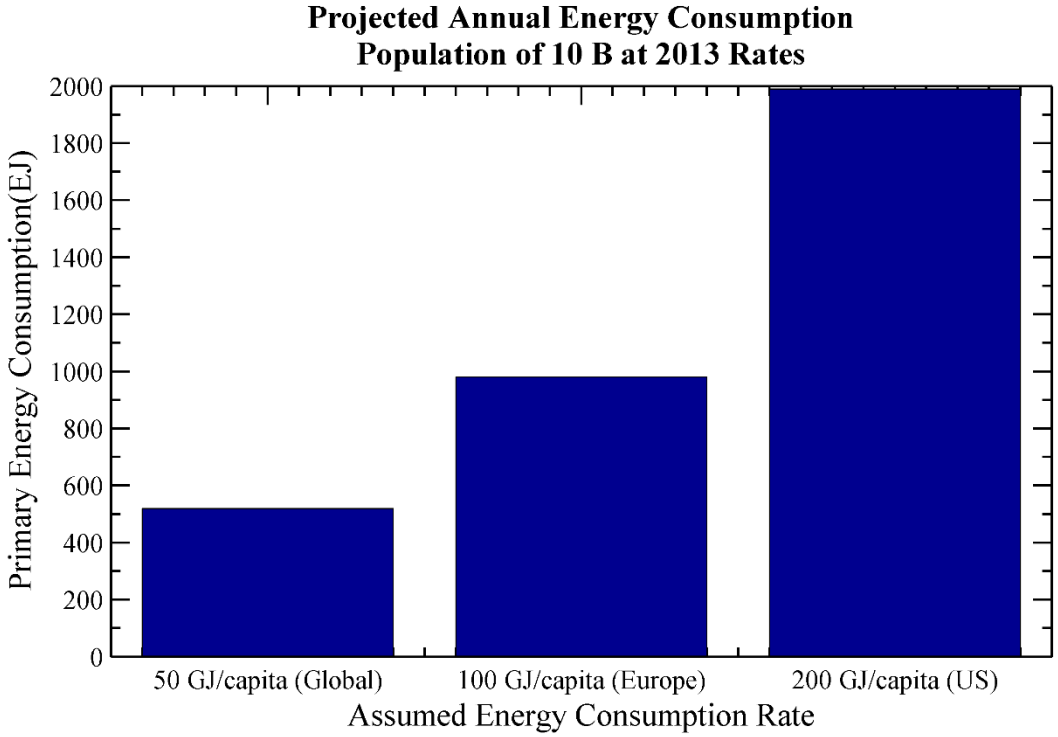

Figure 1.1. Estimated primary energy consumption for a global population of ten billion at per capita rates from 2013 for the United States, Europe, and the entire globe.

Concurrently, environmental concerns such as climate change and air pollution are creating a need to reduce our consumption of inexpensive fossil energy sources with high energy and carbon content, such as coal and oil. Alternative energy sources including renewables, nuclear, and natural gas, have been proposed since the 1970s to meet global energy demand while reducing environmental impact. As of 2014, global net installed capacity of electricity from hydroelectric dams, nuclear plants, wind turbines, solar, and other producer types combined has reached nearly 2100 GW (United Nations,

2014). For comparison, combustible fuels, which inherently emit carbon as a byproduct, have reached 4050 GW.

1.1.1 Current and Future Electricity Generation

As of 2014, global net installed capacity of electricity from hydroelectric dams, nuclear plants, wind turbines, solar, and all other producer types combined has reached nearly 2100 GW_e (United Nations, 2014). For comparison, combustible fuels, which inherently emit carbon as a byproduct, have reached 4050 GW_e. Globally, hydroelectric power dominates electric net capacity in non-combustible forms of electric capacity, accounting for roughly 55%. Roughly equal contributions from nuclear and wind account for a combined 35% while solar accounts for 8.3%. All other sources, including geothermal, tidal, wave, marine and other non-specified sources account for the remaining 0.8% (United Nations, 2014).

In the coming decades, however, political, social, and environmental concerns, as well as resource limitations may prevent meeting increasing global energy consumption with significant growth of hydroelectric and nuclear power. In Jacobson et al. (2015), for example, a plan is discussed in which all of the United States' energy consumption in all sectors will be provided solely by wind, water, and solar power by 2050. This plan suggests decommissioning all nuclear power plants and limiting growth of hydroelectric power to three new plants.

Several other countries throughout the world are taking similar approaches with respect to nuclear power. As a direct result of the Fukushima Daiichi nuclear power plant accident in March 2011, multiple countries, including Germany and Japan, have decommissioned nuclear power stations. Germany, for example, decommissioned seven of their oldest nuclear power plants in 2011 and have set end dates for the remaining nine by 2022 (Brendebach, 2016).

As of 2017, growth of electric capacity whose availability is intermittent has already been dominated by renewable solar and wind energy sources that vary daily and seasonally. Between 2011 and 2014, solar PV net capacity more than doubled with an increase of 150% while wind capacity increased by 60%.

1.1.2 Generation, Transmission, and Distribution of Electricity

Conventionally, consumers receive electricity through an electric grid operated by an Independent System Operator (ISO). The ISO is responsible for monitoring and managing the transmission and distribution of electricity from electricity generators (e.g. coal-fired power plants) to individual consumers (e.g., a family's home). Due to the lack of commercially-viable energy storage solutions, electricity must be dispatched under continuous monitoring and control by the ISO.

To provide stable electricity throughout the year at a minimal cost, ISOs have relied upon electric generators that can meet fluctuating demand within various timespans. A generator can thus be categorized by its ability to "ramp"

from one level of generation to another within a certain time. Historically, electric generators have been broadly classified into three unit types: (1) base load; (2) cycling; and (3) peaking. Each of these have inherent trade-offs related to their cost, net capacity, and availability. Intermittent sources, such as wind turbines and solar PV, are considered too unreliable to be grouped into one of the three major classifications. Therefore, ISOs consider these sources as "negative-load." As a result, the increased attention to intermittent sources over the last two decades has been met with significant concern that high levels of grid penetration by intermittent sources will lead to unreliable electricity production (Hart et al., 2012).

1.1.3 Intermittent Producers

There have been numerous studies on the viability of intermittent generators to provide a large percentage of net electric capacity (e.g., MW_e) and generation (e.g., MW_eh). As discussed in Hart et al. (2012), however, many of these studies neglect time-series data and uncertainty. As a result, some studies have over-estimated the ability of intermittent sources to meet energy demand at high levels of grid penetration.

As of 2017, there remains substantial uncertainty with regards to providing a reliable electric grid with intermittent energy sources. In New York State, for example, a large study was conducted by the New York State Independent System Operator (NYISO) to examine the "potential impacts of increased solar and other intermittent energy sources on grid operations" (NYSISO, 2016). Based on capacity increases the authors felt were realistic over

the next 5 to 15 y, they found that 9000 MW of solar PV and 4500 MW of wind could be integrated into New York without substantial impacts to grid stability. They also suggested that, as of 2016, the "application and physical characteristics of emerging technologies such as electric storage is too premature to model."

While this growth in intermittent energy supply has not caused wide-scale interruptions in electricity, relatively high grid penetrations in areas such as California, Hawaii, New York, Germany, and Ontario Canada have had some negative impacts, including: (1) increased occurrence of negative energy prices; (2) curtailment of renewable generation in favor of conventional generators; (3) additional regulatory oversight; (4) higher operating and maintenance costs; (5) increased investments into transmission and distribution; (6) innovations in resource forecasting; (7) surplus loads; (8) innovations in visualizing data in real-time (NYISO, 2016). Therefore, without dramatic improvements in financing energy storage, wind and solar power may not be able to displace nuclear and fossil-fuels nor reliably meet increasing global demand.

1.2 Geothermal: Earth's Heat as a Sustainable Energy Source

The baseload characteristics of geothermal energy would provide grid stability in a future renewable energy market with high penetration of unreliable and intermittent renewable sources. To substantially increase global capacity and accessibility to larger regions of the world, however, low-grade geothermal resources must be considered. This dissertation addresses a major obstacle in commercializing low-grade geothermal resources: how to predict the

length of time that energy can be extracted from a geothermal system (i.e. “thermal lifetime”).

Geothermal energy has been utilized for millennia as an inexpensive and convenient source of heat. As of 2014, there are 13.3 GWe (Matek, 2016) and 70.3 GWt (Lund and Boyd, 2015) of installed capacity globally. The vast majority of electricity generated is from high-grade resources in which high permeability, high geothermal gradients, and large volumes of groundwater make geothermal energy a commercial success (Diaz et al., 2016). Such conditions are limited, however, as they only exist in tectonically active or volcanic regions. As a result, geothermal energy represents roughly 0.3% of the US and 0.2% of global nameplate installed capacity.

In high-grade hydrothermal resources, such as at the Geysers geothermal field in California or in Iceland, shallow subsurface temperatures are typically above 150 °C within roughly 2 km depth. In addition, natural subsurface permeability and high fluid contents ideally produce convective circulation in the subsurface which promotes long-term energy extraction (>20 yr) by ensuring an even distribution of subsurface fluid flow and heat exchange through the reservoir connected between the injection and production wells.

1.2.1 Engineered (or Enhanced) Geothermal Systems (EGS)

For geothermal energy to reach its potential on a global scale, lower grade geothermal systems must be considered. Low-grade geothermal resources typically have lower production temperatures (<~150 °C) and they

include reservoirs in which one or more of the following three conditions are not met: (1) high thermal gradient; (2) high permeability; and (3) high fluid saturation. In these situations, the reservoir will require intervention to create interwell connectivity and/or inject water to make the reservoir commercially viable. The resulting geothermal option is commonly referred to as an Engineered (or Enhanced) Geothermal System (EGS).

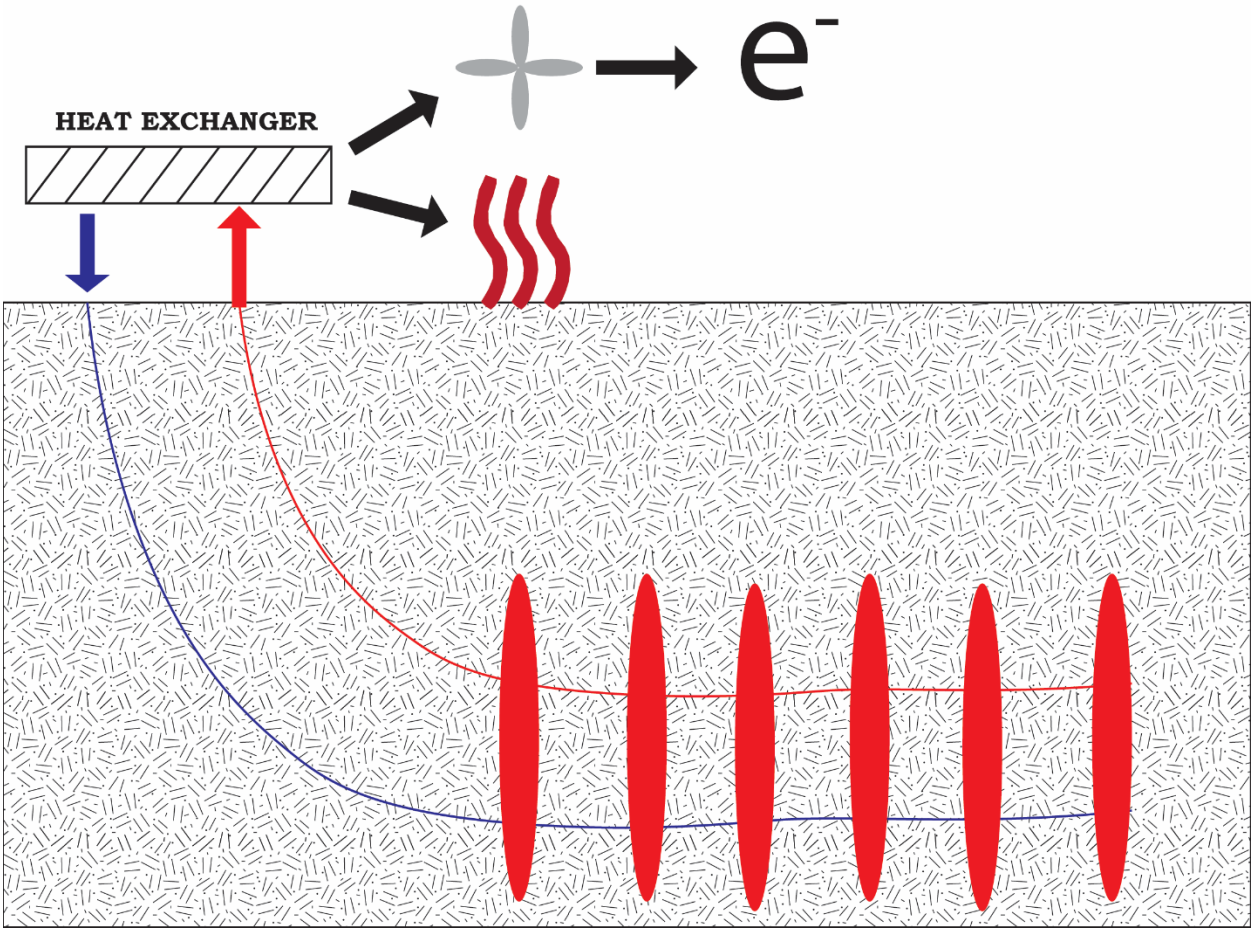

Figure 1.2. Cross-section schematic of an EGS. Fluids are continuously circulated through multiple fractures at elevated temperature. High temperature fluids produced at ground surface are used to directly as a heat source or converted into electricity. Due to rapid heat extraction, production well temperature can decline which reduces performance.

To create an EGS, subsurface permeability may require alteration through hydroshearing, which improves permeability by propping open pre-existing fractures, or by hydrofracturing, which generates permeability by inducing new fractures. To reach ideal temperatures for direct-use (> ~80 °C) or for electricity generation (> ~150 °C) an EGS may also require drilling to great depths. In the United States, a depth of 10 km would be required for all states to access temperatures greater than 150 °C (Tester et al., 2006).

Limited fluid availability is an additional concern for a commercial EGS. In contrast to some high-grade areas such as those available at the Geysers (California), Wairakei (New Zealand), and Nesjavellir (Iceland), subsurface fluid volumes in an EGS may be limited by low (or no) natural recharge. In this circumstance, artificial recharge may be necessary to efficiently extract (or "mine") Earth's heat. To reduce the demand for artificial recharge, produced fluids may be reinjected into the subsurface for additional heat extraction. For an EGS, the practice of enhancing reservoir fluid recharge by reinjecting fluids is considered a fundamental aspect (Axelsson et al., 2000).

1.3 Goals, Approach, and Organization

The research discussed in this dissertation focuses on developing and testing reservoir characterization techniques for the purpose of forecasting the thermal performance of geothermal reservoirs, particularly with respect to an EGS dominated by discrete fractures. Tracer tests, using both inert and reactive compounds, are the target methods explored in this study for

characterizing subsurface attributes, such as fracture aperture distribution, effective heat transfer surface area, distribution of fluid residence times, and reservoir fluid volume.

In regards to predicting the thermal performance of an EGS, there is no established and tested method to adequately forecast the length of time an EGS reservoir can provide sufficient fluid temperatures and flow rates over its anticipated commercial operating lifetime. A particular cause of concern is that fluid flow in fractured rock is known to exhibit flow channeling in the presence of heterogeneous permeability, which is often present in discretely fractured rock. Flow channeling may negatively impact the commercial success of an EGS, because it can lower effective heat transfer surface areas and, as a consequence, cause production well temperature to decline faster than required to meet operating and design criteria for the power plant. Due to a substantial lack of field-tested methods for predicting reservoir lifetime, Goal 1 of this dissertation is:

> Goal 1: *Demonstrate, using field measurements, that heat transport in the presence of flow channeling can cause rapid thermal breakthrough.*

Inert tracers that flow passively through the subsurface are commonly used to replicate the flow distribution of reservoir fluids as they are circulated between one or more injection and production wells. An ideal inert tracer will not chemically degrade or adsorb on rock surfaces. Inert tracers have been used for characterizing the Residence Time Distribution (RTD) of circulating

fluids for decades (e.g., Horne, 1985; Pruess and Bodvarsson, 1984; Shook, 2001; Tester et al., 1979).

In addition to measuring fluid RTD between wells, measurements of inert tracer returns are commonly used to make forward models of reservoir performance. A "forward model", as it is utilized here, is essentially a prediction of transient production well temperature based on specified flow and temperature conditions in a reservoir with an idealized geometry calibrated via tracer return measurements. As will be discussed in detail in Chapter 2, however, forward models derived from inert tracer measurements do not provide a viable means for forecasting thermal breakthrough in geothermal reservoirs. In addition, often as a result of limited field data, numerous researchers deploy simplistic one-dimensional models of inert tracer transport which are used to infer effective formation properties and subsequently forecast thermal performance. In practice, tracer testing has failed to advance this goal, and led to Goal 2 of this dissertation which is:

> Goal 2: *Prove that inert tracer RTDs alone should be considered insufficient in efforts to forecast the thermal performance of an EGS.*

Because inert tracer tests provide insufficient information of reservoir properties needed for forecasting thermal performance, numerous researchers over several decades have supported the use of reactive tracers that can interrogate subsurface temperature distribution or heat transfer surface area (e.g. Robinson et al., 1988; Vetter and Crichlow, 1979). Unfortunately, as will

be discussed further in Chapter 2, reactive tracer testing remains as an experimental characterization technique for geothermal reservoir performance prediction. This shortcoming led to Goal 3 of this research, which is:

> Goal 3: *Promote the combined use of adsorbing, thermally degrading, and inert tracers for forecasting thermal breakthrough.*

1.3.1 Research Approach

Field experiments and even laboratory experiments have shown limited success in applying these methods in physical applications. What little success that has been achieved in laboratory studies has rarely been extended to large-scale field applications. Furthermore, lessons learned from large-scale field studies have been limited and unclear, due to insufficient characterization of the subsurface flow paths and fluid/rock surface interaction between injectors and producers.

An extensive review of studies investigating the use of reactive tracers was carried out before designing field experiments. As documented in Chapter 2, the review demonstrated that computational studies have shown, for decades now, that combining reactive and inert tracers should be investigated as a useful characterization technique. The shortcomings of these techniques in commercial operations, however, suggests that the following approach will benefit the advancement of reactive tracers:

1. Collect field measurements of inert and reactive tracer returns in a well-characterized fractured meso-scale reservoir to provide transient

thermal conduction relevant to and scalable to operating geothermal reservoirs.

2. Forecast thermal performance of the meso-scale system using various models for heat, mass, and reactive transport calibrated and validated with tracer return data.
3. Compare forecasted thermal performance from thermal-hydraulic models to field measurements.

1.3.2 Organization

The bulk of the dissertation will discuss the results of field measurements and modeling studies conducted between 2013 and 2016 (Chapters 5 to 9). Prior to these results, a literature review is presented in Chapter 2, followed by a description of the Altona field site in Chapter 3, and descriptions of some of the modeling approaches used in multiple chapters in Chapter 4. Finally, Chapter 10 presents major conclusions as well as an overall summary of these research efforts.

Chapters 5, 6, 7, and 8 cover heat exchange experiments, inert tracer tests, adsorbing tracers, and thermally degrading traces, respectively. The five inert tracer tests, four thermally degrading tracer tests, and the six day heat exchange experiment were all conducted over eight days in late October 2015. The Adsorbing tracer test data were collected in August 2016.

1.4 References

Axelsson, G., G. Björnsson, and F. Montalvo (2005), Quantitative interpretation of tracer test data, Proceedings, in *World Geothermal Congress*, Antalya, Turkey.

Brendebach, B. (2016), Decommissioning of nuclear facilities: Germany's experience, *IAEA Bulletin*, 57, 24-25.

Diaz, A. R., E. Kaya, and S. J. Zarrouk (2016), Reinjection in geothermal fields – A worldwide review update, *Renewable and Sustainable Energy Reviews*, 53, 105-162.

Hart, E. K., E. D. Stoutenburg, and M. Z. Jacobson (2012), The potential of intermittent renewables to meet electric power demand: Current methods and emerging analytical techniques, *Proceedings of the IEEE*, 100, 322-334.

Horne, R. N. (1985), Reservoir engineering aspects of reinjection, *Geothermics*, 14, 449-457.

Jacobson, M. Z., M. A. Delucchi, G. Bazouin, Z. A. F. Bauer, C. C. Heavey, E. Fisher, S. B. Morris, D. J. Y. Piekutowski, T. A. Vencill, and T. W. Yeskoo (2015), 100% clean and renewable wind, water, and sunlight (WWS) all-sector energy roadmaps for the 50 United States, *Energy & Environmental Science*, 8, 2093-2117.

Lund J., and T. Boyd (2015), Direct utilization of geothermal energy 2015 worldwide review. Proceedings, in *World Geothermal Congress*, Melbourne, Australia.

Matek, M. (2016), 2016 annual U.S. & global geothermal power production report, *Geothermal Energy Association*, Washington, D.C.

NYISO (2016), Solar Impact on grid operations – An initial assessment, *New York State Independent System Operator*.

Pruess, K., T. van Heel, and C. Shan (2005), Tracer testing for estimating heat transfer area in fractured reservoirs, Proceedings, in *World Geothermal Congress*, Antalya, Turkey.

Robinson, B.A., J.W. Tester, and L.F. Brown (1988), Reservoir sizing using inert and chemically reacting tracers, *SPE Formation Evaluation*, 2, 227-234.

Shook, G.M. (2001), Predicting thermal breakthrough in heterogeneous media from tracer tests, *Geothermics*, 30, 573-589.

Tester, J. W., R. M. Potter, R. L. Bivins (1979), Interwell tracer analyses of a hydraulically fractured granitic geothermal reservoir, Proceedings, in *54th Annual Technical Conference Exhibition of the Society of Petroleum Engineers of AIME*, Las Vegas, Nevada.

Tester, J. W. et al. (2006), The future of geothermal energy: Impact of enhanced geothermal systems (EGS) on the United States in the 21st century, *Technical Report*, Massachusetts Institute of Technology and Department of Energy Report, Idaho National Laboratory, INL/EXT-06-11746.

UN (2013), *Energy Statistics Yearbook*, Statistics Division, United Nations.

UN (2014), *Energy Statistics Yearbook*, Statistics Division, United Nations.

UN (2015), *World Population Prospects: The 2015 Revision*, Population Division, United Nations.

Vetter, O.J., and H.B. Crichlow (1979), Injection, injectivity and injectability in geothermal operations: Problems and possible solutions (Phase I – Definition of the Problems, *Technical Report*, U.S. Department of Energy – Geothermal Energy, SAN-2044-1.

CHAPTER 2: A REVIEW OF TRACER TESTING AND THERMAL PERFORMANCE IN GEOTHERMAL RESERVOIRS

2.1 Thermal Lifetime of Geothermal Systems

In geothermal reservoirs that actively reinject relatively cold fluids, reservoir operators are tasked with evaluating the potential for thermal drawdown at production wells due to interference from injection wells. As early as 1914, reinjecting fluids has been considered as a potentially ideal solution for geothermal waste water disposal (Horne, 1982b). The practice began as a convenient waste disposal method in hydrothermal systems (Einarsson et al., 1975; Gulati et al., 1978; Giovannoni et al., 1981), but substantial concern about the potential for production well temperature interference was raised (Horne, 1982b).

Bodvarsson (1972) was one of the first to point out this concern. Results of simple analytical models in one-dimension suggested that thermal effects may reach out several kilometers from the points of injection. As a result, it was suggested that reinjection wells must be sited considerable distances from producing wells. The concern has been discussed in numerous studies since then (e.g., Horne, 1982a, 1982b, Horne, 1985).

Fortunately, numerous studies demonstrated that reinjection could actually increase the longevity of a commercial geothermal operation (e.g., Tsang and Tsang, 1978; Bodvarsson et al., 1985; Pruess, 1995; Gringarten and Sauty, 1975; Kocabas and Horne, 1990; Gilardi and Horne, 1985). For

reinjection to benefit reservoir thermal longevity, it was proposed that injection would cause “sweeping” of heat from reservoir rocks and result in more efficient heat extraction (Horne, 1985).

2.1.1 Summary of Impacts from Reinjection

The first comprehensive review of the effects of reinjection was provided by Horne (1985). At this time, there was little data available and few reservoirs that had extensive experience with reinjection. Already, however, there was a mix of empirical data that suggested reinjection has an uncertain impact on the thermal performance of a geothermal reservoir. The data revealed that highly fractured geothermal reservoirs do not permit an even sweep of flow between injectors and producers. Instead, fluids appeared to be concentrated through highly permeable regions of the reservoir that thermally depletes a smaller portion of the rock than desired (Horne, 1985) (i.e. flow “channels”)

By 1997, there had been over 40 different geothermal fields developed in hydrothermal resources that conducted reinjection experiments. Of the 44 fields, 16 operated with reinjection as an integral part of reservoir management (Stefánsson, 1997). Reinjection induced cooling appeared to effect three of these fields, including Ahuachapán, in El Salvador (Vides-Ramos, 1985), Palinpinon, in the Philippines (Malate and O’Sullivan, 1991), and Svartsengi, in Iceland (Björnsson and Steingrimsson, 1992). Experience in these reservoirs suggested that reservoir cooling from reinjection did not result in major operational interruption. In Palinpinon, operators found that increasing well separation distance and/or allowing a reservoir to “rest” was an effective

strategy for dealing with thermal cooling. In reservoirs where reinjection is not performed, however, thermal cooling had been observed numerous times.

A more recent review by Diaz et al. (2016) has found that reinjection has in fact caused interruptions to production well temperature in numerous commercial reservoirs. In existing commercial reservoirs similar to an EGS (with non-boiling fluids at temperatures below 220 °C), this was found to be particularly true, largely because injection fluids for these types of reservoirs is typically intended to completely return to the production zone and are thus often closely spaced. Out of 19 global commercial operations actively reinjecting fluids with sufficient publically available data, Diaz et al. (2016) found that ten operations experienced production well thermal drawdown, likely as a direct result of thermal interference by reinjection wells.

2.1.2 Predicting Thermal Performance

Over the course of the commercial lifetime of a geothermal reservoir, proper reservoir management requires careful balancing between often conflicting goals. The following three are of particular concern for reservoirs which actively reinject production fluids: (1) optimize daily plant energy output; (2) dispose of waste water; and (3) prevent excessive declines in production well temperature (or enthalpy for two-phase or vapor-dominated systems). Reservoir engineers are commonly tasked with quantifying the potential for thermal interference by an injection well in a particular field and design and develop an appropriate reinjection scheme accordingly (Horne, 1985).

Theoretical studies investigating production well thermal drawdown have been a common starting point for anticipating production well thermal drawdown (e.g., Bodvarsson 1972, 1983; Dash et al., 1983; Murphy and Tester, 1979; O'Sullivan et al., 2001; Pruess and Bodvarsson, 1984; etc.). For many years, computational limitations prompted most researchers to use thermal-hydraulic analytical models that dramatically simplify fracture geometry and the pathway for fluid passing through them (e.g., Bodvarsson 1972, 1983; Dash et al., 1983; Gringarten et al., 1975; Murphy and Tester, 1979; Pruess and Bodvarsson, 1984; etc.).

Computational reservoir simulations that incorporate more sophisticated reservoir geometries and transport phenomena (e.g., dipole-flow, non-uniform permeability, fracture intersections, dual-porosity, etc.) had been utilized by a limited number of research groups (e.g. Los Alamos National Laboratory), but did not become well-established until in the 1980's, largely as a result of the 1980 Code Comparison Study (Stanford Geothermal Program, 1980). Despite overcoming computational limitations, simple one-dimensional analytical models are often still relied upon for practical investigations at a particular site (e.g. Axelsson et al., 1995, 2000, 2001, 2005; Kocabas, 2004; Kristjánsson et al., 2016; Shook, 2001; etc.). In general, this is because our computational ability for simulating complex reservoir geometries far outweighs our ability to quantitatively characterize fluid flow in a particular field-scale reservoir.

2.2 Inert Tracers

2.2.1 Background

Interrogating subsurface flow properties is remarkably difficult, particularly in geothermal reservoirs where fluid flow must be characterized over distances and at depths on the scale of 100s to 1000s of meters. Early treatment of fluid Residence Time Distribution (RTD) theory for chemical reactors and separators by Danckwerts (1953) provided a mathematical framework for characterizing fluid flow in geothermal reservoirs. Due to the importance of properly designing a reinjection program, tracer testing emerged as one of the most important tools for geothermal reservoir engineers (Horne, 1985; Shook and Forsmann, 2005).

Since the 1960's, tracer testing has been an invaluable tool for understanding subsurface flow characteristics in groundwater studies and oil and gas development (e.g., Brigham and Smith, 1965; Lewis, 1966; Mercado and Halevy, 1966). Initial tracer tests were conducted in oil and gas reservoirs as a means to characterize subsurface flow patterns induced during reservoir flooding for secondary oil recovery. Initial analysis was predominantly qualitative, focusing on tracer Residence Time Distribution (RTD), directional flow, and mass recovery. As discussed in Brigham (1965), predictive techniques emerged that could permit forecasting measures of extraction performance, such as the swept reservoir volume. For geothermal applications, however, reports of tracers used in geothermal reservoirs were scarce even up to 1981 (Vetter and Zinnow, 1981).

One notable exception, however, was the first interwell tracer tests conducted at the Fenton Hill Hot Dry Rock (HDR) experimental site in 1976 and 1977 (Tester et al., 1979). In these experiments, fluorescent dyes and radioactive bromide and iodide were used in tracer tests to "delineate changes in the fracture system, particularly in diagnosing new injection and production zones." They used advanced computational methods to compare the effectiveness of one- and two-dimensional dispersive models with single and dual porosity fracture zones. In addition, they managed to improve reservoir impedance through chemical leaching, although the improvements were considered insufficient for a major heat extraction test.

2.2.2 Applications in Geothermal Systems

Conventional tracer testing in geothermal reservoirs uses an inert (or "conservative") tracer which passively flows through the reservoir without undergoing surface reactions or thermal degradation. Empirical evidence presented in Horne (1982b, 1985) suggested that the tracer return speed is indicative of an injection wells propensity for causing thermal interference at a production well. Additional evidence supporting the use of inert tracers was presented in Tester et al. (1986). Through the use of field measurements and one-dimensional analytical equations, it was demonstrated that there was a roughly linear dependency between the mean tracer RTD and the surface area available for heat transfer based on field experiments conducted at the Fenton Hill EGS Experimental Site and the Rosemanowes Quarry in Cornwall, U.K.

It has long been known, however, that one-dimensional models provide no theoretical explanation for the correlations observed in Horne (1982b, 1985) and Tester et al. (1986). As discussed in Pruess and Bodvarsson (1984), the geometric simplifications required in a one-dimensional model prevent reasonable constraint of thermal impacts of reinjection, unless independent information regarding the surface area available for heat exchange is available.

Limitations of inert tracers, as pointed out in Pruess and Bodvarsson, (1984), prompted investigators to suggest the use of reactive tracers to interrogate heat transfer surface area and spatial and temporal temperature distribution (Vetter and Crichlow, 1979). Subsequent modeling efforts conducted at MIT and Los Alamos National Laboratory (LANL) during the Fenton Hill Hot Dry Rock geothermal project demonstrated that reactive tracers could be an invaluable tool for reservoir characterization and monitoring (Chemburkar, Brown, Travis, & Robinson, 1991; Nicol & Robinson, 1990; Robinson, Tester, & Brown, 1988). The two most prominent classes of reactive tracers are those which interrogate heat transfer surface area via adsorption reactions and those which interrogate subsurface temperature evolution via temperature-dependent reactions, such as thermal degradation.

2.3 Adsorption Tracers

Tracers experiencing adsorption are conventionally considered non-ideal in terms of characterizing geothermal reservoirs, particularly because of a “retardation” effect in which the true fluid velocities are obscured by “retarded” velocities that result from reversible and rapid adsorption. Combining an

adsorbing tracer with an inert tracer, however, may provide critical measurements of the surface area of rock in contact with circulating fluids. If a tracer with known adsorption properties is used in conjunction with an inert tracer, the adsorbing tracer will exhibit a time delay relative to the inert tracer that is proportional to the reactive surface area. Therefore, with sufficient knowledge of fracture surface roughness, the effective heat transfer surface area can be estimated with an appropriate mathematical model and tracer RTD measurements.

2.3.1 Background

Hill and Lake (1978) evaluated adsorbing tracers to be used as predictive techniques in forecasting oil and gas reservoir flooding for secondary recovery. They found that divalent-cation/surfactant interaction appears to be complicated by "characteristics of complex-ion formation." They conclude that "further knowledge regarding interactions between the surfactant system and reservoir components, such as rock minerals, crude oil, and divalent cations, is required before calculation of the changes in the ionic environment of a surfactant flowing through the reservoir can be accomplished satisfactorily."

In Byegård et al. (1998), a comprehensive laboratory investigation into ion adsorption on mineral surfaces was completed for the Äspö Hard Rock Laboratory in Sweden. This field laboratory produced numerous technical reports describing field and lab experiments relevant to fracture-dominated fluid flow in crystalline rock. Batch experiments showed that adsorption increases in the order of $Na^{+}<Ca^{2+}\approx Sr^{2+}<Rb^{2+}<Cs^{+}$. Adsorption partition

coefficients were found to depend greatly on mineralogy for some cations. Cs^+, for example, ranged over three orders of magnitude from 10^{-3} to 0.4 m^3/kg. In general, the report concludes that "it will be difficult to apply a simple reversible sorption-diffusion model to interpret the *in situ* results of the TRUE experiments with sorbing tracers." The TRUE experiments (Tracer Retention Understanding Experiments) were part of a program within the Äspö Hard Rock Laboratory that sought to "increase the understanding of the processes that govern retention of radionuclides in crystalline rock and to increase confidence in the computer models for radionuclide transport." They suggest that this difficulty is related to the challenges in measuring critical parameters relevant for adsorption.

2.3.2 Applications in the Geothermal Industry

In the geothermal industry, tracers experiencing adsorption were first investigated due to a concern that tracer retention would negatively impact tracer mass recovery and tracer test interpretations (e.g., D'Hooge et al., 1979; Horne et al., 1982c; Vetter and Crichlow, 1979; Wagner, 1977;). Specifically, the concern was that the retention of adsorbing tracers would produce a retardation effect in which true fluid velocities are greater than measured via tracer tests (Horne et al., 1982c; Vetter and Crichlow, 1979). In Vetter and Zinnow (1981), they state that, in "normal flow testing" adsorption on rock surfaces is "considered detrimental, and otherwise unaccountable losses of tracer are blamed on it."

Even with these initial concerns, however, researchers in the geothermal industry and the oil and gas industry noted that if adsorption reactions could be adequately characterized, they may permit insights into the Flow-Wetted Area (FWA). For example, Horne (1982c) concludes that "there is both a need and a significant advantage to quantifying the holdup mechanism." In Vetter and Crichlow (1979) they suggest using multiple tracers as a means to determine what effect adsorption had on apparent fluid velocities. They go on to claim that "different time delays between the breakthroughs of the different tracers are directly related to the surface area contacted by the two tracers injected into each well."

The first thorough laboratory investigation into the use of adsorbing tracers in geothermal reservoirs is presented in Vetter and Zinnow (1981). They conducted a comprehensive set of experiments investigating more than 20 candidate tracers, six lithologies, and three different brines. Despite some useful insights into inert tracer candidates, any adsorptive processes resulted in negligible curve separations.

The limited success in Vetter and Zinnow (1981) led to further laboratory investigations into tracer retention in geothermal reservoirs by Breitenbach (1982). It was determined that potassium iodide showed smaller retention values than sodium bromide under identical conditions. However, concentration was measured via ion electrodes. As a result, independent measurements of ions and cations are not available. They also found that the

effect of temperature appears to be a minor factor, although the results were not conclusive.

From 1982 to the 2000's, there was little interest in the use of adsorbing tracers for geothermal reservoir characterization. Several modeling studies completed in the 2000's and 2010's brought attention back to adsorption tracers for geothermal systems. Pruess et al. (2005) investigated the ability of adsorbing tracers to quantify heat transfer surface area using one-dimensional analytical models that incorporates the combined effects of advection, dispersion, matrix diffusion, and equilibrium adsorption. They found that the use of an adsorbing tracer may aid in identifying different transport mechanisms, such as matrix diffusion, hydrodynamic dispersion, and flow channeling. They added, however, that inadequate knowledge of mineralogical composition and aqueous solute chemistry will complicate making an unambiguous characterization of FWA.

At the end of the 2000's, the U.S. Department of Energy's Geothermal Technology Office invested over $350 million in geothermal projects with major funding provided by The American Recovery and Reinvestment Act of 2009. Several investigators were awarded research funds related to tracer testing. A collaboration between Pacific Northwest National Laboratory, Los Alamos National Laboratory, and Brookhaven National Laboratory developed models to simulate inert and reactive tracer behavior specifically for EGS reservoirs. They investigated ion exchange using a multicomponent numerical model for cation-

exchanging tracers. This approach attempted to account for all ion-exchanging species and incorporated a Cation Exchange Capacity (CEC) to describe the equilibrium between non-adsorbed and adsorbed ions (Williams et al., 2010).

The numerical work presented in Williams et al. (2010) was followed up with application to a field experiment in Williams et al. (2013). The main goal of the application to field data was to determine fracture aperture by fitting an inverse model to measured data. An adsorbing tracer test conducted at the commercially operating Soda Lake, Nevada site. The field experiments used 1,6-napthalene disulfonate (1,6-NDS) as an inert tracer and Safranin-T as combined adsorbing and thermally degrading tracer. Estimates of fracture aperture ranged dramatically from 0.2 to 20 mm. The wide range is attributed to inadequate knowledge of the adsorption partition coefficient and variable assumptions related to parameters involved in a “rim-zone” model. The “rim-zone” was introduced to explain tracer RTDs that deviate from the simple retardation approach, which assumes adsorption occurs only on the fracture surface. The rim-zone permits diffusive mass transfer of an adsorbing species.

Dean et al. (2015) conducted laboratory experiments to investigate cesium and lithium adsorption parameters in column and batch laboratory experiments relevant to the Newberry Volcano EGS Demonstration Project in central Oregon. They found numerous conflicting and concerning behaviors while conducting experiments under variable temperatures from 25 to 275 °C

and in the presence of five minerals (albite, calcite, chlorite, epidote, and quartz).

In summary, they found that:

1. Room temperature experiments under-predict lithium exchange and over-predict cesium exchange.
2. Lithium, which is typically considered a weakly adsorbing cation, experienced greater retardation than cesium, which is considered a strongly adsorbing cation.
3. Lithium and cesium appeared to exhibit dual-porosity behavior at high temperature, despite column experiments designed with only single-porosity.

They concluded that future work on adsorption tracers should "include more detailed examination of both the physical and chemical characteristics of the rim zone, which are likely to be system specific." The "rim zone" they refer to was presented as a possible explanation for the complex observations listed above.

2.3.3 Summary

Despite being proposed several decades ago, the use of adsorbing tracers has advanced little as of 2017. Computational models continue to suggest adsorption tracers would be an ideal reactive tracer for characterizing the flow-wetted area. However, laboratory studies and field studies have not proven that adsorbing tracers can be practically used. The major issues in characterizing adsorption can be broadly grouped into three categories: (1) poorly constrained reaction parameters (e.g., Reimus et al., 2003. 2007; Fox and Horne, 1988;

Gray and Darley, 1980; Breitenbach, 1982; Sumner, 1963; Sullivan et al., 2003; Staunton et al., 2002; Giannakopoulou et al., 2007); (2) incomplete models for adsorption (e.g., Donato and Blunt, 2004; Toride at al., 1993, 1995; Carroll et al., 2010; James and Rubin, 1979; Fortin et al., 1997) and (3) complex fracture fluid/matrix interactions (e.g., Shang et al., 1994; Pot and Genty, 2005; Natarajan and Kumar, 2014). A detailed review of the major factors influencing adsorption of ions on mineral surfaces is provided in Cornell (1993).

2.4 Thermally Degrading Tracers

2.4.1 Background

The first extension of RTD theory to reactive transport was discussed in the context of catalytic reactors. Orcutt et al. (1962) was the first to apply RTD theory to conditions other than homogeneous and isothermal. Nauman (1977) presents the theory of "thermal time distributions" which is a temperature-weighted time determined from integrating the Arrhenius temperature-dependent rate constant over the flow path of a molecule traveling through a reactor. Similar developments are described in Nauman (1981) and Nauman and Buffham (1983).

In the oil and gas industry, temperature-dependent reactive tracers were first proposed and tested in the 1970's. Tomich et al. (1973) described and demonstrated that residual oil saturation in water could be measured, in-situ, by taking advantages of reaction in which a reaction product or reactant is insoluble in one of the two phases. The technique was successfully

demonstrated in four field tests at temperatures as high as 90 °C and in wide ranging salinities. They found that residual oil saturations measured via reactive tracers was within the range measured by water-flooding in a core sample, but higher than obtained by vacuum distillation of cut core. Water flooding uses pressure driven water to flow through the unsaturated media which displaces the residual oil. Vacuum distillation removes residual oil from the core by circulating an inert gas (e.g., argon) through the core kept at high temperature.

2.4.2 Application to the Geothermal Industry

Thermally degrading tracers are intended to permit forecasting of thermal breakthrough in geothermal reservoirs that actively inject relatively cold fluids within geothermal production zones. The first work on thermally degrading tracers in geothermal reservoirs was done by Bruce Robinson and Jefferson Tester at the Massachusetts Institute of Technology (MIT) and other colleagues at Los Alamos National Laboratory (e.g., Robinson et al., 1984, 1988; Robinson, 1985; Robinson and Birdsell, 1987; Tester et al., 1986). Their initial work in the 1980's primarily covered theory and laboratory experiments, with some applications to the limited field data that was available. Theoretical work began with steady-state flow through a non-isothermal system including the effects of advection, dispersion, and thermal degradation. Flow geometry assumed a parallel plug flow reactor model that treats a measured tracer RTD as a series of flow channels with different geometric properties.

The initial experimental work investigated the use of several candidate tracers, including silicic acid, ethyl acetate, ethyl propionate, benzamide, etc. For eight tracers, reaction rates were measured as a function of temperature to determine parameters of the Arrhenius Equation. Lab experiments were also conducted in which the transient temperature response of column effluent as monitored as cold fluid circulated through hot sediments. Using the same experimental apparatus, inert and reactive column tests were carried out to determine if theoretical developments could be successfully applied to measured data in the presence of a non-isothermal flow field.

2.4.3 Field Experiments in Geothermal Reservoirs

After the initial theoretical and laboratory work in the early and mid-1980's showed considerable promise, several attempts were made to conduct degrading tracer tests in field experiments in commercial or experimental geothermal sites. The first documented field test was conducted at the Rosemanowes Phase II HDR experimental reservoir (Kwakwa, 1988; Batchelor, 1986; Tester et al., 1986). Two degrading tracers with different reaction rates were used in combination with the inert sodium-fluorescein tracer. Isopentyl acetate (slow reaction rate) and Ethyl Acetate (rapid reaction rate) were used as the thermally degrading tracers. After 13.4 h, ethyl acetate experienced roughly 50% degradation, based on the molar recovery of the reactant and the product, ethanol. This field test was encouraging, suggesting that hydrolysis of esters could be used as a target reaction in geothermal fields. Only a qualitative analysis was available, however, because the Arrhenius Equation parameters

were not independently measured. No further tracer tests were documented in published records at the Rosemanowes site.

In 1989, another thermally degrading tracer test was conducted, this time at a commercial geothermal field known as the Dixie Valley Geothermal field in Nevada. In this experiment, benzoic acid and fluorescein were used as inert and reactive tracers, respectively (Adams et al., 1989, Adams and Davis, 1991). The investigators claim that they were able to accurately estimate a reservoir temperature of roughly 230 °C.

After reviewing the work of Adams and co-workers, however, their conclusion that the thermally degrading tracer experienced degradation consistent with measured downhole temperature does not appear to be the only explanation for the observed tracer behavior. The results of their tracer test are reproduced below in Figure 2.1. In Adams et al. (1989, 1991), they present the tracer return concentration as a raw value (i.e., without normalizing for differing mass injected). In Figure 2.1, tracer concentration has been normalized using their reported values for the mass of tracer injected. As can be seen in the figure, the concentration of the thermally degrading tracer and the inert tracer appear to converge at late residence times. This result should have been considered unexpected, because a thermally degrading tracer transported through a reservoir at a constant temperature should experience greater degradation at longer residence times. In their measurements, however,

they observed a lower reactivity at late time. The authors did not provide an explanation for this apparent discrepancy.

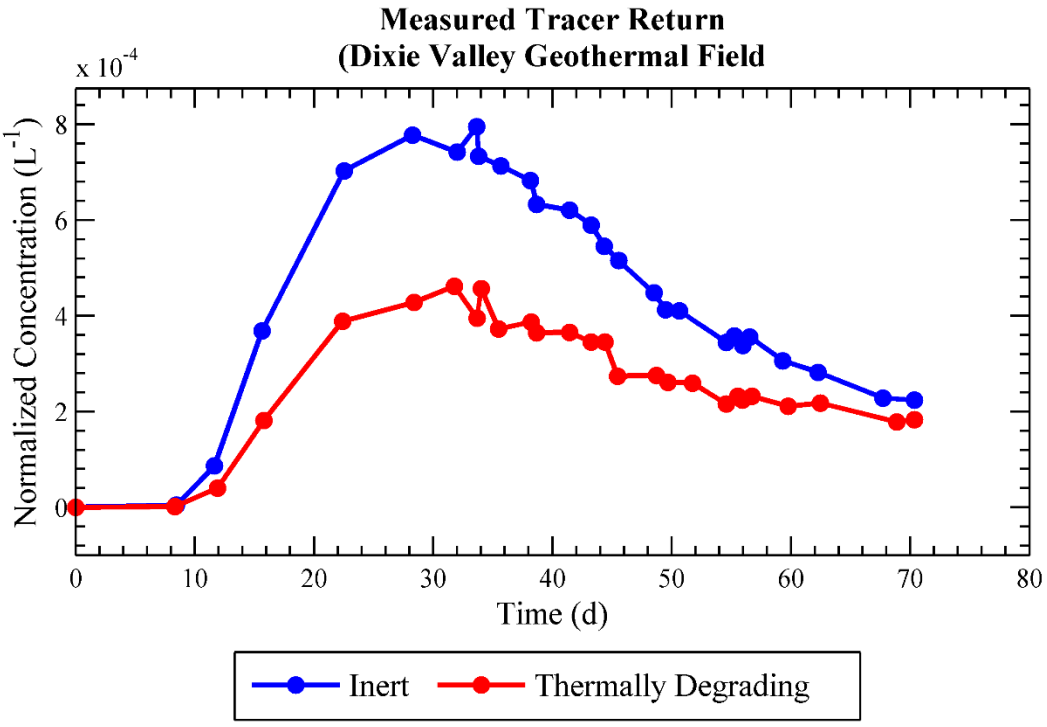

Figure 2.1. Tracer return data reproduced from Adams et al. (1989, 1991). Data were collected as part of a thermally degrading tracer test conducted at the Dixie Valley Geothermal Field. The thermally degrading tracer, fluorescein, is marked by orange dots and the inert tracer, benzoic acid, is marked by blue dots. Concentration is normalized by dividing measured concentration by the reported mass injected of each tracer.

In Rose et al. (2001) and Rose and Clausen (2015), the tracer test data collected at Dixie Valley in 1997 was further investigated using the latest information regarding Amino G as a thermally degrading tracer. They did not, however, provide new interpretation of the original analysis presented in Adams et al. (1989, 1991). Reed (2007) investigated the Dixie Valley data using temporal moment analysis, but was limited to analysis of only the inert tracers.

At the Fenton Hill HDR experimental site operated by Los Alamos National Laboratory, an attempt was made to use reactive tracers to determine the progression of a thermal front after roughly 2 months of continuous heat extraction and reinjection (Du Teaux and Callahan, 1996). In May of 1992, sodium fluorescein was used as a thermally degrading tracer in conjunction with the inert tracer p-toluene sulfonic acid. After two months of heat extraction, the reactive tracer test was repeated to determine if the cold front progression could be determined.

Unfortunately, the results of these two field tests were inconclusive, because the reactive tracer experienced less mass recovery after two months of cold water injection. At the measured modal volume, where the recovered tracer concentration reaches a maximum, the initial thermally degrading tracer experienced a difference of 24% less recovery than the inert tracer. After two months of heat extraction, however, the thermally degrading tracer experienced even greater degradation, with 44% less recovery at the modal volume compared to the inert tracer. Since this is a hot reservoir with cold water injection, the second tracer test should have exhibited an increased reactive tracer recovery if a significant cold front had developed.

The authors provide little explanation for this discrepancy except to suggest that dynamic changes in reservoir geometry could have resulted in injection fluids accessing new regions of the reservoir which were at colder temperatures. They suggest that this could result in higher reactive tracer

recovery as well as a higher modal volume (277 vs. 369 m^3). This explanation is not supported by any theory or field measurements provided in their article.

During long-term circulation tests at a HDR test site in Hijiori, Japan, 12 tracer tests were conducted between 2000 and 2002 (Matsunaga et al., 2002). They used salts of potassium-iodide and potassium-bromide as well as NDS, and uranine (i.e. di-sodium fluorescein). While uranine is a thermally degrading tracer, it likely did not experience appropriate conditions for reaction under the short residence times (roughly 1 – 7 days) and temperatures (injection at roughly 25 °C and production roughly 100 - 180 °C) experienced. Nevertheless, the tracer tests conducted at Hijiori likely represent the most consistent set of tracer experiments conducted over the duration of heat extraction (12 tracer tests over roughly 2 y).

In 2003, three experiments were conducted in HDR type reservoirs in Germany (Behrens et al., 2006, 2009; Jung et al., 2005; Ghergut et al., 2007, 2010, 2013a, 2013b). In 2003, dual tracer push/pull tests were conducted at Urach-3, which is a geothermal well in the Southern-German crystalline basement in the Deep Continental Drilling program. Fluorescein di-sodium was used as the degrading tracer in combination with the inert tracer napthalene-1,5-disulfonate. Conflicting tracer returns revealed that the inert and reactive tracers experienced mass recoveries of 33 and 55%, respectively, after producing a volume three times larger than the volume injected. The fact that three times the injection volume was removed suggests that this particular

reservoir had significant water saturation prior to the tracer test. According to Behrens et al. (2009), the most probable explanation was that the inert tracer did not dissolve completely prior to the start of the field test. They reason that even though the inert tracer had very good solubility, it dissolves at slower rate than the reactive tracer.

In 2004, push-pull tests were conducted in a pilot well at the Kontinentale Tiefbohrung (KTB) site. Five different tracer compounds were used in the tests, including tritiated water (i.e., tritium), krypton gas, uranine, NDS, and pyrene-1,3,6,8-tetra sulphonic acid (PTS). The thermally degrading tracer, uranine, experienced a mass recovery of roughly 50%. In contrast, the inert tracers tritium, NDS, and PTS, which ranged from roughly 85% to 90% (Ghergut et al., 2007). There does not appear to be mass recovery data available for krypton. Behrens et al. (2009) suggests that interpretation of these tracer data "remains speculative," because the controlling processes of adsorption and diffusion were not yet clarified. As of 2017, no further documentation of the analysis of the tracer data at KTB was found.

At the Hortsberg site, the thermally degrading tracer uranine was used in combination with two inert tracers (tritium and NDS) (Behrens et al., 2006; Ghergut et al., 2007, 2009; Jung et al., 2005). Initial analysis of uranine was performed in the field with the use of a fluorometer. Despite detecting the two inert tracers, uranine was not found during in-field measurements. It was later discovered, however, that uranine experienced reduction and, as a

consequence, lost its fluorescent properties. After correcting the tracer data, the result of the push-pull test showed that 6.4% of uranine was recovered compared to 7.4% and 10% for HTO and NDS, respectively.

The three examples of thermally degrading tracer tests conducted at the Deep Continental Drilling program in Germany were a mixed success. On one hand, they were able to demonstrate that uranine experiences reduced mass recovery relative to several inert tracers, including tritium, NDS, and PTS. This was demonstrated at the Hortsberg site and the KTB site. At the Urach-3 site, however, the inert tracer NDS had less mass recovery than the degrading tracer, fluorescein di-sodium. Behrens et al. (2009) suggests that this apparent discrepancy resulted from inadequate tracer preparation. Analysis of the successful field tests was limited to qualitative comparisons, however, likely because the necessary Arrhenius reaction rate parameters were not available. Behrens et al. (2009) makes an additional note that "it seems difficult to guarantee that thermal decay parameters quantified under laboratory conditions will remain predictable under reservoir conditions."

From 2008 to 2011, there was a large effort to investigate new thermally degrading tracers and subsequently test them in field experiments. In 2008 and 2010, tracer tests were conducted at the Raft River Geothermal site as part of a large effort to evaluate thermally degrading tracers. These two experiments used only inert tracers while a thermally degrading tracer test was planned afterwards.

For example, Plummer et al. (2011) repeated the results of two thermally degrading tracer tests conducted at the Raft River site in 2010. The first used fluorescein disodium and butyramide as an inert and reactive tracer, respectively. The second test was conducted one month later and used NDS and acetamide as the inert and reactive tracer, respectively. The results were very encouraging, revealing that the deviation in concentration between inert and reactive tracers RTDs match extremely well with simulations using known Arrhenius parameters from Robinson and Tester (1990) and measured down-hole temperature (139.3 °C). Because of the short time span in-between, however, thermal drawdown in the reservoir was likely insufficient to see a change in the reactive tracer. Nevertheless, this field test may be considered the first well described and successful field application of a thermally degrading tracer to measure sub-surface reservoir temperature. As of 2017, however, the analysis of their reactive tracer tests could not be found in the scientific literature or conference proceedings.

Table 2.1 Summary of previous field tests using thermally degrading tracers.

Location	*Year*	*Result*	*Field Tests*	*Temperature Change?*	*Reference*
Rosemanowes	1986	Qualitative success	1	no	Kwakwa, 1988
Dixie Valley	1989	Possible success	1	no	Adams and Davis, 1991
Fenton Hill	1992	Inconclusive	2	n/a	Du Teaux and Callahan, 1996
Steamboat Hills	1998	Qualitative Success	2	no	Rose et al., 1999
Hijiori	2000	Inconclusive	12	n/a	Matsunaga et al., 2005
Urach-3	2003	Unsuccessful	1	no	Behrens et al., 2009
KTB	2003	Qualitative success	1	no	Behrens et al., 2009
Hortsberg	2003	Qualitative success	1	no	Behrens et al., 2009
Raft River	2010	Quantitative success	2	no	Plummer et al., 2011
Soda Lake	2011	Inconclusive	1	no	Rose et al., 2012
Dessert Peak	2015	Qualitative	1	no	Rose et al., 2017

2.4.4 Laboratory and Computational Investigations

In the 1990s, investigations into candidate tracers included Adams [1992], Rose and Adams (1994). More recent laboratory studies investigating candidate tracers is presented in Behrens et al. (2009), Nottebohm et al. (2012), Rose and Clausen (2015), and Schaffer et al. (2015). Recent column tests are presented in Maier et al. (2015). Computational investigations were presented in Plummer et al. (2010, 2011a, 2011b, 2012), Williams et al. (2010, 2013), and Ghergut et al. (2014).

2.4.5 Summary

As is the case for adsorbing tracers, the use of thermally degrading tracers remains an attractive, yet unproven, method for characterizing geothermal reservoirs. The initial work primarily done in collaboration between MIT and Los Alamos National Laboratory began over 30 years ago. Since then, thermally degrading tracers have been used in at least 10 different geothermal reservoirs. Of these, five can be broadly classified as a "qualitative" success as they were able to demonstrate reduced tracer mass recoveries relative to an inert tracer.

To date, however, these tracers are not considered reliable as a practical tool for measuring *in situ* temperature or forecasting thermal performance. Typically, unknown, poorly constrained, or inappropriate reaction kinetics are, at least partially, at fault. Examples of this can be seen in the experimental results of tests at Rosemanowes, Fenton Hill, Hijiori, and Soda Lake (Du Teaux and Callahan, 1996; Kwakwa, 1988; Matsunaga et al., 2005; Rose et al., 2012). In other examples, inadequate tracer injection strategies may have been involved, such as at Urach-3 (Behrens et al., 2009) or at Steamboat Hills (Rose et al., 1999).

The only field test shown in Table 2.1 that is reasonably considered a quantitative success was conducted at the Raft River geothermal field (Plummer et al., 2011). However, as of this writing the results of this test could only be found in reporting documents between the researchers and their funding agency, the Department of Energy's Geothermal Technology Office. An

independent evaluation of their analysis was attempted, but the documents presented did not contain sufficient details of the experiment and analysis.

2.5 References

Adams, M. C., W. P. Benoit, C. Doughty, G. S. Bodvarsson, J. N. Moore (1989), The Dixie Valley, Nevada tracer test, *Transactions of the Geothermal Resources Council*, 13, 215-220.

Adams, M. C., and J. Davis (1991), Kinetics of fluorescein decay and its application as a geothermal tracer, *Geothermics*, 20, 53-66.

Adams, M. C., J. N. Moore, G. L. G. Fabry, and J. H. Ahn (1992), Thermal stabilities of aromatic acids as geothermal tracers, *Geothermics*, 21, 323-339.

Axelsson, G., G. Bjornsson, Ó. G. Flovenz, H. Kristmannsdóttir, G. Sverrisdóttir (1995), Injection experiments in low-temperature geothermal areas in Iceland, Proceedings, in *World Geothermal Congress*, Florence, Italy.

Axelsson, G., Ó. G. Flovenz, A. Hjartarson, S. Hauksdottir, G. Sverrisdottir, F. Arnason, A. Arnason, and R. Bodvarsson (2000), Thermal energy extraction by reinjection from the Laugaland geothermal system in N-Iceland, Proceedings, in *World Geothermal Congress*, Kyushu-Tohoku, Japan.

Axelsson, G., O.G. Flovenz, S. Hauksdottir, A. Hjartarson, and J. Liu (2001), Analysis of Tracer Test Data, and Injection-Induced Cooling, in the Laugaland Geothermal Field, N-Iceland, *Geothermics*, 30, 573-589.

Axelsson, G., G. Björnsson, and F. Montalvo (2005), Quantitative Interpretation of Tracer Test Data, Proceedings, in *World Geothermal Congress*, Antalya, Turkey.

Batchelor, A. S. (1986), Reservoir behaviour in a stimulated Hot Dry Rock system, Proceedings, in *11th Workshop on Geothermal Reservoir Engineering*, Stanford University, Stanford, California.

Behrens, H., I. Ghergut, T. Licha, M. Lodemann, J. Orzol, and M. Sauter (2006), Reactive behavior of uranine (fluorescein) in a deep geothermal-reservoir tracer test, *Geophysical Research Abstracts*, 8, 10448.

Behrens, H., I. Ghergut, M. Sauter, and T. Licha (2009), Tracer properties and spiking results (from geothermal reservoirs), Proceedings, in *34th Workshop on Geothermal Reservoir Engineering*, Stanford University, Stanford, California.

Björnsson, G., and B. Steingrimsson (1992), Fifteen years of pressure and temperature monitoring in the Svartsengi geothermal field, Iceland, *GRC Transactions*, 16, 627-632.

Bodvarsson, G. (1972), Thermal problems in the siting of reinjection wells, *Geothermics*, 1, 63-66.

Bodvarsson, G. S., K. Pruess, and M. J. O'Sullivan (1983), Injection and energy recovery in fractured geothermal reservoirs, *Society of Petroleum Engineers Journal*, 25, 303-312.

Bodvarsson, G. S., K. Pruess, V. Stefansson, S. Bjornsson, and S. B. Ojiambo (1985), A summary of modeling studies of the East Olkaria Geothermal Field, Kenya, Proceedings, in *Geothermal Resources Council International Symposium on Geothermal Energy*, Kailua-Kona, Hawaii.

Breitenbach, K. A. (1982), Chemical tracer retention in porous media, *M.S. Thesis*, Stanford University.

Brigham, W. E. and D. H. Smith (1965), Prediction of tracer behavior in five-spot flow, Proceedings, in *Society of Petroleum Engineers Conference on Production Research and Engineering*, Tulsa, Oklahoma.

Byegård, J., H. Johansson, and M. Skålberg (1998), The Interaction of Sorbing and Non-Sorbing Tracers with Different Äspö Rock Types, *Technical Report*, Swedish Nuclear Fuel and Waste Management Co, Stockholm, Sweden.

Carroll, S., R. Tinnacher, A. Kersting, M. Zavarin (2010), A discussion of reversible and irreversible sorption for Sr, Cs, Np, and Pu, Livermore, California: *Lawrence Livermore National Laboratory*.

Chemburkar, R. M., F.F. Brown, B.J. Travis, and B.A. Robinson (1991), Numerical determination of temperature profiles in flowing systems from conversions of chemically reacting tracers, *Chemical Engineering Science*, 46, 1349-1360. doi: 10.1016/0009-2509(91)85062-3.

Cornell, R. M. (1992), Adsorption of cesium on minerals: A review, *Journal of Radioanalytical and Nuclear Chemistry, Articles*, 171, 483-500.

Dash, Z. V., H. D. Murphy, R. L. Aamodt, R. G. Aguilar, D. W. Brown, D. A. Counce, H. N. Fisher, C. O. Grigsby, H. Keppler, A. W. Laughlin, R. M. Potter, J. W. Tester, P.E. Trujillo Jr., G. Zyvoloski (1983), Hot Dry Rock Geothermal Reservoir Testing – 1978 to 1980, *Journal of Volcanology and Geothermal Research*, 15, 59-99.

Dean, C., P. Reimus, J. Oates, P. Rose, D. Newell, and S. Petty (2015), Laboratory experiments to characterize cation-exchanging tracer behavior for fracture surface area estimation at Newberry Crater, OR, *Geothermics*, 53, 213-224.

D'Hooge, J. A., C. Q. Sheely, and B. J. Williams (1981), Interwell tracers – an effective reservoir evaluation tool: West Sumatra field results, *Society of Petroleum Engineers*, 33, 779-782.

Diaz, A. R., E. Kaya, and S. J. Zarrouk (2016), Reinjection in geothermal fields – A worldwide review update, *Renewable and Sustainable Energy Reviews*, 53, 105-162.

Donato, G. D. and M. J. Blunt (2004), Streamline-based dual-porosity simulation of reactive transport and flow in fractured reservoirs, *Water Resources Research*, 40, W04203, doi: 10.1029/2003WR002772.

Du Teaux, R. T., and J. Callahan (1996), Comparing reactive and non reactive tracers to measure changes in liquid dominated, fractured geothermal reservoirs, Proceedings, in *Annual Meeting of the Geothermal Resources Council*, Portland, Oregon.

Einarsson, S. S., A. Vides, G. Cuellar (1975), Disposal of geothermal waste by reinjection, Proceedings, in *Second United Nations Symposium on the Development and Use of Geothermal Resources*, 2, 1349-1363.

Fortin, J., M. Flury, W. A. Jury, and T. Streck (1997), Rate-limited sorption of simazine in saturated soil columns, *Journal of Contaminant Hydrology*, 25, 219-234.

Fox, C.E., and R. N. Horne (1988), Determination of fracture aperture: A multi-tracer approach, *Transactions of the Geothermal Resources Council*, 12, 449-456.

Ghergut, I., M. Sauter, H. Behrens, T. Licha, C. I. McDermott, M. Herfort, P. Rose, G. Zimmerman, J. Orzol, R. Jung, E. Huenges, O. Kolditz, M. Lodemann, S. Fischer, U. Wittig, F Güthoff, and M. Kühr (2007), Tracer testing evaluating hydraulic stimulation at deep geothermal reservoirs in Germany, Proceedings, in *32nd Workshop on Geothermal Reservoir Engineering*, Stanford, California.

Ghergut, I., M. Sauter, H. Behrens, T. Licha, T. Tischner, and R. Jung (2009), Single-well dual-tracer spikings during EGS creation in Northern-German sedimentary layers, Proceedings, in *34th Workshop on Geothermal Reservoir Engineering*, Stanford University, Stanford, California.

Ghergut, I., H. Behrens, M. Sauter (2010), Tracer properties and tracer test results (from geothermal reservoir testing): Part 2, Proceedings, in *35th Workshop on Geothermal Reservoir Engineering*, Stanford University, Stanford, California.

Ghergut, I., H. Behrens, T. Licha, and M. Sauter (2013a), Tracer-based prediction of thermal lifetime: Scope, limitations, and the role of thermosensitive tracers, Proceedings, in *38th Workshop on Geothermal Reservoir Engineering*, Stanford University, Stanford, California.

Ghergut, I., H. Behrens, R. Jung, M. Sauter, and T. Tischner (2013b), A piece of 'Geothermal Art' in the N-German Basin: Hortsberg 2004, Revisited, Proceedings, in *38th Workshop on Geothermal Reservoir Engineering*, Stanford University, Stanford, California.

Ghergut, I., H. Behrens, M. Sauter (2014), Tracer-based quantification of individual frac discharge in single-well multiple-frac backflow: Sensitivity study. *Energy Procedia*, 59, 235-242.

Giannakopoulou, F., C. Haidouti, A. Chronopoulou, and D. Gasparatos (2007), Sorption behavior of cesium on various soils under different pH levels, *Journal of Hazardous Materials*, 149, 553-556.

Gilardi, J., and R. N. Horne (1985), Experimental determination of tracer dispersivity in fractures, Proceedings, in *10th Workshop on Geothermal Reservoir Engineering*, Stanford University, Stanford, California.

Giovannoni, A., G. Allegrini, G. Cappetti, and R. Celati (1981), First results of reinjection experiment at Larderello, Proceedings, in *7th Workshop on Geothermal Reservoir Engineering*, Stanford University, Stanford, California.

Gray, G. R., and H. C. H. Darley (1980), *Composition and Properties of Oil Well Drilling Fluids*, 4th ed. Gulf Publishing Co., Houston, Texas.

Gringarten, A.C., P.A. Witherspoon, and Y. Ohnishi (1975), Theory of heat extraction from fractured hot dry rock, *Journal of Geophysical Research.*, 80, 1120-1124.

Gulati, M. S., S. C. Lipman, and C. J. Strobel (1978), Tritium tracer tests at the Geysers, *Transactions of the Geothermal Resources Council*, 2, 237-239.

Hill, H. J., and L. W. Lake (1978), Cation exchange in chemical flooding: Part 3 – Experimental, Proceedings, in *Society of Petroleum Engineers of AIME*, Denver, Colorado.

Horne, R. N. (1982a), Geothermal reinjection experience in Japan, Proceedings, in *Society of Petroleum Engineers of AIME*, Bakersfield, California

Horne, R. N. (1982b), Effects of water injection into fractured geothermal reservoirs: A summary of experience worldwide, *Technical Report*, Stanford Geothermal Program, SGP-TR-57.

Horne, R. N., K. A. Breitenbach, and M. P. Fossum (1982c), Retention of chemical tracers in geothermal reservoirs, Proceedings, in *8th Workshop on Geothermal Reservoir Engineering*, Stanford University, Stanford, California.

Horne, R. N. (1985), Reservoir engineering aspects of reinjection, *Geothermics*, 14, 449-457.

James, R. V., and J. Rubin (1979), Applicability of the local equilibrium assumption to transport through soils of solutes affected by ion exchange, Proceedings, in *the 176th meeting of the American Chemical Society*, Miami Beach, Florida.

Jung, R., J. Orzol, R. Jatho, P. Kehrer, and T. Tischner (2005), The Genesys-Project: Extraction of geothermal heat from tight sediments, Proceedings, in 30th *Workshop on Geothermal Reservoir Engineering*, Stanford University, Stanford, California.

Kocabas, I., and R. N. Horne (1990), A new method of forecasting the thermal breakthrough time during reinjection in geothermal reservoirs, Proceedings, in *15th Workshop on Geothermal Reservoir Engineering*, Stanford University, Stanford, California.

Kocabas, I (2004), Geothermal reservoir characterization via thermal injection backflow and interwell tracer testing, *Geothermics*, 34, 27-46.

Kristjánsson, B.R., G. Axelsson, G. Gunnarsson, I. Gunnarsson, and F. Óskarsson (2016), Comprehensive tracer testing in the Hellisheidi Geothermal Field in SW-Iceland, Proceedings, in *41st Workshop on Geothermal Reservoir Engineering*, Stanford University, Stanford, California.

Kwakwa, K. A. (1988), Tracer measurements during long-term circulation of the Rosemanowes HDR geothermal system, Proceedings, in *13th Workshop on Geothermal Reservoir Engineering*, Stanford University, Stanford, California.

Lewis, D. C., G. J. Kriz, Burgy, R. H. (1966), Tracer diultion sampling to determine hydraulic conductivity of fractured rock. *Water Resources Research*, 2, 533-542.

Maier, F., M. Schaffer, and T. Licha (2015), Temperature determination using thermo-sensitive tracers: Experimental validation in an isothermal column heat exchanger, *Geothermics*, 53, 533-539, doi:10.1016/j.geothermics.2014.09.007.

Malate, R. C. M., and M. J. O'Sullivan (1991), Modelling of chemical and thermal changes in well PN-26 Palinpinon geothermal field, Phillipines, *Geothermics*, 20, 291-318.

Matsunaga, I, N. Yanagisawa, H. Sugita, and H. Tao (2002), Reservoir monitoring by tracer testing during a long term circulation test at the Hijiori HDR site, Proceedings, in *37th Workshop on Geothermal Reservoir Engineering*, Stanford University, Stanford, California.

Mercado, A., and E. Halevy (1966), Determining the average porosity and permeability of a stratified aquifer with the aid of radioactive tracers, *Water Resources Research*, 2, 525-531.

Murphy, H. D., and J. W. Tester (1979), Heat production from a geothermal reservoir formed by hydraulic fracturing – comparison of field and theoretical results, Proceedings, in *SPE Annual Technical Conference and Exhibition*, Las Vegas, Nevada.

Natarajan, N., and G. S. Kumar (2014), Spatial moment analysis of solute transport with Langmuir sorption in a fracture-skin-matrix coupled system, *Journal of King Saud University – Engineering Sciences*, 28, 157-164.

Nauman, E. B. (1977), Nonisothermal reactors: Theory and application of thermal time distributions, *Chemical Engineering Science*, 32, 359-367.

Nauman, E. B. (1981), Residence time distributions and micromixing, *Chemical Engineering Communications*, 8, 53-131.

Nauman, E. B., and Buffham, B. A. (1983), *Mixing in Continuous Flow Systems*. Wiley, New Jersey.

Nicol, D. A., and B. A. Robinson (1990), Modelling the heat extraction from the Rosemanowes HDR reservoir. *Geothermics*, 19.

Nottebohm, M., T. Licha, and M. Sauter (2012), Tracer design for tracking thermal fronts in geothermal reservoirs, *Geothermics*, 43, 37-44.

Orcutt, J. C., J. F. Davidson, R. L. Pigford (1962), Reaction time distributions in fluidized catalytic reactors, *Chemical Engineering Program Symposium Series*, 32, 1-15.

O'Sullivan, M. J., K. Pruess, and M. J. Lippmann (2001), State of the art of geothermal reservoir simulation, *Geothermics*, 30, 395-429.

Plummer, M. A., C. D. Palmer, E. D. Mattson, G. D. Redden, L. C. Hull (2010), Advancing reactive tracer methods for monitoring thermal drawdown in geothermal enhanced geothermal reservoirs, Proceedings, in *35th Workshop on Geothermal Reservoir Engineering*, Stanford University, Stanford, California.

Plummer, M. A., C. D. Palmer, E. D. Mattson, and L. C. Hull (2011a), A reactive tracer analysis method for monitoring thermal drawdown in geothermal reservoirs, Proceedings, in the *36th Workshop on Geothermal Reservoir Engineering*, Stanford University, Stanford, California.

Plummer, M. A., E. D. Mattson, C. D. Palmer, G. Redden, G. Elias, and L. Hull (2011b), Advancing reactive tracer methods for measurement of thermal evolution in geothermal reservoirs: Final report, *Technical Report*, Stanford Geothermal Program, Idaho National Laboratory Geothermal Technologies Program, Idaho Falls, Idaho, INL/EXT-11-22632.

Plummer, M. A., C. D. Palmer, L. C. Hull, and E. D. Mattson (2012), Sensitivity of a reactive-tracer based estimate of thermal breakthrough in an EGS to properties

of the reservoir and tracer, Proceedings, in *37th Workshop on Geothermal Reservoir Engineering*, Stanford University, Stanford, California.

Pot, V., and A. Genty (2005), Sorbing and non-sorbing solute migration in rough fractures with a multi-species LGA Model: Dispersion dependence on retardation and roughness, *Transport in Porous Media*, 59, 175-196.

Pruess, K., and G. S. Bodvarsson (1984), Thermal effects of reinjection in geothermal reservoirs with major vertical fractures, *Journal of Petroleum Technology*, 36, 1567-1578.

Pruess, K., T. van Heel, and C. Shan (2005), Tracer testing for estimating heat transfer area in fractured reservoirs, Proceedings, in *World Geothermal Congress*, Antalya, Turkey.

Reed, M. J. (2007), An investigation of the Dixie Valley Geothermal Field, Nevada, using temporal moment analysis of tracer tests, Proceedings, in *32nd Workshop on Geothermal Reservoir Engineering*, Stanford University, Stanford, California.

Reimus, P., G. Pohll, T. Mihevc, J. Chapman, M. Haga, B. Lyles, S. Kosinski, R. Niswonger, and P. Sanders (2003), Testing and parameterizing a conceptual model for solute transport in a fractured granite using multiple tracers in a forced-gradient test, *Water Resources Research*, 39, doi:10.1029/2002WR001597.

Reimus, P.W., and T.J. Callahan (2007), Matrix diffusion rates in fractured volcanic rocks at the Nevada Test Site: Evidence for a dominant influence of effective fracture apertures, *Water Resources Research*, 43, doi:10.1029/2006WR005746.

Robinson, B., and J. W. Tester (1984), Dispersed fluid-flow in fractured reservoirs – an analysis of tracer-determined residence time distributions, *Journal of Geophysical Research*, 89(NB12), 374-384, doi: 10.1029/JB089iB12p10374.

Robinson, B. A. (1985), Non-Reactive and Chemically Reactive Tracers: Theory and Applications, *Ph.D Dissertation*, Massachusetts Institute of Technology.

Robinson, B. A., and S. A. Birdsell (1987), Tracking thermal fronts with temperature-sensitive chemically reactive tracers, Proceedings, in *5th Geothermal Program Review*, Washington, D.C.

Robinson, B.A., J.W. Tester, and L.F. Brown (1988), Reservoir sizing using inert and chemically reacting tracers, *SPE Formation Evaluation*, 2, 227-234.

Robinson, B. A., and J. W. Tester (1990), Kinetics of alkaline hydrolysis of organic esters and amides in neutrally-buffered solution, *International Journal of Chemical Kinetics*, 22, 431-448.

Rose, P. E., and M. C. Adams (1994), The application of Rhodamine WT as a geothermal tracer, *Transactions of the Geothermal Resource Council*, 18, 237-240.

Rose P., W. Benoit, and P. Kilbourn (2001), The application of the polyaromatic sulfonates as tracers in geothermal reservoirs, *Geothermics*, 30, 617-640.

Rose, P., and S. Clausen (2015), The use of Amino G as a thermally reactive tracer for geothermal applications, Proceedings, in *World Geothermal Congress*, Melbourne, Australia.

Shang, S., R. N. Horne, and H. J. Ramey, Jr. (1994), Experimental study of water vapor adsorption on geothermal reservoir rocks, *Technical Report*, Stanford Geothermal Program, SGP-TR-148.

Shook, G.M. (2001), Predicting thermal breakthrough in heterogeneous media from tracer tests, *Geothermics*, 30, 573-589.

Shook, G.M., and J.H. Forsmann (2005), Tracer Interpretation using Temporal Moments on a Spreadsheet, *Technical Report*, Idaho National Laboratory, Idaho Falls, Idaho.

Stanford Geothermal Program (1980), *Proceedings*, in Special Panel on Geothermal Model Intercomparison Study at the 6th Workshop on Geothermal Reservoir Engineering, SGP-TR-42.

Staunton, S., C. Dumat, and A. Zsolnay (2002), Possible role of organic matter in radiocaesium adsorption in soils, *Journal of Environmental Radioactivity*, 58, 163-173.

Stefansson, V. (1997). Geothermal reinjection experience, *Geothermics*, 26, 99-139. doi:10.1016/s0375-6505(96)00035-1.

Sullivan, E. J., P. W. Reimus, and D. A. Counce (2003), Transport of a reactive tracer in saturated alluvium described using a three-component cation-exchanging model, *Journal of Contaminant Hydrology*, 62-63, 675-694.

Sumner, M. E. (1963), Effect of iron oxides on positive and negative charges in clays and soils, *European Journal of Soil Science*, 17, 218-226.

Tester, J. W., R. M. Potter, R. L. Bivins (1979), Interwell tracer analyses of a hydraulically fractured granitic geothermal reservoir, Proceedings, in 54th *Annual Technical Conference Exhibition of the Society of Petroleum Engineers of AIME*, Las Vegas, Nevada.

Tester, J. W., B. Robinson, and J. H. Ferguson (1986), Inert and reacting tracers for reservoir sizing in fractured, hot dry rock systems, Proceedings, in *11th Workshop on Geothermal Reservoir Engineering*, Stanford University, Stanford, California.

Tomich, J. F., R. L. Dalton, H. A. Deans, L. K. Shallenberger (1973), Single-well tracer method to measure residual oil saturation, *Journal of Petroleum Technology*, 25, 211-218.

Toride, N., F. J. Leij, and M. T. Vangenuchten (1993), A comprehensive set of analytical solutions for nonequilibrium solute transport with 1st-order decay and zero-order production, *Water Resources Research*, 29, 2167-2182. doi: 10.1029/93wr00496.

Toride, N., F. J. Leij, and M. Th. van Genuchten (1995), The CXTFIT code for estimating transport parameters from laboratory or field tracer experiments (V. 2.0), *Technical Report*, U. S. Salinity Laboratory, USDA, ARS, Riverside, CA, 137.

Tsang, Y. W., and C. F. Tsang (1978), An analytic study of geothermal reservoir pressure response to cold water reinjection, Proceedings, in *4th Workshop on Geothermal Reservoir Engineering*, Stanford University, Stanford, California.

Vetter, O.J., and H.B. Crichlow (1979), Injection, injectivity and injectability in geothermal operations: Problems and possible solutions (Phase I – Definition of the Problems, *Technical Report*, U.S. Department of Energy – Geothermal Energy, SAN-2044-1.

Vetter, O.J., and K. P. Crichlow (1981), Evaluation of well-to-well tracers for geothermal reservoirs, *Technical Report*, U.S. Department of Energy, W-7405-ENG-48.

Vides-Ramos, A. (1985), Ahuachapán, El Salvador, field management, Proceedings, in *Geothermal Resource Council*: *International Volume*, 397-404.

Wagner, O. R. (1977), The use of tracers in diagnosing interwell reservoir heterogeneities – field results, *Journal of Petroleum Technology*, 29, 1410-1416.

Williams, M. D., V. R. Vermeul, P. W. Reimus, D. Newell, and T. Watson (2010), Development of models to simulate tracer behavior in Enhanced Geothermal Systems, Richland, Washington: *Pacific Northwest National Laboratory*.

Williams, M. D., T. Watson, P. W. Reimus, D. Newell, V. R. Vermeul, K. B. Leecaster, P. E. Rose, E. M. Brauser, and C. A. Dean (2013), Development of models to simulate tracer tests for characterization of Enhanced Geothermal Systems, Richland, Washington: *Pacific Northwest National Laboratory*.

CHAPTER 3: ALTONA FIELD SITE

All field experiments discussed in this dissertation were conducted between 2013 and 2017 at a meso-scale "field laboratory" located in a geographic region commonly referred to as the "Altona Flat Rocks", in northern New York State, USA about 6 km northwest of West Chazy and north of Plattsburgh. Within the Altona Flat Rocks, there is an experimental forest owned by the William H. Miner Agricultural Institute (http://www.whminer.com/) (Figure 3.1). The experimental site has been the focus of numerous studies on fractured rock hydrology due to its lack of soil cover, the shallow water levels, and the presence of strong sub-horizontal bedding plane fracturing.

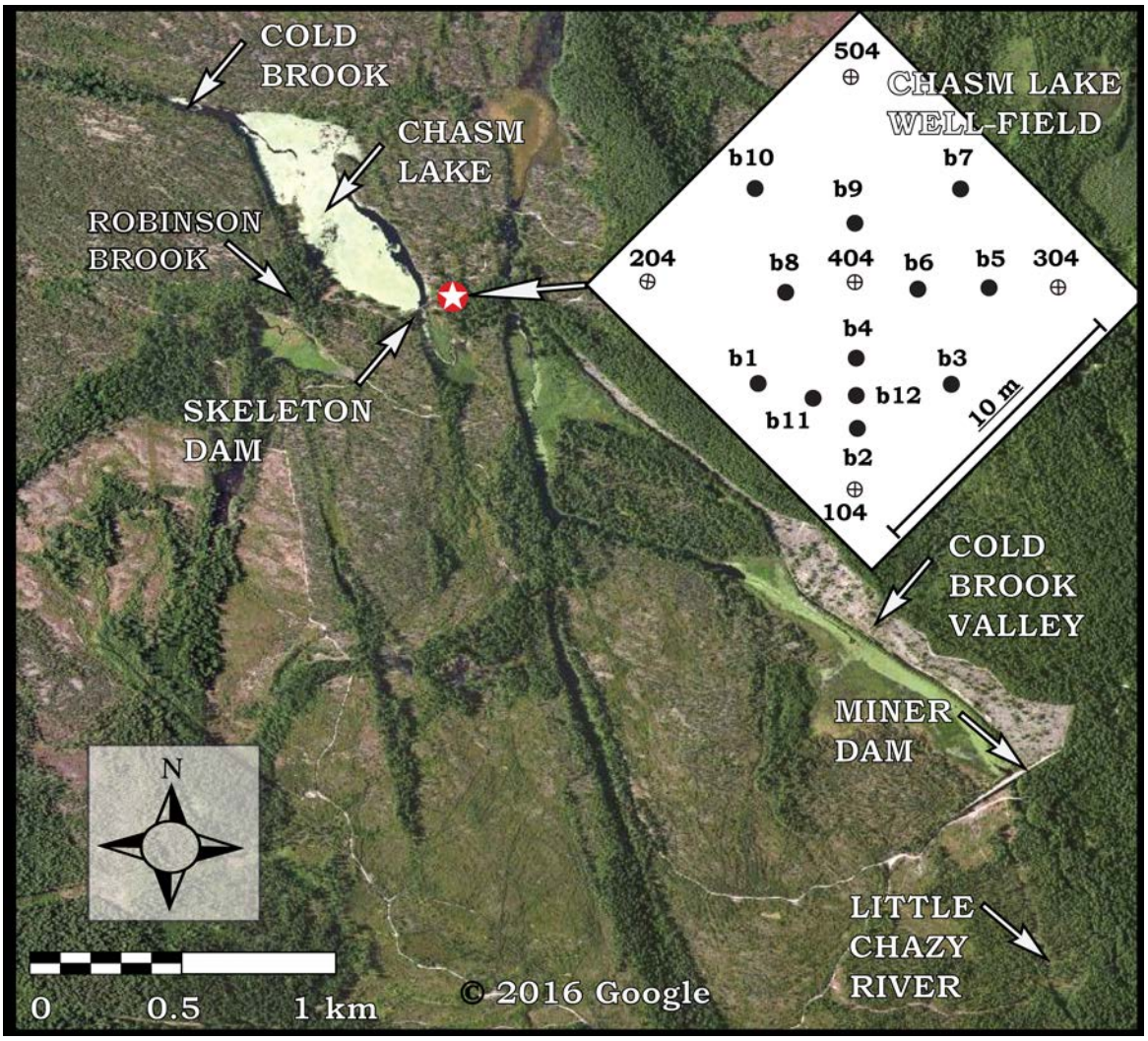

Figure 3.1. Satellite image of the Miner Experimental Forest. Chasm Lake Well-Field inset shows the position of the 12 boreholes and five wells.

3.1 Million-Dollar Dam

In 1904, a wealthy inventor and business man named William H. Miner returned to his family's farm in Chazy, NY to bring electricity to the rural community. Prior to returning home, he had amassed a fortune as the inventor of the friction draft rig for railroad cars. He now aimed to use his fortune to electrify the town where Miner, an orphan, was raised by his aunt and uncle.

In 1910, he began work on a hydroelectric plant after purchasing several thousand acres in the region now known as the Altona Flat Rocks (Sullivan and Martin, 1970). A 700 m long concrete dam was constructed over the course of three years (Gooley, 1980) (Figure 3.2). Unfortunately, the newly constructed dam leaked rapidly through the glacial deposits below it and through the highly fractured sandstone surrounding the reservoir.

Figure 3.2. Northern view of Miner Dam at the southeastern edge of Cold Brook Valley.

An extensive (and expensive) effort was made to control seepage out of the reservoir by grouting the sandstone ledges that line the Cold Brook Valley (Figure 3.1). In addition, a second dam (Skeleton Dam) was constructed 1.5 km upstream enable to provide more flexible control of flow into the Miner Reservoir. The resulting reservoir, known as “Chasm Lake” provided a source of water storage and hydraulic control (Figure 3.3). After seven years of intermittent operation, the hydroelectric project was abandoned completely, reportedly due to mechanical problems. As a result of the hydroelectric dam’s minimal success and expensive construction, Miner’s dam has since been colloquially referred to as the “Million-Dollar Dam” (Franzi et al., 2004). Miner

did, however, provide his community with hydroelectric power through several other nearby projects.

Figure 3.3. Southwest view of Skeleton Dam at the southern boundary of Chasm Lake.

After his death in 1930, his vast farming estate was used to establish a research institute to study dairy farming and agronomy. The William H. Miner Agricultural Institute, as it was named, continues its research to this day. As part of his estate, the "Miner Institute," as it will subsequently be referred to, also received the Altona Flat Rock property, including the remains of the hydroelectric dam.

3.2 Ecosystems Studies Field Laboratory (ESFL)

In 1992, a collaboration between the Miner Institute and faculty members of the State University of New York (SUNY) in Plattsburgh led to the creation of the Ecosystems Studies Field Laboratory (ESFL). The site was set up for instruction and research in environmental science (Franzi et al., 2004). ESFL infrastructure includes a solar-powered cabin, several kilometers of dirt and gravel roads, a storage shed, and 36 groundwater wells. Research tools available at the site include weather stations, lake and stream gauges, rain gauges, and various other hydrologic testing equipment. In addition, the site has an earthquake monitoring system from the Lamont-Doherty Earth Observatory at Columbia University.

3.3 Geology

The Altona Flat Rocks region is unique in the Northeastern United States, because a glacial flood stripped soil overburden off large regions of bedrock, exposing an expanse of sandstone with shallow groundwater in bedrock fractures (Rayburn et al., 2005). Roughly 12,000 years ago, glacial meltwater flooded upper New York State and Vermont as it was suddenly released from an over-flowing Lake Iroquois. Over roughly 150 to 300 y, three major flood events occurred which drained a total of 4700 km^3; a volume slightly less than present day Lake Michigan (EPA, 1995). Flow rates as high as 1.1 million m^3/s resulted in the erosion of surficial sediments in the region locally referred to as “Flat Rock” which includes the ENSFL. For comparison, the entire global flow of freshwater surface discharge into the ocean is roughly

1.2 million m^3/s (Lagerloef et al., 2010). The glacial flooding produced a unique ecosystem that exists today with only centimeters of soil and limited shrubbery. In these otherwise unfavorable conditions, a particularly robust Jack Pine Tree thrives where most of New York's most abundant tree species cannot.

The Cambrian-aged Potsdam Sandstone is exposed throughout the region. Its sediments were initially deposited as beach sands during the breakup of the Grenville supercontinent (Isachsen et al., 1991). Grain size is medium to coarse-grained at its base and grades upwards to fine and medium-grained (Isachsen et al., 1991). Extensive siliceous and calcareous cement fill matrix porosity resulting in matrix porosities frequently less than 1%.

Lowe (2016) conducted a large study of the stratigraphic characteristics of the Potsdam Sandstone in southern Quebec, Canada and northern New York State, USA. On the northern boundary of Chasm Lake (Figure 3.1), Lowe described a facies association termed "cross-stratified sandstone with local conglomerate" or (FA1). This facies is dominated by "poorly- to moderately-sorted, coarse-grained, dune cross-stratified sandstone with subordinate unit bar cross-stratified sandstone and tractional conglomerate, and rare upper plane bed stratified sandstone, silty mudstone and gravel-rich slope talus conglomerate." The interpretation for this facies is that sediment was deposited in an "energetic, steady unidirectional subaqueous currents in a terrestrial, braided fluvial environment with perennial discharge in a humid climatic

setting." An analysis of paleo current direction for a sample collected at the northern edge of Chasm Lake suggests that the direction of flow ranged from 090 to 144° with a mean of 120°.

Zircons were used to age the sediments of the Potsdam Sandstone (Lowe, 2016). From an outcrop located at the northern edge of Chasm Lake, 96 detrital zircons were picked for U-Pb dating. Based on the lead isotope ratio for Pb^{206}/Pb^{207}, detrital age was roughly 1.17 billion years before present. This age represents the age of the igneous source rock that was eroded, transported, and finally deposited in an aqueous environment. After lithification, these sediments became the Potsdam Sandstone.

The bedding planes of the Potsdam Sandstone that outcrop in the region surrounding the ESFL are typically gently dipping ~ 3° NE. A normal fault with roughly 100 m vertical offset in bedrock units outcrops roughly 1.5 km southwest of the five-spot (Williams et al., 2010). The fault strikes 346° and dips steeply to the north-east. Between 1973 and 2012, there were 15 earthquakes in Clinton County, New York (USGS, 2014). Typically, the magnitude of these earthquakes were between 2.0 and 2.9. Several events were in the range of 3.0 and 3.9 and the largest two events were between 4.0 and 5.2. No connection was made between these earthquakes and the normal fault located near the well-field.

The Potsdam Formation is typically referred to as a sandstone, however, the uppermost layers, which outcrop at the well-field, are more consistent with

an orthoquartzite. This member of the Potsdam is referred to as the Ausable Formation. Throughout the ESFL, numerous ripple marks and cross-bedding textures can be observed on the sandstone pavement. Within the 100 m^2 well-field, these textures have a preferred orientation of roughly [NW-SE] near Skeleton Dam.

3.3.1 Chemical Composition

The chemical composition of the Potsdam Sandstone was determined via X-ray fluorescence (XRF), which is a non-destructive analytical technique that measures the fluorescent X-ray emitted from a sample when it is excited by a primary X-ray. Four rock samples were collected from rock debris at ground surface near the well-field. The samples were shipped to Lawrence Berkeley National Laboratory and received by two researchers, John Christensen and Shaun Brown. XRF results indicate that silica dominates the chemical composition, with a relative abundance of roughly 90% (Table 3.1). Oxides of aluminum, potassium, iron, and titanium account for roughly 7% while several other oxides were measured in abundances less than 0.5%. Zircons were found in relatively high abundances ranging from 0.3 to 2.3% (Table 3.2). The XRF measurements are relatively consistent with reported values for the Potsdam Sandstone in Wiesnet (1961). Mean silica abundance for five samples was roughly 93%. Measured abundances of oxides of Aluminum and potassium/sodium were roughly 3.5 and 2.9%, respectively. In contrast to the XRF measurements, iron oxides (Fe_2O_3 and FeO) were relatively low at roughly 0.4%.

Table 3.1. Bulk chemical composition of the Potsdam Sandstone.

Mineral	*Minimum*	*Maximum*	*Mean*
SiO2	87.4%	91.8%	89.9%
Al2O3	2.8%	3.4%	3.0%
K2O	1.8%	2.2%	2.0%
FeO	0.9%	2.8%	1.9%
TiO2	0.4%	2.8%	1.4%
MgO	0.2%	0.4%	0.3%
P2O5	0.0%	0.2%	0.1%
CaO	0.0%	0.2%	0.1%
Na2O	0.1%	0.1%	0.1%
MnO	0.0%	0.0%	0.0%

Table 3.2. Relative abundance of minor elements in the Potsdam Sandstone.

Element	*min*	*max*	*mean*
Zr	282.0 ‰	2340.5 ‰	1120.4 ‰
Ba	118.4 ‰	163.1 ‰	145.6 ‰
Rb	31.1 ‰	42.3 ‰	37.9 ‰
Ce	12.6 ‰	68.6 ‰	35.1 ‰
V	13.9 ‰	42.3 ‰	29.1 ‰
Nb	7.5 ‰	62.0 ‰	28.5 ‰
Hf	7.4 ‰	53.7 ‰	26.3 ‰
Sr	20.1 ‰	27.4 ‰	23.8 ‰
Cr	16.6 ‰	26.8 ‰	22.5 ‰
Y	7.6 ‰	26.5 ‰	16.8 ‰
Th	3.1 ‰	24.8 ‰	14.1 ‰
Nd	3.2 ‰	27.9 ‰	13.9 ‰
La	4.9 ‰	27.0 ‰	13.3 ‰
Ga	4.0 ‰	7.0 ‰	5.0 ‰
Pb	2.3 ‰	5.0 ‰	3.9 ‰
Yb	2.4 ‰	6.3 ‰	3.9 ‰
Ni	2.1 ‰	5.2 ‰	3.7 ‰
Sm	1.6 ‰	6.0 ‰	3.6 ‰
Zn	2.5 ‰	4.0 ‰	3.1 ‰
U	1.3 ‰	4.4 ‰	2.9 ‰
Dy	1.3 ‰	4.3 ‰	2.8 ‰
Cu	1.0 ‰	2.2 ‰	1.6 ‰
Sc	0.0 ‰	1.7 ‰	0.8 ‰
Cs	0.0 ‰	2.4 ‰	0.6 ‰
Bi	0.0 ‰	0.9 ‰	0.4 ‰
Mo	0.0 ‰	0.9 ‰	0.3 ‰
Tl	0.0 ‰	0.4 ‰	0.2 ‰
Br	0.0 ‰	0.5 ‰	0.2 ‰

3.4 Hydrology

3.4.1 Surface Water

The ESFL lies within the Upper Little Chazy River Watershed, which is roughly 140 km^2 and lies mostly within the Champlain Lowlands (Franzi et al., 2004). Two streams, Cold Brook and Robinson Brook (Figure 3.4 and Figure 3.5), flow through ESFL and join together at Chasm Lake. After flowing underneath the Miner Dam, it continues southeast until the Little Chazy River. The headwaters of Cold Brook can be traced to the northwest roughly 4 km from Chasm Lake. Robinson Brook can be tracer roughly 4 km to the southwest and flows northeast until it reaches Chasm Lake.

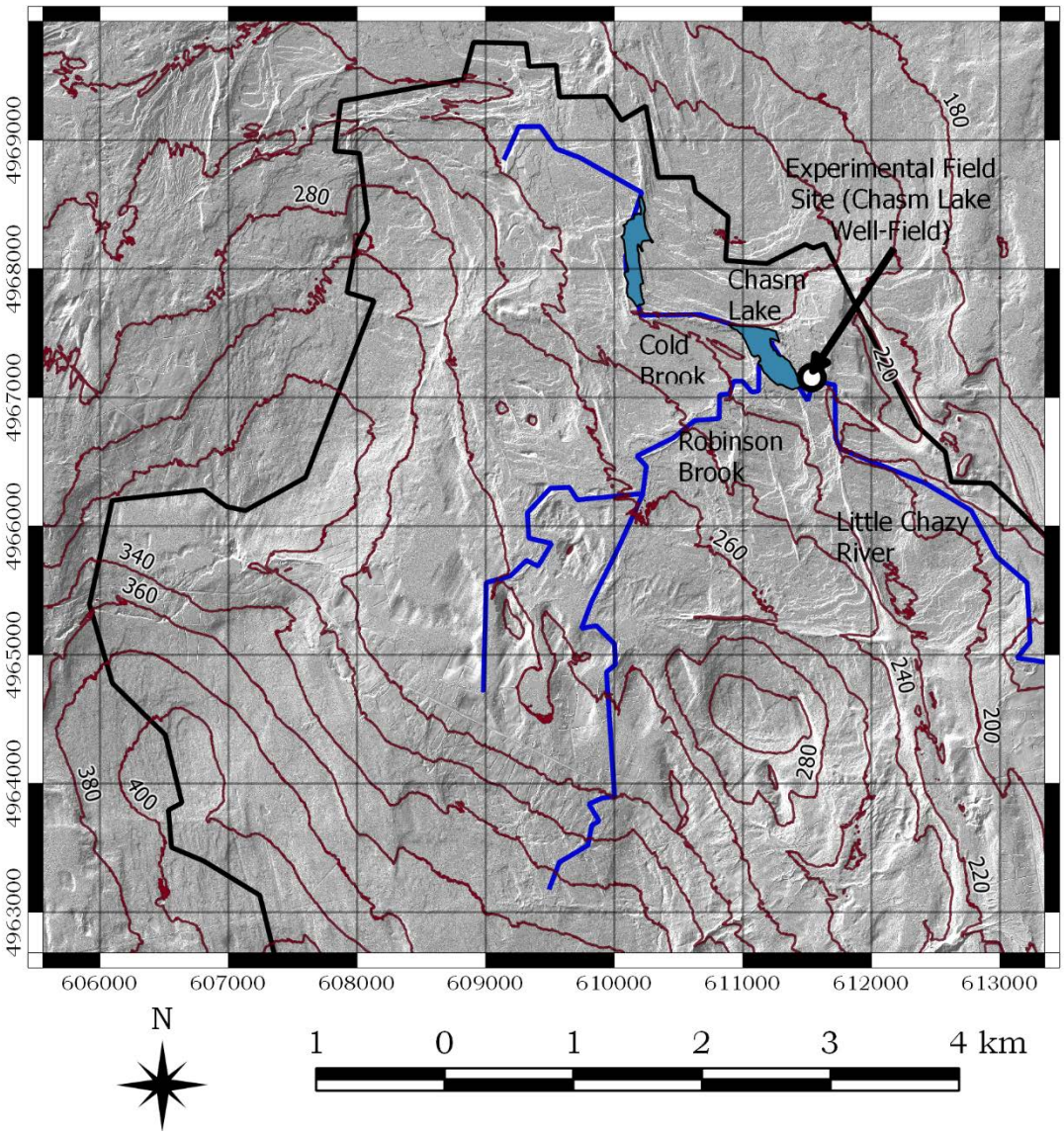

Figure 3.4. Digital Elevation Map (DEM) and contour map of the northwestern boundary of the Little Chazy River Water Shed. The experimental field site ("Chasm Lake Well-Field") is indicated at the top right of the image. The black outline is the spatial boundary of the watershed.

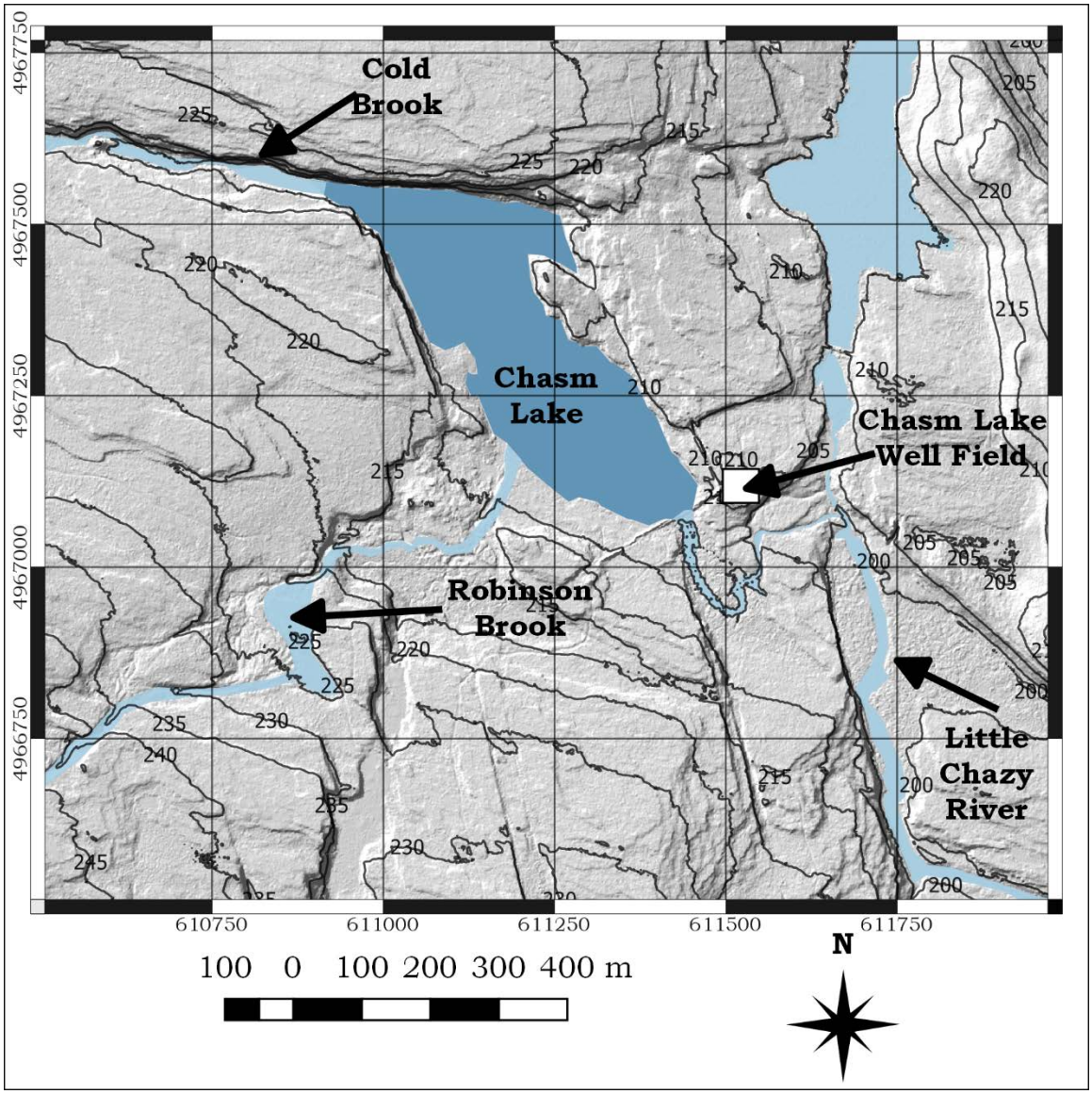

Figure 3.5. Digital Elevation Map (DEM) of the region surrounding the Chasm Lake Five-Spot.

3.4.2 Groundwater

Throughout northern New York State and southern Quebec, Canada, the Potsdam Formation is commonly used as an aquifer for drinking water (Olcott, 1995). Groundwater in the Potsdam is dominated by sub-horizontal fractures that make it highly permeable. Its matrix porosity, however, is very low. Thin section analysis of rock samples collected from ground surface at the Chasm

Lake Well-Field indicate that matrix porosity ranges from less than 1% to about 2% (Remmen, 2013). Throughout the Potsdam formation, matrix porosity is generally less than 10% (Olcott, 1995). Groundwater recharge, therefore, occurs through contacts between permeable fractures and various surface water bodies, including streams, lakes, and wetlands.

While Chasm Lake is full, Skeleton Dam produces a relatively constant hydraulic boundary as water flows over the dam. As a result, water levels measured at groundwater wells located roughly 50 m to the southeast show very little fluctuation in hydraulic head. In contrast, groundwater wells located downstream towards the Miner Dam experience relatively large water level fluctuations. For example, heavy rains in June and July of 2004 produced little water level fluctuation near Chasm Lake. Close to Miner Dam, however, water levels dropped 8 m during the summers of 2001, 2002, and 2003 when surface waters dried during warm summer months (Talley, 2005).

Since 1992, 36 groundwater wells have been drilled in the ESFL, ranging in depth from roughly 9 to 40 m below ground surface. The first eight wells were completed in 1992 and are located southeast of Chasm Lake with separation distances ranging from roughly 50 to 400 m. Heat-pulse flowmeter tests conducted in the 1992 wells yielded transmissivities ranging from roughly 2 to 60 m^2/d (Paillet, 2000).

Chasm Lake produces a natural hydraulic background gradient which produces a natural groundwater flow away from the lake. Reservoir water flows

over the top of the Skeleton Dam towards the main Miner Dam. As a result, hydraulic head in the lake remains relatively stable as the lake drains. In the Chasm Well Cluster, a hydraulic gradient of roughly 0.004 [-] was measured with a flow direction orientation away from Chasm Lake (Becker and Tsoflias, 2010). Presumably, groundwater is recharged from Chasm Lake, flows through the target fracture. It is then discharged at a seepage face located roughly 100 m southeast of Skeleton Dam. Pump tests described in Talley (2005) indicate that transmissivity of the target fracture at 7.6 m depth is roughly 5 m^2/d which suggests a mean hydraulic aperture of roughly 0.5 mm.

Concentrations of major cations were measured in water samples collected from Chasm Lake, well 304, and from a groundwater seep located roughly 50 m east of well 304. All water samples were collected in July of 2016 and analyzed by John Christensen of Lawrence Berkeley National Laboratory. Concentration of major cations were measured via Inductively Coupled Plasma Optical Emission Spectroscopy (ICP-OES). Two samples were collected from the water surface of Chasm Lake near its outlet at Skeleton Dam. The measured samples contained relatively abundant concentrations of sodium (25 ppm), calcium (6.4 ppm), and magnesium (2.5 ppm) (Table 3.3). A sample collected from well 304 showed iron concentrations were much higher in well 304 (17.4 ppm) compared to Chasm Lake (0.26 ppm). Sum of major cations was nearly double in well 304 and the relative abundance of sodium fell from 72 to 36%.

Table 3.3. Concentration of major cations in water samples collected from Chasm Lake, well 304, and a nearby groundwater seep.

	Chasm Lake		*Well 304*		*Groundwater Seep*	
	ppm	%	ppm	%	ppm	%
Na	25	72%	22	36%	24	51%
Fe	0.26	0.7%	17.44	29%	12.33	26%
Ca	6.41	18%	15.4	26%	6.25	13%
Mg	2.5	7.2%	4.1	6.8%	2.35	5%
K	0.53	1.5%	0.81	1.3%	0.94	2%
Mn	0.02	0.1%	0.5	1%	0.77	2%
Sr	0.03	0.1%	0.07	0.1%	0.04	0.1%
Li	0.05	0.1%	0.05	0.1%	0.05	0.1%
SUM	**34.8**	**100%**	**60.4**	**100%**	**46.7**	**100%**

Additional measurements of groundwater cation concentrations was performed from groundwater samples collected from well 104 in August of 2016 (Table 3.4). As before, ICP-OES was used to determine the major cations present in groundwater samples. After purging roughly 100 L from the well at ~ 4 L/min, three 15 mL samples were collected and filtered through a 0.2 μm syringe filter. Minimal air was left within the samples and the samples were immediately stored on ice and remained cooled until they were analyzed. Prior to analysis via ICP-OES, the three samples were acidified by adding 2% (by volume) nitric acid. As was found in well 104, the most abundant cations in groundwater at the Chasm Lake Well-Field are sodium (~21 ppm), calcium (~13 ppm), and iron (~7 ppm). Silicon, magnesium, and potassium have moderately high concentrations ranging from ~2 to 6 ppm.

Table 3.4. Concentration of cations in groundwater collected from well 104.

	Concentration (ppm)		
	Minimum	Maximum	Mean
Na	21.2	21.4	21.3
Ca	12.9	13.1	13.0
Fe	7.0	7.1	7.1
Si	5.8	5.8	5.8
Mg	2.6	2.7	2.7
K	1.6	1.6	1.6
B	0.33	0.34	0.33
Mn	0.29	0.30	0.29
Zn	0.12	0.12	0.12
Ba	0.12	0.12	0.12
Sr	0.06	0.06	0.06
Al	0.04	0.05	0.04
Mo	<0.01	0.01	0.01
Zr	0.004	0.006	0.01
Cu	0.002	0.003	0.003
Li	0.001	0.004	0.002
V	0.001	0.004	0.002
Co	0.001	0.002	0.001
Cr	<0.019	0.002	0.001
Ni	<0.009	<0.009	<0.009
Ti	<0.01	<0.01	<0.01
SUM	**51.0**	**51.7**	**51.4**

3.5 Chasm Lake Five-Spot

The experiments discussed in this dissertation were conducted exclusively in the "Chasm Lake Well-Field" which was originally developed as a five-spot well configuration within a 10 x 10 m area roughly 50 m southeast of Skeleton Dam (Figure 3.6). Since the initial well development in 2004, 11 additional groundwater wells have been added with well separations ranging from 2.5 to 14 m and depths ranging from 9 to 21 m below ground surface.

Figure 3.6. Northern view of the Chasm Lake Well-Field in July 2016. The fiber-optic cable used in FO-DTS measurements are installed within the gray conduits, which connect each monitoring borehole. Photo Credit: John Christensen, Lawrence Berkeley National Laboratory.

The wells were initially drilled under the direction of Matthew Becker who, prior to joining California State University, Long Beach, was a professor of Geology at SUNY, Buffalo. A radar wave reflection, located 7.6 m below ground surface, was identified by reconnaissance Ground Penetrating Radar (GPR) surveys conducted by Matthew Becker and his colleagues in 2003 (Figure 3.7). The reflection was interpreted as an open bedding plane fracture and a five-spot well-field was subsequently drilled in 2004. Since then, numerous experiments have been carried out at the site to investigate heat and mass transport in fractured rock. See sub-section 3.6 below for descriptions of select studies previously conducted at the Chasm Lake Five-Spot.

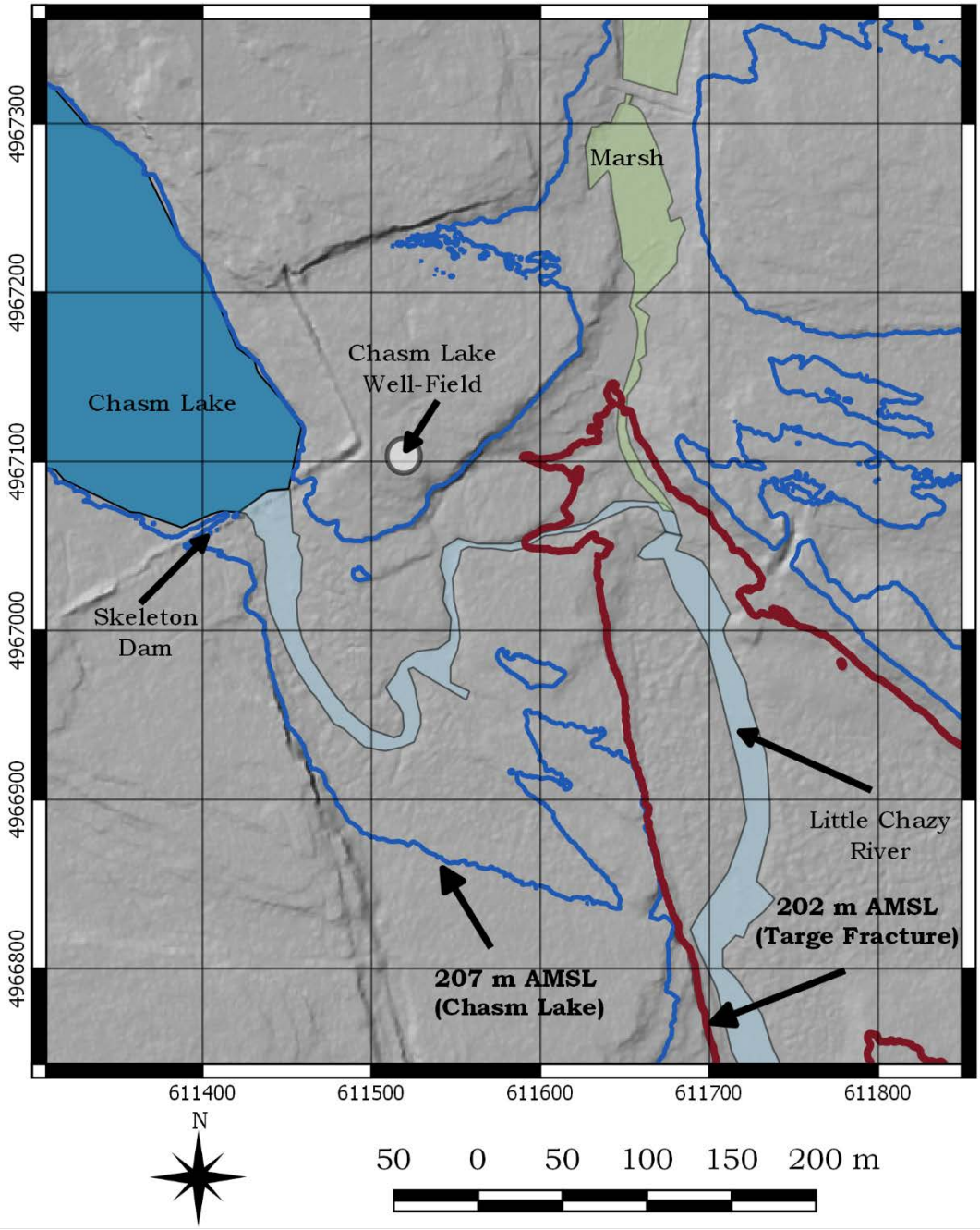

Figure 3.7. Map of the elevation contours of Chasm Lake and the target fracture. The blue contour line represents the elevation of the Chasm Lake surface (207 m Above Mean Sea Level (AMSL)). The Red contour line is the elevation of the target fracture measured in well 104 (202 m Above Mean Sea Level (AMSL)). The background image is a Digital Elevation Map (DEM).

The wells of the five-spot configuration, drilled using a water rotary drill in May of 2004, are 15 cm in diameter and were originally drilled to a depth of 12.2 m with a 0.91 m surface casing and open borehole below (Table 3.5 and Figure 3.8). In July of 2011, all five wells were deepened with a percussion air rotary drill with a 14 cm diameter bit. The new well depths ranged from 18.3 m to 21.3 m. PVC casings were installed from ground surface to roughly 0.7 m below surface. An open borehole in the sandstone rock remained below the bottom of casing. Roughly 15 to 30 cm of PVC casing was left exposed above ground surface. Bentonite clay was used to seal the casings to the formation.

An additional part of the July 2011 drilling activities was the advancement of ten dry boreholes within the 100 m^2 are of the five-spot well-field to a target depth of 7 m below ground surface. At 7 m, the borehole termination depth is roughly 0.5 m above the target fracture and therefore did not fill with groundwater. These ten boreholes were used in heat transport experiments in which Fiber-Optic Distributed Temperature Sensing (FO-DTS) was used to monitor fracture/matrix heat exchange as hot water was circulated through the relatively cold formation. Fiber-optics were installed within the dry boreholes and these experiments are described in detail in Chapter 5. Previous experiments using the fiber-optic network are presented in Hawkins (2013). In August of 2016, the ten boreholes were deepened and samples of the fracture surface were collected (Appendix D).

Table 3.5. Well locations and depths in 2011 and after deepening in 2016.

Location	*Latitude*[a] *(deg)*	*Longitude*[a] *(deg)*	*Elevation*[b] *(m)*	*Casing Height (m)*	*Depth (2011) (m)*	*Depth (2016) (m)*
b1	44.848646	-73.588869	185.4	0.22	7.17	8.48
b2	44.848640	-73.588824	185.4	0.16	7.05	7.79
b3	44.848658	-73.588785	185.1	0.16	7.28	8.46
b4	44.848660	-73.588829	185.2	0.14	7.32	8.57
b5	44.848690	-73.588778	185.1	0.18	7.30	8.41
b6	44.848686	-73.588807	185.1	0.12	7.34	8.39
b7	44.848716	-73.588801	185.1	0.14	7.64	9.12
b8	44.848676	-73.588864	185.3	0.06	7.32	8.40
b9	44.848702	-73.588840	185.0	n/a	7.29	8.43
b10	44.848705	-73.588885	185.1	0.12	7.30	8.58
b11	44.848647	-73.588842	185.4	n/a	n/a	3.27
b12	44.848647	-73.588826	185.4	0.10	n/a	7.95
well 104	44.848619	-73.588818	185.5	0.30	18.29	18.00
well 204	44.848668	-73.588925	185.3	0.31	20.92	20.62
well 304	44.848694	-73.588748	185.0	0.19	21.34	21.15
well 404	44.848681	-73.588835	185.1	0.19	19.98	19.80
well 504	44.848743	-73.588852	184.8	0.38	20.44	20.06

a. Latitude and Longitude measured by a TRIMBLE® R10 GNSS system borrowed from Georgios Tsoflias, University of Kansas.
b. Elevation in m Above Mean Sea Level (AMSL). Elevation at well 104 was measured via the TRIMBLE® R10 GNSS system while the elevation of all others were determined by subtracting the measured height difference between each location and well 104 using a laser level.
c. Depth measured below ground surface (bgs) using a weighted open reel measuring tape.

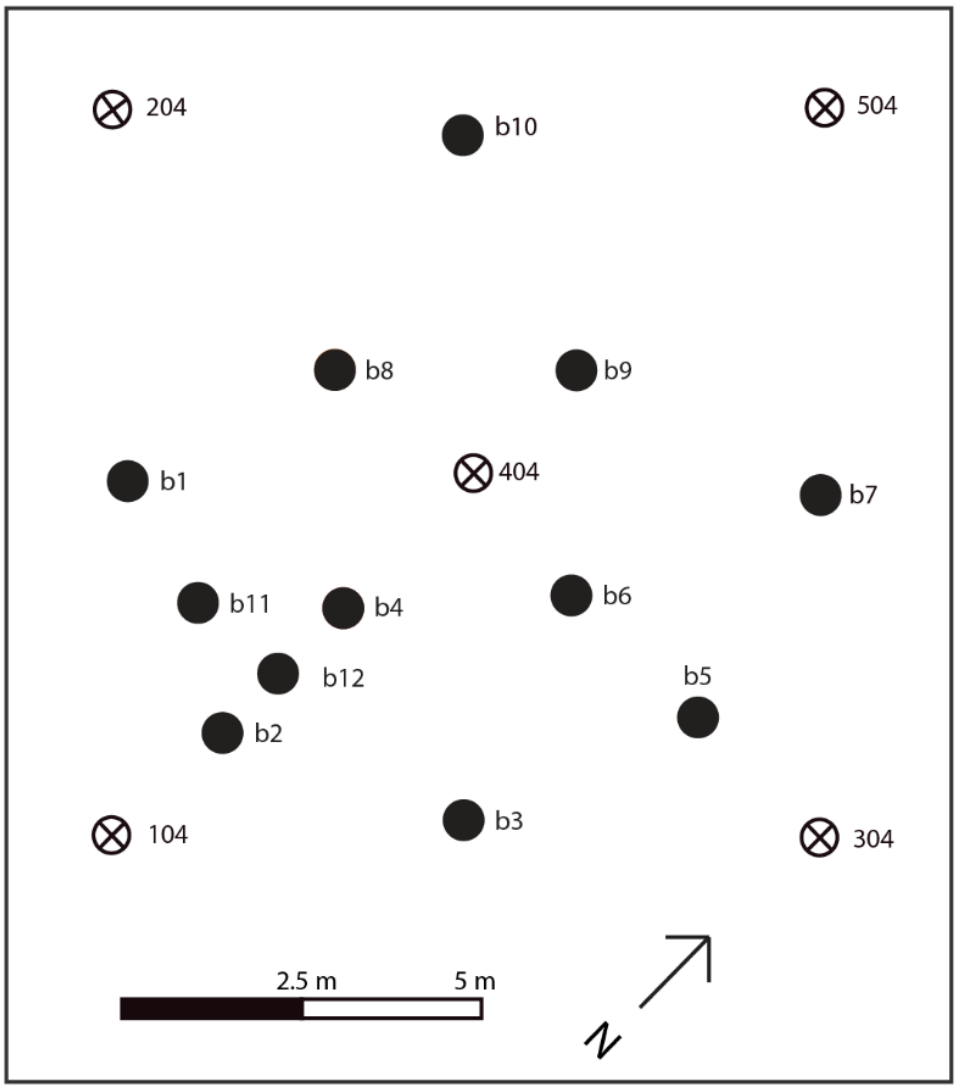

Figure 3.8. Chasm Lake Well-Field site map showing the relative locations of the original five wells (marked as crosses within circles) and all 12 of the boreholes cored in 2016 (black circles).

3.6 Summary of Previous Experiments

Since the original five-spot well-field was drilled in 2004, there have been numerous studies conducted at the Chasm Lake Five-Spot. The documentation of these studies include seven Master's Theses, seven publications in peer-reviewed journals, a dissertation chapter by Yushi Zhao (Zhao, 2015), and presentations at over 15 academic conferences. A complete list of literature and

presentations related to the Chasm Lake Five-Spot is provided in Appendix A. In addition, Appendix A includes literature relevant to the hydrogeology, geology, and history of the Altona Flat Rocks and the surrounding area.

Numerous institutions have been involved including State University of New York, Buffalo, the University of Maine, California State University, Long Beach, the University of Kansas, Cornell University, State University of New York, Plattsburgh, the Lawrence Berkeley National Laboratory, and the Power Environmental Energy Research Institute (PEERI). Field experiments have included Ground Penetrating Radar (GPR) imaging, hydraulic pump tests, sinusoidal pulse tests, and numerous tracer tests. Previous studies that are relevant to this dissertation are described in the following sub-sections and site activities are summarized in Table 3.6.

Table 3.6. Summary of field activities at the Chasm Lake Well-Field since 2003.

Date	*Field Activities*	*Reference*
2003	GPR identified target fracture	N/A
2004	Initial five-spot well pattern drilled	N/A
2004	3D GPR tracer imaging	Talley et al., 2005
2009	Stationary GPR tracer imaging	Becker and Tsoflias, 2010
2010	Sinusoidal Hydraulic Tests	Guiltinan and Becker, 2015
2011	3D GPR tracer imaging	Tsoflias et al., 2015
2011	Tracer Tests (LiBr, fluorescein)	Remmen, 2013
2011	10 dry boreholes advanced and original five wells deepened	N/A
2011	Heat Exchange Experiments	Hawkins, 2013
2012	Tracer Tests (Carboxylic Acids)	N/A
2014	Tracer Tests (C-Dots, CsI)	Hawkins et al., 2015
	Covered in this Dissertation:	
2015	Tracer Tests (C-Dots, PhAc, and CsI) and Heat Exchange Experiment	
2016	Tracer Tests (C-Dots, PhAc, and CsI)	
2016	Core Logging	

3.6.1 Ground Penetrating Radar (GPR)

The first two studies at the Chasm Lake Five-Spot used GPR to investigate fracture network characteristics and to image the spatial distribution of salt tracer circulating through the fracture plane (Beyrle, 2005; Talley, 2005). Beyrle (2005) investigated the spatial distribution of vertical and horizontal fracture intersections throughout the 10 x 10 m well-field from ground surface to a depth of roughly 18 m. Identification of fracture intersections was performed based on the behavior of radar waves as they interact the intersection between vertical and horizontal fractures.

The results of this study identified two major continuous sets of fracture intersections, one oriented roughly east-west with several parallel fractures and another oriented north-south. As can be seen in Figure 3.9, the 100 MHz radar

identified a particularly interesting pattern of diffraction apices which have a linear form that extends roughly 14 m in-between well 304 and 204.

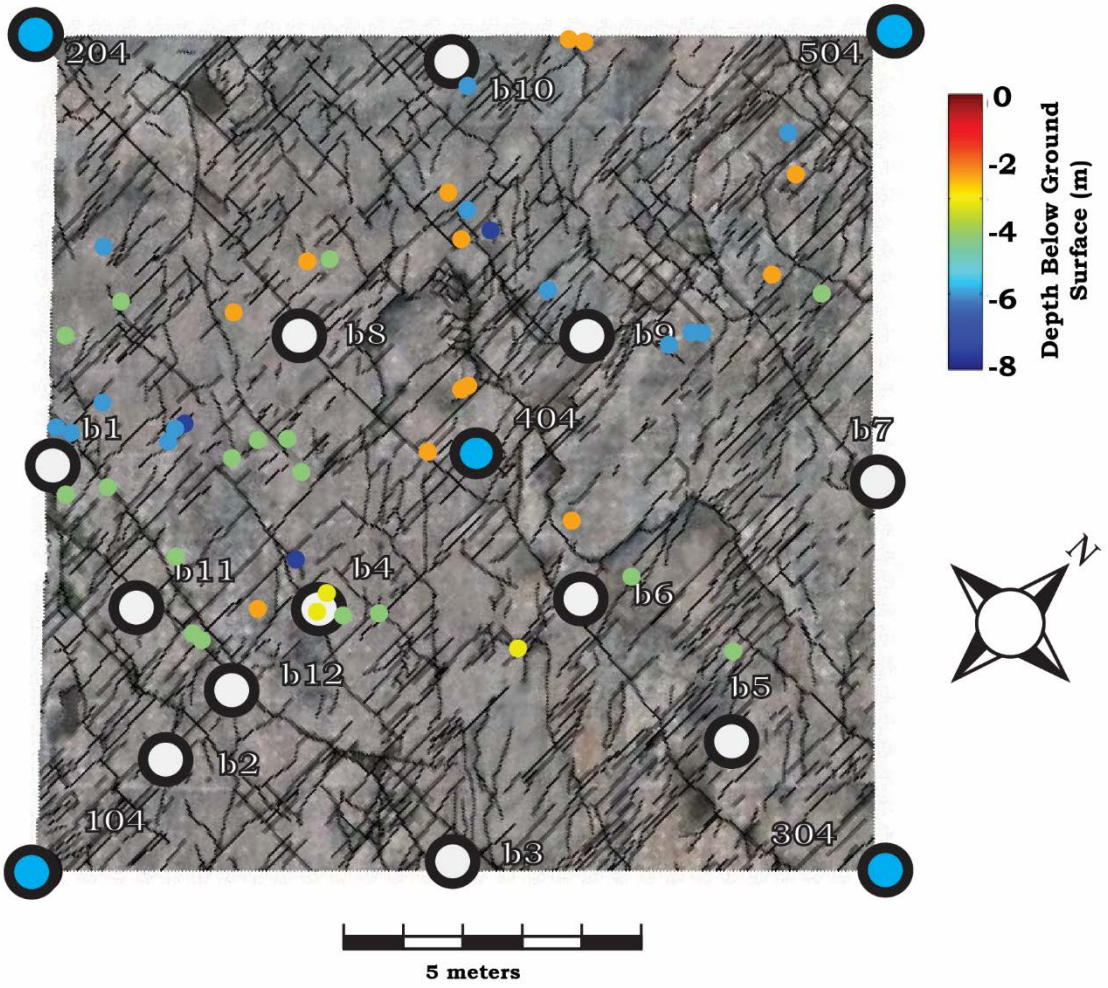

Figure 3.9. Map of fracture intersection locations. GPR diffraction apices from Beyrle (2005) were used to identify the relative position of these intersections, including their depth below ground surface, which is indicated by the color spectrum. The Background image is of the well-field surface with surface fracture traces lined in black (Talley, 2005).

During the GPR experiments conducted by Beyrle (2005), additional GPR surveys were conducted by Talley (2005) in which the spatial distribution of a saline tracer was imaged via GPR. As an initial step, a GPR tracer survey is

conducted in one, two, or three-dimensions at ambient subsurface conditions. This initial survey is conducted by collecting GPR traces that penetrate into the subsurface. The results of this survey provides a "background" image of the subsurface in the absence of a tracer solution.

The next step is to use GPR to image the subsurface as a saline tracer is continuously circulated through the target fracture. The GPR survey is repeated at the same locations used in the background survey. The survey is initiated once steady-state conditions in the injection and production well have been reached for both hydraulic head and production/injection well salinity. After extensive signal processing, the background survey can be compared to the tracer survey and the differences in wave amplitude is, in theory, proportional to the fluid salinity in the fracture (Tsoflias and Becker, 2008).

Eight GPR surveys were conducted between May and August of 2004. Flow rates ranged from 3.2 to 12.4 L/min and a variety of tests were conducted under the following test configurations: (1) push-pull; (2) full-dipole; (3) weak-dipole; and (4) natural hydraulic gradient. A sodium-chloride salt (NaCl) was used as the tracer imaged via GPR with injected masses ranging from 1.1 to 4.4 kg.

For the first dipole test, saline tracer was circulated between well 204 (inject) and well 304 (pump) at a circulation rate of 3.2 L/min. A two-dimensional GPR survey was conducted along a 15 m transect orthogonal (north-south) to the primary flow direction (east-west) and 5 m east of the

injection well. The target fracture, located at a radar travel time of ~140 ns, experienced a roughly two-fold increase in its raw positive amplitude. The increase was localized in a 3 m section of the GPR line lying in-between the injection and production well (Figure 3.10).

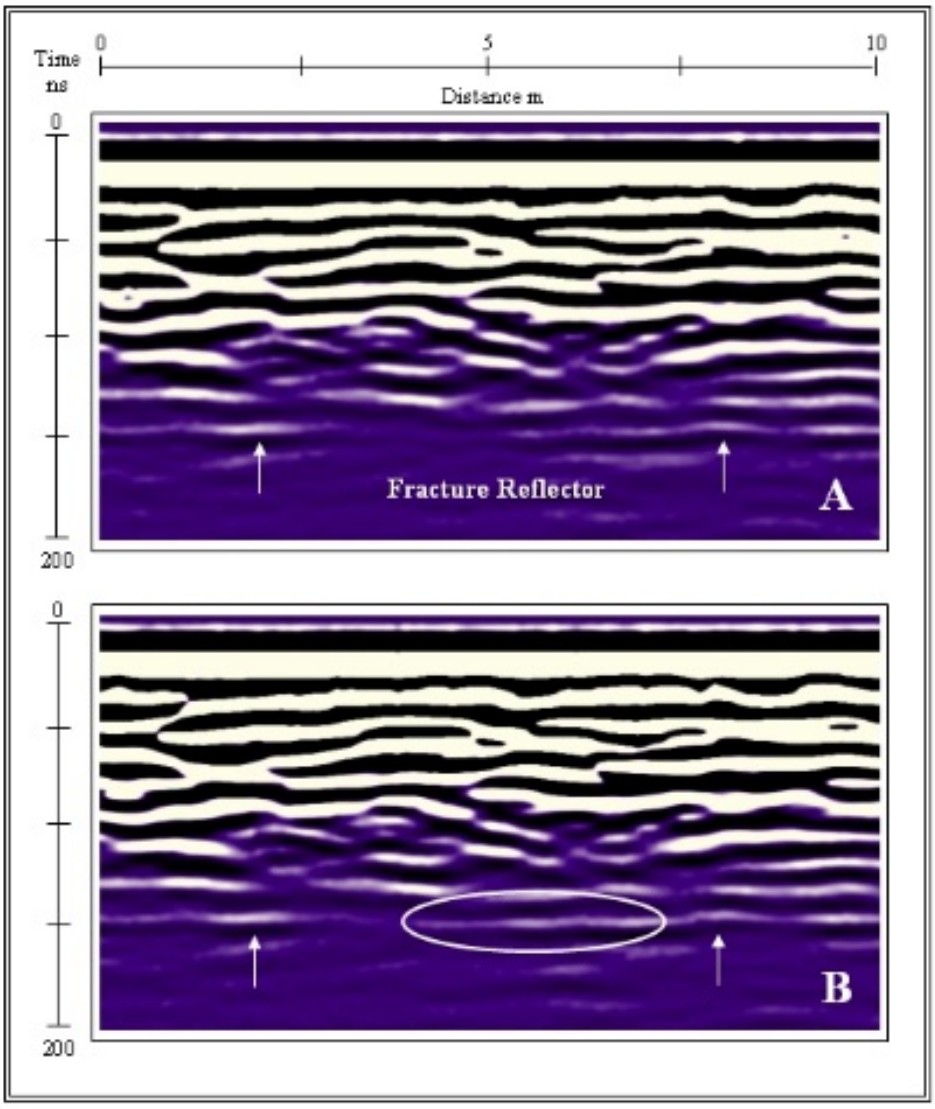

Figure 3.10. Cross-section of GPR radar response before saline tracer circulation (top) and during tracer circulation (bottom) from Talley (2005).

In 2009, Matthew Becker of California State University, Long Beach and Georgios Tsoflias of the University of Kansas were the recipients of a Department of Energy grant from the Geothermal Technologies Office with funds supported by the American Recovery and Reinvestment Act of 2009. The project they undertook included tracer testing, heat exchange experiments, and GPR imaging. The heat exchange experiment and tracer testing are discussed in Hawkins (2013) and Remmen (2013). The results of the GPR studies are described in Perll (2013), Baker (2014), and Tsoflias et al. (2015). Baker (2014) continued the investigation of fracture permeability and tracer transport in the plane of the target fracture initiated by Beyrle (2005) and Talley (2005). Using 50 and 100 MHz antennae, 16 surveys in an area of roughly 100 m^2 were conducted with ~650 to 950 individual radar traces performed in each survey.

There are three general categories these GPR surveys can be grouped by: (1) background survey; (2) full-dipole; and (3) natural gradient. The background survey was conducted under ambient reservoir conditions with no hydraulic control. The full-dipole surveys were conducted under forced fluid flow conditions with equal injection and production flow rates and tracer conductivities ranging from roughly 200 to 800 mS/m. The natural gradient test was conducted by continuously injecting saline solution into well 204 at a low flow rate for the duration of the GPR survey.

Their study produced an enormous three-dimensional GPR data set which is still being analyzed to this day. Baker (2014) provides a detailed

analysis of the background grids and the tracer surveys for six different dipole configurations, three different tracer salinity tests, and both 50 and 100 MHz antennae with multiple antennae polarizations. It also provides analysis of both amplitude changes and wave phase changes related to the salt tracer tests.

Figure 3.11 presents the results of four GPR surveys. The upper and lower rows show data collected using a 50 and 100 MHz antennae, respectively. The left column is the GPR amplitude signal reflected off the target fracture at 7.6 m below ground surface. The right column is the background amplitude signal subtracted from the amplitude reflected off the target fracture while saline tracer was circulated at steady-state through the fracture. The background survey represents the spatial distribution of fracture aperture by the strength of the amplitude, measured in relative amplitude units. In theory, areas with the largest fracture aperture exist where the greatest amplitudes were measured. Both the 50 and 100 MHz antennae measurements reveal a narrow region of large aperture extending roughly NW/SE.

The spatial distribution and concentration of saline tracer is represented by the strength of the amplitude difference, measured in relative amplitude units, between the amplitude measured prior to and during tracer circulation. Therefore, the areas of greatest tracer concentration exist where the greatest amplitude difference was measured. The GPR saline survey for the 100 MHz antennae shows a strong signal in a narrow path extending between the injection and production well over a distance of 14.1 m. The width of the flow

channel directly connecting the two wells is roughly 1 – 2 m based on the extent of the amplitude difference in the range of -100 to -500 on the relative scales shown in Figure 3.11. Saline tracer collected from the 50 MHz antennae show a similar pattern, but it generally has a broader signal along the width of the flow channel. In addition, the 50 MHz saline survey appears to show two flow channels in the northern region of the grid near wells 404 and 504 and limited circulation to the south near well 104.

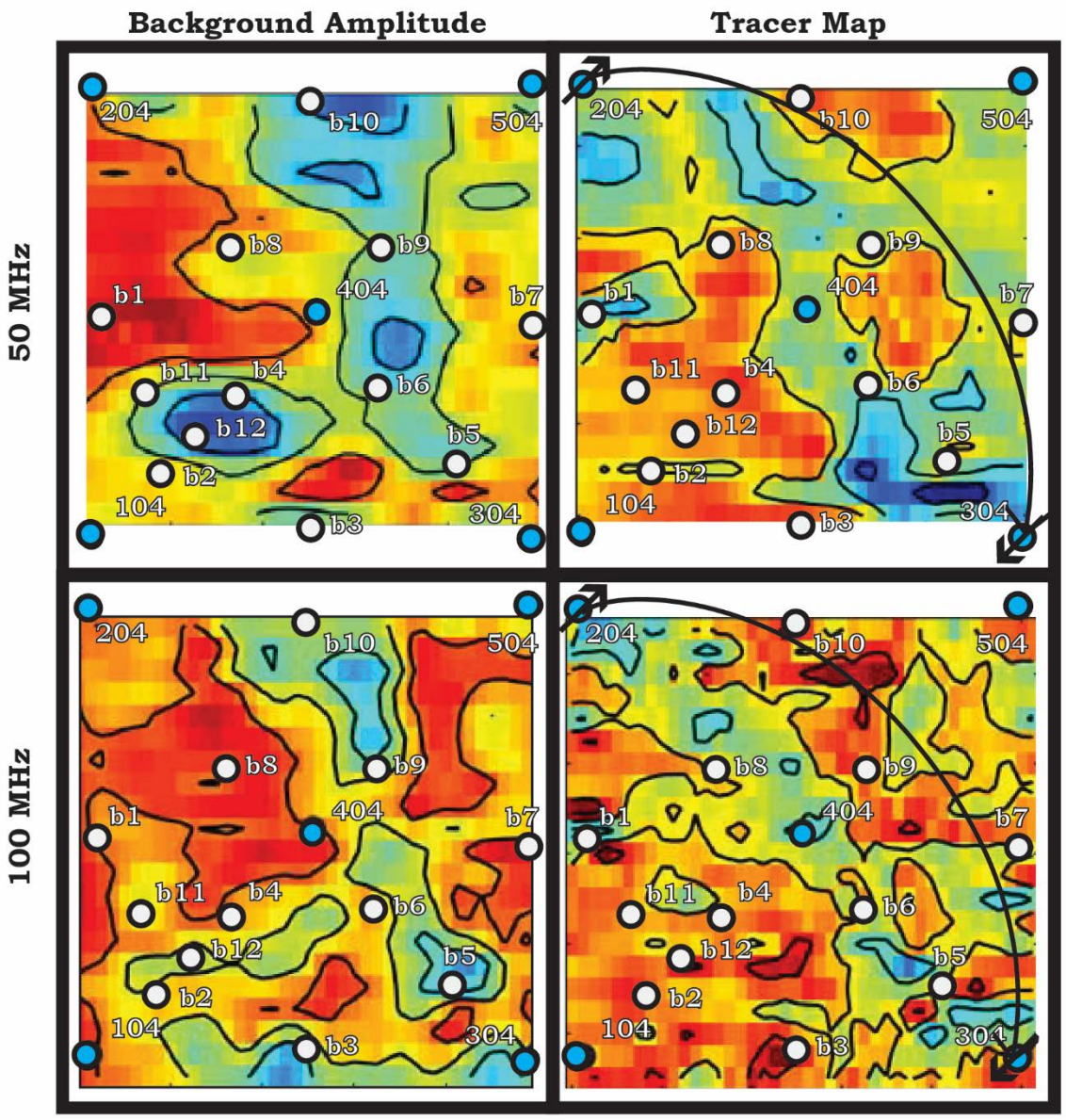

Figure 3.11. Co-polarized GPR survey summary for radar amplitude measurements at Altona. The background GPR survey (left column) was subtracted from the measured saline tracer image to produce the background-subtracted tracer image (right column). The top and bottom rows are for a 50 and 100 MHz antennae, respectively.

Perll (2013) investigated the same spatial flow path distributions that were the subject of Baker (2014), but focused on the use of cross-polarized, rather than co-polarized, antennas. The motivation for using cross-polarized in

addition to co-polarized antennae is primarily related to improving subsurface imaging of saline and aperture variations that are preferentially oriented in a direction that is oblique to the preferred survey direction. In the Altona experiments, the data were collected along 21 to 23 parallel lines oriented NE-SW and separated by 0.5 m. As a result, cross-polarized GPR surveys should perform better than co-polarized surveys, if the primary feature imaged extends preferentially in an oblique direction than it does in the NE-SW direction.

Select results from Perll (2013) are shown in Figure 3.12. These data and the data shown in Figure 3.11 were collected simultaneously at each point in the same GPR survey. In general, the background surveys (first column in Figure 3.12) provide marginal evidence for dominant patterns in a N-S or E-W orientation. The 50 MHz tracer image (top right image in Figure 3.12) does reveal a particularly important pattern extending along a narrow (~ 1 m) path oriented E-W. This pattern suggests that the saline tracer injected into well 304 flowed preferentially through this narrow flow "channel" directly towards the producing well at well 204. Because this flow channel is orientated in a direction that is favorable to cross-polarization, this image of saline flow paths should be considered a more accurate representation than the co-polarized tracer images shown in Figure 3.11. Furthermore, the 50 MHz cross-polarized image should also be considered more accurate than the 100 MHz cross-polarized image, because low-frequencies are favorable for resolving salinity changes (Tsoflias and Becker, 2008).

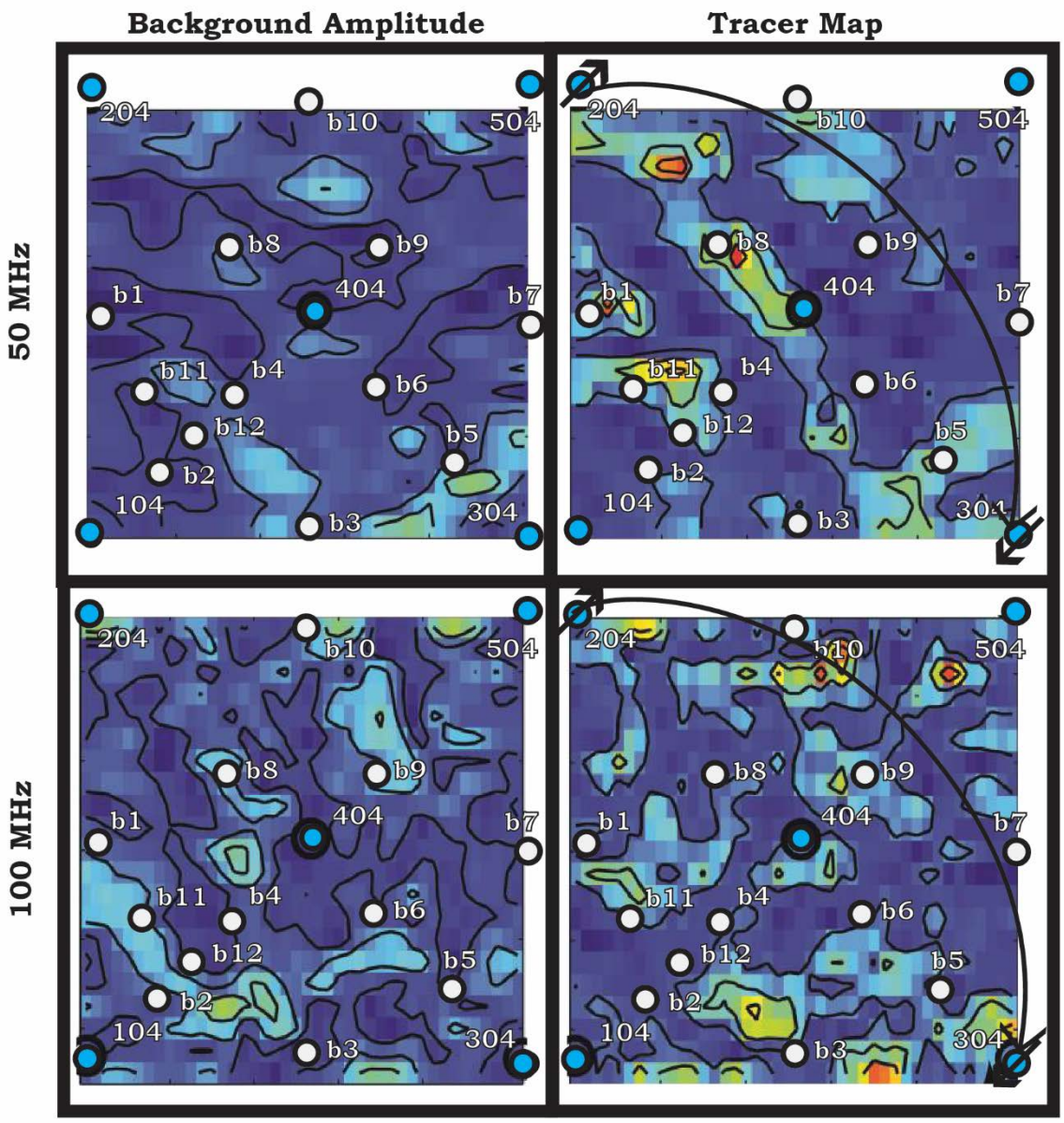

Figure 3.12. Cross-polarized GPR survey summary for radar amplitude measurements at Altona. The background GPR survey (left column) was subtracted from the measured saline tracer image to produce the background-subtracted tracer image (right column). The top and bottom rows are for a 50 and 100 MHz antennae, respectively.

3.6.2 Sinusoidal Slug Tests

From 2009 to 2010, harmonic hydraulic tomography experiments were conducted by Guiltinan and Becker (2015) at the Chasm Lake Well-Field. This was performed by introducing a periodic hydraulic head disturbance in a target well and measuring the phase shift and attenuation of hydraulic head in one or more observation wells. In theory, these two measurements should be a function of hydraulic transmissivity and storativity. Therefore, an inverse model can be used to determine these two parameters given an appropriate analytical solution for transient hydraulic response from a sinusoidal pressure pulse. The results of this technique applied at the Altona site is described in Guiltinan (2012) and Guiltinan et al. (2015).

Transmissivity was estimated for all 40 combinations of pressure pulse sources and sinks that are possible among five wells. Transmissivity was found to range from 1.8 cm^2/s to 32.0 cm^2/s. Data from Guiltinan (2012) is shown in Figure 3.13 which provides a map view of the Chasm Lake Well-Field with the magnitude of hydraulic transmissivity estimated from the sinusoidal slug test plotted. The values reported in Figure 3.13 are the average of two measurements from a given well-pair; the two values are produced from inverting the water well used as the source and sink. In addition, values for three different sinusoidal periods were averaged. The average transmissivities shown suggest the fracture aperture ranges from roughly 5 to 6 mm, based on the local cubic law. For all 40 estimates, however, the minimum and maximum aperture is roughly 4 to 8 mm.

The benefit of using a sinusoidal pressure signal is that the spatial extent in the plane of the fracture that is influenced by the hydraulic sources/sinks can be scaled by varying the sinusoid's period. As a result, a larger range of transmissivity is estimated compared to a more conventional approach, such as a constant flow rate pump test. When such a test was conducted at Altona, estimated transmissivity between the pumping well (well 404) and wells 104, 204, 304, and 504 ranged little and resulted in a fracture aperture of roughly 1 mm (Guiltinan and Becker, 2015).

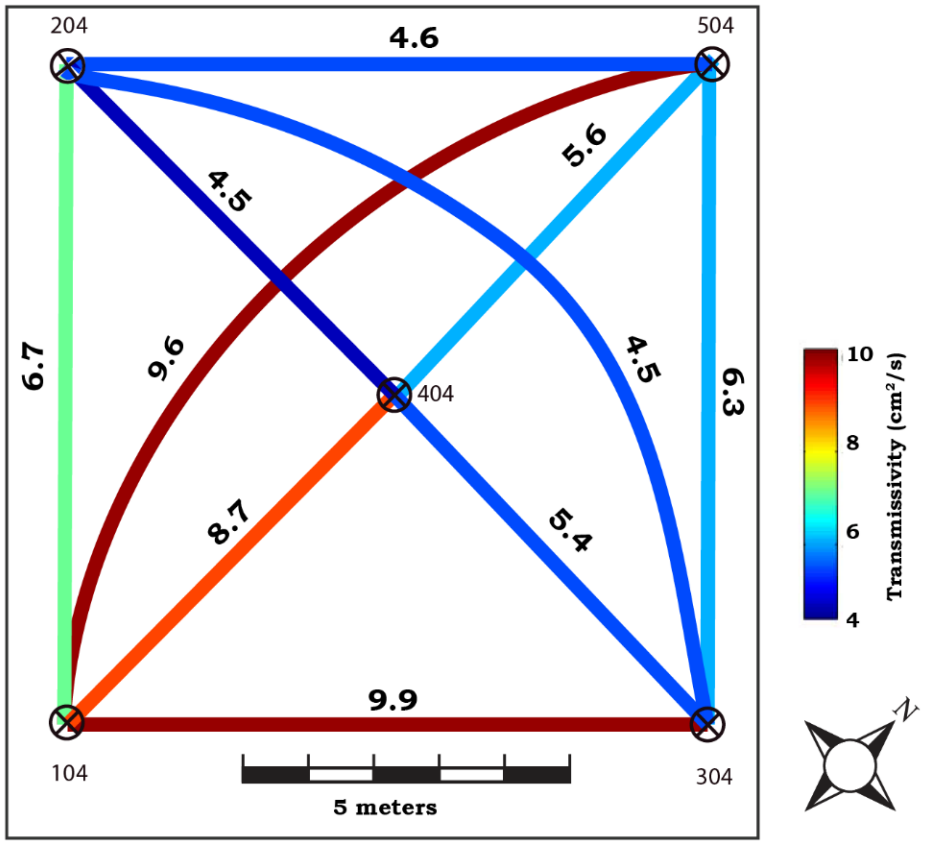

Figure 3.13. Inter-well transmissivity estimated via analysis of sinusoidal slug tests. Values reported on the map represent the average in both directions and for three different wave periods.

3.7 References

Baker, M. (2014), Ground-Penetrating Radar Imaging of Fluid Flow through a Discrete Fracture, *M.S. Thesis*, University of Kansas.

Becker, M. W., and G.P. Tsoflias (2010), Comparing flux-averaged and resident concentration in a fractured bedrock using ground penetrating radar, *Water Resources Research*, 46, W09518, doi:10.1029/2009WR008260.

Beyrle, N. K. (2005), Using Polarized Ground Penetrating Radar to Improve Subsurface Imaging of Bedrock Fractures, *M.S. Thesis*, State University of New York, Buffalo.

EPA (1995), *Great Lakes and Environmental Atlas and Resource Book, Volume 3*, Great Lakes National Program Office, U.S. Environmental Protection Agency; Government of Canada, EPA 905-B-95-001.

Franzi, D. A. et al. (2004), An instrumented watershed for undergraduate instruction and research in hydrogeology and ecology, Proceedings, in *International Instrumented Watershed Symposium*, Edmonton, Alberta, Canada.

Gooley, L. P. (2005), *A History of the Altona Flat Rock*. Bloated Toe Enterprises, Peru, New York.

Guiltinan, E. (2012), Characterizing Well Connectivity in Fractured Bedrock using Periodic Hydraulic Tests, *M.S. Thesis*, California State University, Long Beach.

Guiltinan, E. and M. W. Becker (2015), Measuring well hydraulic connectivity in fractured bedrock using periodic slug tests, *Journal of Hydrology*, 521, 100-107.

Hawkins A. J. (2013), Measurement of the Spatial Distribution of Heat Exchange in a Geothermal Analog Bedrock Site using Fiber-Optic Distributed Temperature Sensing, *M.S. Thesis*, California State University, Long Beach.

Hawkins, A. J., D. B. Fox, R. Zhao, J. W. Tester, L.M. Cathles, D. L. Koch, and M.W. Becker (2015), Predicting thermal breakthrough from tracer tests: simulations and observations in a low-temperature field laboratory, Proceedings, in *47th Workshop on Geothermal Reservoir Engineering*, Stanford University, Stanford, California.

Isachsen, Y.W., E. Landing, J. M. Lauber, L. V. Rickard, and W. B. Rogers (1991), *Geology of New York: A Simplified Account*, New York State Museum and Geological Survey, Albany, NY.

Lagerloef, G., R. Schmitt, J. Schanze, and H.-Y. Kao (2010), The Ocean and the global water cycle, *Oceanography*, 23, 82-93.

Lowe (2016), Sedimentology, Stratigraphic Evolution and Provenance of the Cambrian – Lower Ordovician Potsdam Group in the Ottawa Embayment and Quebec Basin, *Ph.D. Dissertation*, University of Ottawa.

Olcott, P.G. (1995), *Ground Water Atlas of the United States*, United States Geological Survey (USGS), Reston, Virginia.

Paillet, F. L. (2000), A field technique for estimating aquifer parameters using flow log data, *Ground Water*, 38, 510-521.

Perll, C. P. (2013), Evaluating GPR Polarization Effects for Imaging Fracture Channeling and Estimating Fracture Properties, *M.S. Thesis*, University of Kansas.

Rayburn, J. A., P. L. K. Knuepfer, and D. A. Franzi (2005), A series of large, Late Wisconsinan meltwater floods through the Champlain and Hudson Valleys, New York State, USA, *Quaternary Science Reviews*, 24, 2410-2419.

Remmen, K.D. (2013), A reactive tracer method for the measurement of specific surface area in EGS reservoirs, *M.S. Thesis*, California State University, Long Beach.

Sullivan, N. J. B., and D. K. Martin (1970), *A History of the Town of Chazy*, Clinton County, New York. G. Little Press, Burlington, Vermont, 360.

Talley, J. (2005), Imaging Channelized Flow in Fractured Rock using Surface GPR, *M.S. Thesis*, State University of New York, Buffalo.

Talley, J., G. S. Baker, M. W. Becker, and N. Beyrle (2005), Four dimensional mapping of tracer channelization in subhorizontal bedrock fractures using surface ground penetrating radar, *Geophysical Research Letters*, 32, doi:10.1029/2004GL021974.

Tsoflias, G. P., and M. W. Becker (2008), Ground-penetrating-radar response to fracture-fluid salinity: Why lower frequencies are favorable for resolving salinity changes, *Geophysics*, 73, doi:10.1190/1.2957893.

Tsoflias, G. P., C. Perll, M. Baker, and M. W. Becker (2015), Cross-polarized GPR imaging of fracture flow channeling, Journal of Earth Science, 26, 776-784, doi:10.1007/s12583-015-0612-1.

USGS (2014), 2014 New York State Hazard Mitigation Plan, *Technical Report*, in National Seismic Hazard Model (NSHM) Earthquake Catalogs.

Wiesnet, D. R. (1961), Composition, grain size, roundness, and sphericity of the Potsdam Sandstone (Cambrian) in northeastern New York. *Journal of Sedimentary Petrology*, 31, 5-14.

Williams, J. H., R. J. Reynolds, D. A. Franzi, E. A. Romanowicz, and F. L. Paillet (2010a), Hydrogeology of the Potsdam Sandstone in northern New York. *Canadian Water Resources Journal,* 35, 399-416.

Zhao, Y. (2015), The use of Nanoparticles to Assess Subsurface Flow Heterogeneity, *Ph.D Dissertation*, Cornell University.

CHAPTER 4: COMPUTATIONAL METHODS

Fluid flow paths in fractured rock are complex due to variations in permeability and other geometric constraints and, as a result, often experience flow channeling. Therefore, historical approaches to modeling flow have varied in terms of assumptions about reservoir geometry. Assumed fracture flow geometries have ranged from simple one-dimensional flow "channels" to relatively complex two-dimensional flow through a heterogeneous fracture with a specified permeability field. Similarly, our modeling approaches also include a range of complexity in reservoir geometry. Detailed descriptions of heat and mass transport models along with mathematical formulations to produce results are covered. In subsequent chapters, the reader is referred back to sub-sections of this chapter for details of a given model and/or computational method.

4.1 Variations in Reservoir Geometry

The motivation for investigating flow in reservoirs with ranging geometries is related to: (1) the balance between known and unknown flow parameters and (2) computational efficiency. Simple reservoir geometries can provide computationally efficient models with relatively few unknown parameters, such as hydrodynamic dispersion and fracture aperture. More complex reservoir geometries resulting from a non-uniform permeability field, for example, may require extensive computing time even with access to advanced computing capabilities, such as a "super" computer with multiple

parallel processing capabilities. In addition, complex geometries frequently employ a large number of unknown parameter values that are specified *a priori* or fit to existing data or extracted using an inverse model.

This dissertation considers reservoirs with geometries of wide-ranging complexity in an effort to establish what level of complexity is required to produce meaningful forward-models. For example, in Chapter 7 a simple one-dimensional flow channel model with uniform flow velocity is used to forecast thermal breakthrough based on adsorbing and inert tracer return data. This approach is computationally efficient and straight-forward to implement with few fitted-parameters. A downside, however, is that there is no dependency on the spatial distribution of fluid flow velocities and realistic fracture aperture variations within the reservoir that are likely to exist.

Chapter 9 presents the results of computational models that represent more complex reservoir geometries with dipole-flow induced in a heterogeneous aperture field. This approach is computationally intensive (e.g., up to 7 d computing time to determine 9000 aperture values on a machine with 32 GB RAM and 8 cores), but it is more realistic than a uniform one-dimensional flow channel model, because simulated tracer RTDs result from aperture variations that are spatially correlated based on measured statistical properties of rock core. In addition, inducing a dipole-flow through a heterogeneous fracture produces a tracer Residence Time Distribution (RTD) that reflects the combined

influence of velocity variations in dipole-flow as well as hydrodynamic dispersion and flow-channeling.

In contrast, a one-dimensional flow channel model replicates such effects by incorporating multiple flow channels and varying hydrodynamic dispersion. Regardless of the model used, there is still a lack of understanding of how fracture aperture variations at measureable length scales (millimeters to centimeters) correlate to permeability distribution at the scale of field experiments with larger interwell spacing (meters to kilometers). Therefore, even the approach adopted for identifying a spatially varying aperture field should be considered loosely connected to physically realistic statistics regarding spatially correlated permeability fields.

4.2 One-Dimensional Transport Models

4.2.1 Inert and Reactive Tracers

In Chapter 7, the effective surface area available for heat exchange will be calculated based on a particular thermal-hydraulic model and the results of an inert and adsorbing tracer test conducted at the Altona Field site. Simulation of inert and adsorbing tracer transport was performed using a one-dimensional analytical model for the combined effects of tracer advection, dispersion, and rate-limited adsorption in which the governing partial differential equation is

$$\frac{\partial c}{\partial t} = D_f \frac{\partial^2 c}{\partial x^2} - v\frac{\partial c}{\partial x} - \frac{2}{w}\frac{d\Gamma}{dt}, \qquad (4.1)$$

where w is the fracture aperture [L], c is tracer fluid concentration in the fracture [M/L^3], t is time, Γ is tracer surface concentration [M/L^2], D_f is the one-dimensional hydrodynamic dispersion coefficient [L^2/t], and v is the average fluid velocity across the fracture aperture [L/t] (Figure 4.1). The dispersion coefficient, D_f describes hydrodynamic dispersion which can be expressed as a linear function of mean fluid velocity, longitudinal dispersivity, a_L and the mass diffusion coefficient, D^*, such that (Bear, 1972)

$$D_f = \alpha_L v + D^*. \tag{4.2}$$

In the above formulation, transverse dispersivity is assumed negligible relative to longitudinal dispersivity, because transverse dispersivity is dominated by the mass diffusion coefficient, which is typically much smaller than the product of velocity and dispersivity.

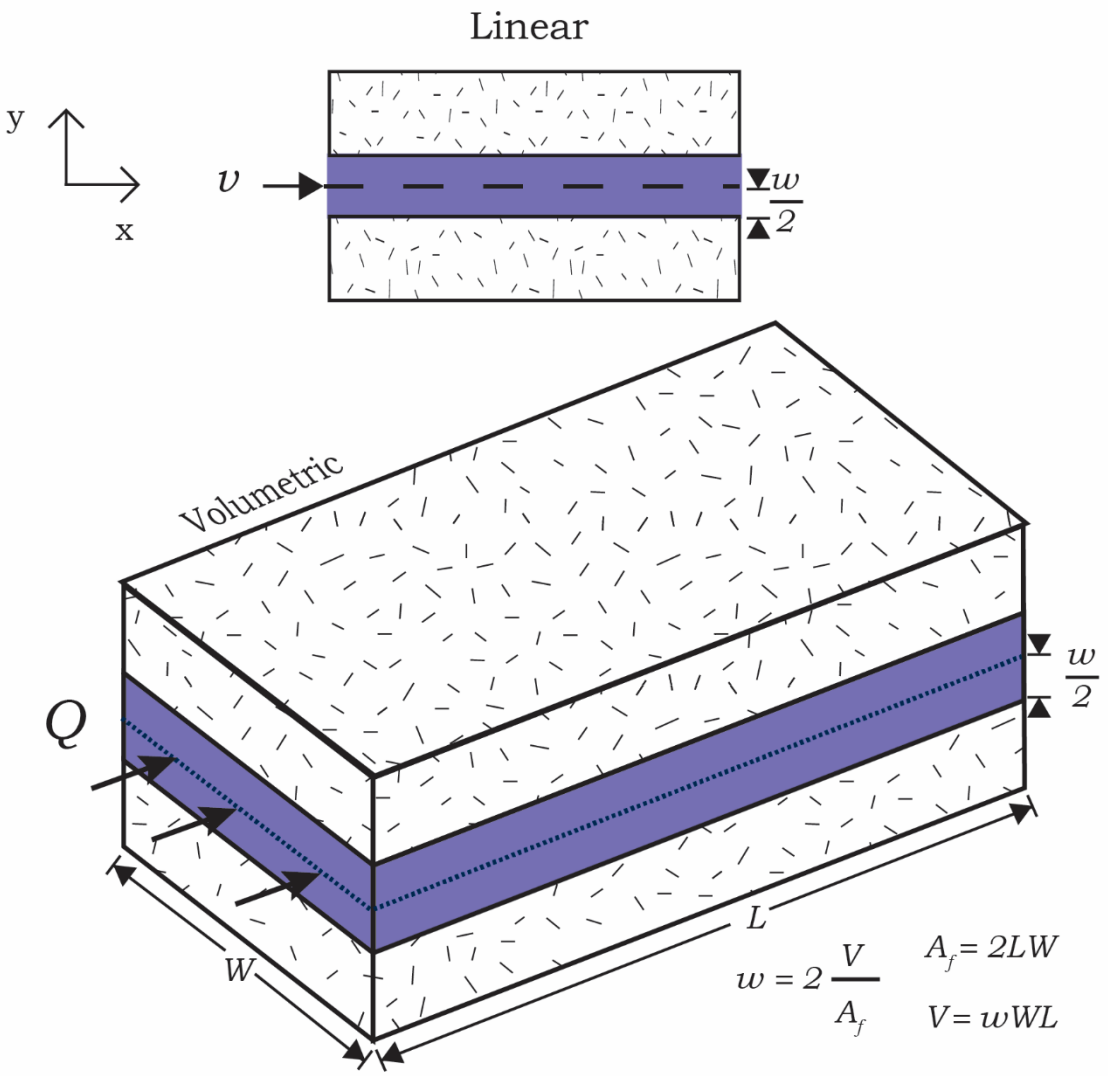

Figure 4.1. One-dimensional model schematic used in one-dimensional tracer transport model for advection, dispersion, and adsorption. Both a linear (upper figure) and volumetric (lower figure) geometry can be assumed.

A number of adsorption equation formulations are available to relate tracer fluid concentration to fracture surface concentration. The most basic form assumes equilibrium is rapid and there is a linear relationship between surface and fluid concentration. More sophisticated forms incorporate kinetics and/or non-linear isotherms (e.g., Langmuir or Freundlich). For our purposes, a non-equilibrium condition was necessary, because the half-life of cesium

adsorption reaction on rock has been found to be much longer than the duration of the tracer experiments (Fujikawa, 1991). From Bear (1972), a suitable non-equilibrium form for the time-derivative of surface concentration is

$$\frac{d\Gamma}{dt} = k_{ads}\left(P_f c - \Gamma\right), \tag{4.3}$$

where k_{ads} and P_f are the first-order adsorption rate constant [1/t] and the fracture/fluid partition coefficient [L], respectively.

In Laplace space, the solution for Equation 4.1 is

$$\bar{c}(s) = F_T \exp\left[\frac{Pe}{2}\left(1 - \sqrt{1 + \frac{4}{Pe}\frac{\left(sV + \kappa A_f\right)}{Q}}\right)\right]. \tag{4.4}$$

Equation 4.4 represents a tracer RTD resulting from one flow channel where F_T is a transfer function in Laplace space describing the initial tracer concentration at the injection well, Pe is the dispersional Peclet number, V is flow channel volume, Q is the volumetric flow rate, A_f is the surface area available for adsorption, s is the Laplace transform variable, and the adsorption reaction is characterized by κ where

$$\kappa = \frac{sP_f k_{ads}}{k_{ads} + s}.$$

Derivation of Equation 4.4 is provided in Appendix B, including the conversion from dispersion and position to the Peclet number and mean tracer residence time.

Following Reimus et al. (2003), a suitable transfer function to describe the tracer tests conditions at Altona includes a finite mass of tracer, M_{inj}, dissolved in a fluid volume, V_{inj}, at a constant volumetric flow rate, Q, such that

$$F_T = \frac{M_{inj}}{V_{inj}} \left(\frac{1 - \exp\left(-\frac{V_{inj}}{Q} s \right)}{s} \right).$$

To find a solution for tracer concentration as a function of time, Equation 4.4 is numerically inverted using a Laplace transform inversion routine for MATLAB® (Hollenbeck, 1998).

In the case of multiple flow channels, Equation 4.4 can be modified such that the tracer mass injected and the volumetric flow rate are divided into N flow channels. In this case, Equation 4.4 becomes

$$\overline{C}(s) = \sum_{i=1}^{N} f_i F_T \exp\left[\frac{Pe_i}{2} \left(1 - \sqrt{1 + \frac{4}{Pe_i} \frac{\left(sV_i + \kappa A_{f,i} \right)}{Q}} \right) \right], \tag{4.5}$$

where the subscript i refers to an individual within a series of flow channels. The f_i term refers to the fraction of the total mass recovered for each flow channel, i, where $0 < f_i \leq 1$. For cases where tracer mass recovery at a production well is less than 100% of the injected amount, the sum of f_i will be

less than one, unless measured tracer data has been extrapolated such that tracer mass recovery is 100%.

4.2.2 Thermal Advection and Conduction

In Chapter 5, heat transport in an idealized rectangular channel will be modeled assuming one-dimensional advection within the fracture and thermal conduction perpendicular to the fracture. Thermal conduction in the direction of fluid advection is assumed negligible. Far field rock temperature, T_r, and the temperature of the injected fluid, T_w, are assumed to be constant in time. The solution for temperature at a production well, T_{prod} as a function of time, t, is

$$T_{prod}(t) = T_r + (T_w - T_r)\,\mathrm{erf}\left[\frac{A_f}{2\dot{m}C_{p,w}}\sqrt{\frac{(\rho C_p K)_r}{t}}\right], \tag{4.6}$$

where A_f is the surface area available for heat exchange (i.e., Flow-Wetted Area, FWA), ρ is density, C_p is heat capacity, K is thermal conductivity, and $\dot{m}$ is the mass flow rate (Fox, 2016). The subscripts r and w refer to the bulk rock matrix and fluid within the fracture, respectively. Solutions for production well temperature in similar geometries under steady flow conditions have been solved numerous times (e.g., Carslaw and Jaeger, 1959; Gringarten et al., 1975; Bear, 1972; etc.).

In the case of multiple flow channels acting independently, Equation 4.6 can be modified to account for the temperature increase of each flow channel as was done for Equation 4.4. Assuming negligible variations in fluid heat capacity among flow channels and no thermal interactions between them, production well temperature from N flow channels is

$$T_{prod}(t) = T_r + (T_w - T_r)\sum_{i=1}^{N} f_i \,\mathrm{erf}\left[\frac{A_{f,i}}{2\dot{m}C_{p,w}}\sqrt{\frac{(\rho C_p K)_r}{t}}\right]. \quad (4.7)$$

The unknown parameters in Equation 4.7 include the fraction of each flow channel, f_i, and the surface area available for heat exchange, A_f. These two parameters can be determined indirectly by fitting a computational transport model for inert and adsorbing tracer transport (Equation (4.5 or 4.6) to measured data. Thermal breakthrough can subsequently be predicted by inputting the surface area and flow channel fraction identified via the inverse model into Equation 4.7. It is important to note, however, that the surface area available for adsorption is not necessarily identical to the effective surface area available for heat exchange. To account for the difference in heat transfer surface area and adsorptive surface area, laboratory experiments were conducted in which the surface area available for heat transfer was assumed to be equal to the surface area of the tested rock fragment independent of the small-scale surface heterogeneities on the rock surface (see sub-section 7.3.1 for additional details).

4.3 Two-Dimensional Transport Models

In Chapters 6 and 9, two-dimensional heat and mass transport in a non-uniform aperture field are simulated using a finite element method (FEM) solver developed in our group (Fox et al., 2015). The pressure and velocity field for simulations involving both heat and mass transfer were determined using the same FEM. To simulate tracer transport, the effects of advection, hydrodynamic dispersion and adsorption were incorporated into the FEM

model. For heat transport, hydrodynamic dispersion was assumed negligible and three-dimensional thermal conduction between the fracture fluids and the rock matrix was solved via the boundary element method. After a sensitivity analysis indicated that there are negligible difference between a one-dimensional and three-dimensional treatment of thermal conduction, one-dimensional thermal conduction was assumed. In addition, no-flux boundaries were applied to the fracture surface (i.e., no fluid flow into the rock matrix) and at the edge of the model domain.

For tracer tests and heat exchange, two-dimensional fluid flow in the plane of the fracture is solved via the FEM. Fluid advection was modeled as a flow of a Newtonian fluid in a thin fracture, mathematically represented as a rectangular channel with a variable aperture. An internal fluid pressure field within the fracture was simulated using a two-well pattern with an injection well (source) and production well (sink) under steady-state flow conditions. No-flux boundary conditions were applied at the surfaces of the fracture and the edges of the fracture domain. Combining a reduced Navier-Stokes equation and the solution for Poiseuille flow (as described in Fox et al. (2015)), the pressure field can be determined from the following equation:

$$-\nabla\cdot\left(\frac{\rho_w w^3}{12\mu}\nabla P\right)=\sum_l \dot{m}_l\delta(\mathbf{r}-\mathbf{r}_l) \tag{4.8}$$

where ρ_w, w, μ, and P, are fluid density, fracture aperture, dynamic fluid viscosity, and pressure, respectively. The right hand side of the equation describes the influence of sources and sinks where $\dot{m}$ is the mass flow rate of

each source or sink, $\delta(\ldots)$ is the Dirac delta function, and **r** is the position in the fracture. The vector $\mathbf{r_l}$ represents the position of the sources and sinks in the fracture plane. The two dimensional pressure gradient is in the plane of the fracture. Once the pressure field is determined via the FEM using Equation 4.8, the average velocity vector, <**v**> across the fracture aperture, w, is calculated as

$$\langle \mathbf{v} \rangle = -\frac{w^2}{12\mu} \nabla P. \tag{4.9}$$

4.3.1 Inert and Reactive Tracers

The differential tracer mass balance on a control volume inside the fracture includes transient accumulation of tracer, tracer dispersion, and advective bulk flow and can be represented by the following governing equation:

$$w\frac{\partial c}{\partial t} = w\nabla \cdot \left(\mathbf{D_f} \cdot \nabla c\right) - w\langle \mathbf{v} \rangle \cdot \nabla \mathrm{c} \tag{4.10}$$

where c, t, $\mathbf{D_f}$, <**v**>, and k are tracer concentration, time, dispersion coefficient tensor, and velocity vector, respectively. The spatial dimension of the concentration gradient ∇c is in the two-dimensional plane of the fracture. For simulating tracer transport, time discretization was performed using the Crank-Nicholson method. The dispersion coefficient tensor, $\mathbf{D_f}$, is a function of fluid velocity, longitudinal hydrodynamic dispersivity, a_L, and molecular diffusion, D^*, and is expressed as

$$\mathbf{D_f} = \alpha_L \frac{\langle \mathbf{v} \rangle \langle \mathbf{v} \rangle}{|\langle \mathbf{v} \rangle|} + D^* \mathbf{I} \tag{4.11}$$

where **I** is the identity matrix (Bear, 1972). When simulating temperature-dependent chemical reactions, the temperature field at a specified time of circulation is solved first followed by the tracer concentration field.

4.3.2 Thermal Advection and Conduction

For modeling heat transport, the equation for two-dimensional convective transport in the fracture used for tracer transport simulations (Equations 4.8 and 4.9) is coupled to an equation for three-dimensional heat conduction in the rock matrix orthogonal to the fracture plane. Assuming negligible transient heat accumulation in the liquid contained by the fracture and negligible thermal conduction through that liquid, the fluid energy balance inside the fracture is given by

$$q_s = (\rho C_p)_w w \langle \mathbf{v} \rangle \cdot \nabla T \tag{4.12}$$

where q_s is the surface heat flux from the fracture surface going into the fluid and ρ and C_p are density and heat capacity, respectively, with subscript w referring to water and T is temperature. The two dimensional temperature gradient is in the plane of the fracture. The governing equation for thermal conduction in the rock matrix surrounding the fracture is

$$(\rho C_p)_r \frac{\partial T}{\partial t} - \nabla \cdot (K_r \nabla T) = q_s \delta(z - z') \tag{4.13}$$

where ρ, C_p, and K are density, heat capacity, and thermal conductivity, respectively, with subscript r referring to rock properties. The distance, z, into

the surrounding rock matrix orthogonal to the fracture surface, in which $z = 0$ represents the fracture surface, z' refers to the position, orthogonal to the fracture, of the heat source, q_s, and $\delta(\ldots)$ is the Dirac delta function. For the entire model domain, the fluid-filled fracture is the heat source (or sink) which results from the temperature difference between fluids within the fracture aperture and the bulk rock. For Equation 4.13, the spatial dimension of the temperature gradient,∇T, is three dimensional.

Because the surface heat flux depends on the rock thermal conductivity and temperature gradient orthogonal to the fracture surface, Equation 4.13 cannot be solved independently. Therefore, a three-dimensional Green's function was used to present the temperature of the system dependent on the fracture surface heat flux (see Fox et al. (2015), for details). For a heat source located at $z=0$ and confined to the extent of the fracture, the temperature of the system is expressed as

$$T(x,y,z,t) = T_r + \int_0^t \int_{A_f} G(x-x', y-y', z, t-t') \frac{q_s(x', y', t')}{(\rho C_p)_r} dx' dy' dt' \qquad (4.14)$$

where A_f is the fracture area, G is the three-dimensional Green's function for transient conduction and T_r is the original reservoir rock temperature, which is assumed to be homogeneous in space and constant in time.

Under specific conditions, computational efficiency can be improved by adopting a one-dimensional solution for thermal conduction in the rock matrix. A characteristic length scale for one-dimensional thermal conduction is

represented by the square root of the product of thermal diffusivity and a characteristic time. If neither the well spacing nor the width of a preferential flow channel is smaller than the characteristic length, then negligible error is introduced by assuming one-dimensional thermal conduction. For application to the Altona field site where modal tracer residence time is roughly 20 min, a one-dimensional approximation is justified for any well spacing or flow channel width larger than roughly 3.5 cm, which is substantially less than the smallest length scale considered, which was roughly 0.9 m.

4.4 References

Bear, J. (1972), *Dynamics of Fluids in Porous Media*, Elsevier, New York City, New York.

Carslaw, H., and J. Jaeger (1959), *Conduction of Heat in Solids, 2nd ed.*, Oxford University Press, Oxford, U.K.

Fox, D. B., D.L. Koch, and J.W. Tester (2015), The effect of spatial aperture variations on the thermal performance of discretely fractured geothermal reservoirs, *Geothermal Energy*, 3, 1-29.

Fox, D. B. (2016), Thermal Hydraulic Modeling of Discretely Fractured Geothermal Reservoirs, *Ph.D Dissertation*, Cornell University.

Fujikawa, Y., and M. Fukui (1991), Analysis of radioactive cesium and cobalt adsorption to rocks using the two-site kinetic model equations, *Journal of Contaminant Hydrology*, 8, 43-69.

Gringarten, A.C., P.A. Witherspoon, and Y. Ohnishi (1975), Theory of heat extraction from fractured hot dry rock, *Journal of Geophysical Research*, 80, 1120-1124.

Hollenbeck, K.J. (1998), INVLAP.m: A MATLAB® function for numerical inversion of Laplace transforms by the de Hoog algorithm, http://www.isva.dtu.dk/staff/karl/invlap.htm.

Reimus, P., G. Pohll, T. Mihevc, J. Chapman, M. Haga, B. Lyles, S. Kosinski, R. Niswonger, and P. Sanders (2003), Testing and parameterizing a conceptual model for solute transport in a fractured granite using multiple tracers in a forced-gradient test, *Water Resources Research*, 39, doi:10.1029/2002WR001597.

CHAPTER 5: HEAT EXCHANGE EXPERIMENT

5.1 Introduction

Heat exchange experiments were conducted at the Altona field site to provide measurements of thermal breakthrough data with short residence times and a well-constrained flow field. In addition, Fiber-Optic Distributed Temperature Sensing (FO-DTS) was used to measure the spatial distribution of temperature between flowing fluids at different times in the target fracture and the bulk rock matrix. Results from this chapter will be compared to results of studies described in Chapters 6 through 9.

The measured temperature data were used to estimate the effective fracture surface area available for heat exchange using a one-dimensional thermal-hydraulic model for multiple flow channels (see sub-section 4.2.2 for model description). The Non-Linear Conjugate Gradient (NLCG) method was used to search for an optimum fit to measured temperature data using the Sum of Square Errors (SSE) as the objective function and an analytical model for heat advection and conduction to simulate temperature. The optimization provided a means for inverting the model to estimate the effective heat transfer surface area.

5.2 Field Experiment Setup

The heat exchange experiment was conducted under forced convection conditions between well 204 (inject) and well 304 (pump) (Figure 5.1). Prior to reinjection into the formation the water was heated with a propane-fired

tankless water heater (AO Smith, Model #: T-H3-OS) up to 74 °C. Flow was induced by a variable speed positive displacement pump (Rediflow-2, Grundfos). Production water was directly reinjected into the injection well after circulating through the tankless water heater (Figure 5.2). Flow rate was maintained at 5.7 L/min and was monitored using the digital flow gauge accompanying the tankless water heater. Injection and pumping were conducted from a hydraulically isolated zone in the wellbores that were aligned with the 7.6 m deep test fracture. Hydraulic isolation in the injection well and three observation wells was achieved using two modified inflatable pipe packers (Lansas Products, Lodi, California) in each well and the spacing in-between the two packers ranged from 0.2 to 0.5 m (see Appendix E for photographs). In the production well, one packer was inflated below the target fracture.

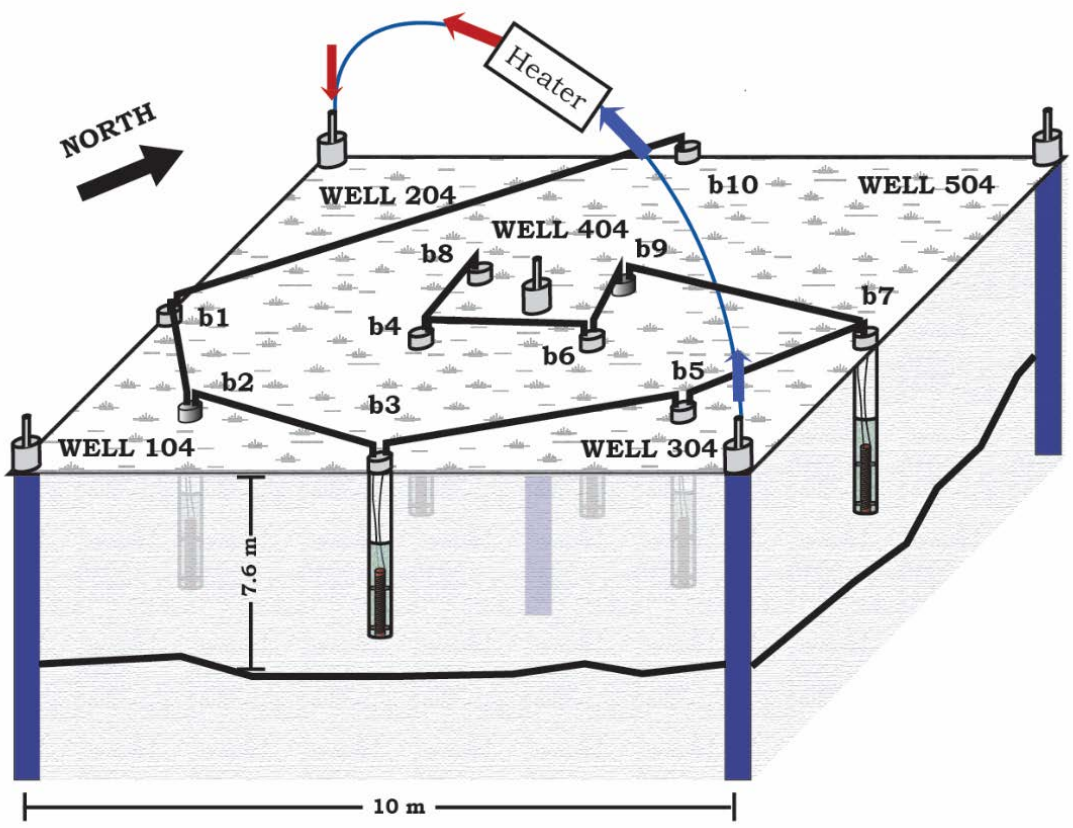

Figure 5.1. Three-dimensional schematic of the heat exchange experiment in which hot water (74 °C) was continuously circulated between injection well 204 and production well 304. Three observation wells (wells 104, 404, and 504) are indicated on the schematic as well as the ten dry boreholes (b1 to b10) which contain the fiber-optic cable used to measure temperature via FO-DTS during the heat exchange experiment.

Figure 5.2. Photograph of the tankless water heater used to continuously heat produced fluids prior to circulating fluids through the target fracture.

Water temperature and hydraulic head in three monitoring wells (wells 104, 404, and 504 in Figure 5.1) were recorded via autonomous pressure/temperature loggers (Solinst Leveloggers®, Model #: 3001). A temperature transducer (RBR *solo* T ®) was placed within well 304 to record temperature rise in the production.

As hot water was continuously circulated through the relatively cold formation, FO-DTS continuously monitored the spatial distribution of fracture/matrix heat exchange at ten locations situated with the 100 m^2 well-field (Figure 5.1). The ten boreholes were drilled to a target depth of 0.5 m above the fracture. Therefore, there was no direct hydraulic connection between the dry boreholes and the target fracture (Figure 5.3). As a result, given the lower permeability of the bulk rock, only conductive heat exchange

between the fracture and the bulk rock matrix was monitored via FO-DTS. FO-DTS recorded temperature rise over lengths of roughly 1 to 1.5 m. The closest temperature measurements to the target fracture ranged from 0.6 to 1.5 m.

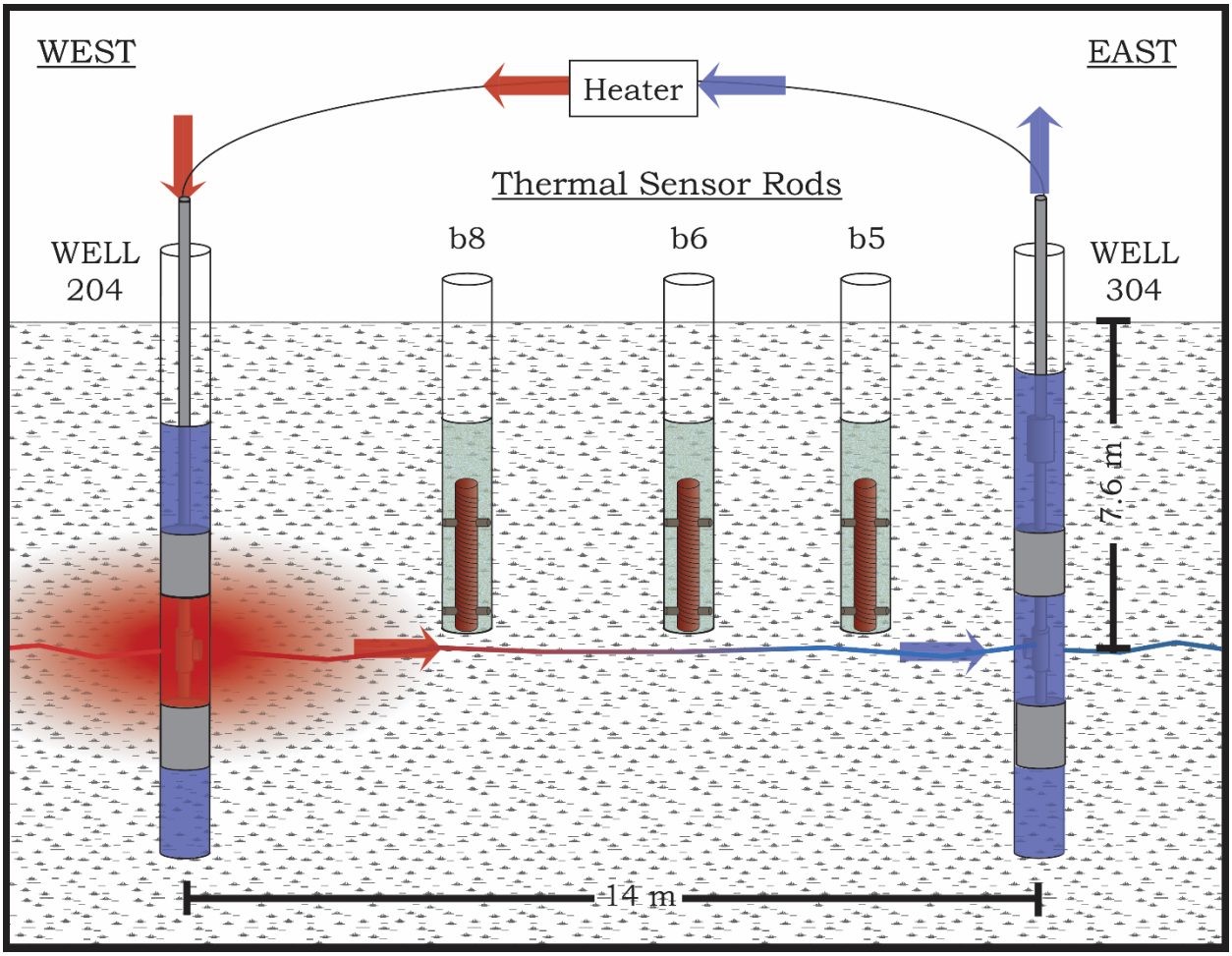

Figure 5.3. Cross section view from well 204 to well 304 demonstrating the relative positions of the fiber optic cable network at three locations and the injection and production well.

FO-DTS is a relatively new means of thermometry (developed in the 1980s) that has high thermal resolution (~0.01 °C). Temperature measurements are made along a fiber-optic cable by observing the backscatter of laser light projected along the fiber (Smolen and Spek, 2003). An Oryx FO-

DTS (Sensornet Ltd) was rented from the Center for Transformative Environmental Monitoring Programs (CTEMPs) which is funded by the National Science Foundation and jointly operated by Oregon State University, Corvallis and the University of Nevada, Reno.

The Oryx collects temperature measurements on a sampling interval of 1 m with a spatial averaging interval of 2.4 m, according to laboratory tests. In this context, the spatial averaging interval was defined as the distance along the fiber-optic cable required for the Oryx FO-DTS to respond to 80% of a step change in temperature after Smolen and Spek (2003). Sensornet's Oryx data sheet states an optimum temperature resolution of ±0.01 °C when collecting laser backscatter data continuously for 30 min (Sensornet, 2007). Resolution worsens continuously with increasing distance traveled along the fiber-optic cable. At 1400 m, which is the length of cable used in these experiments, the temperature resolution is ±0.02 °C when collecting data for about 30 min.

The effective FO-DTS sampling interval was improved from 1.0 m to 2.1 cm by wrapping the fiber-optics around a specially fabricated, externally threaded, 5.7 cm O.D., schedule-80 PVC pipe. Fiber-optics were wrapped around the threaded pipe using modified lathe and spool feed (Figure 5.4). Two coils of cable were left at the top of each pipe enable to arc fusion splice the fiber-optics of each borehole in the field. The wrapped pipes were then shipped to New York where they were placed within each borehole and arc fusion spliced using a Fujikura SpliceMate™ during the summer of 2011. Five pipes

were 3 m in length and five were 1.5 m. Arc fusion splicing is a method of joining two fiber-optic cables by melting each end. Fusion splicing produces less signal attenuation compared to mechanical splicing.

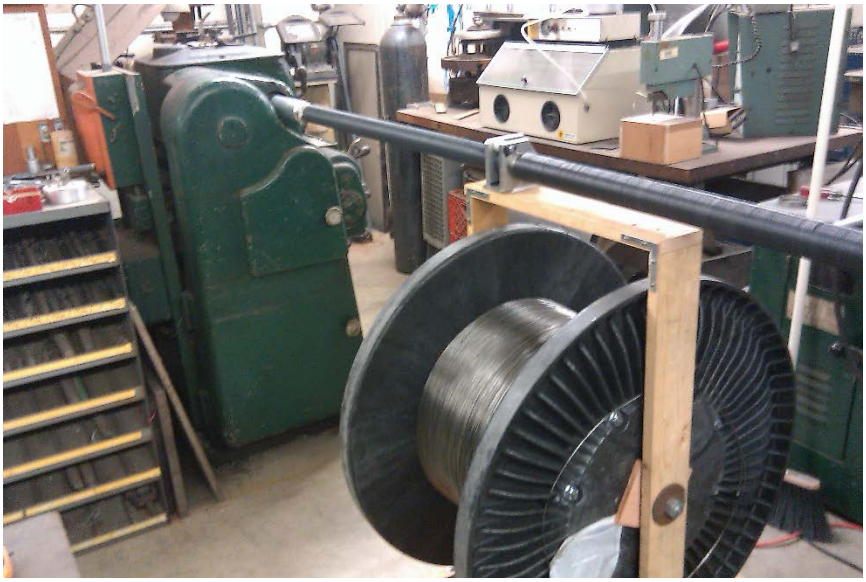

Figure 5.4. Photograph demonstrating the procedure for wrapping fiber-optic cable around a threaded pipe. A lathe spins the pipe while the spool of cable is uncoiled around the pipe. Electrical tape secured the cable to the pipe.

The process of wrapping fiber-optic cable around a threaded PVC pipe increases the attenuation of light within the fiber-optic cable, thereby decreasing the maximum length of cable suitable for accurate FO-DTS deployment. To reduce the impact of bending, a high numerical aperture fiber-optic cable (AFL, model DNS-2528) with a 37.5 mm static bend radius for 0.05 dB loss was used. A high numerical aperture cable reduces signal attenuation by permitting light with a larger maximum angle of incident rays to be transported through the fiber-optic cable.

To prevent surface water runoff into the boreholes, a 15 cm diameter well casing was installed in the top meter with an additional 0.20 to 0.45 m exposed at the surface. Below the surface casing, the wells were left uncased. The 4.1 cm annular space between the fiber-optic cable and the borehole wall was filled with a mixture of sand and water in order to enhance thermal coupling between the rock formation and the fiber-optic cable. Clean sand (Quickrete © Play Sand #1113) was introduced into the borehole roughly 0.5 L at a time and water was poured in-between to wash sand from the sides of the borehole. The wrapped cable rod was vibrated during pouring to assure compaction. Because the saturated sand has similar thermal conductivity to the sandstone, and the filled annular space is narrow, heat was not conducted preferentially along the FO-DTS probes.

5.3 Analytical Modeling

The two key unknown parameters from Equation 4.6 are the fraction of each flow channel, f_i, and the effective surface area available for heat exchange, A_f. These two parameters were indirectly determined by solving an inverse model that fit simulated to measured temperature rise. The objective function was the Sum of Square Errors (SSE) and the Non-Linear Conjugate Gradient (NLCG) method was used to solve the inverse problem.

The thermal conductivity of the Potsdam Sandstone at the Altona site was measured using the RK-1 Rock Sensor Package of the KD2 Pro manufactured by Decagon Devices. A value of 7.6 W/m-K was recorded in a rock sample collected from ground surface at the well-field. The measured

thermal conductivity is slightly greater than the maximum value for sandstone published in Robertson (1988) which ranges from 5 W/m-K to 7.5 W/m-K for sandstones with 60-90% quartz, 0-10% matrix porosity, and water filled pores. The density of the Potsdam Sandstone was determined to be 2.5 g/cm3 by weighing a rock sample collected at ground surface and measuring its volumetric displacement in water. The specific heat was assumed to be 930 J/kg-K based on reported average values of sandstone in Robertson (1988). Specific heat and density of water was assumed to be 4200 J/kg-K and 1 g/cm^3, respectively, appropriate for the temperature conditions at Altona.

5.4 Results and Discussion

5.4.1 Field Experiments

Circulation between the injection well and production well began 5.8 h prior to hot water injection. For the first 3.8 h, hydraulic head gradually fell by 10 cm in observation wells 104, 404, and 504. After this point in time, hydraulic head measurements in these three observation wells remained relatively stable. Two hours prior to hot water injection 62 water temperature measurements in the production well recorded an average reservoir fluid temperature of 11.74 ± 0.02°C.

The heat exchange experiment was initiated by setting the tankless water heater to 74 °C via the digital controller connected to the heater. Injection temperature was monitored at the outlet of the heater using the temperature readouts provided by the tankless water heater. Injection temperature remained at 74 ± 2 °C for the duration of the experiments (6 d).

The heat exchange experiment lasted 6 d with a steady fluid circulation rate of 5.7 L/min amounting to a total volume circulated of 49,250 L. FO-DTS began detecting a temperature increase 83 min after hot water injection began at borehole b8. By the end of the experiment, temperature increases were observed in all boreholes (Figure 5.5). Measured temperature rise among the ten boreholes ranged from 0.4 °C in borehole b2 to 18.5 °C in borehole b8 (Figure 5.5).

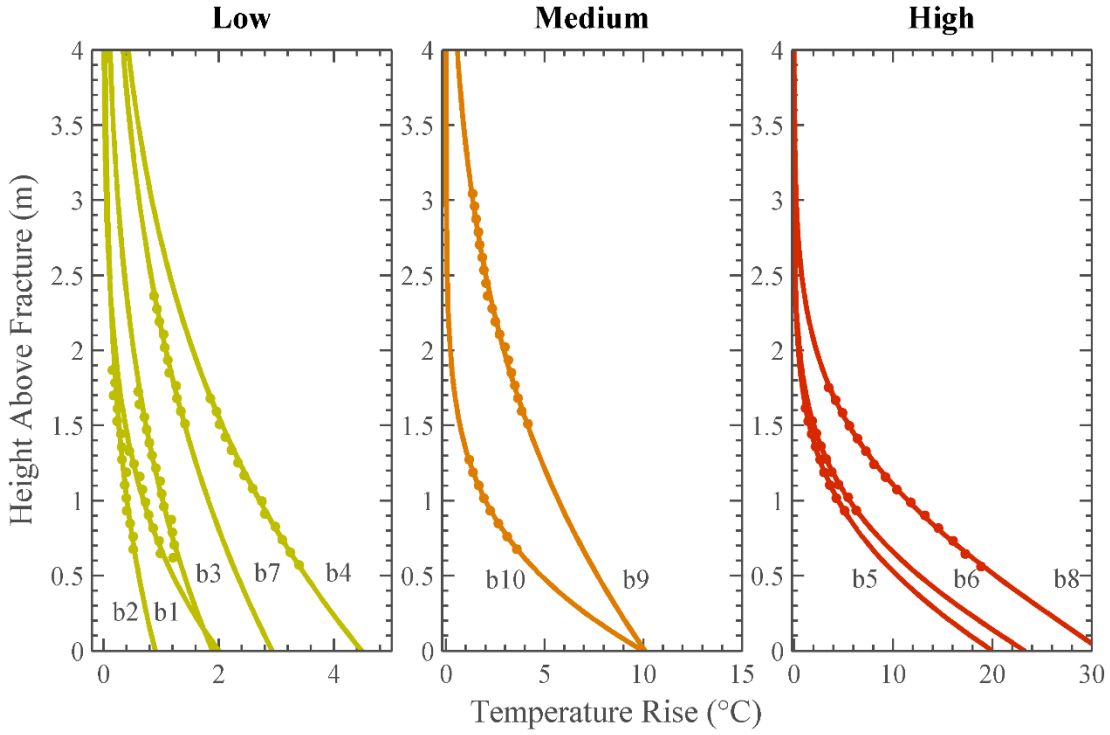

Figure 5.5. Temperature rise versus height above the target fracture surface for all ten monitoring locations after 144 h of hot (73 °C) water circulation. The graphs are separated by the relative magnitude of temperature rise. The measured temperature data are shown as points and an error function extrapolation to the fracture surface are shown as solid lines.

The FO-DTS thermal sensors were intentionally installed in contact with undisturbed rock between the fracture and the bottom of the sensor with a

thickness of 0.6 to 1.5 m. Therefore, fracture fluid temperature as a function of time was estimated by extrapolating the FO-DTS data from the bottom of the FO-DTS sensors to the fracture surface. Data extrapolation was performed using an error function fit of temperature vs. height above the fracture surface. An error function is roughly an appropriate model for thermal conduction because it permits an equilibrium value at large distances, which is not possible with some other simple mathematical fits, such as a linear or logarithmic fit. Based on this extrapolation, temperature in the fracture after 144 h of circulation ranged from 0.9°C to 31.1 °C. The boreholes which experienced the greatest temperature rise were spatially distributed in a narrow path directly between the injection well and production well (Figure 5.6).

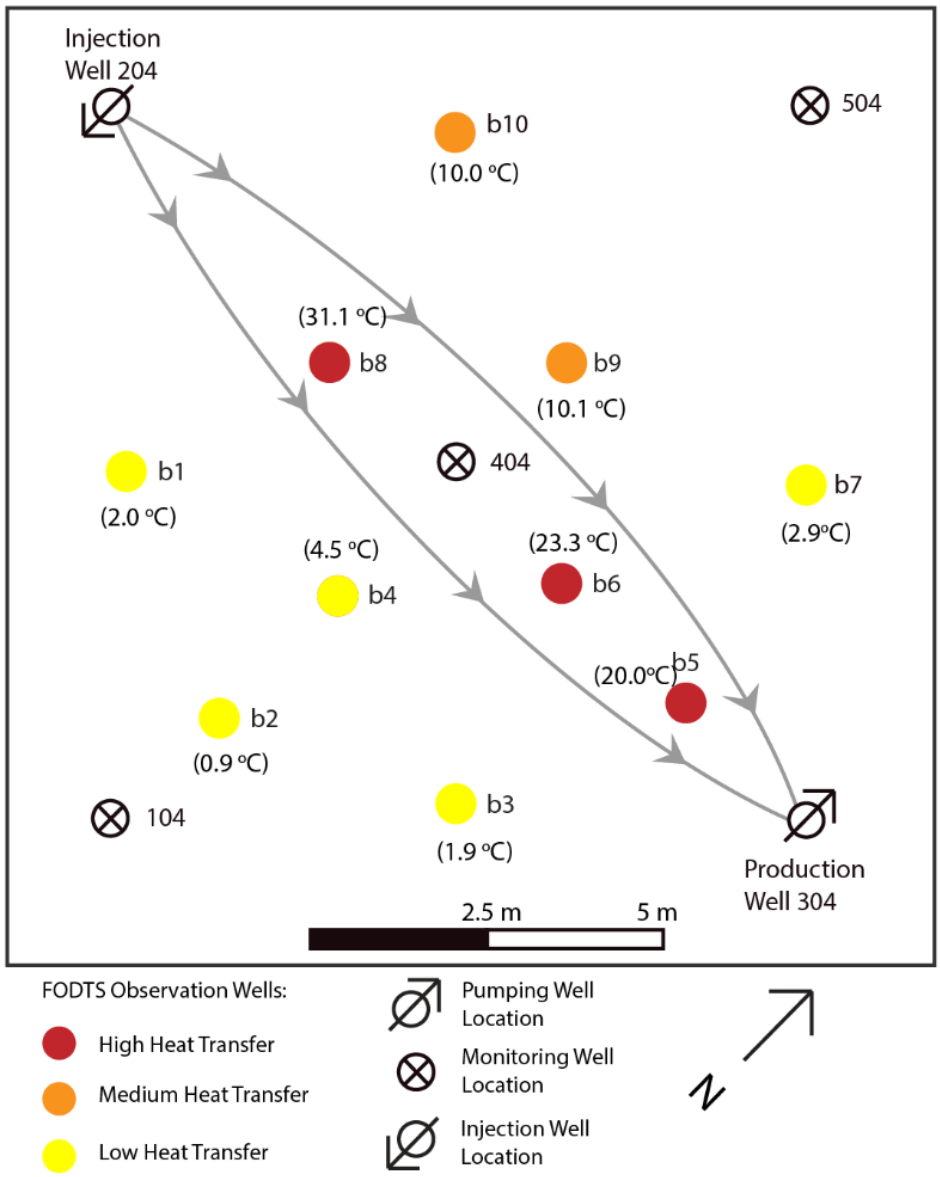

Figure 5.6. Map view representation of temperature rise, as recorded via FO-DTS after 144 h of hot water circulation. Values in parentheses are the fracture fluid temperature determined by an error function extrapolation of the data shown in Figure 5.5.

At the production well, groundwater temperature ranged between 11.72 and 11.75 °C until the onset of thermal breakthrough occurred 40 min after the initiation of hot water injection (Figure 5.7). Thermal breakthrough roughly followed a logarithmic time dependence at times greater than roughly 10 h.

From 1.3 to 4 h into the heat exchange experiment, the maximum slope of production temperature was 0.7 °C/h. The slope fell to 0.04 °C/h by the end of the experiment after 144 h of hot water injection. Reservoir fluid temperature at the production well rose 17.4 °C from 11.7 °C to 29.8 °C which corresponds to 29% of the difference between the initial temperature of groundwater pumped at well 304 and the temperature of water reinjected into well 204 (74 °C).

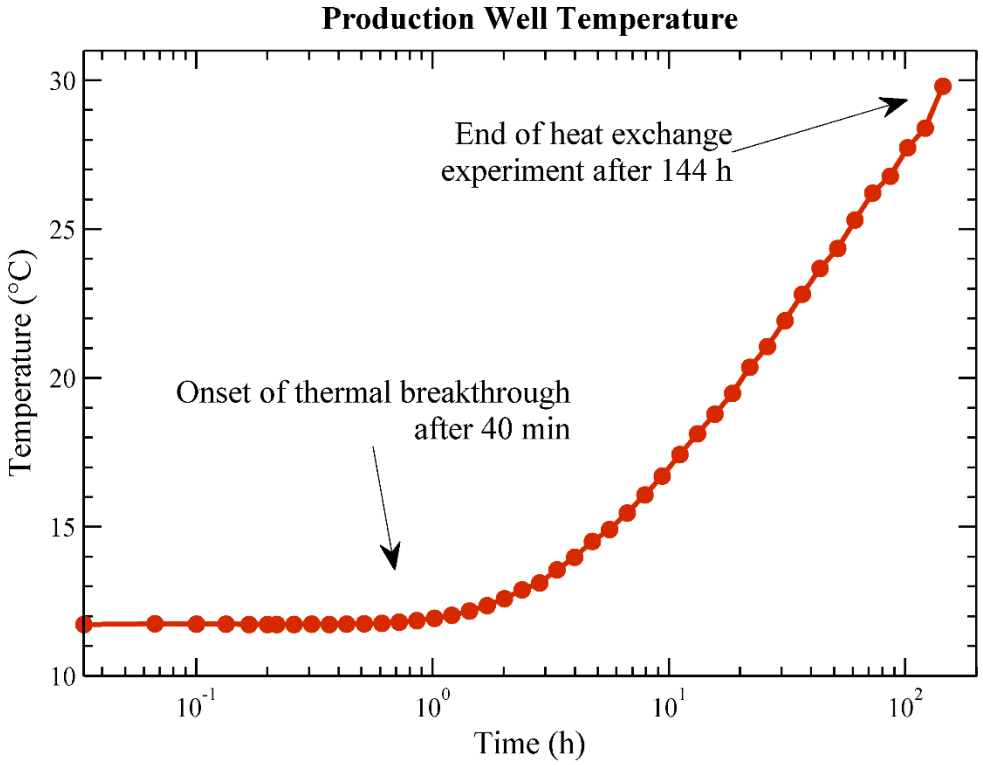

Figure 5.7. Measured production well temperature as a logarithmic function of time.

The three FO-DTS observations wells that experienced the greatest temperature rise are located in the direct path between the injection and production well as shown in Figure 5.6. The fracture fluid temperature at these

three locations and at four different times are shown in Figure 5.8. In addition, Figure 5.8 shows fluid temperature measured at the depth of the fracture in monitoring well 404 as well as the temperature going into the injection well (well 204) and just before entering the pump in the production well (well 304). Monitoring well 404 lies half-way between the injection and production well (Figure 5.6)

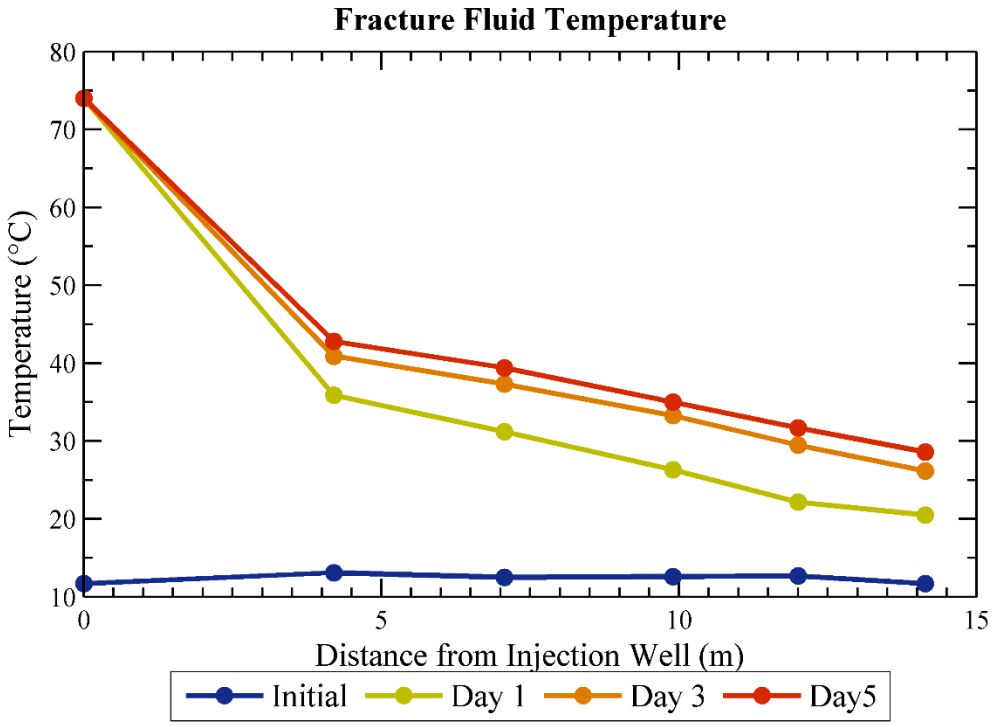

Figure 5.8. Temperature profile in-between the injection (distance = 0 m) and production well (distance = 14.1 m), spaced 14.1 m apart. The temperature measurements at 7.1 and 14.1 are measured fluid temperature in monitoring well 404 and production well 304.

5.4.2 Analytical Model

Measured temperature data shown in Figure 5.7 were used to solve for the heat transfer surface area in connection between the injection and production well. Two flow channels representing reservoir fractions of 0.22 and

0.21 were able to match simulated and measured temperature well (Figure 5.9). Inferred effective surface area of the two flow channels were 22 and 65 m^2, respectively. Results are summarized in Table 5.1.

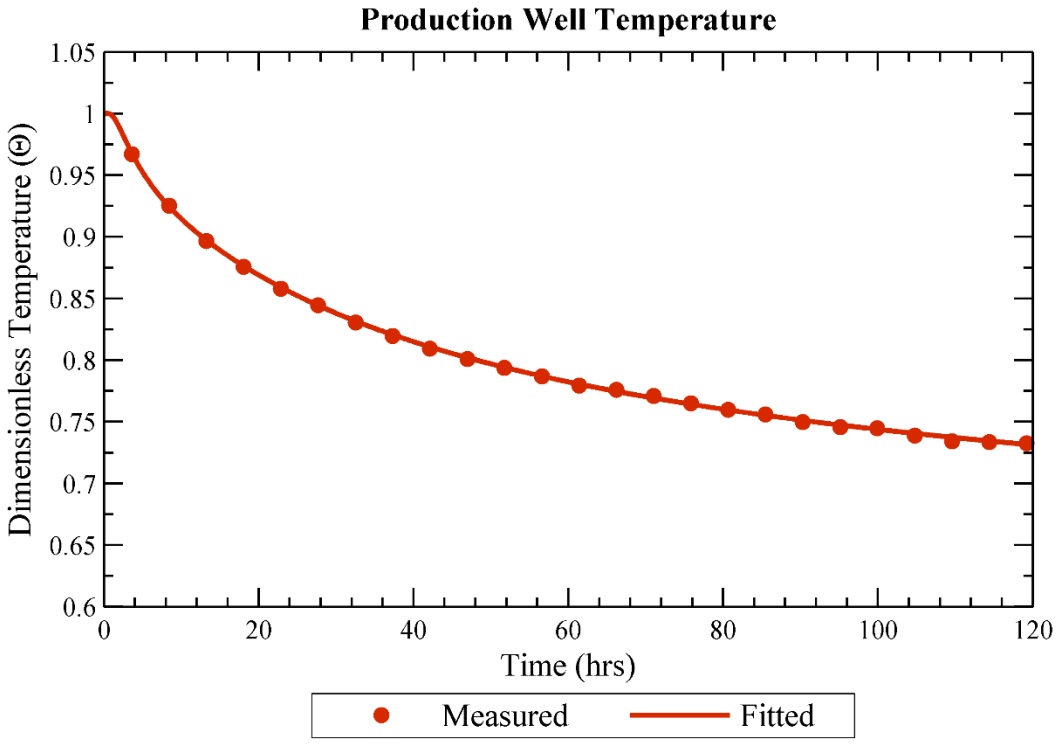

Figure 5.9. Comparison of the measured temperature data (in dimensionless units) and a model-fit to the measured data using two flow channels.

Table 5.1. Results of the best-fit reservoir geometry for the measured temperature data shown in Figure 5.7 and Figure 5.9.

	Surface Area (m^2)	*Volume fraction*
Channel 1	22	0.22
Channel 2	65	0.21

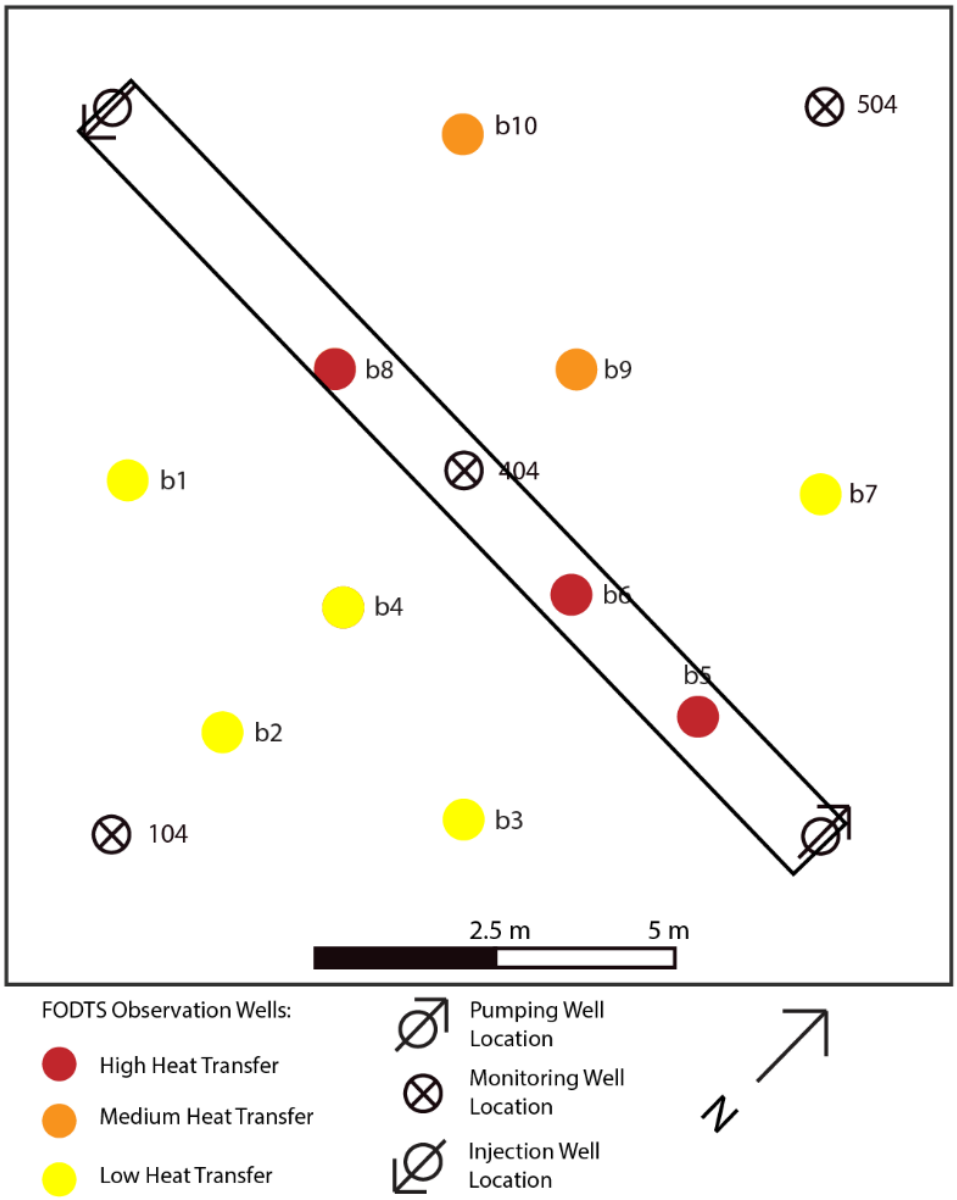

Figure 5.10. Comparison of the measured distribution of temperature rise and the surface area of "Channel 1" (0.8 m wide box outlined in black) determined for the best-fit reservoir geometry using measured temperature data. "Channel 2" is 65 m^2 which would produce a flow channel roughly 2.3 m wide, which is roughly consistent with the observation at b10 and b9 of "medium" heat transfer.

5.5 Conclusion

An analytical model for heat transport in multiple flow channels was used to estimate the fracture surface area available for heat exchange. Using

an inverse model to fit measured temperature, it was found that two flow channels with areas of 22 and 65 m^2 could produce nearly an exact match to measured production temperature data. The fraction of the total reservoir volume in connection between the two wells were found to be 0.22 and 0.21, respectively.

The spatial distribution of temperature increase recorded using FO-DTS probes provided experimental evidence that a narrow flow channel dominates fluid flow between the injection and production wells in the fractured region. The high thermal rise in the rock matrix above the direct path between the two wells suggests that flow was concentrated in a narrow path between injection and production wells (Figure 5.6). Compare, for instance, the temperature rise in boreholes b5 and b4. Borehole b4 is roughly 2 m away from the direct path between the injection and production well and experienced only 4.5 °C temperature rise. In contrast, borehole b5 is only 2.5 m away from the production well, but experienced a temperature rise of 20.0 °C.

A qualitative evaluation of GPR imaging of fluid flow through the fracture (Figure 3.12) generally agrees with the observed heat exchange results. Both datasets reveal a flow channel width smaller than ~3 m directly connecting the injection and production well. This is true, despite the fact that fluid circulation was reversed in the two experiments, suggesting that the hydraulic background gradient was not responsible for the rapid thermal breakthrough measured.

The experimental results from Altona indicate that flow channeling can dominate the spatial distribution of fluid flow paths, even in a single bedding plane fracture. While the Altona field site is assumed to be a reasonable meso-scale geothermal analog, it is unclear how the results at Altona will compare with large commercial geothermal reservoirs, which operate at much larger spatial and temporal scales, 100s to 1000s of meters and years rather than days. Nonetheless, the Altona experiments have provided a unique platform to test and validate tracer methods and to investigate how models can be used synergistically to provide new insights into predicting geothermal reservoir performance.

5.6 References

Robertson, E.C. (1988), Thermal Properties of Rocks, *United States Geological Survey (USGS)*, Reston, Virginia, 88-441.

Sensornet (2007), *ORYX DTS,* user manual.

Smolen, J., and S. van der Spek (2003), *A DTS Primer for Oil and Gas Production: SHELL Oil and Gas*, Shell International Exploration and Production, Hague, Netherlands.

CHAPTER 6: INERT TRACERS

6.1 Introduction

Tracer testing has been a common reservoir characterization method for several decades with more than 100 geothermal tests conducted worldwide over more than 50 years (Shook and Forsmann, 2005). As discussed in Shook and Forsmann, tracer tests have been used in a variety of reservoir applications, including constraining and validating numerical models, estimating heat transfer parameters, quantifying well connections, and defining inter-well volumes and flow geometries. In addition, predicting thermal breakthrough using reservoir parameters inferred or derived from tracer test data has long been a goal in the geothermal industry (Tester et al., 1979, 1986; Shook, 2001; Axelsson et al., 2005).

This chapter documents the capabilities of an inert tracer as an indicator of thermal performance using moment analysis, field tests, and a two-dimensional discrete fracture thermal-hydraulic model. First, moment analysis is performed to determine the critical parameters for heat transport. This analysis is performed on a one-dimensional analytical solution for thermal advection, dispersion, and conduction. The first and second moment are determined, which represent the mean and variance of the thermal breakthrough curve, respectively. These parameters are subsequently compared to the reservoir parameters that can be investigated using inert tracers.

The second modeling approach uses the results of inert tracer tests conducted at Altona to calibrate a thermal-hydraulic model in a two-dimensional discrete fracture. Two contrasting flow scenarios are considered which compare idealized and adverse flow fields. The first scenario investigates tracer and heat transport in a uniform aperture experiencing ideal dipole-flow. The second scenario introduces a narrow region of high permeability extending directly between the injection and production well, which concentrates flow and reduces the effective heat transfer area. These homogeneous and heterogeneous permeability fields are subsequently referred to as the "Ideal Dipole-Flow Scenario" (IDFS) and the "Channeled Flow Scenario" (CFS), respectively. While neither fracture scenario represents the true fracture aperture distribution, they do allow us to compare two end-member cases and identify which case is more realistic.

In both the IDFS and the CFS, reservoir hydrodynamic dispersivity was considered as a fitted parameter to be determined via an inverse model. For the IDFS, the second parameter determined via the inverse model was fracture aperture. In the CFS, unknown variables in addition to hydrodynamic dispersivity include: (1) flow channel fracture aperture; (2) flow channel width and (3) fracture aperture outside the flow channel region. A detailed description of the numerical model was previously described in sub-section 4.3.1.

6.2 Field Experiment, Tracers, and Setup

The recently developed "C-Dot" nanoparticle was used as the inert tracer. C-Dots are a relatively new class of carbon nanomaterials that were first

produced as a byproduct during purification of single-walled carbon nanotubes in 2004 (Xu et al., 2004). These nanoparticles are a desirable alternative to Quantum Dots (QDs) in disciplines with high concern for toxicity, such as medicine and environmental science, because carbon is much less toxic than cadmium, which is commonly found in QDs. The use of C-Dots will be described again in Chapter 8, where it was used as an inert reference tracer during thermally degrading tracer tests.

The C-Dot nanoparticle tracer used in these experiments consists of a carbon core decorated with a highly fluorescent polymer (Krysmann et al., 2012). The particles are synthesized in a one-step process from citric acid and ethanolamine. The 3-5 nm diameter particles are highly water soluble and inert (Li et al., 2014). They have a very low molecular diffusivity, and are detectable by their fluorescence to concentrations of ~1 ppb in deionized water. Several previous investigators have studies the transport of these C-Dots in porous media (e.g., Subramanian et al., 2013; Zhao, 2015; Li and Cathles, 2016; etc.).

Similar carbon-cored particles have been developed for medical applications where they have been demonstrated to have very low toxicity (Ray et al., 2009). This particular nanoparticle tracer was ideal for Altona and could be used in other geothermal reservoirs. Maximum temperatures need to be below 200 °C, because preliminary investigations suggest that the particle becomes unstable at higher temperatures.

Within 1 min of sample collection, C-Dots were analyzed using a Varian (Model #: G9800A) fluorescence spectrometer. The peak excitation and emission wavelengths for C-Dots in Altona groundwater were found to be 358 and 440 nm, respectively. The detection limit for C-Dots in Altona ground water was roughly 50 ppb. Groundwater samples were collected using a PVC ball valve to sample fluid at the ground surface in 30 mL Nalgene bottles. Samples were taken from the well-field to the spectrometer located roughly 30 m from the well-field.

Tracer experiments were conducted under forced convection conditions between an injection and production well. To introduce the tracer solution, a 2 L solution consisting 100 ppm C-Dots was placed in a bypass PVC pipe directly inline between the injection and production well prior to entering the tankless water heater (Figure 6.1). When the tracer was ready to be injected, two valves were opened to allow flow through the bypass pipe. The bypass pipe minimized disturbance to the subsurface hydraulic gradient field that may have resulted from other means of introducing tracer, such as gravity drainage of the tracer solution through a funnel into the top of the injection well.

Figure 6.1. Photograph of the injection port used to inject tracers without significantly disturbing the subsurface pressure field during fluid circulation at steady-state conditions. Arrows indicate flow path direction from the inlet to the outlet of the injection port.

6.3 Moment Analysis

The following moment analysis was used to demonstrate two things regarding limitations in one-dimensional flow channel models: (1) heat transport is insensitive to fracture aperture and (2) model analysis of an inert tracer do not provide sufficient information to forecast heat transport. Determination of both aspects was accomplished by comparing the first and second moment of an analytical solution for heat transport to reservoir parameters that govern inert tracer transport.

Heat transport through parallel fractures separated by low permeability matrix can be described by the one-dimensional advection-dispersion equation with coupled thermal conduction perpendicular to fluid flow (Figure 6.2). Tang (1981) presented a Laplace domain solution for solute transport in two fractures experiencing advection and dispersion within the fracture and can interact with each other through diffusive mass transport in the porous rock matrix. A modification of this equation for heat transport is

$$\overline{\Theta}(s) = \frac{1}{s}\exp\left[\frac{Pe}{2}\left(1-\sqrt{1+\frac{4\tau}{Pe}\left(s+\frac{(\rho C_p)_r}{(\rho C_p)_w}\frac{2\sqrt{sD_m}}{w}\tanh\left(\sqrt{\frac{s}{D_m}}\left(\frac{L-w}{2}\right)\right)\right)}\right)\right], \tag{6.1}$$

where $\overline{\Theta}$ is dimensionless temperature in Laplace space, Pe is the dispersional Peclet number for heat transport, τ is the mean fluid residence time of the fluid (or non-reactive tracer), s is the Laplace variable, w is the fracture aperture, ρ is density, C_p is heat capacity, D_m is the effective thermal diffusivity into the bulk rock matrix (fluid and solid), and L is the distance between fractures. The subscripts r and w refer to the bulk rock matrix and the fracture fluid, respectively. Dimensionless temperature is defined as

$$\Theta = \frac{T(t)-T_r}{T_{inj}-T_r} \tag{6.2}$$

where $T(t)$ is the mean fluid temperature across the fracture aperture at time, t, T_r is initial temperature of the rock, and T_{inj} is the temperature of injected fluid.

In most heat transport equation, dispersion in the plane of the fracture is neglected and no Peclet number is included. It is included here to describe the

dispersion-like mechanism of flow channeling. It should be considered purely an empirical exercise that lacks physical meaning. Nevertheless, including it provides a useful means to investigate flow channeling with a simple analytical model by characterizing flow channeling as a dispersive process (e.g., Gelhar et al., 1992; Zhao et al., 2010)

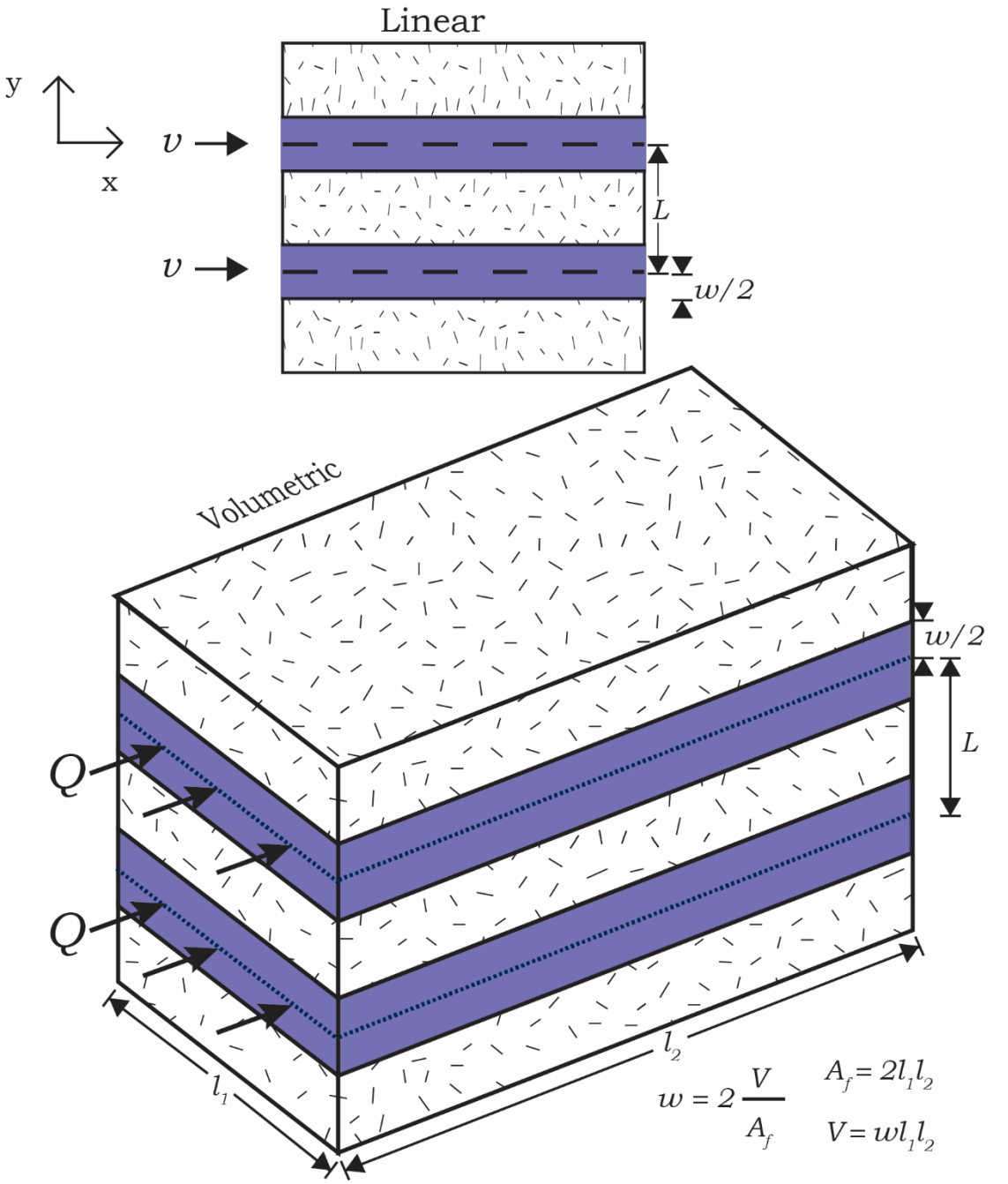

Figure 6.2. Schematic of the one-dimensional model used for heat transport in multiple parallel fractures. The analytical model includes the combined effects of advection, dispersion, and matrix diffusion.

Becker and Charbeneau (2000) demonstrated that the boundary conditions imposed by Tang (1981) are equivalent to those leading to a first passage time (FPT) problem, i.e. transport of heat is considered a transition

probability distribution rather than a local concentration of heat energy. FPT functions are amenable to moment analysis, which provides a convenient reduction of parameters. Moments are readily found using Laplace solutions of FPT such as Equation 6.1 (Becker and Charbeneau, 2000). The first moment, M_1, of Equation 6.1 is

$$M_1 = \frac{(\rho C_p)_r}{(\rho C_p)_w} \frac{L\tau}{w}. \tag{6.3}$$

Because $2/w$ is equivalent to the effective surface area to fluid volume ratio (A_f/V) (Reimus et al., 2003) we can rewrite Equation 6.3 as:

$$M_1 = \frac{(\rho C_p)_r}{(\rho C_p)_w} \frac{L\tau A_f}{V} \tag{6.4}$$

where A_f is the fracture surface area available for heat exchange and V is the reservoir fluid volume. Inter-well fluid volume can be estimated by the product of the volumetric flow rate, Q, and the mean or modal fluid residence time, τ, (Levenspiel, 1972). Therefore, Equation 6.4 can be reduced to:

$$M_1 = \frac{(\rho C_p)_r}{(\rho C_p)_w} L \cdot \frac{A_f}{Q}. \tag{6.5}$$

The second moment is equivalent to the variance of the function and represents the tail of the thermal breakthrough curve. For Equation 6.1, the second moment is:

$$M_2 = M_1 \frac{L^2}{6D_m} + M_1^2 \left(\frac{2+Pe}{Pe} \right). \tag{6.6}$$

Because the flowrate is known, Equation 6.5 confirms that the critical parameters for estimating the first moment of (mean) thermal transport time in one-dimension, M_1, is the mean distance between fractures (L) and the effective surface area of heat exchange, A_f. In addition to the volumetric flow rate, the critical parameters for estimating the second moment (variance) of thermal transport in one-dimension also include the bulk rock matrix diffusion coefficient, D_m, and the dispersional Peclet number for heat transport, Pe. However, since the first term in Equation 6.6 is typically much larger than the second term in rock, the first moment, M_1, fracture spacing, L, and thermal diffusion coefficient, D_m, dominate the second moment. Furthermore, if hydrodynamic dispersion can be represented by the combined influence of velocity gradients across a single fracture opening and diffusion across those gradients (i.e., Taylor dispersion, e.g. Horne, 1983), then hydrodynamic dispersion should be small and the Peclet number should be large (Pe>>1000).

Because the only transport parameter estimated from a conservative tracer experiment is τ, the mean residence time of water, Equation 6.5 demonstrates that one still must know the effective fracture porosity, ω/L, or the effective area of heat exchange, A_f, to anticipate mean thermal transport time, M_1. In addition, the variance of thermal transport time is dominated by the effective area of heat exchange and the bulk rock diffusion coefficient.

Given that the effective fracture porosity is impossible to estimate independently, the mean breakthrough time of a conservative tracer will only

provide a physically realistic estimate of thermal breakthrough if the mean residence time, and thus the mean reservoir volume, scales with the effective reservoir surface area. This scaling behavior has been seen in EGS reservoirs, where the modal tracer volume scaled with the effective heat transfer area based on an empirical model that used data from several experimental EGS reservoirs (Tester et al., 1986). This model is promising, suggesting that an inert tracer's modal time can be used in an empirical model to determine effective heat transfer area. Unfortunately, there remains a lack of sufficient field measurements to confirm this trend holds for other systems.

6.4 Results and Discussion

6.4.1 Tracer Testing

During the heat exchange experiment described in Chapter 5, a total of four inert tracer tests were conducted. The first was conducted 1 d prior to the beginning of the heat exchange experiment. The following three tracer tests were conducted while the reservoir was being heated; one after 1 d of hot water injection, a second after 3 d, and a third after 5 d. In each test, C-Dots were used as an inert tracer. The RTD of the C-Dot tracer experienced a reduced peak and reduced mass recovery as heating time increased (Figure 6.3).

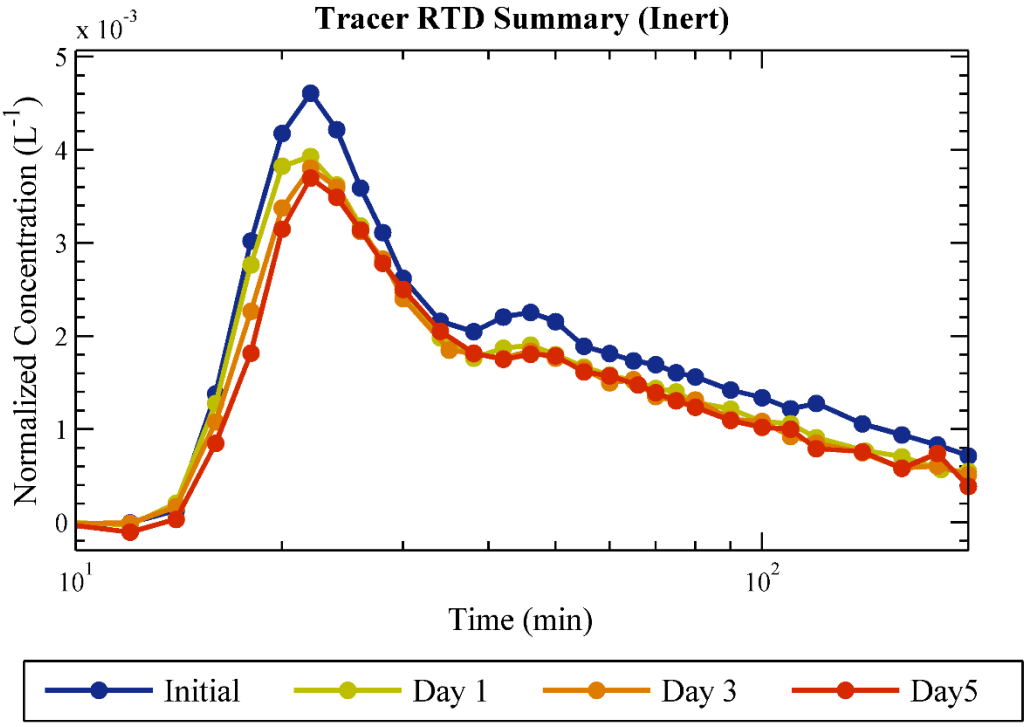

Figure 6.3. Tracer RTD for the inert C-Dot tracer at different times during heating. Concentration is normalized by dividing measured tracer concentration, c, by the mass of tracer injected, Minj.

At the end of the heat exchange experiment, a final tracer test was conducted to compare the tracer RTD curve of C-Dots with two additional inert

tracers, phenol and iodide (see

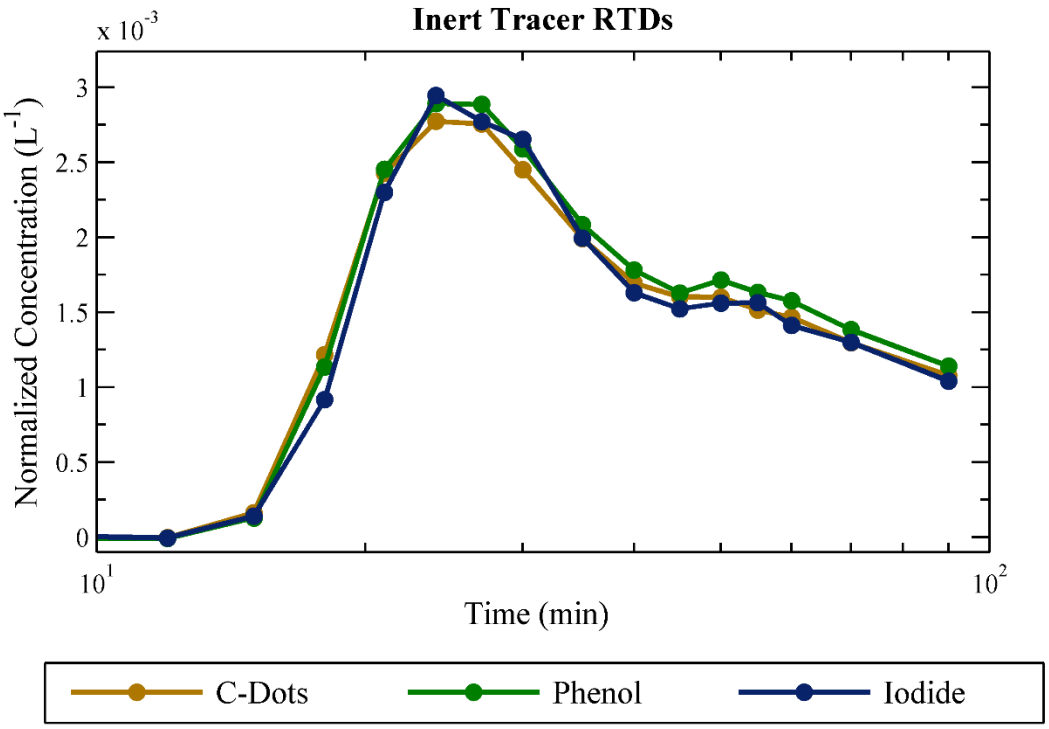

Figure 6.4). At the time of the tracer test, however, the straddle packer assembly in the injection well failed and, as a result, the tracer test was conducted without a straddle packer in the injection well. Figure 6.4 shows that initial tracer arrival for all three tracers at about 15 min. The modal residence time ranged from 24 to 27 min. This tracer test, which ran for 90 min, experienced tracer mass recoveries for C-Dots, phenol, and iodide of 73%, 76%, and 72%, respectively.

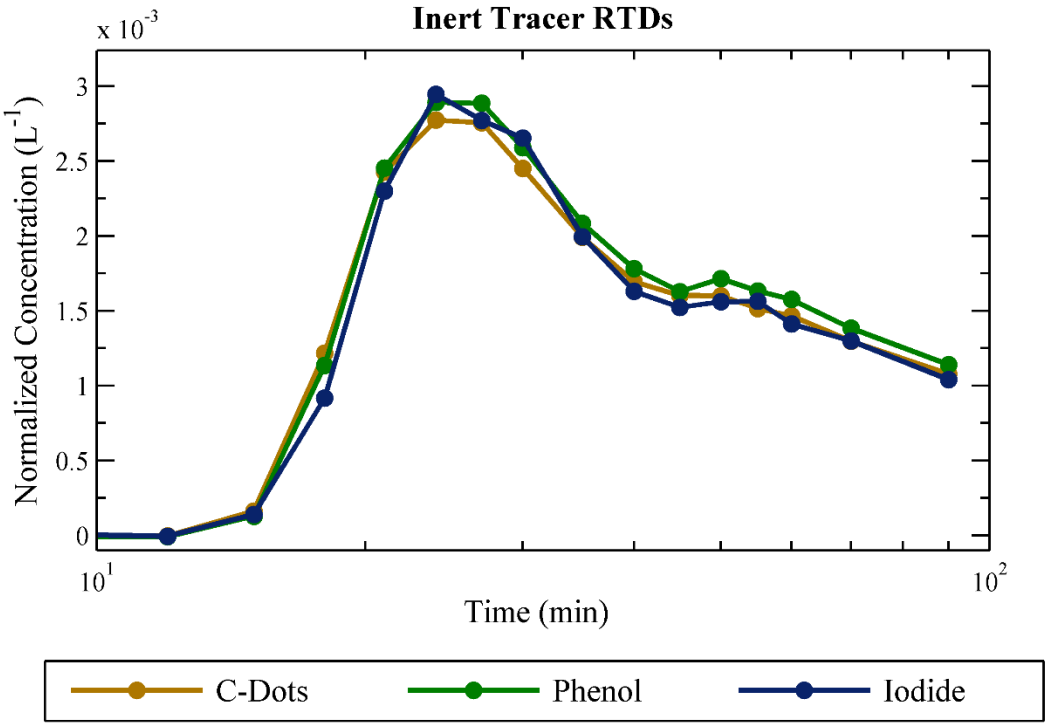

Figure 6.4. RTDs for three inert tracers, including the C-Dot nanoparticle, phenol, and iodide. Concentration is normalized by dividing measured tracer concentration, c, by the mass of tracer injected, M_{inj}.

6.4.2 Numerical Modeling in a Two-Dimensional Fracture

As seen in Figure 6.5, the Ideal Dipole-Flow Scenario (IDFS) and the Channeled-Flow Scenario (CFS) resulted in simulated inert tracer RTDs that agreed well with measured C-Dot tracer return data collected at the Altona site. The simulated tracer RTD was fit to experimental data using the Non-Linear Conjugate Gradient method (NLCG). For the IDFS, the fitted fracture aperture and hydrodynamic dispersivity resulting from the inverse model were 0.14 m and 0.53 mm, respectively.

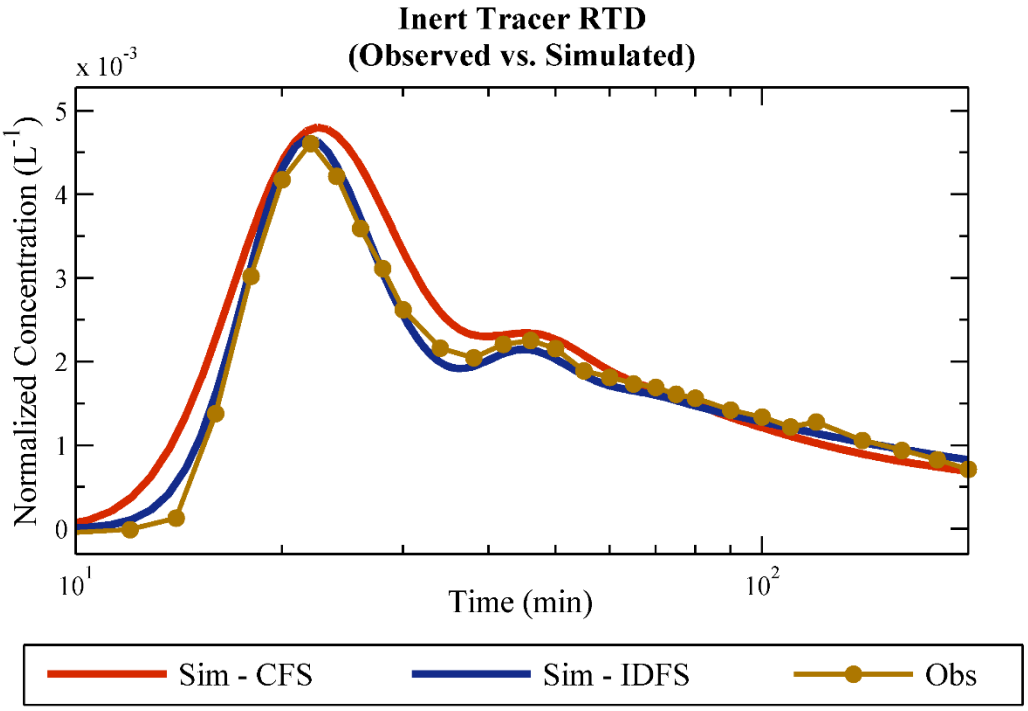

Figure 6.5. Comparison of the measured C-Dot tracer RTD prior to injecting hot water with the Ideal-Dipole Flow Scenario (IDFS) and the Channeled-Flow Scenario (CFS).

For the CFS, the width and fracture aperture of the flow channel were treated as unknown parameters in addition to the fracture aperture of the surrounding region and hydrodynamic dispersivity. The inverse model resulted in a flow channel fracture aperture and width of 5.7 mm and 0.9 m, respectively. Hydrodynamic dispersivity and the fracture aperture of the surrounding region of the model domain were found to be 0.4 m and 1.8 mm, respectively.

Fracture fluid temperature and production well thermal breakthrough were subsequently simulated for both the IDFS and the CFS using the values

from the inverse model. Figure 6.6 compares the observed and simulated results for both scenarios. The heat transport simulations were conducted under the assumption that hydrodynamic dispersivity is negligible for heat transport (as in Taylor dispersion). Negligible dispersion results, according to Taylor dispersion, from the large thermal diffusivity which negates the influence of mechanical dispersion that can result from velocity gradients in the width of the fracture aperture. Despite the good fit to the inert tracer RTD, the IDFS thermal breakthrough simulation dramatically over-predicted thermal performance, showing no temperature change after roughly 140 h.

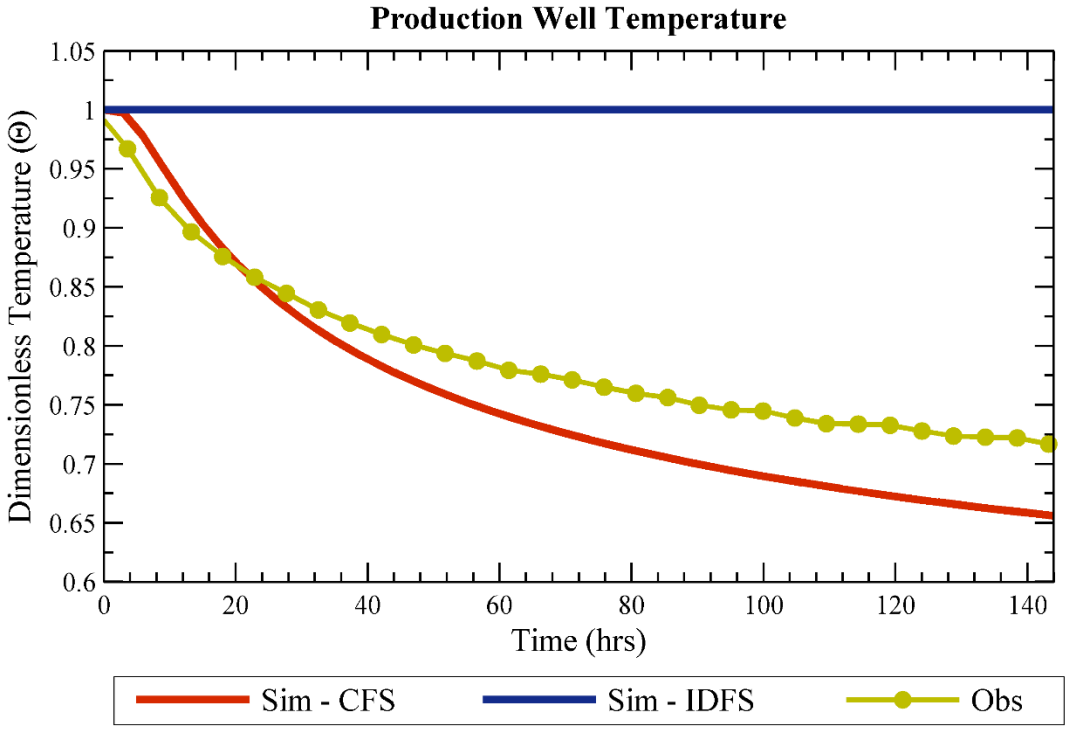

Figure 6.6. Comparison of predicted and measured thermal response at the production well for the Ideal-Dipole Flow Scenario (IDFS) and the Channeled-Flow Scenario (CFS).

For the CFS, predicted thermal breakthrough was relatively rapid with a temperature increase of nearly 4 °C within 8 h of initiating hot water injection. For comparison, measured temperature rise at the production well reached 4 °C within roughly 4 h. By the end of the 6 d heat exchange experiment, the CFS scenario predicts temperature rise of roughly 21 °C, which, compared to the IDFS, is in good agreement with the measured temperature rise of roughly 19 °C.

6.5 Summary

Moment analysis was used to evaluate flow and tracer response resulting from an analytical model for one-dimensional heat transport incorporating the combined effects of advection, dispersion, and matrix diffusion. The results of the moment analysis demonstrate that, strictly for heat transport, neither the first or second moment are influenced by the fracture aperture. This suggests that fracture aperture does not impact the mean of the thermal breakthrough curve (i.e., when drawdown reaches 50% of the temperature difference). Based on the second moment, the rate of temperature change at the production well is also independent of fracture aperture. Because inert tracers can only provide insights into the mean tracer residence time and the mean fracture aperture, an analysis of inert tracers using a one-dimensional model should not be used to determine parameters necessary for forecasting thermal breakthrough. There is potential, however, that the mean fracture aperture may empirically scale inversely with the effective surface area available for heat exchange. If this is true, this commonly used reservoir characterization approach may

provide useful forecasts of thermal breakthrough. As shown in Tester et al. (1986), this behavior has been seen in some experimental EGS sites. Unfortunately, the contrasting flow scenarios described in this chapter suggest that this scaling behavior is not reliable, at least at Altona where flow occurs in sandstone bedding planes.

The two contrasting flow scenarios (uniform vs. non-uniform aperture fields) were used to test the uniqueness of flow fields identified through interpreting inert tracer measurements. The Ideal-Dipole Flow Scenario (IDFS) with uniform aperture resulted in a fracture aperture of 0.53 mm, which is much smaller than the apertures in the Channeled Flow Scenario (CFS) (1.8 and 5.7 mm). These findings are consistent with the idea that large apertures cause low velocities in fractures of uniform aperture but can induce high velocities through a region of large aperture if the surrounding aperture field is relatively small. Furthermore, these results suggests that the concept of a "mean" aperture does not provide meaningful insights in the case where flow is channeled, because the mean aperture from the IDFS was much smaller than the two values found in the CFS.

In the CFS, hydrodynamic dispersivity was estimated to be 0.4 m, which is considerably larger than in the IDFS, where dispersivity was 0.14 m. The physical mechanism that is responsible for the resulting dispersion is ambiguous, because there are multiple dispersive or dispersive-like mechanisms that influence the tracer tests at Altona. If the dominant influence

is mechanical dispersion due to velocity gradients in the width of the fracture, then dispersivity at Altona should be at least 5 m based on the analytical model presented in Horne (1983) and a minimum well separation of 14 m.

If we assume Taylor dispersion dominates, however, constraining dispersivity to a reasonable range becomes complicated at short time-scales. Taylor dispersion describes the combined influence of mechanical dispersion and molecular diffusion, which lessens dispersion by causing diffusion across concentration gradients within the fracture. There are two major conflicts in quantifying Taylor dispersion at Altona. First, Taylor dispersion requires sufficient time to equalize the concentration gradient in the fracture. For apertures ranging from 0.53 to 5.7 mm and reasonable molecular diffusivities for tracers used at Altona, this length of time could be as small as 1.2 min or as large as 30 h based on the model presented in Horne (1983) and an aperture range of 0.53 to 5.7 mm. If this equilibrium time is longer than the tracer test, then mechanical dispersion would dominate over Taylor dispersion.

Second, Taylor dispersion is strongly influenced by the molecular diffusivity of the tracer. Given the range of molecular diffusion for the tracers used at Altona, dispersivity could be as low as 0.05 m or as high as 80 m. Therefore, there is insufficient knowledge of dispersive mechanisms to determine if a reasonable range of dispersion based on an analytical model.

Empirical evidence, however, suggests that the tracers experienced negligible dispersion as a result of mechanical dispersion or Taylor-Dispersion.

Field tests at Altona were conducted with two different inert tracers, iodide and C-Dots. Because the C-Dot tracer is roughly an order of magnitude less diffusive than the iodide tracer, Taylor-Dispersion would suggest that if significant dispersion exists, the C-Dot tracer would be much more dispersed. As shown in Figure 6.4, however, the two tracer return curves are nearly identical, suggesting that the tracers experienced negligible Taylor-Dispersion.

Mechanical dispersion, as described in Horne (1983), must also be negligible. The analytical model for dispersion suggests a minimum dispersivity of 5 m. This is much greater than 0.4 m, however, which is the maximum value determined in the two contrasting flow scenarios. In Chapter 9, the observation that there should have been negligible dispersion is further discussed in the context of identifying non-uniform fracture aperture fields by fitting inert tracers in the absence of hydrodynamic dispersion.

The best-fit fracture aperture for both the IDFS and the CFS were subsequently used in heat transport simulations to compare predicted thermal breakthrough from the two scenarios to measured thermal breakthrough at Altona. While both scenarios were capable of providing good fits to measured inert tracer RTD, only the CFS produced thermal breakthrough consistent with measured temperature. In fact, over the 6 d experiment the IDFS predicted no temperature rise whereas the CFS predicted a temperature rise of 21 °C and measured temperature rise was 19 °C.

In this chapter's treatment of hydrodynamic dispersion, however, it was considered an unknown parameter that was determined using an inverse model fitted to inert tracer return data. Therefore, the analysis presented here may differ if accurate analytical models for hydrodynamic dispersion are available. As previously discussed in this section, however, hydrodynamic dispersion of groundwater solutes in fractures remains largely an empirical exercise that collectively captures a range of dispersive (or dispersive-like) mechanisms which influence fluid flow in fracture reservoirs, such as mechanical dispersion, Taylor dispersion, well-bore dilution, solute storage in stagnant water zones, rough-walled fractures, matrix diffusion, adsorption, chemical or biologically-activated reactions in the fluid phase or at fluid-rock interfaces. Nonetheless, scaling analysis of specific mechanisms that lead to dispersive effects are at the very least qualitatively useful in identifying controlling factors that influence flow in reservoirs.

6.6 References

Axelsson, G., G. Björnsson, and F. Montalvo (2005), Quantitative Interpretation of Tracer Test Data, Proceedings, in *World Geothermal Congress*, Antalya, Turkey.

Becker, M. W., and R.J. Charbeneau (2000), First-passage-time transfer functions for groundwater tracer tests conducted in radially convergent flow, *Journal of Contaminant Hydrology*, 40, 299-310. doi: 10.1016/s0169-7722(99)00061-3.

Gelhar, L.W. (1992), A critical review of data on field-scale dispersion in aquifers, *Water Resources Research*, 28, 1955-1974.

Horne, R. N., and F. Rodriguez (1983), Dispersion in tracer flow in fractured geothermal systems, *Geophysical Research Letters*, 10, 289-292, doi: 10.1029/GL010i004p00289.

Krysmann, M. J., A. Kelarakis, P. Dallas, and E. P. Giannelis (2012), Formation mechanism of carbogenic nanoparticles with dual photoluminescence emission, *Journal of the American Chemical Society*, 134, 747-750, doi:10.1021/ja204661r.

Levenspiel, O. (1972), *Chemical Reaction Engineering*, New York, John Wiley & Sons.

Li, Y. V., L. M. Cathles, and L. A. Archer (2014), Nanoparticle tracers in calcium carbonate porous media, *Journal of Nanoparticle Research*, 16, doi:10.1007/s11051-014-2541-9.

Li, Y. V., and L. M. Cathles (2016), The surface interactions of a near-neutral carbon nanoparticle tracer with calcite, *Journal of Nanoparticle Research*, 18, doi: 10.1007/s11051-016-3383-4.

Ray, S. C., A. Saha, N. R. Jana, and R. Sarkar (2009), Fluorescent carbon nanoparticles: Synthesis, characterization, and bioimaging application, *Journal of Physical Chemistry*, 113, 18546-18551, doi:10.1021/jp905912n.

Reimus, P., G. Pohll, T. Mihevc, J. Chapman, M. Haga, B. Lyles, S. Kosinski, R. Niswonger, and P. Sanders (2003), Testing and parameterizing a conceptual model for solute transport in a fractured granite using multiple tracers in a forced-gradient test, *Water Resources Researc*h, 39, doi:10.1029/2002WR001597.

Shook, G.M. (2001), Predicting thermal breakthrough in heterogeneous media from tracer tests, *Geothermics*, 30, 573-589.

Shook, G.M., and J.H. Forsmann (2005), Tracer Interpretation using Temporal Moments on a Spreadsheet, *Technical Report*, Idaho National Laboratory, Idaho Falls, Idaho.

Subramanian, S. K., Y. Li, and L. M. Cathles (2013), Assessing preferential flow by simultaneously injecting nanoparticles and chemical tracers, *Water Resources Research*, 49, 29-42.

Tang, D. H., E. O. Frind, and A. Sudicky (1981), Contaminant transport in fractured porous media: Analytical solution for a single fracture, *Water Resources Research*, 17, 555-564.

Tester, J. W., R. M. Potter, R. L. Bivins (1979), Interwell tracer analyses of a hydraulically fractured granitic geothermal reservoir, Proceedings, in *54thAnnual Technical Conference Exhibition of the Society of Petroleum Engineers of AIME*, Las Vegas, Nevada.

Tester, J. W., B. Robinson, and J. H. Ferguson (1986), Inert and reacting tracers for reservoir sizing in fractured, hot dry rock systems, Proceedings, in *11th Workshop on Geothermal Reservoir Engineering*, Stanford University, Stanford, California.

Xu, X. Y., R. Ray, Y. L. Gu, H. J. Ploehn, L. Gearheart, K. Raker, and W. A. Scrivens (2004), Electrophoretic analysis and purification of fluorescent single-walled carbon nanotube fragments, Journal of the American Chemical Society, 126, 12736-12737.Zhao, Z., L. Jing, and I. Neretnieks (2010), Evaluation of hydrodynamic dispersion in fractured rocks, *Journal of Rock Mechanics and Geotechnical Engineering*, 2, 243-254.

Zhao, Y. (2015), The use of Nanoparticles to Assess Subsurface Flow Heterogeneity, *Ph.D Dissertation*, Cornell University.

CHAPTER 7: ADSORBING TRACERS

7.1 Introduction

As pointed out in Chapter 6, an additional class of tracers is desired in which the Flow-Wetted Area (FWA) of circulating fluids in contact with the fracture have the potential to advance this goal. Ionic cesium was used as an adsorbing, reactive tracer at the Altona field site to investigate if thermal breakthrough could be predicted, *a-priori*. Field experiments require measured tracer RTDs of both an inert and the adsorbing tracer. The FWA is estimated from an inverse model that utilizes the measured and simulated tracer RTDs in a one-dimensional model for advection, dispersion, and adsorption.

Reactive tracers that react in proportion to the FWA have been suggested for some time as a means to estimate fracture/matrix surface area (e.g. Bear, 1972; Becker et al., 2013; Dean et al., 2012, 2015; Fox and Horne, 1988; Lapidus and Amondson, 1952; Schaffer et al., 2017; Sullivan et al., 2003; Williams et al., 2010; Vetter and Crichlow, 1979). Unfortunately, adsorbing tracers have not yet emerged for practical tracer testing due to a lack of successful applications at the field scale and even at the laboratory scale. As discussed in detail in sub-section 2.3, the lack of success can be broadly grouped into three categories: (1) poorly constrained reaction parameters; (2) inappropriate models for adsorption; and (3) complex fracture fluid/matrix interactions.

The lack of success in earlier investigations using adsorbing tracers to estimate the FWA provided a strong motivation for our study. The coverage of this chapter focuses on comparing the FWA estimated from tracer measurements at the Altona site with the effective heat transfer surface area determined from analysis of the heat exchange experiment presented in Chapter 5. In addition, the FWA identified in the tracer analysis was used to obtain forecasted production well temperatures which are compared to measured temperature data.

7.2 Field Experiment Setup

Tracer testing at Altona in the summer of 2016 was performed under forced gradient, full-dipole flow conditions at a continuous flow rate of 5.8 L/min. Produced fluids from production well 304 were directly reinjected into injection well 204. Injection and production were conducted from a hydraulically isolated zone in the wellbores that were aligned with the 7.6 m deep test fracture. Hydraulic isolation in the injection and three observation wells was achieved using two modified inflatable pipe packers (Lansas Products, Lodi, California) in each well and the spacing in-between the two packers ranged from roughly 0.2 to 0.5 m (see Appendix E for photographs). In the production well, as single packer was inflated below the target fracture.

Cesium-iodide was used as a combined inert/adsorbing tracer. Cesium, a strongly adsorbing cation, was used as the adsorbing tracer in this study due to the short residence times and the small fracture surface areas anticipated. To introduce the tracer solution, a 3 L solution consisting of 217.8 mg iodide

and 153.4 mg cesium was placed in an isolated bypass chamber connected to the fluid injection plumbing. To inject the tracer solution, circulating fluids were redirected through the bypass chamber. This tracer injection approach allowed tracer to be introduced without effecting the steady-state subsurface pressure field. The same tracer injection technique was used in the inert and thermally degrading tracer tests discussed in Chapters 6 and 8.

Groundwater samples were collected in 15 mL polypropylene conical centrifuge tubes manufactured by Corning™ Falcon™. Samples were stored on ice until the time of analysis. Cesium and Iodide were analyzed via Inductively Coupled Plasma Mass Spectrometry (Element 2TM ICP-MS, Thermo Fisher Scientific Inc., MA, USA).

7.2.1 Analytical Transport Model

As discussed in detail in sub-section 4.2.2, heat transport in an idealized rectangular channel can be modeled assuming one-dimensional advection within the fracture and thermal conduction perpendicular to the fracture (Equation 4.6). In the case of multiple flow channels, Equation 4.7 can be used to determine production well temperature. The unknown values for multiple flow channels include the fraction of each flow channel, f_i, and the effective surface area available for heat exchange, A_f. These two parameters can be indirectly measured by solving an inverse model by minimizing the error between simulated and measured tracer data. Subsequent to solving the inverse problem, thermal breakthrough can predicted by incorporating the

effective surface area and flow channel fraction identified via the inverse model into Equation 4.7.

It is important to note, however, that the surface area available for adsorption is not identical to the effective surface area available for heat exchange. The effective heat transfer surface are can be thought of as the "superficial" area, which would neglect the added surface area available for adsorption, which is generated by a rough-walled fracture surface (Figure 7.1). To account for these differences, the superficial surface area of the tested rock fracture was measured and assumed to be equivalent to the effective heat transfer surface area.

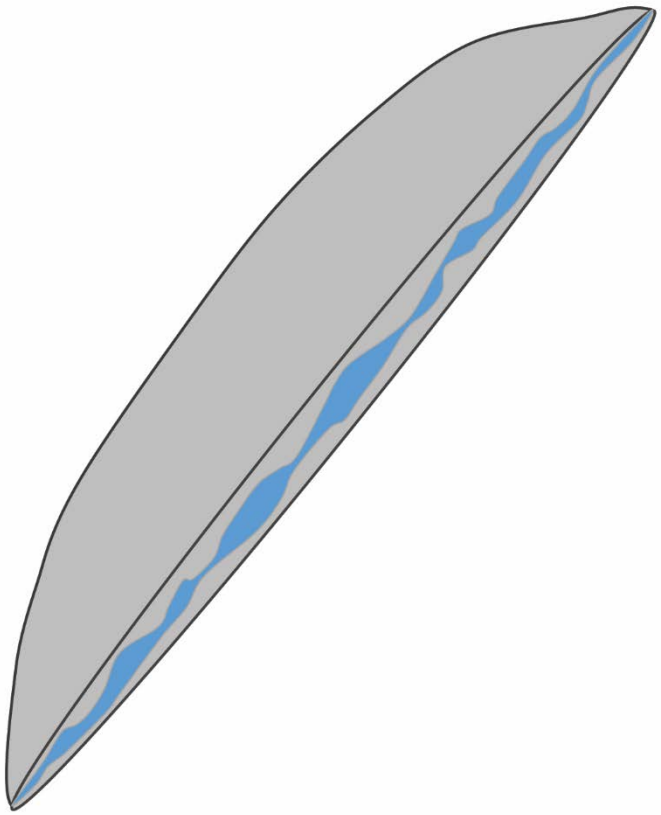

Figure 7.1. Schematic of a rough-walled fracture. The non-planar interface between the fracture surface and fracture fluids results in a reactive surface area that is larger than the effective heat transfer area, which is impacted little by small-scale surface heterogeneities.

For a single flow channel, the unknown parameters to be solved by the inverse model are the fluid volume of the fracture, surface area, and the dispersional Peclet number, which is a non-dimensional parameter describing the ratio of advection to dispersion. In the case of multiple channels, however, the fraction of the total fluid volume and area contributing flow is an additional unknown parameter to be solved by the inverse model. Using the Non-Linear Conjugate Gradient (NLCG) method, the flow channel volume, effective heat transfer surface area, and Peclet number were determined by minimizing the

Sum of Square Errors (SSE) between measured and simulated inert and adsorbing tracer RTDs.

In general, the number of flow channels used to fit an RTD from a given reservoir is somewhat arbitrary and "a-physical." Therefore a generalized approach is used in the analysis of Altona field data, even though Ground Penetrating Radar (GPR) data has indicated that there are roughly two or three channels present in the 10 x 10 m well-field. The generalized approach used was to start with a single flow channel. If the use of a single flow channel did not provide a sufficient fit, an additional flow channel was introduced and the fraction of each channel was included as a fitted parameter. Additional flow channels were added until the median relative error between measured and simulated tracer concentration was less than the maximum relative standard deviation reported in the ICP-MS analysis of iodide and cesium.

7.3 Results and Discussion

7.3.1 Laboratory Measurements

In order to interpret the experimental adsorbing tracer data using Equation 4.4 or 4.5, the rate constant and the partition coefficient must be known independently. These values were measured in a batch reaction consisting of 100 mL fluid and a rock fragment collected from 17.4 m below ground surface at the Altona well-field. The rock fragment had a nominal surface area of 26 cm^2 in contact with the fluid phase volume of 100 mL. This surface area measurement is likely much less than the reactive surface available for adsorption. However, the nominal area should be more

representative of the surface area available for heat exchange, since heat diffuses rapidly through small surface heterogeneities. Unfortunately, this approach may produce inaccurate values if the fracture surface conditions in the field are not comparable to the lab-tested sample. Ideally, numerous samples of the fracture surface would be used in batch experiments to evaluate variability both in terms of surface roughness as well as differences in the mineral composition.

During the batch experiment, the fluid/rock mixture was kept at room temperature and soaked in groundwater collected from the site for 7 d prior to the addition of cesium iodide. Following the approach described in Wingrave (2001), analysis of the data in Figure 7.2 result in a partition coefficient of 14.82 cm and a rate constant of 0.62 d^{-1}. The partition coefficient for adsorption relates the fluid concentration to the surface concentration assuming a linear relationship between the two. The rate constant was determined from the data during the first 22 h of the experiment and the partition coefficient was determined based on the mass adsorbed at the end of the experiment (9.2 d). Limiting the analysis to the first 22 h is the approach described in Wingrave (2001) in which he suggests that the initial data that follows a roughly linear form should be considered for measuring the rate constant.

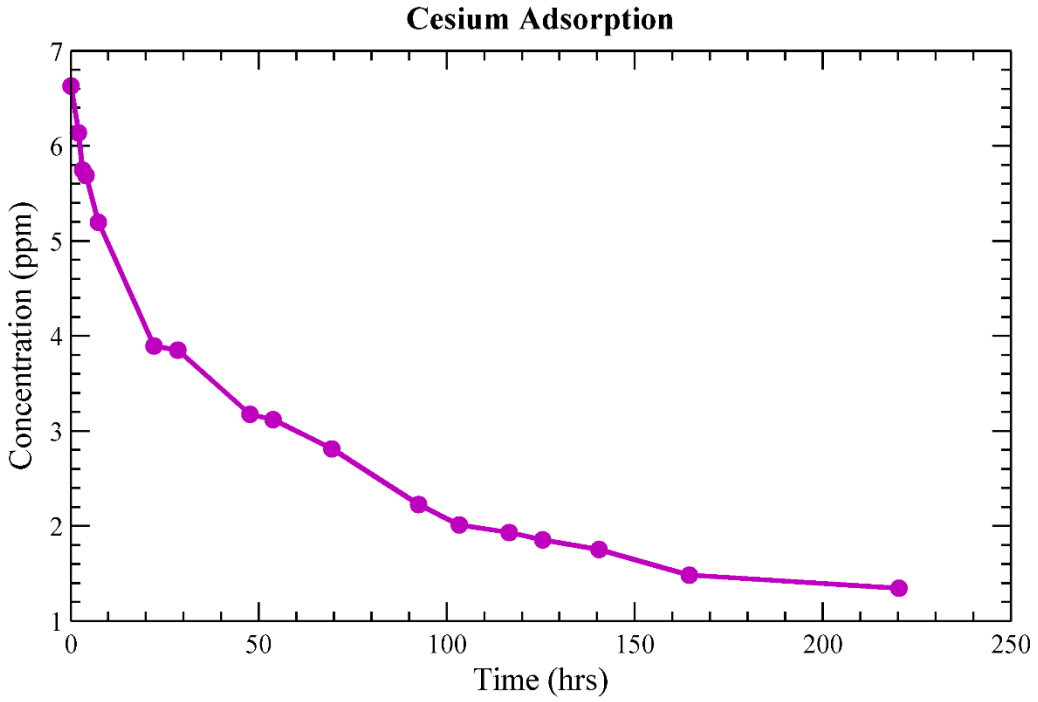

Figure 7.2. Lab-measured adsorption of cesium versus time. Cesium adsorption was measured onto a 26 cm^2 rock fragment collected from the Chasm Lake Well-Field at a depth of 17.4 m below ground surface.

7.3.2 Tracer Testing at Altona

Results of the tracer test are shown in Figure 7.3 where breakthrough curves are plotted as a function of time and concentration is normalized by the mass of tracer injected, c/M_{inj}, where c is the measured effluent concentration and M_{inj} is the tracer mass injected. Tracer test conditions are summarized in Table 7.1. Well 204 and Well 304, shown in Figure 3.8, were the injection and production well, respectively. The average extraction/injection rate was 5.8 L/min and the well separation was 14 m. Because recovered fluid containing tracer was reinjected, deconvolution of the reinjected tracer was performed following the method described in Shook and Forsmann (2005) to determine the mass recovered and mean residence time, a. After deconvolution, the inert

tracer's mean residence time was found to be 38 min and the mass recovered for iodide and cesium are 64 and 24%, respectively.

Table 7.1. Tracer test conditions and results.

Volumetric Flow Rate, Q	5.8	L/min
Mass Injected (I), M_{inj}	217.8	mg
Mass Injected (Cs), M_{inj}	153.4	mg
Mean Residence Time, τ	38	mins
Mass Recovered (I) =	64%	
Mass Recovered (Cs) =	24%	

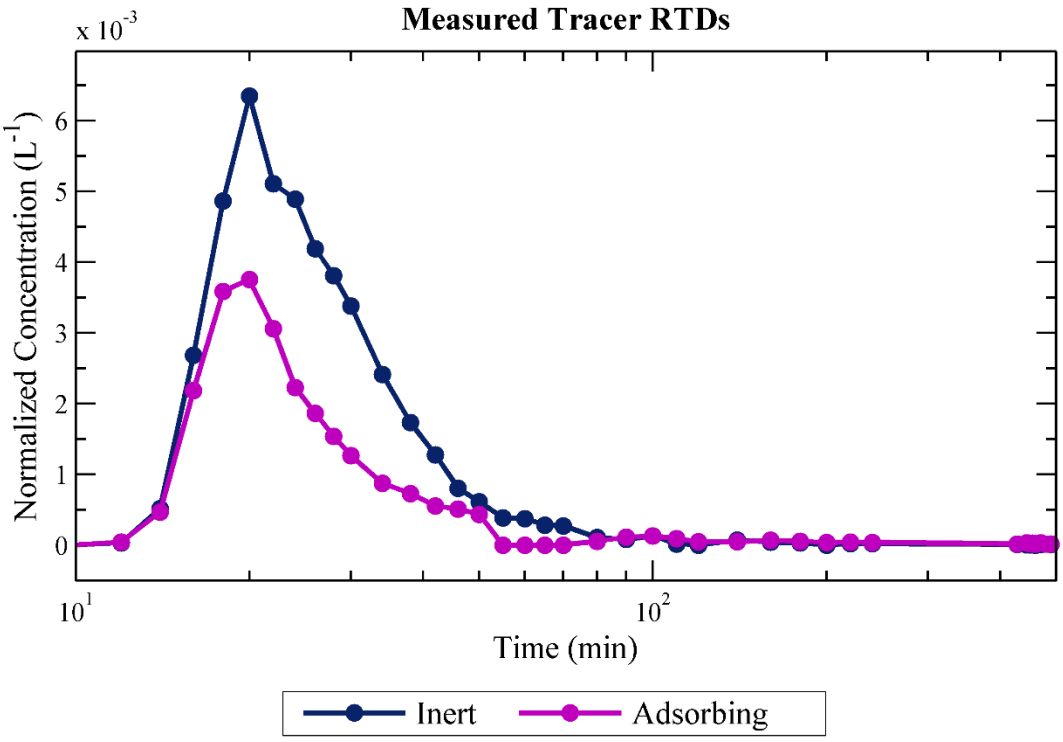

Figure 7.3. Measured tracer RTD for the inert tracer (iodide) and the adsorbing tracer (cesium). Concentration is normalized by dividing measured concentration, *c*, by the mass of tracer injected, M_{inj}.

7.3.3 Inverse Model

The inverse model was used to identify a minimum set of flow channels based on matching simulated and measured inert and adsorbing tracer RTDs

to a specified level of agreement dictated by the laboratory reported measurement error range. Unknown variables included the number of flow channels, flow channel volume, effective surface area, the dispersional Peclet number, and the fraction of the total reservoir represented by an individual flow channel. The measured tracer RTDs were matched by a simulation using five flow channels (Figure 7.4). The volume, FWA, Peclet number, and reservoir fraction for the five channels are given in Table 7.2.

Table 7.2. Results of the inverse model for each of the five flow channels identified by the best-fit between measured and simulated tracer RTDs.

Flow Channel ID	*A*	*B*	*C*	*D*	*E*	
Mean Residence Time, τ	19.4	26.8	35.4	43.2	63.5	min
Volume, V	113	155	206	250	368	L
Reservoir Fraction, f_i	0.16	0.3	0.08	0.05	0.06	(-)
FWA, A_f	28	85	94	28	194	m2
Peclet Number, Pe	103	44	80	121	53	(-)

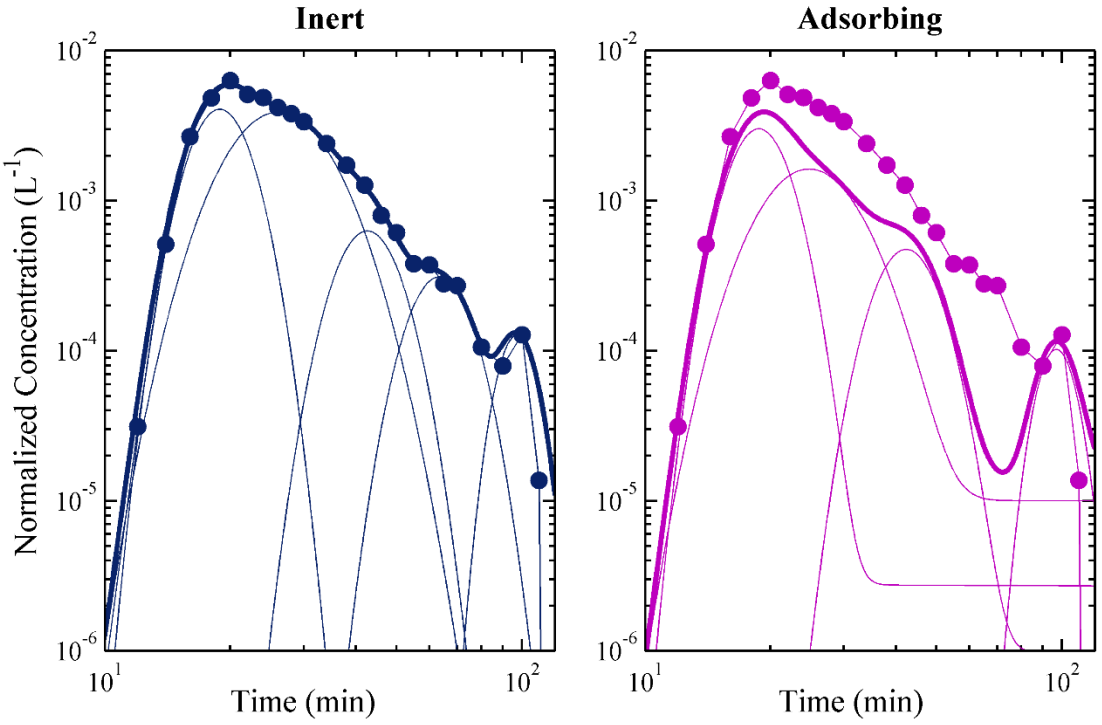

Figure 7.4. Comparison of measured (dots) and best-fit simulation (line) for the inert iodide tracer (left) and the adsorbing cesium tracer (right). The thin lines represent the contribution of tracer from each of the five flow channels used to match tracer RTDs.

The five flow channels identified via the inverse model were subsequently used in the heat transport model to forecast thermal breakthrough at the production well. Forecasted thermal breakthrough occurred within 52 min of circulating hot water (Figure 7.5). By the end of the experiment (6 d), predicted production well temperature reaches 31 °C.

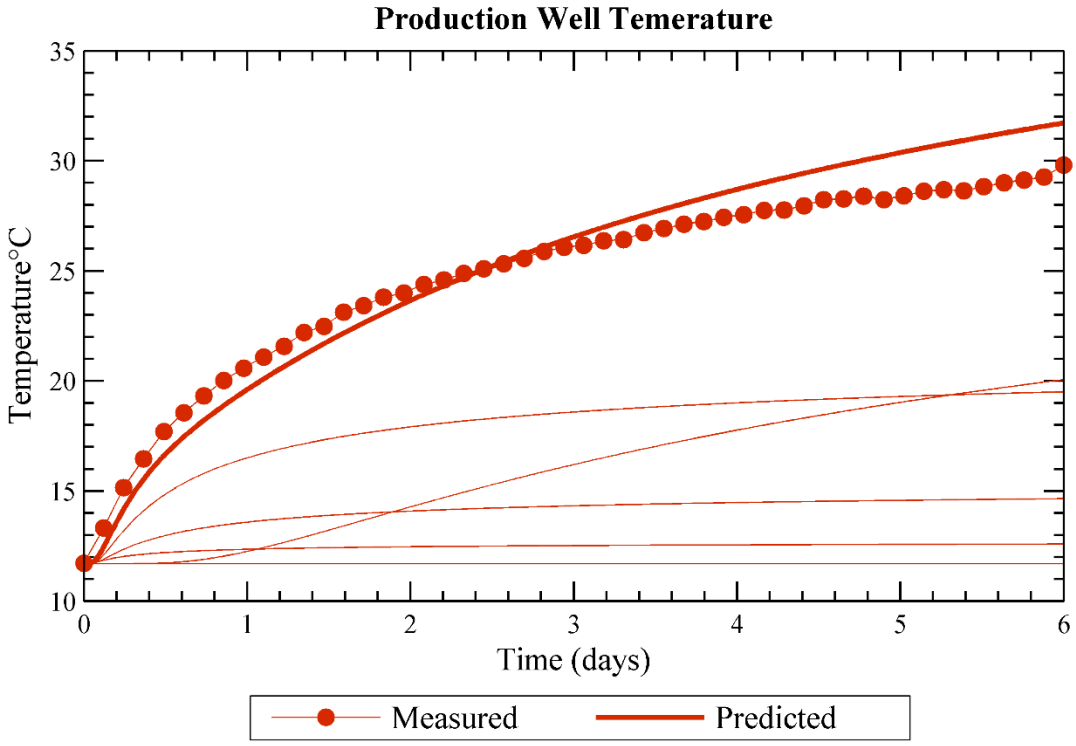

Figure 7.5. Comparison of the measured thermal response (red dots) and predicted (red line) resulting from the best-fit model calibrated with inert and adsorbing tracer data. The thin red lines represent temperature rise for each of the five flow channels.

Measured thermal breakthrough occurred after 44 min of hot water injection. Temperature rose rapidly during the first day of heating then rose at a less rapid rate, remaining relatively low for the duration of the 6 d experiment. For comparison, measured temperature at the production well was 30 °C. The forecasted temperature rise is very good relative to temperature forecasts of temperature rise using a constant aperture as shown in Figure 6.6.

7.4 Summary

The surface area available for heat exchange at the Altona field site was successfully estimated by analyzing adsorbing and inert tracer measurements. The measurements demonstrated that a narrow flow channel (~1 m) extended

14 m, directly between the two wells at Altona. To identify the flow channels' properties, an inverse model utilizing the Non-Linear Conjugate Gradient (NLCG) method was performed based on minimizing the sum of square errors between simulated and measured tracer RTDs for both inert and adsorbing tracers.

Estimated surface area measurements were validated based on a comparison of measured and predicted heat transfer efficiency between heated injectate and the cold, ambient formation at a depth of 7.6 m. After 6 d of continuous heating, the predicted production well temperature rise was 18 °C compared to a measured temperature rise of 17 °C. This shows that the FWA determination made via adsorbing and inert tracer testing were sufficiently accurate for predicting thermal performance, which is strongly influenced by the FWA.

The dominance of the narrow flow channel (~1 m) identified via adsorbing tracers agrees well with Ground Penetrating Radar (GPR) imaging of saline tracer flow paths. Despite the opposing direction of fluid flow in the two experiments, both data sets show that a roughly 1 to 2 m wide flow channel was responsible for the rapid thermal breakthrough measured at Altona. In addition, Fiber-Optic Distributed Temperature Sensing (FO-DTS) was used to measure the spatial distribution of heat exchange between flowing fluids and the bulk rock matrix. The FO-DTS data are consistent with GPR data and the inverse model output revealing that a significant portion of fluids circulating

through the target fracture was constrained to the direct path between the injection and production well. In comparison to estimated effective heat transfer discussed in sub-section 5.4.2, the surface area estimate based on interpreting the adsorbing tracer data (28 to 200 m^2) agrees well, particularly for the primary flow channel that dominates tracer and heat transport at Altona, which was found to be 22 m^2 for the primary flow path in Chapter 5.

The results of this study suggest that adsorbing tracers can be used to quantify the surface area of fluids circulating within fractured rock. The viability of this method was quantitatively demonstrated at the Altona field site, where flow channeling lead to rapid thermal breakthrough. To the best of the authors' knowledge, this is the first field application of adsorbing tracers in which an effective surface area was accurately estimated from adsorbing tracers.

While these results are encouraging, commercial geothermal and oil and gas operations, operate on much larger spatial and temporal scales. In addition, for the case of closely spaced fractures adsorbing tracers may not be suitable for predicting diffusive heat or mass transfer if the fractures are sufficiently close that characteristic thermal conduction or mass diffusion distances are on the same scale as the fracture spacing. Additional complications may arise when heterogeneous chemical and mineral alteration reactions exist and, as a result, the adsorption reaction may be too difficult to characterize independently. Subsequent research articles from our group will

report on further investigation of the influence of temperature, pH, and lithology on the rate and partition coefficient of adsorption. In addition, future field experiments at Altona and several other field sites will use reactive tracers at larger spatial and temporal scales.

7.5 References

Bear, J. (1972), *Dynamics of Fluids in Porous Media*, Elsevier, New York City, New York.

Becker, M. W., K. Remmen, P. Reimus, and G. Tsoflias (2013), Investigating well connectivity using ionic tracers, proceedings in *38th Workshop on Geothermal Reservoir Engineering*, Stanford University, Stanford, California.

Dean, C., P. Reimus, and D. Newell (2012), Evaluation of a cation exchanging tracer to interrogate fracture surface area in EGS Systems, Proceedings, in *37th Workshop on Geothermal Reservoir Engineering*, Stanford University, Stanford, California.

Fox, C.E., and R. N. Horne (1988), Determination of fracture aperture: A multi-tracer approach, *Transactions of the Geothermal Resources Council*, 12, 449-456.

Lapidus, L., and N. R. Amundson (1952), Mathematics of adsorption in beds. VI. The effect of longitudinal diffusion in ion exchange and chromatographic columns. *Journal of Physical Chemistry*, 56, 984-988.

Schaffer, M., W. Warner, S. Kutzner, H. Börnick, E. Worch, and T. Licha (2017), Organic molecules as sorbing tracers for the assessment of surface areas in consolidated aquifer systems, *Journal of Hydrology*, 546, 370-379.

Shook, G.M., and J.H. Forsmann (2005), Tracer Interpretation using Temporal Moments on a Spreadsheet, *Technical Report*, Idaho National Laboratory, Idaho Falls, Idaho.

Sullivan, E. J., P. W. Reimus, and D. A. Counce (2003), Transport of a reactive tracer in saturated alluvium described using a three-component cation-exchanging model, *Journal of Contaminant Hydrology*, 62-63, 675-694.

Vetter, O.J., and H.B. Crichlow (1979), Injection, injectivity and injectability in geothermal operations: Problems and possible solutions (Phase I – Definition of the Problems, *Technical Report*, U.S. Department of Energy – Geothermal Energy, SAN-2044-1.

Williams, M. D., V. R. Vermeul, P. W. Reimus, D. Newell, and T. Watson (2010), Development of models to simulate tracer behavior in Enhanced Geothermal Systems, Richland, Washington: *Pacific Northwest National Laboratory*.

Wingrave, J.A. (2001), *Oxide Surfaces,* Marcel Dekker, Inc., New York.

CHAPTER 8: THERMALLY DEGRADING TRACERS

8.1 Introduction

Tracers that can actively predict the position of a cold thermal front as it migrates from geothermal injection to production wells have long been desired. Thermally degrading chemical tracers, which are sensitive to subsurface changes in temperature distribution, were proposed nearly 30 years ago as a viable means to monitor transient subsurface temperature (Robinson et al., 1988). Thermally degrading tracers are selected based on temperature-dependent reaction properties over the range of in-situ reservoir temperatures anticipated between wells. The Residence Time Distribution (RTD), as expressed by the tracer breakthrough curves of both inert and reactive tracers in the reservoir, is used to estimate the extent of production well temperature decline (i.e., thermal drawdown). The difference in the measured RTD of the inert and thermally degrading tracer decreases as the reservoir cools. In principal, repeated tracer tests using thermally degrading tracers can estimate the progression of the cold thermal front as it approaches a production well prior to observing thermal breakthrough. This knowledge would permit optimization of production rates and well infilling, improving reservoir production and economics.

While thermally degrading tracers have long been considered a viable means to characterize subsurface reservoir temperature distributions, they have been rarely used in actual field experiments. Batchelor (1986) showed

that a thermally degrading tracer will show lower mass recovery relative to an inert tracer. Adams and Davis (1991) used two thermally degrading tracers with differing reaction rates and found good agreement between measured and estimated reservoir temperatures. Du Teaux and Callahan (1996), found conflicting results when a thermally degrading tracer test showed reduced mass recovery after 3 months of heat extraction. See sub-section 2.4 for further discussion of thermally degrading tracer experiments.

This chapter demonstrates that the use of a thermally degrading tracer can be used in field experiments to track the progression of a thermal front. It also identifies the spatial distribution of flow paths between an injector and producer via a network of temperature sensors and Ground Penetrating Radar (GPR).

8.2 Methods

As the relatively cold reservoir was heated, four tracer experiments were conducted over 6 d using an inert and thermally degrading tracer. Experiments were conducted under forced dipole conditions between an injection well (well 204) and production well (well 304) separated by 14 m. The inert tracer used was a carbon-cored nanoparticle referred to as “C-Dots” as the inert tracer and the thermally degrading tracer was phenyl acetate, which is a carboxylic ester that undergoes a rapid hydrolysis reaction.

8.2.1 Tracer Materials

The recently developed “C-Dot” nanoparticle was used as the inert tracer in combination with the thermally degrading tracer, phenyl acetate. As

discussed previously in sub-section 6.2, C-Dots are a relatively new class of carbon nanomaterials that were first produced as a byproduct during purification of single-walled carbon nanotubes in 2004 (Xu et al., 2004). These nanoparticles are a desirable alternative to Quantum Dots (QDs) in disciplines with high concern for toxicity, such as medicine and environmental science, because carbon is much less toxic than cadmium, which is commonly found in QDs.

The C-Dot nanoparticle tracer used in these experiments consists of a carbon core decorated with a highly fluorescent polymer (Krysmann et al., 2012). The particles are synthesized in a one-step process from citric acid and ethanolamine. The 3-5 nm diameter particles are highly water soluble and inert (Li et al., 2014). They have a very low molecular diffusivity, and are detectable by their fluorescence to concentrations of ~1 ppb in deionized water. Several previous investigators have studies the transport of these C-Dots in porous media (e.g., Subramanian et al., 2013; Zhao, 2015; Li and Cathles, 2016; etc.).

Similar carbon-cored particles have been developed for medical applications where they have been demonstrated to have very low toxicity (Ray et al., 2009). This particular nanoparticle tracer was ideal for Altona and could be used in other geothermal reservoirs. Maximum temperatures need to be below 200 °C, because preliminary investigations suggest that the particle becomes unstable at higher temperatures.

Phenyl acetate undergoes a rapid temperature-dependent hydrolysis reaction producing phenol and acetate and is dependent on fluid pH and temperature (Figure 8.1). A detailed description of the use of phenyl acetate as a reactive geothermal tracer is described in Nottebohm et al. (2012) and laboratory experimental evaluation is described in Maier et al. (2015).

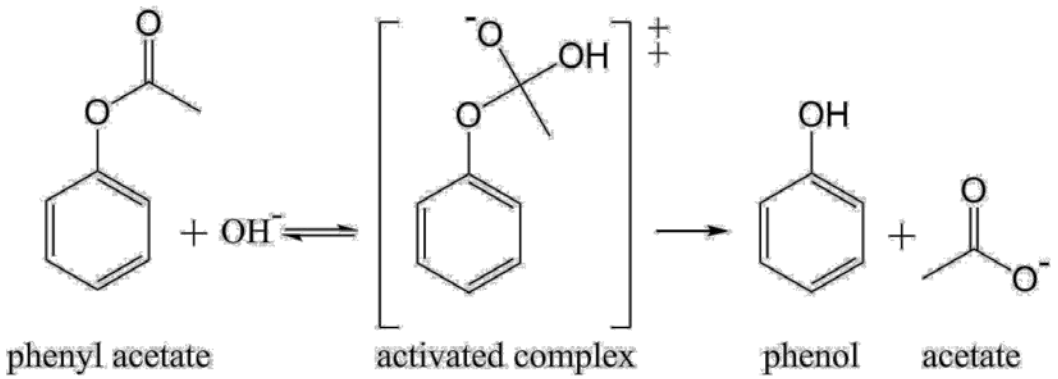

Figure 8.1. Base-catalyzed reaction of phenyl acetate to produce phenol and acetate.

8.2.2 Experimental Procedure

To introduce the tracer solution, a 2 L solution consisting of 250 ppm phenyl acetate and 100 ppm C-Dots was placed in a bypass PVC pipe directly inline between the injection and production well prior to entering the tankless water heater. When the tracer was ready to be injected, two valves were opened to allow flow through the bypass pipe. The bypass pipe minimized disturbance to the subsurface hydraulic gradient field that may have resulted from other means of introducing tracer, such as gravity drainage of the tracer solution through a funnel into the top of the injection well.

Within 1 min of sample collection, both C-Dots and phenol were analyzed using a Varian (Model #: G9800A) fluorescence spectrometer. The peak excitation/emission wavelengths for C-Dots and phenol in Altona groundwater was found to be 358/440 nm and 267/297 nm, respectively. The detection limit for C-Dots and phenol in Altona ground water were found to be roughly 50 ppb. Groundwater samples were collected using a PVC ball valve to sample fluid at the ground surface in 30 mL Nalgene bottles. Samples were taken from the well-field to the spectrometer located roughly 30 m from the well-field.

Because of the high reaction rates associated with phenyl acetate hydrolysis at temperatures encountered in the heat exchange experiment (roughly 10 to 75 °C), each groundwater sample was analyzed within 1 min of collection to prevent significant reaction after collection. Fluorescence of the phenol product was determined to be the most effective detection method, because samples can be rapidly analyzed without the need for sample preparation. The use of a Gas Chromatograph with a Flame Ionization Detector (GC-FID) after separation via Solid Phase MicroExtraction (SPME) could be used to detect both phenyl acetate and phenol. However, sample analysis via GC-FID was found to require, at minimum, 30 mins per sample in our laboratory trials and may take longer depending on the GC method and desired detection limit. Due to the short duration of the tracer experiments (< 3 hrs), the high reaction rates, and the complexities involved in deploying GC-FID in the field, GC-FID was not considered a practical analytical method for these

field experiments. As a result, only the concentration of the reaction product, phenol, was determined.

Due to the rapid reaction rate, the extent of phenyl acetate reacted prior to entering the formation must be considered. For each tracer test, phenyl acetate was dissolved in 2 L of groundwater collected from the site for 3 min. Two minutes later, the tracer solution consisting of C-Dots and phenyl acetate was released into the injection line. Using Arrhenius parameters found in Nottebohm (2012), less than 0.1% of the tracer is expected to have reacted prior to tracer injection. After being heated by the tankless water heater, the tracer experienced a residence time of roughly 2 min before entering the formation. At 74 °C, it is expected that roughly 1% of the tracer reacted prior to entering the formation.

8.2.3 Effective Reservoir Temperature

According to Nottebohm et al. (2012), this reaction follows a (pseudo-) first order reaction with a reaction rate constant, k, dependent upon temperature as described by the Arrhenius law:

$$k = A \cdot exp\left(-E_a/(RT)\right) \tag{8.1}$$

where A is the pre-exponential factor, E_a is the activation energy, R is the universal gas constant, and T is the absolute temperature.

An effective reservoir temperature can be estimated by rearranging Equation 8.1. To do so, the first-order reaction rate constant, k, is replaced by an effective rate constant, k_{eff}, which reflects the relative mass recoveries of a

thermally degrading tracer and an inert tracer as a function of time, *t*. Assuming a first-order reaction, k_{eff} can be determined by the following equation:

$$k_{eff}(t) = -\ln\left(\frac{M_{rxn}(t)}{M_{inert}(t)}\right)\frac{1}{t} \tag{8.2}$$

where M_{rxn} is the reactive tracer mass recovered and M_{inert} is the inert tracer mass recovered. Rearranging Equation 8.1 and incorporating the effective rate constant, k_{eff}, the effective temperature, T_{eff}, is determined by

$$T_{eff}(t) = \frac{-E_a}{R}\ln\left[\frac{k_{eff}(t)}{A}\right]^{-1} \tag{8.3}$$

To apply this method, the temperature dependence of the reaction, described by the Arrhenius Equation, must be known independently. In addition, the transport properties of the inert and thermally degrading tracer must be consistent (e.g., matrix diffusion, hydrodynamic dispersion, and retardation). The method also assumes that a non-uniform temperature field can be represented by a single temperature. This is not strictly true, but it does permit a straight-forward quantitative measure of heat exchange between circulating fluids and the rock matrix. It is anticipated that average and effective temperatures will generally be similar. The reaction rate constant rises exponentially as function of temperature, however, so the estimated effective reservoir temperature will be slightly higher than the actual average reservoir temperature.

8.3 Results and Discussion

8.3.1 Tracer Testing

A total of four tracer tests were conducted in the fall of 2015. The first was conducted 1 d prior to heat injection and the following three were conducted while the reservoir was being heated; one after 1 d of hot water injection, a second after 3 d, and a third after 5 d. In each test, both C-Dots and phenyl acetate were used as tracers. The results of the same C-Dot tracer test was previously discussed in Chapter 6.

Phenol, which is the reaction product of the thermally degrading tracer phenyl acetate, showed increased mass recovery in each tracer test (Figure 8.2). After 44 min of tracer circulation during the initial tracer test, the mass percentage of phenol recovered was 10% compared to 50% mass recovery of inert C-Dot tracer. For each tracer test conducted after the onset of hot water injection, the recovered mass percentage of phenol after 44 min increased whereas the C-Dot mass recovery decreased (Table 8.1).

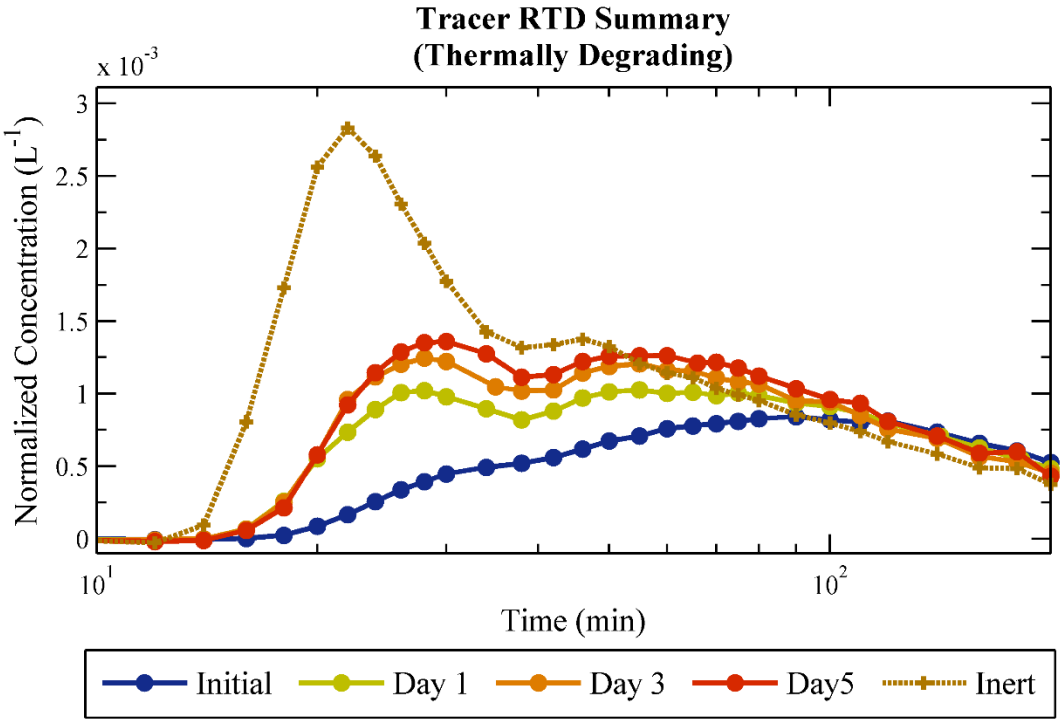

Figure 8.2. Measured tracer RTD for the inert tracer (C-Dots) and the reaction product (phenol) resulting from phenyl acetate hydrolysis. The inert curve represents the average of all four tracer tests conducted while each of the solid lines represent phenol RTD after a specified length of time in which the reservoir was heated. Concentration is normalized by dividing measured tracer concentration, c, by the product of the equivalent phenol mass injected, M_{inj}, and the fraction, X, of the inert C-Dot tracer recovered after 200 min.

Table 8.1. Measured recovery of C-Dots (inert tracer) and phenol (reaction product), and the ratio of phenol/C-Dots after 44 min.

Time (d)	*C-Dots*	*Phenol*	*Phenol/C-Dots*
Initial	50%	10%	20%
1	44%	19%	42%
3	42%	22%	52%
5	41%	23%	56%

In all four tracer experiments, the first arrival of phenol was delayed relative to C-Dots. Prior to heating the reservoir, the first arrival of C-Dots and

phenol was 14 and 20 min, respectively. For all tracer test after the initiation of subsurface heating, the first arrival of C-Dots and phenol was 14 and 16 min, respectively.

8.3.2 Reservoir Temperature Estimation

Because flow was concentrated in a narrow channel directly between the injection well and production well, the average temperature between the injection well and production well should be roughly equal to the average reservoir temperature of the dominant flow path. Average reservoir temperature was therefore determined based on the temperature measurements shown in Figure 5.8. Prior to hot water injection, the average reservoir fluid temperature was 12.5 °C. After 1 d of heating, the average temperature rose to 32.2 °C followed by 38.3 and 41.2 °C after 3 and 5 d, respectively.

In order to estimate the effective reservoir temperature based on Equations 8.2 and 8.3, the Arrhenius parameters and the ratio of recoveries between the thermally degrading tracer and inert tracer must be known. According to laboratory experiments reported in Nottebohm et al. (2012), the Arrhenius parameters, E_a and *ln(A),* for hydrolysis of phenyl acetate at a pH of 7.0 are 77.0 kJ/mol and 25.5 h^{-1}, respectively. The ratios of phenol mass recovered to C-Dots after 44 min for each of the tracer tests is shown in Table 8.1. Assuming the difference in mass recovery between phenol and C-Dots is solely due to thermal degradation, the ratio of the reaction reactant, phenyl acetate to C-Dots can be determined by subtracting the recovery ratios shown in Table 8.1 from 1. A comparison of the measured and effective reservoir

temperature is shown in Figure 8.3. The estimated effective reservoir temperatures are roughly 50 to 65 °C higher than the measured average reservoir temperature.

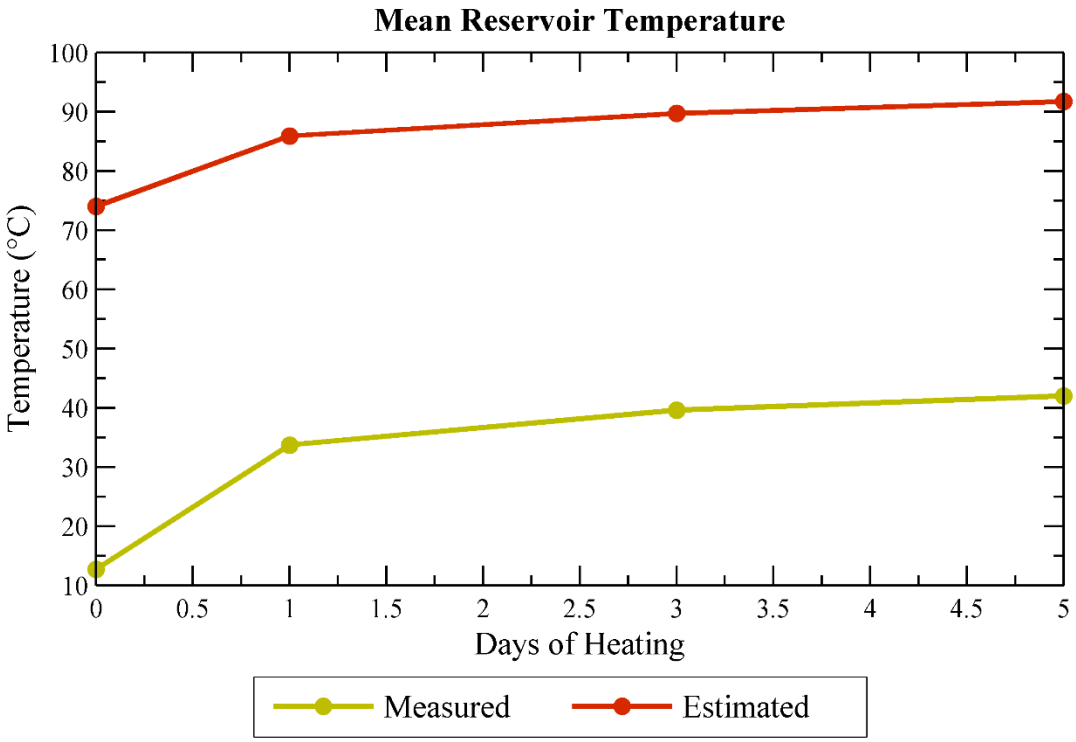

Figure 8.3 Comparison of the measured average reservoir temperature and the estimated effective reservoir temperature.

The Arrhenius parameters for the experimental data obtained in this study were determined based on the average reservoir temperature based on data shown Figure 5.8 and an effective reaction rate constant. The effective reaction rate constant was determined based on the mass recoveries at a residence time of 44 min as shown in Table 8.1. Figure 8.4 shows a linear relationship between inverse temperature and the effective reaction rate constant. Therefore, the thermally degrading tracer exhibits Arrhenius behavior

at the Altona field site. Based on this graph, the Arrhenius parameters, E_a and *ln(A)*, are 33.4 kJ/mol and 12.9 h^{-1}, respectively.

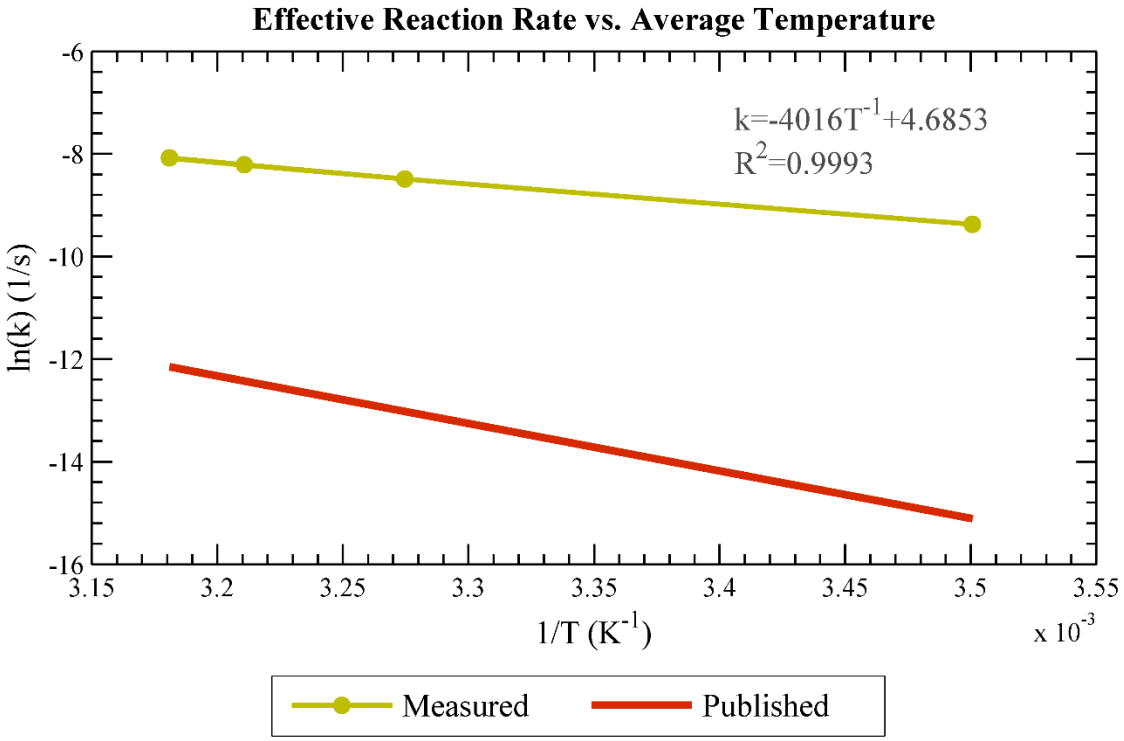

Figure 8.4. Effective reaction rate constant, k_{eff}, versus average reciprocal reservoir fluid temperature, *T*. The effective reaction rate was determined based on the tracer mass fractions recovered after 44 min and the measured average temperature. The red line is based on published data from Nottebohm et al. (2012).

The results of the thermally degrading tracer tests reveal that the extent of phenyl acetate reaction increased with the advancement of the induced thermal front. This shows that the reaction kinetics of phenyl acetate hydrolysis were sufficiently dependent upon temperature even in the extremely small temporal and spatial scale encountered at the Altona field site.

8.4 Summary

The meso-scale field experiments conducted at the Altona field site have shown that thermally degrading chemical tracers react in proportion to the extent of heating in a fractured reservoir undergoing heat exchange with circulating fluids. To the best of our knowledge, this is the first field experiment that successfully demonstrated that thermally degrading tracers can be used at different stages of reservoir heating/cooling to indicate the advancement of a thermal front.

However, the results also revealed that lab-based measurements of Arrhenius parameters were not appropriate in field applications. A possible explanation is that hydrolysis of phenyl acetate experiences a heterogeneous reaction and the fracture surface may act as a catalyst. Other researchers (e.g., Torrents and Stone (1991)) have found that similar carboxylic esters experience heterogeneous reactions in the presence of certain minerals and the catalytic effect also led to adsorption of the reactants. Similarly, the tracer data collected at the Altona site suggest that the reactant, phenyl acetate, experienced adsorption while the product, phenol, did not. Despite this complication, the degradation of phenyl acetate still exhibited a strong linear relationship between inverse temperature and the log of the reaction rate constant. This suggests that the Arrhenius law is still suitable for this reaction, even with complications due to adsorption and catalysis.

Unlike commercial geothermal reservoirs, the spatial distribution of fluid flow and the temporal evolution of subsurface temperature at the Altona field

site is well understood. As discussed in Chapters 3, 6, and 7, this permitted identification of a narrow flow channel that caused early and rapid thermal breakthrough. At the spatial scale of a commercial geothermal reservoir, however, characterization of this nature is currently impractical. This reinforces the need for thermally degrading tracers, particularly because the use of inert tracers alone were shown in Chapter 6 to be an unreliable indicator of thermal performance.

The experiments at Altona also revealed that carboxylic esters, such as phenyl acetate, can be catalyzed in fluids contacting mineral surfaces. This suggests that carboxylic esters may not be suitable as a thermally degrading tracer at the scale of commercial reservoirs. Therefore, appropriate selection of a thermally degrading tracer must carefully consider catalytic effects, in addition to the fluid pH, anticipated temperatures, and tracer residence time.

Inclusion of a thermally degrading tracer in a series of tracer tests conducted during energy production provides a means to qualitatively monitor transient subsurface temperature. This capability was demonstrated at the Altona site in a well characterized meso-scale fracture system. This first field validation is encouraging, suggesting that properly designed thermally degrading tracers can be used to determine heat extraction performance in larger, commercial-sized geothermal reservoirs. When used with inert tracer and other geophysical information, thermally degrading tracers have potential to improve reservoir management strategies to maximize system performance.

However, further research is necessary to understand the impact of surface chemistry on reactions such as base-catalyzed hydrolysis.

8.5 References

Adams, M. C., and J. Davis (1991), Kinetics of fluorescein decay and its application as a geothermal tracer, *Geothermics*, 20, 53-66.

Batchelor, A. S. (1986), Reservoir behaviour in a stimulated Hot Dry Rock system, Proceedings, in *11th Workshop on Geothermal Reservoir Engineering*, Stanford University, Stanford, California.

Du Teaux, R. T., and J. Callahan (1996), Comparing reactive and non reactive tracers to measure changes in liquid dominated, fractured geothermal reservoirs, Proceedings, in *Annual Meeting of the Geothermal Resources Council*, Portland, Oregon.

Krysmann, M. J., A. Kelarakis, P. Dallas, and E. P. Giannelis (2012), Formation mechanism of carbogenic nanoparticles with dual photoluminescence emission, *Journal of the American Chemical Society*, 134, 747-750, doi:10.1021/ja204661r.

Li, Y. V., L. M. Cathles, and L. A. Archer (2014), Nanoparticle tracers in calcium carbonate porous media, *Journal of Nanoparticle Research*, 16, doi:10.1007/s11051-014-2541-9.

Li, Y. V., and L. M. Cathles (2016), The surface interactions of a near-neutral carbon nanoparticle tracer with calcite, *Journal of Nanoparticle Research*, 18, doi: 10.1007/s11051-016-3383-4.

Maier, F., M. Schaffer, and T. Licha (2015), Temperature determination using thermo-sensitive tracers: Experimental validation in an isothermal column heat exchanger, *Geothermics*, 53, 533-539, doi:10.1016/j.geothermics.2014.09.007.

Nottebohm, M., T. Licha, and M. Sauter (2012), Tracer design for tracking thermal fronts in geothermal reservoirs, *Geothermics*, 43, 37-44.

Ray, S. C., A. Saha, N. R. Jana, and R. Sarkar (2009), Fluorescent carbon nanoparticles: Synthesis, characterization, and bioimaging application, *Journal of Physical Chemistry*, 113, 18546-18551, doi:10.1021/jp905912n.

Robinson, B.A., J.W. Tester, and L.F. Brown (1988), Reservoir sizing using inert and chemically reacting tracers, *SPE Formation Evaluation*, 2, 227-234.

Subramanian, S. K., Y. Li, and L. M. Cathles (2013), Assessing preferential flow by simultaneously injecting nanoparticles and chemical tracers, *Water Resources Research*, 49, 29-42.

Torrents, A. and A. T. Stone (1991), Hydrolysis of Phenyl Picolinate at the mineral water interface, *Environmental Science & Technology*, 25, 143-149.

Xu, X. Y., R. Ray, Y. L. Gu, H. J. Ploehn, L. Gearheart, K. Raker, and W. A. Scrivens (2004), Electrophoretic analysis and purification of fluorescent single-walled carbon nanotube fragments, *Journal of the American Chemical Society*, 126, 12736-12737.

Zhao, Y. (2015), The use of Nanoparticles to Assess Subsurface Flow Heterogeneity, *Ph.D Dissertation*, Cornell University.

CHAPTER 9: INVERSE MODEL FOR NON-UNIFORM APERTURE

9.1 Introduction

In geothermal reservoirs that actively inject cold water, reservoir modeling is commonly used to forecast thermal drawdown at production wells. To accomplish this goal, one must have sufficient insight into the spatial distribution of fluid flow paths between injection and production wells. In sparsely-spaced fracture-dominated reservoirs, it is the fracture surface area available for heat exchange between circulating fluids and the bulk rock matrix, or "flow-wetted area" (FWA), which is critically important in forecasting thermal performance (Hawkins et al., 2017a). Ideally, there is sufficient FWA such that the cold injection fluid is adequately heated by the hot reservoir rock before reaching the production well. If FWA is insufficient, however, production well fluid temperature will decline below plant design specifications prior to the end of the project's planned lifetime. In this case, the production well has experienced "premature thermal breakthrough" leading to poor thermal performance, which could be disastrous for a commercial geothermal reservoir.

Tracer testing is a common reservoir characterization technique for investigating subsurface fluid flow in many industries, including geothermal (Shook, 2003). After injecting one or more inert solutes, a conventional tracer test involves monitoring tracer concentration through time at producers. A plot of the tracer concentration versus time provides a Residence Time Distribution

(RTD) which is an invaluable dataset for evaluating flow connectivity between injectors and producers.

In addition, tracer RTDs are commonly used for calibrating fluid flow models which are subsequently used to forecast thermal performance (e.g., Axelsson et al., 2001; Axelsson et al., 2005; Kristjánsson et al., 2016; Robinson et al., 1988; Shook, 2001; etc.). In many applications, a tracer RTD is fit using an analytical solution for tracer transport which includes the influence of advection and dispersion in a single flow channel or in a two-dimensional fracture with uniform aperture. Fitted parameters typically include the fracture aperture and the Peclet Number. The Peclet Number is the ratio of advection to hydrodynamic dispersion within the plane of a fracture; high Peclet Numbers indicate advection dominates.

The classical approach for defining hydrodynamic dispersion in a porous medium is based on the assumption that the process is Fickian (e.g., Taylor-Aris Dispersion) (NRC, 1996, p.273). The validity of this assumption is questionable, however, particularly in rough fractures with spatially varying apertures that produces flow “channeling” (e.g., Bodin et al., 2003; Dagan, 1986; Gelhar, 1986; Neretnieks, 1983; Tsang and Neretnieks, 1998). In these cases, the spread of the tracer RTD may be influenced by Taylor-Aris dispersion, mechanical dispersion, roughness dispersion, and by flow channeling. In such a reservoir, a hydrodynamic dispersion coefficient derived from an inert tracer test RTD will appear to be larger than expected based on

dispersion described by Taylor-Aris. Additional factors that can obscure the nature of dispersion in tracer RTDs include wellbore dilution, adsorption, matrix diffusion, and time scale dependencies (e.g., Reimus et al., 2003; Bodin et al. 2003; Moench, 1989, 1995).

The ambiguity of dispersion mechanisms substantially hinders the reliability of thermal forecasts based on calibrations using inert tracer RTDs. Substantial inaccuracies can be introduced in thermal forecasting because it is unclear how to incorporate dispersion derived from a tracer test in heat transport simulations. According to Taylor-Aris dispersion, heat transport should experience negligible dispersion within the fracture because the high diffusivity of heat negates the influence of velocity profiles within a fracture. This would suggest that dispersion derived from a tracer test can be neglected in heat transport simulations. However, if the dispersion observed in a tracer RTD resulted from flow channeling, this assumption would be inappropriate, because flow channeling can have a substantial influence on FWA and thus strongly influence thermal performance.

Because of uncertain dispersion mechanisms and the possibility of flow channeling, there is a need for the following advancements: (1) a tracer that interrogates FWA; and (2) an inverse model that identifies spatially varying permeability fields. This chapter investigates the use of an inverse model for identifying spatially varying permeability fields by minimizing the L^2 Norm between measured and simulated tracer RTDs.

To investigate the influence of hydrodynamic dispersion and non-uniform aperture, two separate approaches were used in this study. The first uses both the inert and adsorbing tracers in the objective function while the second uses only an inert tracer RTD. In the first approach, hydrodynamic dispersion and the mean fracture aperture are included as unknown parameters to be solved for by the inverse model. In the second approach, hydrodynamic dispersion is assumed negligible and the mean aperture is specified as an input parameter. This approach addresses the point raised in sub-section 6.5, that both mechanical dispersion and Taylor-Dispersion are likely negligible at Altona.

9.2 Methods

9.2.1 Heat and Mass Transport Simulations

Computational modeling of fluid, heat, and tracer transport in a discrete fracture with heterogeneous permeability was accomplished using a finite element method (FEM) solver developed by our group (Fox et al., 2015; Hawkins et al., 2017b). The model was used to simulate the effects of varying aperture distributions on the spatial distribution of heat exchange, thermal breakthrough, and tracer RTD. The heat transport model is a numerical model utilizing a hybrid finite element and boundary element method model for discretely fractured geothermal reservoirs. Two-dimensional fluid flow in the plane of the fracture is solved via the FEM while three-dimensional heat conduction in the rock matrix is captured through a boundary element treatment. The rock matrix surrounding the discrete fractures is assumed to be impermeable with respect to fluid flow.

9.2.2 Non-Uniform Fracture Aperture

Naturally occurring fractures are known to have rough surfaces producing a spatially variable fracture aperture (Figure 9.1). In addition to having a rough surface, fracture core samples have revealed that rough-walled fractures produce fracture aperture distributions that are spatially correlated and self-affine (e.g., Boffa et al., 1999; Brown et al., 1986; Glover et al., 1998; Plouraboué et al., 1995; Ponson et al., 2007; Schmittbuhl et al., 1993, 1995, 2008). The spatial correlation of an aperture field can be described by a spatial correlation function and a Hurst or roughness coefficient, ζ. The variogram function, γ, required for describing the spatial correlation is

$$\gamma(\mathbf{r}') \equiv \left\langle \left[h(\mathbf{r}) - h(\mathbf{r}+\mathbf{r}')\right]^2 \right\rangle = 2\left[\left\langle h^2 \right\rangle - \left\langle h(\mathbf{r})h(\mathbf{r}+\mathbf{r}')\right\rangle\right], \tag{9.1}$$

where h is the local aperture fluctuation, **r**' is the displacement from **r,** and **r** is a point on the surface of the fracture. The variogram function is said to have a self-affine geometry if it has a scaling behavior that follows

$$\gamma(\mathbf{r}') = C\left|\mathbf{r}'\right|^{2\zeta}. \tag{9.2}$$

Core samples have shown Hurst coefficients that range from 0.5 for sandstone (e.g., Boffa et al., 1999; Ponson et al., 2007) to 0.8 for granite (e.g., Schmittbuhl et al., 1993, 1995; Plouraboué et al., 1995). A surface with a lower Hurst coefficient is increasingly rough. Hypothetical self-affine fracture aperture distributions were generated using an algorithm modified from Méheust and Schmittbuhl (2001). The distribution is constructed by random

seeding using Fast Fourier Transforms (FFT) to obtain isotropic self-affine fracture aperture fields on rectangular fractures.

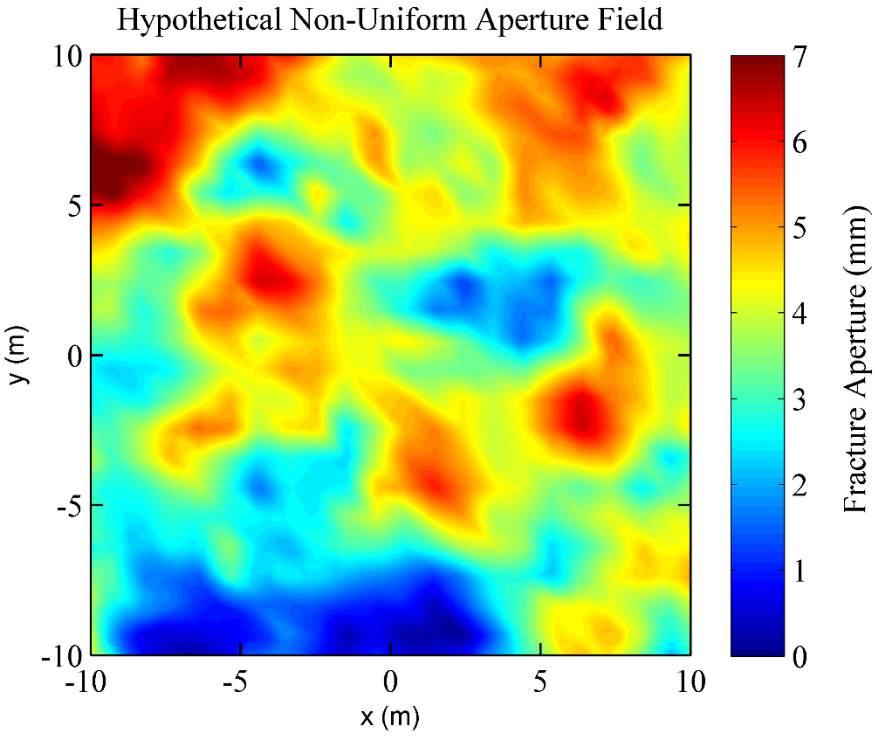

Figure 9.1. Hypothetical fracture rough-walled aperture field represented by the Hurst roughness coefficient, ζ.

9.2.3 Principal Component Analysis (PCA)

Principal Component Analysis (PCA) is a statistical tool commonly used in engineering sciences to identify the dominant behavior of a dataset consisting of two or more independent variables. It can be used to reduce the complexity of a dataset by identifying correlations between 2 or more independent variables that produce the greatest variance. PCA is performed by first determining the covariance matrix of the data set. Then, the eigenvectors and eigenvalues of the covariance matrix are calculated. Each eigenvector

represents a “mode” of the dataset and the matrix is organized from the most to least dominant mode based on the magnitude of the eigenvalues or mode “coefficients.” For spatially correlated fractures, the mode with the largest eigenvalue corresponds to spatial variations over relatively large areas of the fracture. The benefit of PCA for the purpose of identifying representative aperture distributions is that it permits parameter reduction and allows an inversion method to vary large spatially correlated regions of the aperture at once, rather than attempting to solve for aperture at each location in the model domain.

For a data set X_{ij} comprised of n independent variables where each variable has a mean of zero across m observations, the covariance matrix, C_{ij}, between variable i and j is

$$C_{ij} = \sum_{k=1}^{m} X_{ik} X_{jk}. \tag{9.3}$$

For a discrete heterogeneous fracture represented by nodes on a computational mesh, n is the number of nodes and m is the number of aperture fields generated. Once the eigenvectors (or “modes”) and eigenvalues (or “coefficients”) of the covariance matrix have been determined, an aperture field in the matrix of observations can be reproduced by knowing the modes of the entire dataset and the coefficients for the specific aperture field:

$$w_i = \sum_{j=1}^{p} \mathbf{\Phi}_{ij} \alpha_j + \langle w \rangle, \tag{9.4}$$

where w_i is the fracture aperture at node i, $\mathbf{\Phi_{ij}}$ is the matrix of PCA modes, a_j are the coefficients of the PCA modes, and $<w>$ is the mean fracture aperture (Figure 9.2). If p is equal to n, the total number of nodes, then the original dataset is replicated identically. If, however, a reduced order model is desired, p can be selected for any integer value greater than zero and less than n. The lower the value of p, the more the fracture aperture distribution is simplified by neglecting small-scale spatial variations. In addition, entirely new aperture distributions can be produced by altering the magnitude of the mode coefficients. Any new distribution will have a unique aperture field, but the eigenvectors of its covariance matrix (i.e. its PCA modes) are identical to the original data set.

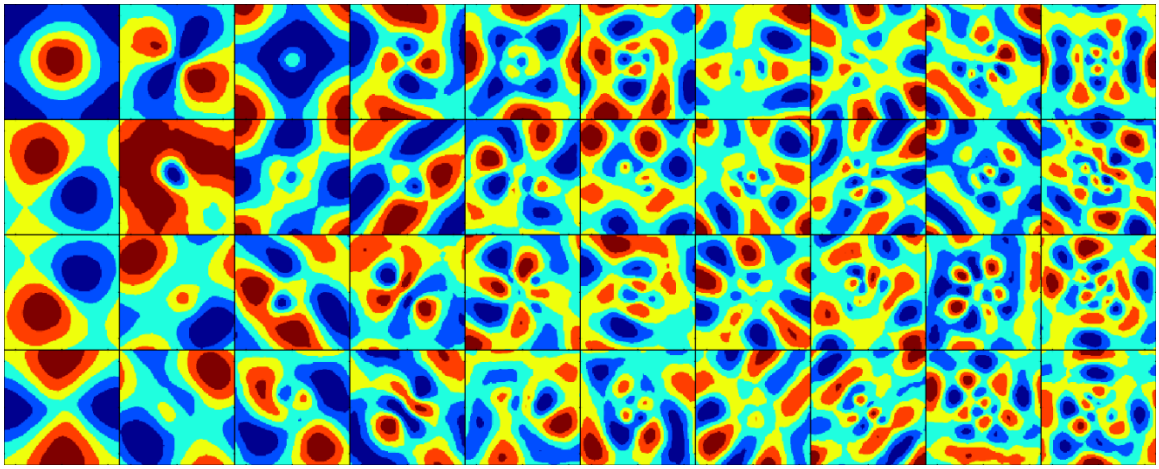

Figure 9.2. PCA modes in two-dimensional space for a self-affine fracture aperture field. The upper left square is the first mode and the bottom right square represents the 40th mode. Mode rank decreases by row first then by column.

9.3 Inverse Model

The challenge in identifying a representative fracture aperture field is that the number of unknown variables is large. For a typical computational mesh used at the Altona field site, there are approximately 9000 nodes in the computational mesh that are used to capture the spatial variability of fracture aperture. Therefore, an attempt to identify a representative aperture distribution by identifying a unique fracture aperture for each node is unrealistic considering the computational time required and the relatively small influence of a local aperture fluctuation on tracer transport.

The inversion procedure utilized in this study intends to reduce the computational time requirements by varying spatially correlated regions of the model domain using PCA. Since PCA reduces the complexity of a dataset by isolating correlated features that produce the most variance among the independent variables (i.e. fracture apertures), this is an ideal approach to identify non-uniform aperture fields.

Even after PCA, there remains several challenging aspects of successfully employing an inverse method for determining a representative aperture fields, including: (1) it is non-linear; (2) there are a large number of unknown variables; and (3) there are likely many local minimums of the objective function. For these reasons, a Genetic Algorithm (GA) was selected as the ideal inverse search method. A GA is a metaheuristic stochastic global optimizer that mimics natural selection to minimize an objective function $f(x_j)$ where x_j is a set of parameter values. The GA is similar to natural selection in that the "fitness"

of an initial population is quantified and new "generations" can be produced by "breeding" or "mutating" individuals in the population that are specified using a suitable selection function (Figure 9.3). New generations are produced until the desired conditions for termination have been satisfied.

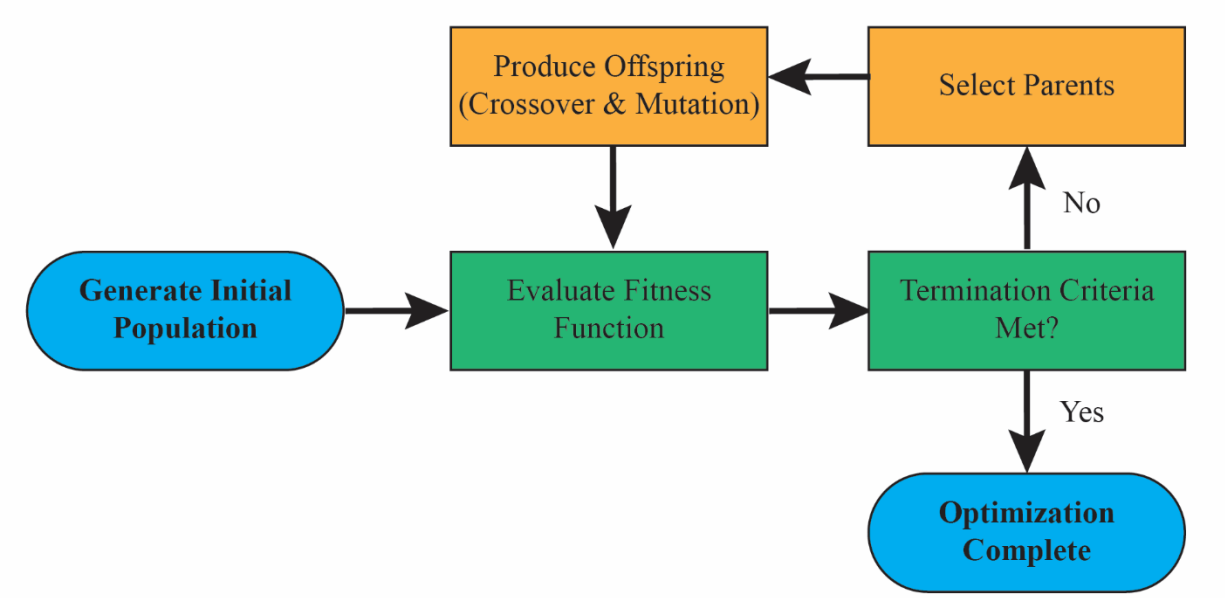

Figure 9.3. Flow diagram for the Genetic Algorithm (GA) demonstrating the inversion process in which offspring are reproduced until the pre-specified termination criteria are met.

For this study, the parameter values for the GA are the PCA mode coefficients and the objective function is the L^2 Norm between the measured and simulated tracer RTDs. Parameters of the initial population were determined using the range of alpha values given an arbitrary standard deviation used during PCA. Individuals are selected for reproduction based on a parent selection function which, in this study, was a "tournament" selection function. This selection function identifies a new parent based on the best-fit individual in a randomly targeted sub-set of the entire population. Most

children were produced using a crossover function that combines the parameters of selected parents. The remaining children were produced through a mutation function that randomly changes the "genes" of individual parents, which in this case are the PCA mode coefficients.

9.4 Results for Approach 1: Inert and Adsorbing Tracers

The inverse model was used to identify a representative fracture aperture field based on matching simulated to measured inert and adsorbing tracer data. As discussed in sub-section 7.3.1, the adsorption reaction was measured in the lab and values for the reaction rate and partition coefficient were determined for cesium adsorption onto the Potsdam Sandstone. The inverted variables included in "Approach 1" are the mean fracture aperture, longitudinal dispersivity, and the coefficients of 100 modes of the PCA. Selecting an appropriate number of modes to include in the inverse model is somewhat arbitrary. The computational efficiency of the GA is weakly influenced by the number of modes, so a conservative number of 100 modes was selected in this study.

The PCA modes were generated assuming a Hurst roughness coefficient of 0.5, which is typical of sandstone (Boffa et al., 1999; Ponson et al., 2007). As discussed in Fox (2016), however, the magnitude of the Hurst coefficient is relatively insignificant and serves rather as a convenient means to produce PCA modes that are consistent with a spatially correlated aperture field. A log-normal distribution of fracture aperture was assumed and 30,000 randomly generated, self-affine fracture aperture fields were produced for PCA.

The inverse problem was solved by minimizing the L^2 Norm between measured and simulated tracer RTDs, including both the inert and adsorbing tracer. Using a population of 30 individuals and 400 generations, the GA produced a sufficient fit to the measured tracer data (Figure 9.4). The fracture aperture field produced reveals a narrow channel (~1 to 2 m) extending in roughly a linear form directly between the injection and production well (Figure 9.5). The flow channel fracture aperture is typically in the range of 4 to 5 mm while the low aperture region surrounding it is roughly 0.3 to 0.9 mm. The inverse model resulted in a mean fracture aperture of 2.8 mm and longitudinal dispersivity of 0.25 m.

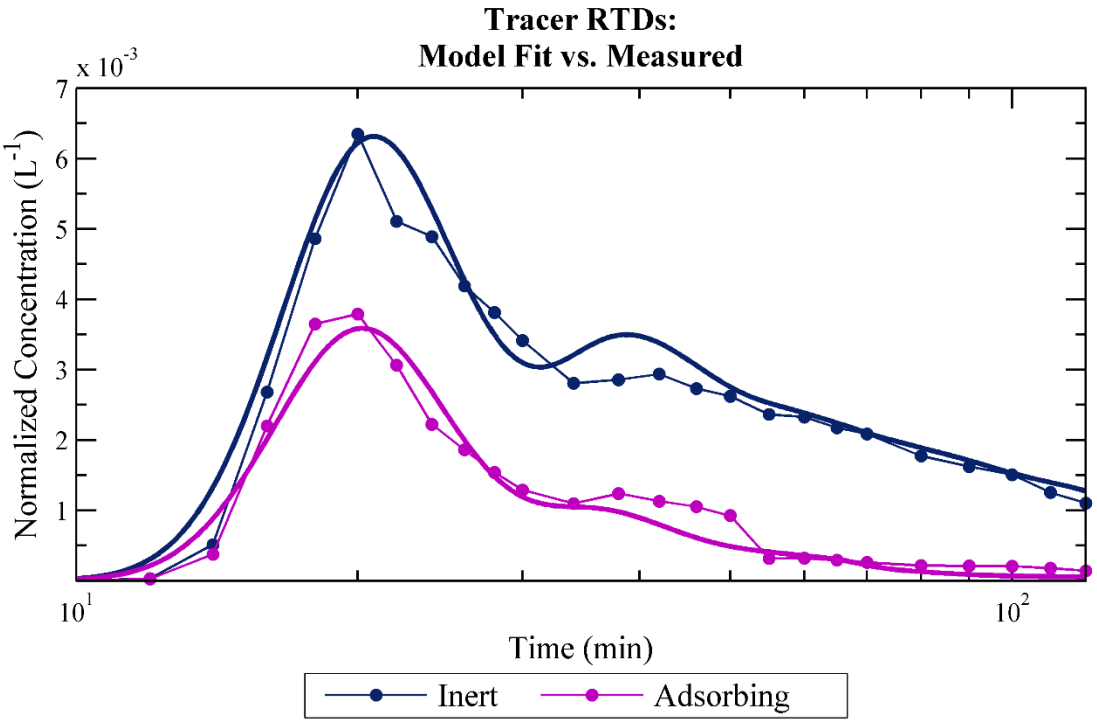

Figure 9.4. Comparison of the measured tracer RTD (dots) versus the simulation (lines) resulting from the solution to the inverse problem.

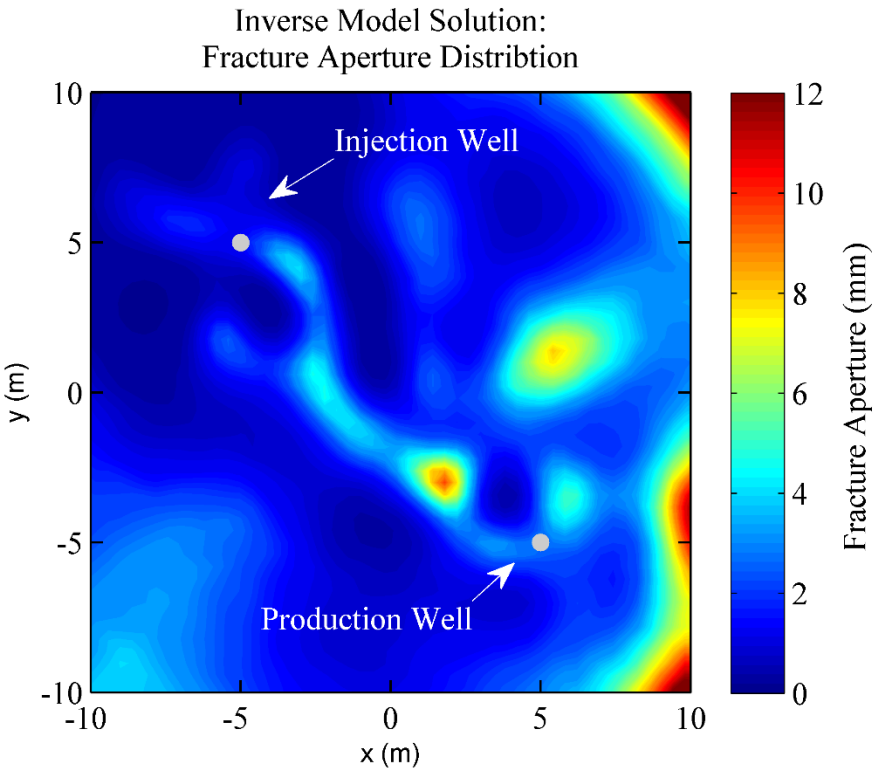

Figure 9.5. Fracture aperture distribution resulting from the solution to the inverse problem.

The solution to the inverse model was used to identify a representative fracture aperture field for forecasting thermal performance at Altona. A 1% change in production well temperature was predicted after roughly 6 h of circulating hot water (Figure 9.6). By the end of the experiment (6 d), predicted production well temperature reaches 27 °C. In the plane of the fracture, the spatial distribution of heat exchange followed the narrow path of the flow channel (Figure 9.7)

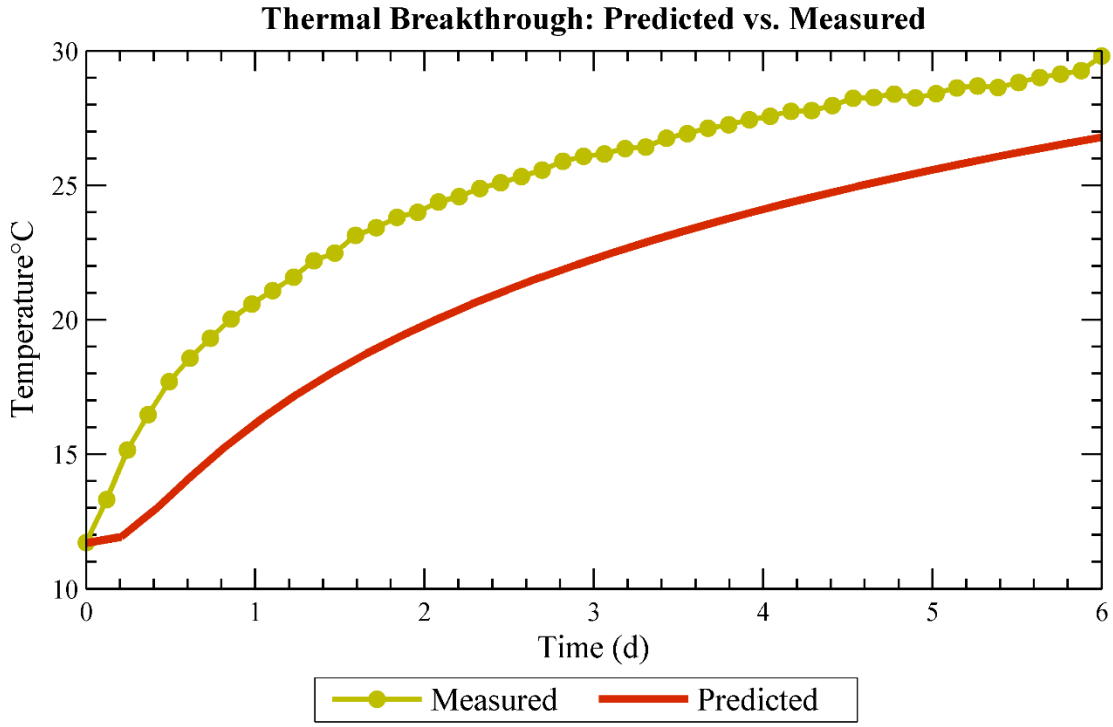

Figure 9.6. Comparison of measured and predicted thermal response at the production well. Predicted thermal response resulted from a heat transport simulation in the fracture aperture distribution identified by the best-fit match between measured and simulated tracer RTD.

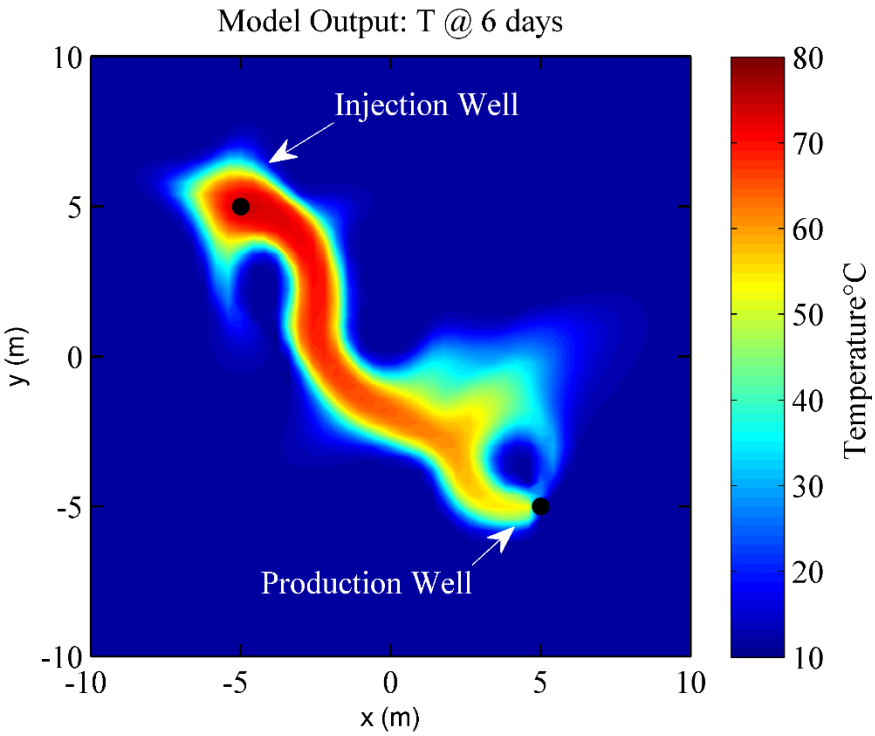

Figure 9.7. Map view representation of predicted temperature distribution in the plane of the fracture. Predicted temperature distribution resulted from a heat transport simulation in the fracture aperture distribution identified by the best-fit match between measured and simulated tracer RTD.

Measured production well temperature experienced a 1% change after 1.6 h of hot water injection (Figure 9.6). The initial rate of temperature rise is rapid and flattens substantially after roughly 1 d of heating. At the end of the experiment (6 d), measured temperature at the production well is 29.8 °C.

9.4.1 Summary of Approach 1

The aperture field that solves the inverse problem suggests that fluid circulation between the injection and production well at the Altona field site is prone to flow channelization and, as a consequence, premature thermal breakthrough would be likely if this geothermal analog were a commercial

operation. The aperture field produced from the inverse model shows a narrow (roughly 1 to 2 m) region of large (roughly 4 to 5 mm) fracture aperture directly connecting the injection well and production well (Figure 9.5). A prediction of the spatial distribution of temperature rise in the plane of the fracture based on this aperture distribution demonstrates that heat exchange is limited to the width of the flow channel (Figure 9.7).

9.5 Results for Approach 2: Inert Tracer and No Dispersion

As shown in Chapters 6 and 7, the ambiguity of dispersion prevents accurate forward models of heat transport if inert tracers are used for calibration. However, if dispersion can be treated as negligible, the variance of the inert tracer RTD may be an indicator of the spatial distribution of fluid flow paths. This approach is a deviation from the conventional approach for interpreting inert tracer RTDs, because a typical analysis will match the variance of the RTD by including the Peclet number, *Pe*, as an unknown parameter to be determined in an inverse model.

As discussed in several articles (e.g., Robinson et al., 1988; Gelhar et al., 1992; etc.), however, this approach often results in Peclet numbers that are much too small relative to dispersive mechanisms in a single-fracture (e.g., Taylor-Dispersion, fracture roughness, matrix diffusion, etc.). In this sub-section, simulated inert tracer RTDs were fit to measured data from Altona in a non-uniform fracture with negligible hydrodynamic dispersion, which would be the case if Taylor-Dispersion was the dominant mechanism of hydrodynamic dispersion encountered by tracers used at Altona.

In the Altona experiments, Taylor dispersion appears to be negligible based on the observation that the C-Dot tracer and iodide tracer have nearly identical RTDs despite the fact that the C-Dot tracer's mass diffusion coefficient is roughly an order of magnitude smaller than iodide. Under Taylor dispersion, however, an order of magnitude difference would produce roughly an order of magnitude difference in hydrodynamic dispersion, based on dispersion described by analytical models such as in Horne (1983).

9.5.1 Inverse Model Setup

As in "Approach 1", the inverse model adopted in "Approach 2" solves the objective function by an inversion procedure that identifies optimal PCA mode coefficients. In this section, however, there are two main differences: (1) only the inert tracer is used in the objective function; and (2) hydrodynamic dispersion, D_f, is assumed negligible. The mean fracture aperture was specified in the inverse model as a known parameter and the inverse model was ran for eight different mean fracture apertures ranging from 0.5 mm to 7 mm.

9.5.2 Results

A total of 50 PCA modes were selected for the inverse model and the genetic algorithm (GA) was ran for a population of 20 with children produced for 30 generations. The best-fitting solution was found for an aperture field with a specified mean fracture aperture of 4 mm (Figure 9.8). The worst fit was found when fracture aperture was specified to be 7 mm.

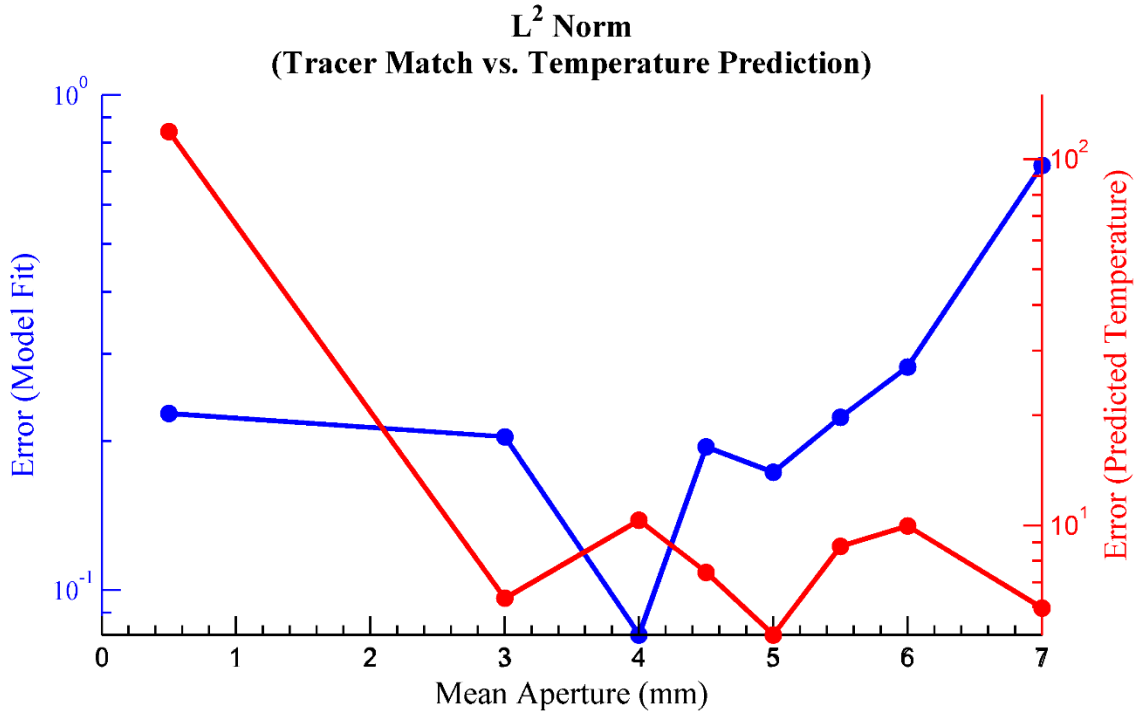

Figure 9.8. L^2 Norm vs. mean fracture aperture for the fitness of the inert tracer simulation (blue) and for the resulting error in predicted temperature.

The solution to the inverse problem was used in a forward-model that predicted production well temperature. For a 75 d long simulation, production well temperature was predicted to change from a dimensionless temperature of 1 (or 11.7 °C) to a dimensionless temperature of 0.58 (or 38 °C) (Figure 9.9). The L^2 Norm of predicted temperature was measured based on the time required for measured and simulated temperature to change 1, 3, 5, and 10%.

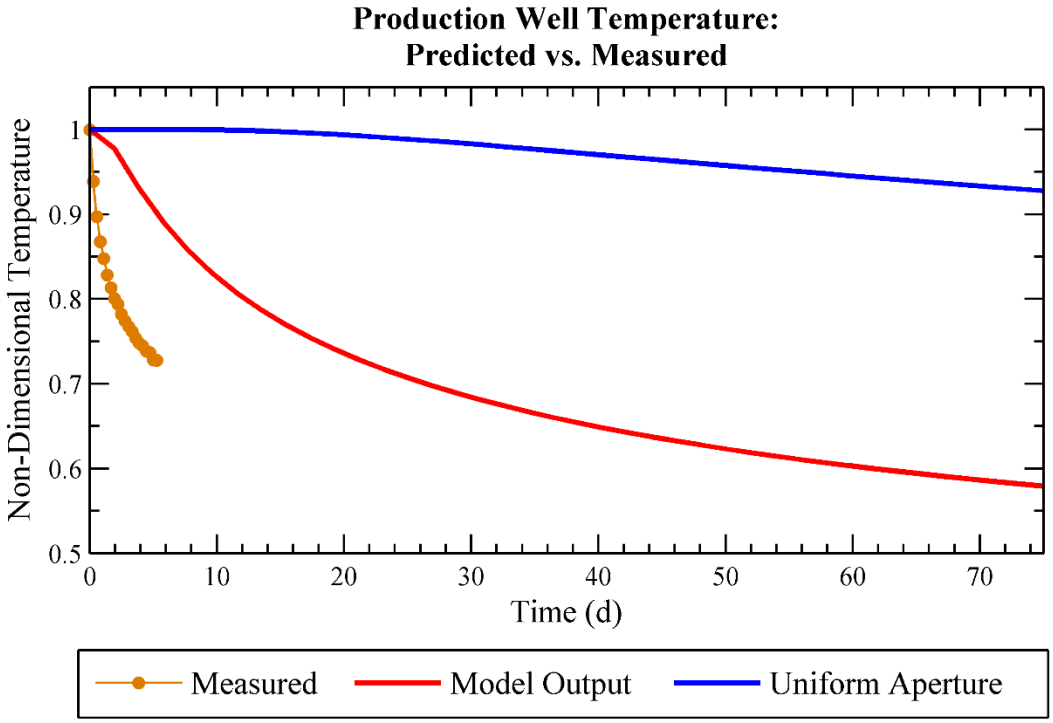

Figure 9.9. Predicted production well temperature (red) resulting from the inverse model fit to inert tracer data. The inverse model's fit parameters included the PCA mode coefficients and the mean fracture aperture. Dispersion was assumed negligible. Measured data (orange dots) and thermal breakthrough for a uniform aperture (blue) are shown for reference.

The inverse model solution over-predicts thermal performance. However, it is significantly more accurate than assuming the fracture aperture is uniform (Figure 9.9). Measured and model predicted time to reach 1% temperature change are 0.56 and 5.8 d, respectively. In contrast, the uniform aperture scenario predicts a 1% change in 23 d.

The objective function of the inverse model minimized the error between measured and simulated inert tracer RTDs over the 490 min tracer test conducted at Altona. The L^2 Norm of the solution for non-uniform aperture

with a mean of 4 mm is 0.08, whereas the L^2 Norm for an inverse model that assumes uniform aperture with negligible dispersion is 0.3. The three tracer RTDs, shown in Figure 9.10, reveal that the uniform aperture inverse solution produces a tracer curve that is too low in concentration prior to roughly 200 min and too high at that point on. The non-uniform aperture, however, provides a superior fit to measured data, because aperture variations allowed for the slope of the RTD tail to steepen, consistent with measured data.

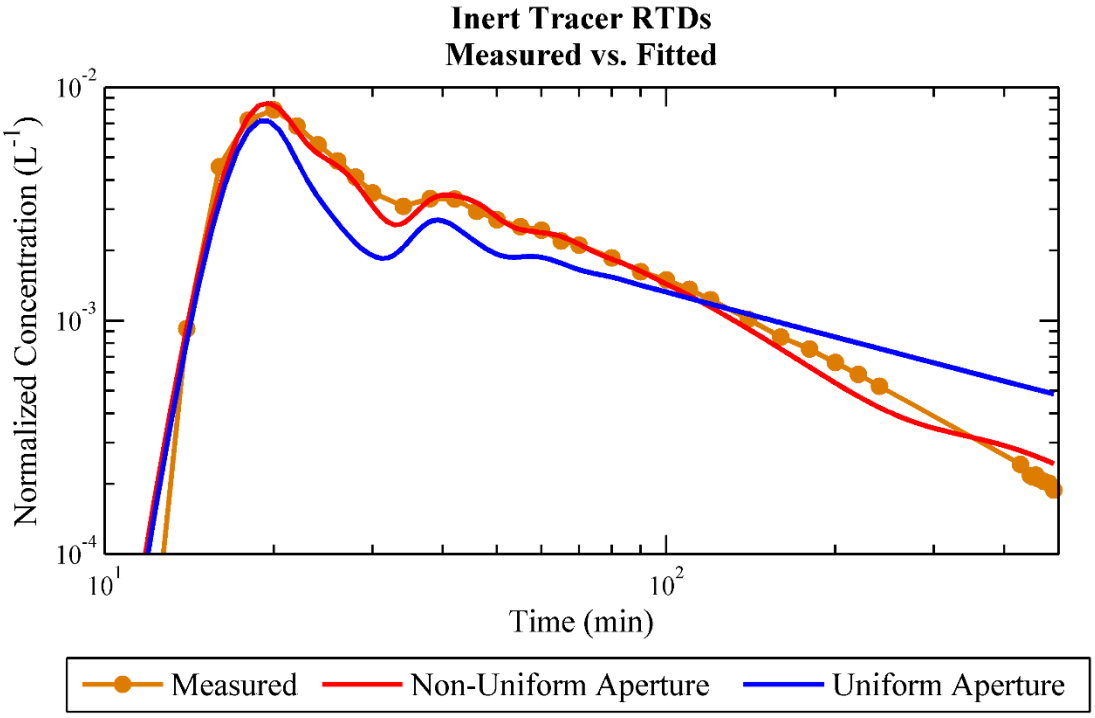

Figure 9.10. Log-log plot of inert tracer RTDs for measured data (orange) and two separate inverse model solutions. The "Non-Uniform Aperture" simulation (red) results from the PCA coefficients that solve the inverse problem with a mean aperture of 4 mm. The "Uniform Aperture" simulation (blue) results from the fracture aperture that solved the inverse problem assuming uniform aperture. Both of the model scenarios assumed dispersion was negligible.

9.6 Summary

Using Principal Component Analysis (PCA) and a Genetic Algorithm (GA), an inverse model for identifying spatially varying permeability fields successfully forecasted the occurrence of premature thermal breakthrough in a geothermal analog field site. Two approaches were adopted which targeted different model parameters. In the first approach, the inverse model minimized the L^2 Norm between measured and simulated inert and adsorbing tracer data. It solved for 100 PCA mode coefficients as well as hydrodynamic dispersion and the mean fracture aperture.

The second approach solved for 50 PCA mode coefficients and assumes hydrodynamic dispersion is negligible. The assumption of negligible dispersion at Altona is supported by the discussion of mechanical dispersion and Taylor-Dispersion in sub-section 6.5 where neither dispersive mechanism could account for the measured C-Dot and iodide tracer RTDs. Without a physical explanation for dispersion, solving the inverse problems discussed in Chapters 6, 7, and the first approach of Chapter 9 essentially treats dispersion as a fitting parameter with no physical basis. The second approach in Chapter 9 investigates the cause of this apparent dispersion by determining if a sufficient match to measured inert tracer data can be reached simply by identifying a non-uniform aperture field. In the second approach, the inverse problem was solved eight times, each with a different assumed value for mean fracture aperture. The pre-specified mean fracture aperture that produced the best fit to

the inert tracer was 4 mm and it was subsequently used to predict thermal performance.

Using Approach 1, inert and adsorbing tracer RTDs were matched fairly well by the inverse solution. The resulting prediction of temperature (Figure 10.3), is much more accurate than a uniform aperture prediction, but less accurate than the one-dimensional approach for interpreting inert/adsorbing tracer data, which is discussed in Chapter 7.

In the second approach, the inert tracer RTD produced by aperture field identified in solving the inverse model fits the measured data better than a uniform aperture, but not as well as the first Approach. The uniform aperture mentioned here was determined assuming negligible dispersion and is discussed in sub-section 9.5.

A particularly interesting comparison can be drawn between the tailing behaviors of the tracer RTDs plotted on a log-log scale (Figure 9.10). Measured tracer return and the results of the non-uniform aperture both exhibit a steeply sloping tail relative to the uniform aperture model. The ability of the non-uniform aperture and the inability of the uniform aperture to replicate this tailing behavior suggests that fracture aperture variations can be used to match RTD curves even if dispersion is negligible. This suggests that the apparent dispersion found in previous modeling efforts was likely a result of flow channeling, not mechanical dispersion or Taylor-Dispersion. For these reasons, it appears feasible that a non-uniform aperture field could provide

reasonably accurate predictions of thermal performance in circumstances where accurate mathematical models for dispersion are available.

However, this study was conducted at the Altona field site, which is much smaller in scale than commercial reservoirs which, ideally, circulate fluids through several fractures, rather than just one. Furthermore, mechanical dispersion and Taylor-Dispersion are just two mechanisms that produce spreading in tracer RTDs. These added complexities may inevitably prevent accurate forward-models of heat transport even in circumstances where inert tracers can be fit with negligible dispersion. Nevertheless, the ability of the inverse model to match inert tracer data under negligible dispersion is promising and suggests that non-uniform aperture fields produce tracer RTD signals that constrain the inverse solution to flow patterns that are consistent in terms of the effective heat transfer area.

9.7 References

Axelsson, G., O.G. Flovenz, S. Hauksdottir, A. Hjartarson, and J. Liu (2001), Analysis of Tracer Test Data, and Injection-Induced Cooling, in the Laugaland Geothermal Field, N-Iceland, *Geothermics*, 30, 573-589.

Axelsson, G., G. Björnsson, and F. Montalvo (2005), Quantitative Interpretation of Tracer Test Data, Proceedings, in *World Geothermal Congress*, Antalya, Turkey.

Bodin, J., F. Delay, G. de Marsily (2003), Solute transport in a single fracture with negligible matrix permeability: 1. fundamental mechanism, *Hydrogeology Journal*, 11, 418-433.

Boffa, J.M., C, Allain, R. Chertcoff, J. Hulin, F. Plouraboué, and S. Roux (1999), Roughness of sandstone fracture surfaces: Profilometry and shadow length investigations, *European Physical Journal B*, 7, 179-182.

Brown, S.R., R. Kranz, and B. Bonner (1986), Correlation between the Surfaces of Natural Rock Joints, *Geophysical Research Letters*, 13, 1430-1433.

Dagan, G. (1986), Statistical theory of groundwater flow and transport: Pore to laboratory, laboratory to formation, and formation to regional Scale, *Water Resources Research*, 22, 120S-134S.

Fox, D. B., D.L. Koch, and J.W. Tester (2015), The effect of spatial aperture variations on the thermal performance of discretely fractured geothermal reservoirs, *Geothermal Energy*, 3, 1-29.

Gelhar, L.W. (1992), A critical review of data on field-scale dispersion in aquifers, *Water Resources Research*, 28, 1955-1974.

Glover, P. W. J., K. Matsuki, R. Hikima, and K. Hayashi (1998), Fluid flow in synthetic rough fractures and application to the Hachimantai Geothermal Hot Dry Rock Test Site, *Journal of Geophysical Research*, 103, 9621-9635.

Hawkins, A.J., M.W. Becker, and G.P. Tsoflias (2017a), Evaluation of inert tracers in a bedrock fracture using ground penetrating radar and thermal sensors, *Geothermics*, 67, 86-94.

Hawkins, A.J., D.B. Fox, M.W. Becker, J.W. Tester (2017b), Measurement and simulation of heat exchange in fractured bedrock using inert and thermally degrading tracers, *Water Resources Research*, 53, doi: 10.1002/2016WR019617.

Horne, R. N., and F. Rodriguez (1983), Dispersion in tracer flow in fractured geothermal systems, *Geophysical Research Letters*, 10, 289-292, doi: 10.1029/GL010i004p00289.

Méheust, Y., and J. Schmittbuhl (2001), Geometrical heterogeneities and permeability anisotropy of rough fractures, *Journal of Geophysical Research: Solid Earth*, 106, 2089-2102.

Moench, A. F. (1989), Convergent radial dispersion: A Laplace Transform solution for aquifer tracer testing, *Water Resources Research*, 25, 439-447.

Moench, A. F. (1995), Convergent radial dispersion in a double-porosity aquifer with fracture skin: Analytical solution and application to a field experiment in fractured chalk, *Water Resources Research*, 31, 1823-1835.

Kristjánsson, B.R., G. Axelsson, G. Gunnarsson, I. Gunnarsson, and F. Óskarsson (2016), Comprehensive tracer testing in the Hellisheidi Geothermal Field in SW-Iceland, Proceedings, in *41st Workshop on Geothermal Reservoir Engineering*, Stanford University, Stanford, California.

Neretnieks, I. (1983), A note on fracture flow dispersion mechanisms in the ground, *Water Resources Research*, 19, 364-370.

NRC (1996), *Rock Fractures and Fluid Flow: Contemporary Understanding and Applications*, National Resource Council, National Academy Press, Washington, D.C.

Plouraboué, F., P. Kurowski, J. P. Hulin, S. Roux, and J. Schmittbuhl (1995), Aperture of rough cracks, *Physical Review E*, 51, 1675.

Ponson, L., H. Auradou, M. Pessel, V. Lazarus, and J. P. Hulin (2007), Failure mechanisms and surface roughness statistics of fractured Fontainebleau Sandstone, *Physical Review E,* 76, 036108.

Reimus, P., G. Pohll, T. Mihevc, J. Chapman, M. Haga, B. Lyles, S. Kosinski, R. Niswonger, and P. Sanders (2003), Testing and parameterizing a conceptual model for solute transport in a fractured granite using multiple tracers in a forced-gradient test, *Water Resources Research*, 39, doi:10.1029/2002WR001597.

Robinson, B.A., J.W. Tester, and L.F. Brown (1988), Reservoir sizing using inert and chemically reacting tracers, *SPE Formation Evaluation*, 2, 227-234.

Schmittbuhl, J., S. Gentier, and S. Roux (1993), Field measurements of the roughness of fault surfaces, *Geophysical Research Letters*, 20, 639-641.

Schmittbuhl, J., F. Schmitt, and C. Scholz (1995), Scaling invariance of crack surfaces, *Journal of Geophysical Research: Earth Surface*, 100, 5953-5973.

Schmittbuhl, J., A. Steyer, L. Jouniaux, and R. Toussaint (2008), Fracture morphology and viscous transport, *International Journal of Rock Mechanics and Mining Sciences*, 45, 422-430.

Shook, G.M. (2001), Predicting thermal breakthrough in heterogeneous media from tracer tests, *Geothermics*, 30, 573-589.

Shook, G. M. (2003), A simple, fast method of estimating fractured reservoir geometry from tracer tests, *Transactions of the Geothermal Resource Council*, 27.

Tsang, C.F., and I. Neretnieks (1998), Flow channeling in heterogeneous fractured rocks, *Reviews of Geophysics*, 36, 275-298.

CHAPTER 10: OVERALL SUMMARY AND CONCLUSIONS

10.1 Summary

This dissertation reports on the latest in a series of field experiments conducted at the Altona field site in Altona, New York in late October 2015 and August 2016. In addition, computational models were developed and/or tested with respect to calibrating forward models of heat transport utilizing inert and reactive tracer measurements. In this chapter, field experiments and computational efforts conducted between 2013 and 2017 are summarized. The results of these most recent experiments at Altona are then compared to previous site investigations that used Ground Penetrating Radar (GPR) to image the relative magnitude of the fracture aperture and the spatial distribution of saline tracer circulating through the fracture. Conclusions and Recommendations are provided in the final two sub-sections of this chapter.

10.1.1 Heat Exchange Experiment

In late October and early November 2015, a heat exchange experiment was performed over 6 d. As hot water (74 °C) was circulated through the relatively cold formation (~12 °C), temperature rise was monitored throughout the bulk rock matrix, at the production well, and at three observation wells. At the production well, temperature increased by roughly 20 °C. At the ten monitoring locations, fluid temperature rise in the plane of the fracture was found to be roughly 20 to 30 °C directly between the injection and production well. Outside this narrow region, temperature increased by roughly 1 to 10 °C.

The measured production well temperatures were used to determine an effective heat transfer surface area for fluids circulated between wells 204 and 304. An analytical model for heat transport in a rectangular flow channel with uniform velocity was used to capture the influence of heated fluid advection in the fracture and thermal conduction in the rock matrix, orthogonal to the fracture. Using this analytical solution for production well temperature, an inverse model that matched simulated and measured temperature provided a very good fit using two flow channels. The inverse model estimates that these two flow channels each represent roughly 20% of the total interwell fluid volume. Estimated surface area for these two flow channels are 22 and 65 m^2, respectively.

A surface area of 22 m^2 is in good agreement with the spatial distribution of heat exchange measured via FO-DTS. They are compared in Figure 10.1 and these results are overlain on the saline GPR survey described previously in sub-section 3.6.1. The GPR image, FO-DTS measurements, and the estimated surface area all indicate that a very narrow flow channel roughly 0.8 to 1 m wide extends directly between the injection and production well. This is true even though the GPR tracer imaging was performed with fluid velocity oriented to the west whereas the heat exchange experiment was to the east. This consistency despite opposing flow directions suggests that the hydraulic background gradient did not influence the spatial distribution of fluid flow observed at Altona.

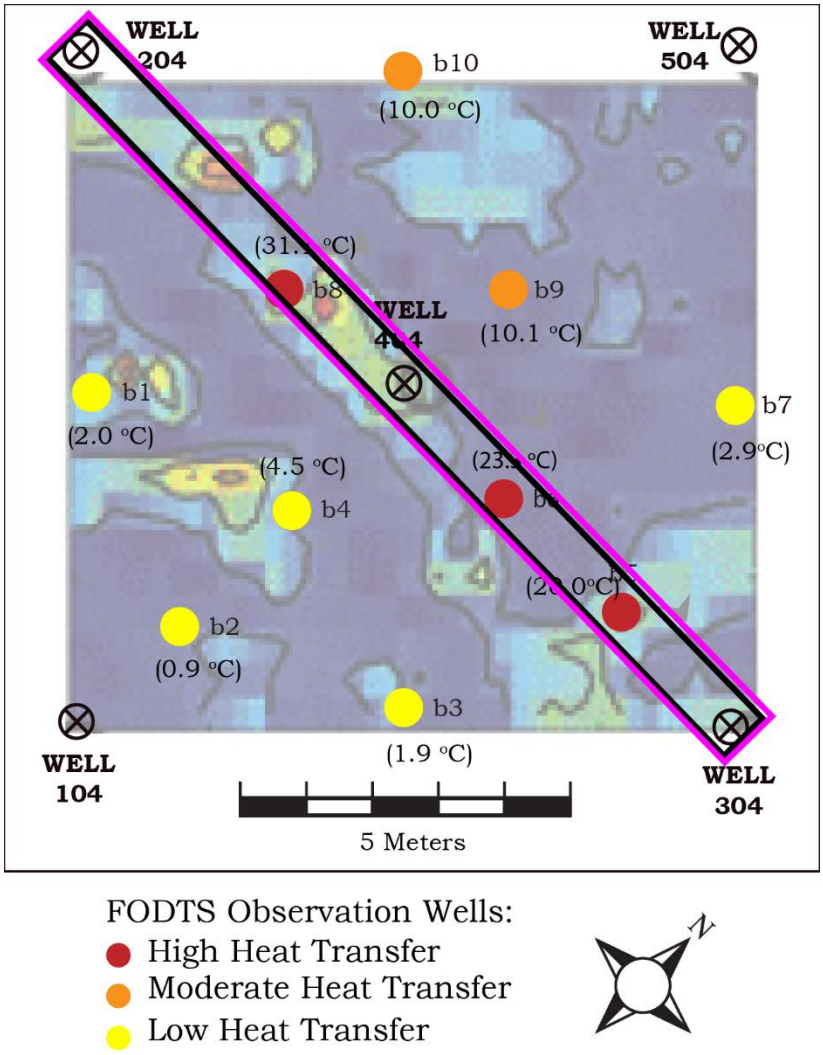

Figure 10.1. Map view comparison between GPR imaging of saline tracer (background image), FO-DTS measured temperature rise (colored dots), and the effective surface area available for heat exchange estimated using measured production well temperature and an analytical heat transport model (black rectangle inside the purple rectangle). Just outside of the black rectangle, the purple rectangle represents the effective heat transfer surface area estimated in the analysis of adsorbing tracer data.

10.1.2 Summary of Altona Tracer Testing

A total of 13 tracer Residence Time Distributions (RTDs) were collected at the Altona site between well 204 and 304, separated by 14 m. Tracer

compounds included, primarily, C-Dots, iodide, cesium, and phenyl acetate. C-Dots and iodide were used as inert tracers while cesium adsorbs to mineral surfaces phenyl acetate reacts as function of temperature. Tracer test results are summarized in Figure 10.2 with concentration normalized by dividing measured concentration by the tracer mass injected. Note that for each test, produced fluids were immediately reinjected. All of the tracer tests were conducted under forced-dipole conditions at a specified flow rate of either 5.7 or 5.8 L/min.

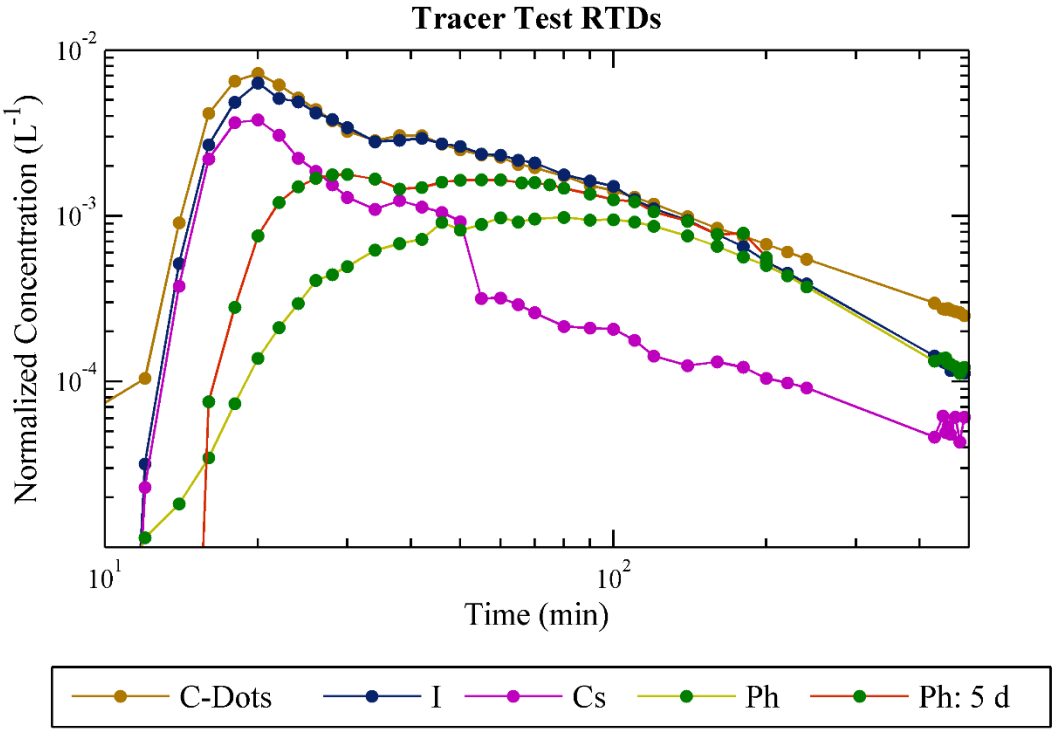

Figure 10.2. Plot of a representative tracer return for the two inert tracers, C-Dots and iodide, the adsorbing tracer cesium, and phenol, which is the product of the thermally degrading tracer phenyl acetate. Two phenol curves are plotted; the first was conducted at ambient reservoir temperatures and the second was after 5 d of heating the reservoir.

10.1.3 Inert Tracers

In Chapter 6, inert tracers were evaluated based on their use in aiding forecasts of geothermal reservoir thermal performance. First, moment analysis demonstrated that thermal performance does not depend on reservoir attributes that can be determined by analyzing inert tracers. Second, the non-uniqueness of aperture fields identified by inert tracer analysis were evaluated based on thermal breakthrough predicted by these two scenarios. The results showed that a uniform aperture with idealized dipole flow provides a sufficient fit to measured inert tracer data collected at Altona.

Unfortunately, the same reservoir structure, when used to predict thermal performance, failed to provide useful results. No temperature increase was predicted over the 6 d heat exchange experiment. Measured temperature, however, had begun increasing within 45 min of the experiment and increased by roughly 20 °C after 6 d. In contrast, the opposing flow scenario introduced a narrow region of relatively large aperture extending directly between the injection and production well. Despite a relatively poor fit to the inert tracer data, predicted temperature increased by 21 °C, which is in good agreement with measured temperature.

10.1.4 Adsorption Tracers

Adsorption tracer tests were conducted at Altona to estimate the effective heat transfer surface area of fluids circulating between injection well 204 and production well 304 (Chapter 7). After lab experiments demonstrated that the adsorption reaction was slow relative to measured RTDs at Altona, an

analytical solution for advection, dispersion, and rate-limited adsorption was developed. The derivation of this model is described in detail in Appendix B and also provides an analytical model for additional transport phenomena, including matrix diffusion and thermal decay. Using an inverse model, several flow channels were identified. The flow channel that dominates heat and tracer transport was estimated to half an effective heat transfer area of 28 m^2. For comparison, 22 m^2 was estimated to be the effective heat transfer surface area based on matching simulated and measured production well temperature (Chapter 5). The surface area estimated in the adsorption tracer analysis is also in good agreement with the spatial distribution of heat exchange measured via FO-DTS and GPR cross-polarized imaging of saline tracer when circulating between wells 304 and 204 (Figure 10.1). For further details regarding the GPR survey, refer to sub-section 3.6.1.

The surface area estimated via adsorption tracers was subsequently used to predict production well temperature. The forward-model predicts thermal breakthrough occurs within roughly 1 h of hot water circulation which agrees well with the measured thermal breakthrough time of roughly 45 min. By the end of the 6 d heat exchange experiment, predicted and measured temperature was 31 and 30 °C, respectively. In Figure 10.3, predicted temperature from the adsorption tracer analysis is compared to measured temperature. In addition, temperature predictions are also provided from the two approaches to identifying a non-uniform aperture field (Chapter 9), and the two approaches described in Chapter 6, which compared temperature predictions resulting

from a uniform aperture and from a two-dimensional fracture with inlet/outlet well short-circuiting.

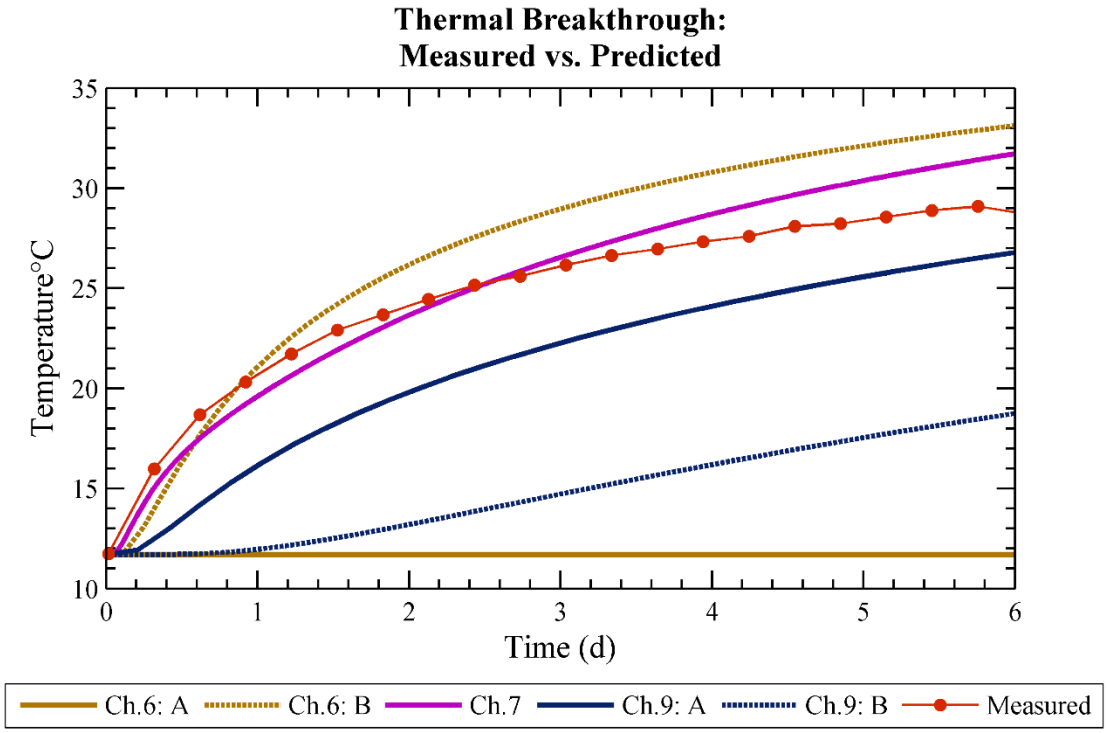

Figure 10.3. Measured production well temperature compared to five different approaches to predicting thermal breakthrough. In Chapter 6, both a uniform aperture field ("Ch.6: A") and a channeled-flow scenario ("Ch.6: B") were used to predict production well temperature. In Chapter 7, results of a combine inert/adsorbing tracer test were used to predict temperature ("Ch.7"). In Chapter 9, a non-uniform aperture field was identified using both the inert and adsorbing tracer data ("Ch.9: A") and just the inert tracer data ("Ch.9: B").

10.1.5 Thermally Degrading Tracers

Thermally degrading tracer tests were repeated four times at Altona after increasing levels of reservoir heating over 6 d. After one, three, and five days, mean reservoir temperature was predicted to increase roughly 12, 4, and 2 °C, respectively. For comparison, measured mean reservoir temperature increase

was 20, 6, and 3 °C, respectively. Absolute temperature estimates, however, were over-predicted by 70 to 80 °C.

The short-comings of this analysis were later found to result from tracer-rock interactions in which the fracture surface catalyzed the hydrolysis reaction, even at temperatures as low as ~10 °C (Appendix C). Subsequent laboratory experiments revealed that 2 and 5 g of crushed rock increased the reaction rate by a factor of roughly 15 and 40, respectively.

An additional complication was observed in which the crushed rock required sufficient "activation" time to develop a catalytic effect. If the rock surfaces were in contact with tap water at room temperature for less than roughly 2 d, no catalytic effect was observed. After two days, however, the crushed rock surfaces did produce catalysis. The catalytic effect strengthens with continued fluid-rock contact for at least 28 d. The catalytic effect of the fracture surface continues to be investigated by members of our group. Current and future research involves measuring the strength of the catalyst as a function of activation time, water temperature, surface area to volume ratio, pH, and fluid salinity.

10.1.6 Inverse Model for Determining Non-Uniform Aperture Fields

In Chapter 9, a non-uniform or "heterogeneous" fracture aperture field was identified using Principal Component Analysis (PCA) to make the inverse problem tractable in the presence of thousands of unknown aperture values. Rather than determining each fracture aperture value independently, PCA

simplified the problem by varying spatially correlated aperture values simultaneously. This made the inversion computationally feasible by preventing the inverse model from wasting computational time modifying a single fracture aperture which has little to no influence on fluid flow. Using a Genetic Algorithm (GA) the inverse model was solved resulting in a non-uniform aperture field that was subsequently used to forecast thermal performance.

Two contrasting approaches were used where each incorporated different parameters to be determined by the inverse model. In the first approach, the inverse model minimized the L^2 Norm between measured and simulated inert and adsorbing tracer data. It solved for 100 PCA mode coefficients as well as hydrodynamic dispersion and the mean fracture aperture. This two-dimensional analysis of inert and adsorbing tracer data is essentially equivalent to the one-dimensional analysis presented in Chapter 7.

The second approach solves for 50 PCA mode coefficients and assumes mean fracture aperture is known and hydrodynamic dispersion is negligible. The assumption of negligible dispersion at Altona is supported by the discussion of mechanical dispersion and Taylor-Dispersion in sub-section 6.5 where neither dispersive mechanism could account for the measured C-Dot and iodide RTDs. Without a physical explanation for dispersion, solving the inverse problems discussed in Chapters 6, 7, and the first approach of Chapter 9 essentially treats dispersion as a fitting parameter with no physical

explanation. The second approach in Chapter 9 investigates the cause of this apparent dispersion by determining if a sufficient match to measured inert tracer data can be reached simply by identifying a non-uniform aperture field. In the second approach, the inverse problem was solved eight times, each with a different assumed value for mean fracture aperture. The pre-specified mean fracture aperture that produced the best fit to the inert tracer was used as the "representative" aperture distribution and was subsequently used to predict thermal performance.

Using Approach 1, inert and adsorbing tracer RTDs were matched fairly well by the inverse solution. The resulting prediction of temperature (Figure 10.3), is much more accurate than a uniform aperture prediction, but less accurate than the one-dimensional approach for interpreting inert/adsorbing tracer data, which is discussed in Chapter 7.

In the second approach, the inert tracer RTD produced by aperture field identified in solving the inverse model fits the measured data better than a uniform aperture. The uniform aperture mentioned here was determined assuming negligible dispersion and is discussed in sub-section 9.5. A particularly interesting comparison is of the tailing behavior in log-log space for the non-uniform and uniform aperture fields. Because hydrodynamic dispersion is assumed negligible in both these cases, it is clear that the non-uniform aperture field was able to increase the spread of the tracer RTD consistent with measured data. This suggests that the apparent dispersion

found in previous modeling efforts was likely a result of flow channeling, not mechanical dispersion or Taylor-Dispersion. For these reasons, a non-uniform aperture field should be considered in efforts to calibrate forward models using inert tracer RTDs.

10.2 Conclusions

Heat and tracer experiments conducted at the Altona field site have provided critical measurements of fluid flow paths in fractured rock which are rarely available in field studies of fracture fluid flow. With regards to understanding channeled-flow in fractured rock, the following measurements are particularly beneficial:

1. Spatial distribution of fluid flow
2. Production well and inter-well thermal profile
3. Adsorbing tracer RTDs and rate-limited adsorption
4. Thermally degrading tracer RTDs and fracture surface catalysis.

Beyond the breadth of data collected, the field experiments, laboratory studies and computational modeling efforts have produced several significant insights into heat and mass transport in fracture-dominated reservoirs. These insights are summarized in the following sub-sections.

10.2.1 Inert Tracer Testing

Based on field testing, moment analysis, and numerical modeling, the common practice of using inert tracers for calibrating thermal-hydraulic models under idealized flow conditions appears to be an inadequate approach to predict geothermal reservoir thermal performance. In one-dimension,

moment analysis revealed that the critical parameters that govern thermal drawdown are the surface area available for heat exchange, the volumetric flow rate, and the thermal diffusivity of the bulk rock. The mean fracture aperture, effective reservoir fluid volume, and mean tracer residence time, however, do not influence thermal performance. Therefore, the common practice of measuring mean tracer residence time and estimating the mean fracture aperture for use in thermal-hydraulic forward models is not mathematically supported in the context of a one-dimensional flow channel model.

The results of the moment analysis were reinforced in a computational exercise that compared heat and mass transport in two contrasting flow scenarios under two-dimensional dipole-flow. This exercise showed that inert tracer data could be fit using both a uniform fracture aperture of roughly 0.5 mm as well as a scenario in which a 1 m wide flow channel extended directly between the two wells. In this scenario, the fracture aperture was 6 mm and the surrounding region was roughly 2 mm.

This non-uniqueness can be explained by considering the two flow scenarios in terms of an “effective” fluid volume and heat transfer surface area. The inert tracer data could be fit by both flow scenarios because they had roughly equivalent effective fluid volumes. However, the flow channel scenario lowered the effective heat transfer area and, as a result, predicted thermal performance in better agreement with measured temperature at Altona. In contrast, the ideal dipole-flow in a uniform aperture provided an even sweep of

flow between the wells and dramatically over-predicted thermal performance by effectively increasing the heat transfer surface area.

However, there may be an empirical relationship that can relate mean fracture aperture and/or mean residence time to the effective heat transfer surface area. Evidence for this relationship was provided in Tester et al. (1986) where heat transfer surface area was compared to inert tracer tests for several experimental Enhanced Geothermal System (EGS) reservoirs. Unfortunately, this relationship has not been observed for a sufficiently wide range of reservoir conditions and spatial/temporal scales.

Simulations presented in Chapter 9, however, suggest that inert tracer RTDs produced from a non-uniform fracture aperture may exhibit patterns that can only be produced if the effective heat transfer surface area is reasonably accurate. This was shown by demonstrating that the estimates of hydrodynamic dispersion provided in Chapters 6 and 7 and sub-section 9.4 were not consistent with models for mechanical dispersion or Taylor-Dispersion. Instead, non-uniform flow was able to provide a sufficient fit to measured inert tracer RTDs without the need for including hydrodynamic dispersion. In effect, treating hydrodynamic dispersion as an unknown value at Altona is simply an aphysical tuning parameter that is not a dispersive mechanism. Rather, it is related to flow channeling, which, strictly speaking, is not a Fickian process.

10.2.2 Adsorption Tracer Testing

The adsorbing tracer cesium was used in conjunction with the inert tracer iodide at the Altona site. The field data show that the adsorbing tracer experienced less mass recovery than the inert tracer, which suggests cesium interacted with the fracture surface whereas iodide did not. The measured RTDs were used in two computational efforts to predict thermal performance. Using an analytical equation with fluid flowing through a series of rectangular flow channels, good agreement between predicted and measured temperature was possible.

The second computational effort was to use Principal Component Analysis (PCA) to simplify the parameter space needed to identify a non-uniform aperture field. Using a Genetic Algorithm (GA), a sufficient fit to both inert and adsorbing RTDs was possible. The resulting prediction of production well temperature appropriately identified the occurrence of rapid thermal breakthrough, although it did not produce as accurate results as the first computational approach using simple flow channels.

In conclusion, combined inert/adsorbing tracer tests used to calibrate fluid flow models with lab-measured adsorption parameters provided accurate forward-models that predicted premature thermal breakthrough. Inert tracers alone, however, were found to provide dramatically different predictions using a two-dimensional fracture with variable aperture distributions. Despite initial work on adsorbing tracers starting nearly 40 years ago, the studies presented in this dissertation appear to be the first field validation of the adsorption

tracer concept for predicting thermal breakthrough. No other study published in conference proceedings or peer-reviewed journal articles could be found in which temperature predictions could be quantitatively validated.

These results are promising, suggesting that an appropriately selected adsorption tracer could be used to forecast geothermal reservoir thermal performance. However, field experiments were conducted at the Altona Field Laboratory which is a meso-scale field site. Future work will attempt to further bridge the scale-gap between overly-simplified lab experiments and intractable field tests at the scale of 100s to 1000s of meters. In addition, the influence of fracture roughness, heterogeneous fracture surface and fluid chemistry, and higher temperature and salinity fluids will need to be investigated with respect to their influence on adsorption reactions. In particular, investigating adsorption in these conditions should help determine if adsorption reactions at large field scales with varying conditions can be adequately measured at the laboratory scale.

10.2.3 Thermally Degrading Tracer Tests

Field experiments at Altona demonstrated, qualitatively, that thermally degrading tracers could be used to estimate changes in interwell fluid temperatures. During continuous reservoir heating, four tracer tests over the course of six days demonstrated that as the reservoir was heated, the mass recovery of the reaction product increases relative to the recovery of a reference inert tracer. At Altona, phenyl acetate was used as a thermally degrading tracer and the C-Dot carbon-cored nanoparticle was used as an inert tracer.

Unfortunately, previously published measurements in laboratory batch experiments (Nottebohm et al., 2012), failed to provide parameters of the Arrhenius Equation that were appropriate for the conditions of the field test. As a result, absolute temperature estimates from the thermally degrading tracer were roughly 70 to 80 °C larger than measurements made at numerous locations throughout the well-field. Nonetheless, estimated changes in the effective reservoir temperature (~ 2 to 12 °C) were fairly consistent with field measurements (~ 3 to 20 °C). In addition, the mean reservoir temperature was found to scale linearly with the relative mass fraction recovered of the degrading tracer (Figure 8.4). This suggests that in the presence of catalysis, phenyl acetate conversion may still be treated as a first-order reaction.

With regards to the pre-exponential factor and activation energy that describe temperature-dependent reactions, these estimates suggests that the pre-exponential factor was influenced more strongly than the activation energy. This is because the pre-exponential factor and the activation energy are, respectively, the y-intercept and slope of a linear-fit between the reaction rate and reciprocal temperature. Most likely, if the change in temperatures were relatively accurate but not the magnitude, the slope of the linear fit would remain relatively unchanged while the y-intercept was increased.

10.2.4 Concluding Remarks

The Altona field site provides a unique opportunity to evaluate reactive and inert tracers in the context of characterizing geothermal reservoirs, particularly under channeled-flow conditions. Because this is a “meso-scale”

field site, predictions are readily evaluated against measured data over the course of days or weeks rather than at commercial scales which may require months, years, or even decades before models can be validated. As a result, adsorption tracers were successfully used to calibrate forward-models of heat transport and accurately predict rapid thermal breakthrough. In addition, thermally degrading tracers were successful, qualitatively, in tracking the progression of the thermal front.

A major benefit of this meso-scale field site is that experimental tracers, such as phenyl acetate and cesium, can be applied under field conditions that permit practical investigations in circumstances where anticipated and observed tracer behavior do not agree. For instance, phenyl acetate decay was found to be catalyzed by the fracture surface. Since 2012, several studies have investigated their use as a potential thermally degrading tracer. None of these studies, however, suggested that catalytic effects can interfere with quantitative temperature estimates. Because the field site is sufficiently constrained, however, a limited number of possible explanations were realistic. For instance, variable temperatures, non-uniform pH, fluctuating dissolved oxygen are all potential sources of error, but are not likely at the Altona site. This led to an investigation of catalytic effects and subsequent laboratory experiments that demonstrated this effect. This has led to ongoing laboratory experiments which have revealed that the catalytic effect may not be identified, unless the mineral surface is treated such that it's surface conditions are consistent with field conditions (Appendix C).

Going forward, the success of these field experiments, laboratory measurements, and modeling efforts should serve as a “stepping-stone” between overly-simplified laboratory experiments and large-scale commercial reservoirs. Future studies will focus on developing laboratory methods that adequately reproduce field conditions and on further bridging the “scale-gap” between bench-scale and commercial scale. In addition, the origin of flow channeling at Altona will be investigated, particularly with respect to mechanisms responsible for concentrating fluid flow through a narrow flow channel.

Despite several tracer-calibrated forward models that predict rapid thermal breakthrough, these experiments also demonstrate that characterizing fluid flow in fractured rock remains largely an empirical exercise that relies on often overly-simplified flow models, even in a single sub-horizontal fracture as is the case at Altona. This is evident, for example, by the two contrasting flow scenarios shown in Figure 6.5 and Figure 6.6, which reveal that a uniform aperture scenario with significant dispersion provides the best-fit for the inert tracer, but fails at forecasting even reasonable thermal profiles at the production well.

The challenge of characterizing fluid flow under channeled-flow is particularly evident in practical applications of reactive tracers that rely on independently quantified measurements. For example, the catalytic effect could be identified at the Altona site, because fluid and flow conditions are relatively

known. At larger spatial and temporal scales, however, the 40-fold difference in reaction rates may not have been explained, particularly in geothermal fields where circulating tracer may experience spatial and temporal variations in pH, temperature, and dissolved oxygen, for example.

10.3 References

Nottebohm, M., T. Licha, and M. Sauter (2012), Tracer design for tracking thermal fronts in geothermal reservoirs, *Geothermics*, 43, 37-44.

Tester, J. W., B. Robinson, and J. H. Ferguson (1986), Inert and reacting tracers for reservoir sizing in fractured, hot dry rock systems, Proceedings, in *11th Workshop on Geothermal Reservoir Engineering*, Stanford University, Stanford, California.

APPENDIX A: LITERATURE RELAVENT TO ALTONA FIELD SITE

Peer-Reviewed Journal Publications

Talley, J., G. S. Baker, M. W. Becker, and N. Beyrle (2005), Four dimensional mapping of tracer channelization in subhorizontal bedrock fractures using surface ground penetrating radar, *Geophysical Research Letters, 32*, doi:10.1029/2004GL021974.

Becker, M. W., and G.P. Tsoflias (2010), Comparing flux-averaged and resident concentration in a fractured bedrock using ground penetrating radar, *Water Resources Research*, 46, *W09518,* doi:10.1029/2009WR008260.

Guiltinan, E. and M. W. Becker (2015), Measuring well hydraulic connectivity in fractured bedrock using periodic slug tests, *Journal of Hydrology,* 521, 100-107.

Tsoflias, G. P., C. Perll, M. Baker, and M. W. Becker (2015), Cross-polarized GPR imaging of fracture flow channeling, *Journal of Earth Science*, 26, 776-784, doi:10.1007/s12583-015-0612-1.

Hawkins, A.J., M.W. Becker, and G.P. Tsoflias (2017a), Evaluation of inert tracers in a bedrock fracture using ground penetrating radar and thermal sensors, *Geothermics, 67*, 86-94.

Hawkins, A.J., D.B. Fox, M.W. Becker, J.W. Tester (2017b), Measurement and simulation of heat exchange in fractured bedrock using inert and thermally degrading tracers, *Water Resources Research*, *53*, doi: 10.1002/2016WR019617.

Graduate Theses

Beyrle, N. K. (2005), Using polarized ground penetrating radar to improve subsurface imaging of bedrock fractures, *M.S. Thesis,* State University of New York, Buffalo.

Talley, J. (2005), Imaging channelized flow in fractured rock using surface GPR, *M.S. Thesis*, State University of New York, Buffalo.

Guiltinan, E. (2012), Characterizing well connectivity in fractured bedrock using periodic hydraulic tests, *M.S. Thesis,* California State University, Long Beach.

Hawkins A. J. (2013), Measurement of the spatial distribution of heat exchange in a geothermal analog bedrock site using fiber-optic distributed temperature sensing, *M.S. Thesis*, California State University, Long Beach.

Perll, C. P. (2013), Evaluating GPR polarization effects for imaging fracture channeling and estimating fracture properties. *M.S. Thesis*, University of Kansas.

Remmen, K. D. (2013), A reactive tracer method for the measurement of specific surface area in EGS reservoirs, *M.S. Thesis*, California State University, Long Beach

Baker, M. (2014), Ground-penetrating radar imaging of fluid flow through a discrete fracture. *M.S. Thesis*, University of Kansas.

Zhao, Y. (2015), The use of nanoparticles to assess subsurface flow heterogeneity, *Ph.D Dissertation*, Cornell University.

Conference Proceedings

Guiltinan, E. J., and M. W. Becker (2010), Using harmonic hydraulic tests to estimate fracture bedrock properties and predict local heterogeneity, Proceedings, in Geological Society of America.

Hawkins, A. J., and M.W. Becker (2012), Measurement of the spatial distribution of heat exchange in a geothermal analog bedrock site using fiber optic distributed temperature sensing, Proceedings, in *37th Workshop on Geothermal Reservoir Engineering*, Stanford, California.

Becker, M. W., K. Remmen, P. Reimus, and G. Tsoflias (2013), Investigating well connectivity using ionic tracers, proceedings in *38th Workshop on Geothermal Reservoir Engineering*, Stanford, California.

Becker, M., G. Tsoflias, M. Baker, and A. Hawkins (2015), Confirmation of hydraulic, tracer, and heat transfer characterization of a fractured bedrock using Ground Penetrating Radar, Procedings, in *40th Workshop on Geothermal Reservoir Engineering*, Stanford University, Stanford, California.

Hawkins, A. J., D. B. Fox, R. Zhao, J. W. Tester, L.M. Cathles, D. L. Koch, and M.W. Becker (2015), Predicting thermal breakthrough from tracer tests: simulations and observations in a low-temperature field laboratory, Proceedings, in *47th Workshop on Geothermal Reservoir Engineering*, Stanford, California.

Hawkins, A. J., D. B. Fox, M. W. Becker, and J. Tester, (2016), Meso-scale field testing of reactive tracers in a model geothermal reservoir. Proceedings, in *42nd Workshop on Geothermal Reservoir Engineering* Stanford University, Stanford, California.

Christensen, J. N., A. Hawkins, S. T. Brown, E. Sonnenthal, N. Sturchio, and D. J. DePaolo (2017), Proceedings, in *42nd Workshop on Geothermal Reservoir Engineering* Stanford University, Stanford, California.

Hawkins A. J., D. B. Fox, M. W. Becker, and J. W. Tester (2017), An inverse model for predicting reservoir structure and thermal lifetime using inert and adsorbing tracers, Proceedings, in *42nd Workshop on Geothermal Reservoir Engineering* Stanford University, Stanford, California.

Conference Presentations

Baker, G. S., J. L. Talley, M. W. Becker, and N. J. Beyrle (2004), Flow-channeling in fractured bedrock: Ground penetrating radar investigations and interpretations, Presentation, *American Geophysical Union Fall Meeting*, San Francisco, California.

Hawkins, A. J., and M. W. Becker (2012), Use of DTS to measure heat flow in fractured rock, Presentation*, American Geophysical Union Fall Meeting*, San Francisco, California.

Hawkins, A. J., and M. W. Becker (2012b), Measurement of the spatial distribution of fracture/matrix heat exchange using fiber optic distributed temperature sensing, Presentation, *Symposium on the Application of Geophysics to Engineering and Environmental Problems*, Tucson, Arizona.

Tsoflias, G. P., M. Baker, and M. W. Becker (2012), Field GPR monitoring of flow channeling in fractured rock, Presentation*, American Geophysical Union Fall Meeting*, San Francisco, California.

Tsoflias, G. P., and M. W. Becker (2012b), GPR characterization of discrete fractures and monitoring of channeled flow: Elucidating the forward model, Presentation, *Symposium on the Application of Geophysics to Engineering and Environmental Problems*, Tucson, Arizona.

Hawkins, A. J., and M. W. Becker (2013), Measurement of the spatial distribution of heat exchange using fiber optic distributed temperature sensing, Presentation, *NGWA conference on Groundwater in Fractured Rock and Sediments*, Burlington, Vermont.

Tsoflias, G. P., M. Baker and M. W. Becker (2013), Imaging fracture anisotropic flow channeling using GPR signal amplitude and phase, Proceedings, in *SEG Technical Program Expanded Abstracts*, Houston, Texas.

Tsoflias, G. P., C. Perll, M. Baker, and M. Becker (2014), Fracture flow channel imaging using cross-polarized GPR signals, Presentation, *American Geophysical Union Fall Meeting*, San Francisco, California.

Hawkins, A. J., L. M. Cathles, R. Zhao (2015), Comparison of C-Dot nanoparticle & iodide breakthrough curves in a shallow fracture-dominated aquifer, Presentation, *Geological Society of America's Annual Meeting*, Baltimore, Maryland.

Hawkins, A. J., D. L. Koch, L. M. Cathles, M. W. Becker, and J. W. Tester (2015), Field validation of reactive tracers for geothermal reservoir characterization and monitoring, Presentation, in *American Geophysical Union's Annual Fall Meeting*, San Francisco, California.

Pálsdóttir, A., A. Hawkins, M. Ishmael, and J. Tester (2017), Applications of engineered materials for geothermal resource utilization, Presentation, *The Minerals, Metals, & Materials Society 146th Annual Meeting*, San Diego, California.

Altona Flat Rock and the Surrounding Area

Wiesnet, D. R. (1961), Composition, grain size, roundness, and sphericity of the Potsdam Sandstone (Cambrian) in northeastern New York, *Journal of Sedimentary Petrology*, 31, 5-14.

Sullivan, N. J. B., and D. K. Martin (1970), *A History of the Town of Chazy, Clinton County, New York*. G. Little Press, Burlington, Vermont, 360.

Engelder, J. T., and M. L. Sbar (1976), Evidence for uniform strain orientation in the Potsdam Sandstone, northern New York, from in situ measurements, *Journal of Geophysical Research*, 81, 3013-3017.

Olcott, P.G. (1995), *Ground Water Atlas of the United States*, United States Geological Survey (USGS), Reston, Virginia.

Paillet, F. L. (2000), A field technique for estimating aquifer parameters using flow log data, *Ground Water*, 38, 510-521.

Gooley, L. P. (2005), *A History of the Altona Flat Rock*. Bloated Toe Enterprises, Peru, New York.

Rayburn, J. A., P. L. K. Knuepfer, and D. A. Franzi (2005), A series of large, Late Wisconsinan meltwater floods through the Champlain and Hudson Valleys, New Yofpa State, USA, *Quaternary Science Reviews,* 24, 2410-2419.

Williams, J. H. R. J. Reynolds, and M. Nastev (2006), Hydrogeology of the Potsdam sandstone aquifer and springs in the Chateaugay area, northern New York, Presentation, *Geological Society of America Annual Meeting*, Philadelphia, Pennsylvania.

Selleck, B. (2008), *Stratigraphy, Sedimentology and Diagenesis of the Potsdam Formation, Southern Lake Champlain Valley, New York*. New York State Geological Association and Colgate University, Hamilton, New York.

Williams, J. H., R. J. Reynolds, D. A. Franzi, E. A. Romanowicz, and F. L. Paillet (2010), Hydrogeology of the Potsdam Sandstone in northern New York, *Canadian Water Resources Journal*, 35,399-416.

Klein, A. M. Altwerger, C. Hinchman, S. Sullivan, M. Drutjons, and E. Romanowicz (2013), Temporal variations in a fracture controlled specific conductivity front in a bedrock well, Altona Flatrock Field Site (Chazy, NY), Presentation, Northeastern Section - *48th Annual Meeting, Geological Society of America*, Bretton Woods, New Hampshire.

Brink, R. A. (2015), Sedimentological comparison of the Late/Lower Early Middle Cambrian Altona Formation and the Lower Cambrian Monkton Formation, *M.S Thesis*, University of Vermont.

Grenier, J. –F., M. Malo, B. Long, D. Lavoie (2015), Porosity assessment of sandstones of the Potsdam Group, St. Lawrence Platform, Québec, Canada: Utilization of the CT scanning techniques, Proceedings, in *2nd International Conference on Tomography of Materials and Structures*, Québec City, Canada.

Lowe, D. G. (2016), Sedimentology, stratigraphic evolution and provenance of the Cambrian – Lower Ordovician Potsdam Group in the Ottawa Embayment and Quebec Basin, *Ph.D Dissertation*, University of Ottawa.

Miscellaneous

Becker, M. (2012), Verification of geothermal tracer methods in highly constrained field experiments, Presentation, *Geothermal Technologies Office 2012 Peer Review*.

Ma, J. (2013), Novel multidimensional tracers for geothermal inter-well diagnostics, Presentation, *Geothermal Technologies Office 2013 Peer Review.*

Tester, J. W., D. Fox, A. Hawkins, and M. Becker (2015), A reactive tracer method for predicting EGS reservoir geometry and thermal lifetime: Development and field validation, *Geothermal Technologies Office 2015 Peer Review*.

APPENDIX B: REACTIVE TRANSPORT MODEL DERIVATION

As previously discussed in Chapters 4 and 7, reactive tracer transport in a flow "channel" was simulated in one-dimension using a solution for advection, dispersion, diffusion, and reaction (Figure B.1). The main use of this model, as was to simulate advection, dispersion, and rate-limited adsorption. In the derivation of this equation that follows, matrix diffusion and thermal decay are also included. In the case of negligible matrix diffusion and thermal decay, this analytical model is identical Equation 4.4.

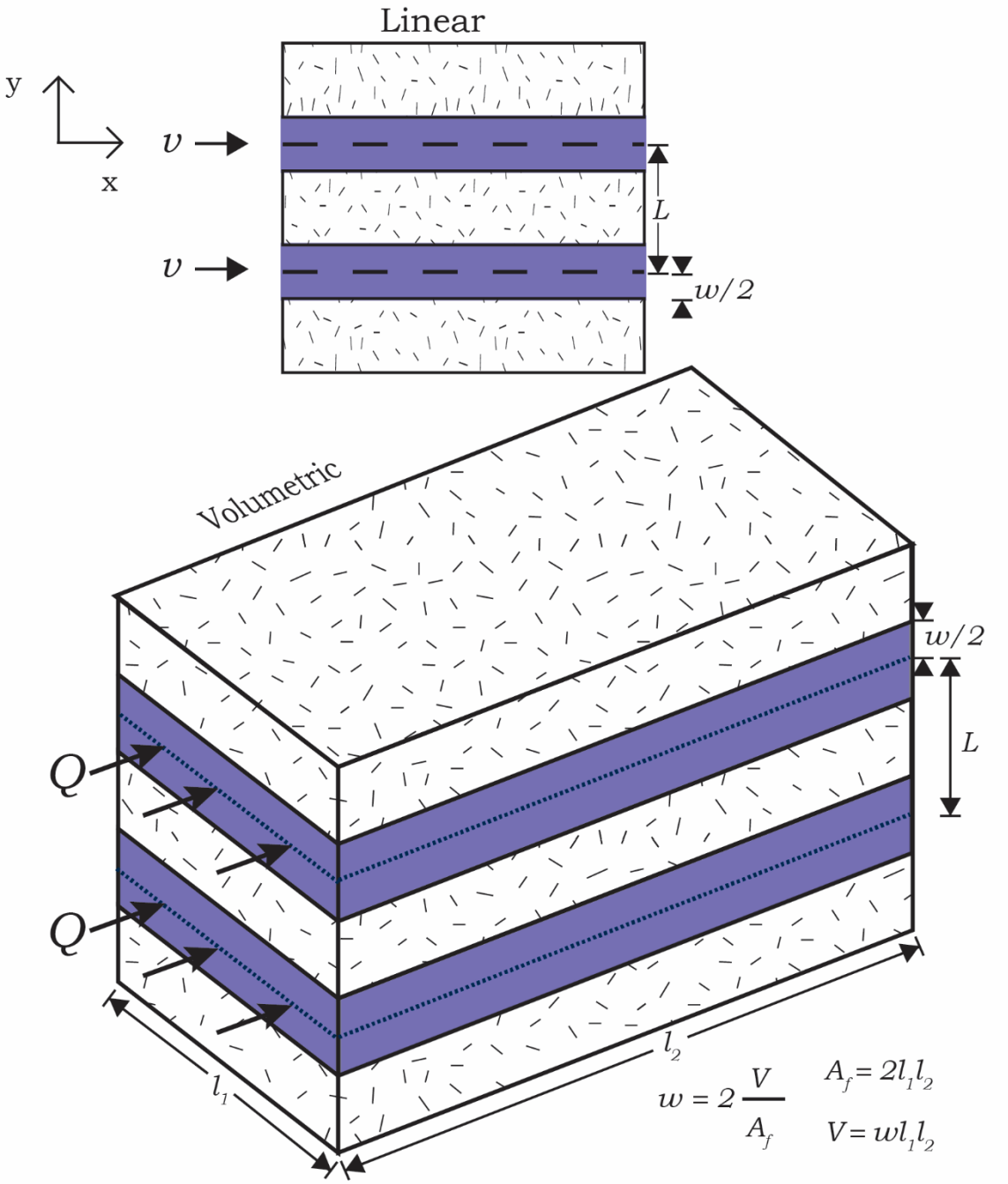

Figure B.1 Model geometry for of one-dimensional transport. The upper and lower schematics represents linear and volumetric flow, respectively. Equations at the lower right describe the relationship between linear and volumetric geometries. The model derivation assumes infinite parallel flow channels of constant separation distance, *L*.

Tracer transport in the bulk rock matrix is limited to diffusive mass transfer perpendicular to the fracture. Tracer originates at *y*=0 (center of the

fracture) and experiences diffusion into the porosity, Φ, of the saturated bulk rock. A solution was determined in Laplace space and solved in the time-domain through numerical inversion as described in sub-section 4.2.1.

The four coupled partial differential equations that follow govern adsorptive mass transport via advection, dispersion, and matrix diffusion:

$$\frac{\partial c_f}{\partial t} = D_f \frac{\partial^2 c_f}{\partial x^2} - v\frac{\partial c_f}{\partial x} - kc_f - \frac{2k_{ads}}{w}\left(Pc - \Gamma\right)_f + \frac{2\phi D_m}{w}\frac{\partial c_m}{\partial y}\bigg|_{y=w/2}, \qquad \text{B.1}$$

$$\frac{\partial c_m}{\partial t} = D_m \frac{\partial^2 c_m}{\partial y^2} - kc_f - \frac{k_{ads}}{\phi}\left(Pc - \Gamma\right)_m, \qquad \text{B.2}$$

$$\frac{\partial \Gamma_m}{\partial t} = k_{ads}\left(Pc - \Gamma\right)_m - k\Gamma_m, \qquad \text{B.3}$$

and

$$\frac{\partial \Gamma_f}{\partial t} = k_{ads}\left(Pc - \Gamma\right)_f - k\Gamma_f. \qquad \text{B.4}$$

The analytical model was solved assuming the following initial and boundary conditions:

Fracture	*Matrix*
$c_f(x,0) = 0$	$c_m(x,y,0) = 0$
$c_f(\infty,t) = 0$	$c_m(x,w/2,t) = c_f(x,t)$
$c_f(0,t) = \delta(t)$	$\frac{\partial c_m}{\partial y}(x,L/2,t) = 0$

A second order homogeneous ordinary differential equation results from combining the governing equations after conversion to Laplace space. In Laplace space, the governing equations are

$$s\bar{c}_f = D_f \frac{\partial^2 \bar{c}_f}{\partial x^2} - v\frac{\partial \bar{c}_f}{\partial x} - k\bar{c}_f - \frac{2k_{ads}}{w}\left(P\bar{c} - \bar{\Gamma}\right)_f + \frac{2\phi D_m}{w}\left.\frac{\partial \bar{c}_m}{\partial y}\right|_{y=w/2}, \qquad \text{B.5}$$

$$s\bar{c}_m = D_m \frac{d^2\bar{c}_m}{dy^2} - k\bar{c}_f - \frac{k_{ads}}{\phi}\left(P\bar{c} - \bar{\Gamma}\right)_m, \qquad \text{B.6}$$

$$s\bar{\Gamma}_m = k_{ads}\left(P\bar{c} - \bar{\Gamma}\right)_m - k\bar{\Gamma}_m, \qquad \text{B.7}$$

and

$$s\bar{\Gamma}_f = k_{ads}\left(P\bar{c} - \bar{\Gamma}\right)_f - k\bar{\Gamma}_f. \qquad \text{B.8}$$

Equation B.6 is a second-order differential equation which has the solution

$$\bar{c}_m = \bar{c}_f \frac{\cosh\left[\sqrt{\frac{s+k+\alpha}{D_m}}\left(L/2 - y\right)\right]}{\cosh\left[\sqrt{\frac{s+k+\alpha}{D_m}}\left(\frac{(L-w)}{2}\right)\right]}, \qquad \text{B.9}$$

where

$$\alpha = \frac{k_{ads}P_m}{\phi} - \frac{{k_{ads}}^2 P_m}{\phi\left(k_{ads} + k + s\right)}.$$

The derivative of Equation B.9 at the matrix/fracture interface is

$$\left.\frac{d\bar{c}_m}{dy}\right|_{y=w/2} = -\bar{c}_f\sqrt{\frac{s+k+\alpha}{D_m}}\tanh\left[\sqrt{\frac{s+k+\alpha}{D_m}}\left(\frac{L-w}{2}\right)\right]. \qquad \text{B.10}$$

Substitution of Equations B.7, B.8, and B.10 results in the following second order homogeneous ordinary differential equation:

$$0 = D_f \frac{\partial^2 \bar{c}_f}{\partial x^2} - v\frac{\partial \bar{c}_f}{\partial x} - \ldots$$

$$\left(\frac{2P_f k_{ads}}{w} \cdot \frac{k+s}{k_{ads}+k+s} + \frac{2\phi D_m}{w}\sqrt{\frac{s+k+\alpha}{D_m}} \tanh\left[\sqrt{\frac{s+k+\alpha}{D_m}}\left(\frac{L-w}{2}\right)\right] + k + s \right)\bar{c}_f \qquad \text{B.11}$$

In Laplace space, the solution to Equation B.11 is

$$\bar{c}_f = \exp\left[\frac{x}{2D_f}\left(v - \ldots\right.\right.$$

$$\left.\left.\sqrt{v^2 + 4D_f\left(\frac{2P_f k_{ads}}{w} \cdot \frac{k+s}{k_{ads}+k+s} + \frac{2\phi D_m}{w}\sqrt{\frac{s+k+\alpha}{D_m}} \tanh\left[\sqrt{\frac{s+k+\alpha}{D_m}}\left(\frac{L-w}{2}\right)\right] + k + s \right)}\right)\right], \qquad \text{B.12}$$

In tracer simulations, a common approach to simplify advection and dispersion is to introduce the dimensionless Peclet number, *Pe*, where

$$Pe = \frac{xv}{D_f} \qquad \text{B.13}$$

and the mean fluid residence time, τ, where

$$\tau = \frac{x}{v}. \qquad \text{B.14}$$

After substitution, Equation B.12 becomes

$$\bar{c}_f(s) = \exp\left[\frac{Pe}{2}\ldots\right.$$

$$\left(1-\sqrt{1+\frac{4\tau}{Pe}\left(\frac{2P_f k_{ads}}{w}\cdot\frac{k+s}{k_{ads}+k+s}+\frac{2\phi D_m}{w}\sqrt{\frac{s+k+\alpha}{D_m}}\tanh\left[\sqrt{\frac{s+k+\alpha}{D_m}}\left(\frac{L-w}{2}\right)\right]+k+s\right)}\right), \quad \text{B.15}$$

To make the geometric form of Equation B.15 volumetric rather than linear, the inter-well fluid volume, V, is introduced based on the assumption that

$$\frac{v}{x}=\frac{V}{Q}=\tau. \quad \text{B.16}$$

The total flow channel surface area of the upper and lower flow channel surface combined, A_f, can be introduced by assuming

$$w=2\frac{V}{A_f}. \quad \text{B.17}$$

Therefore, the final mathematical model tracer advection, dispersion, diffusion, thermal decay, and rate-limited adsorption is

$$\bar{c}_f(s)=F_T\exp\left[\frac{Pe}{2}\left(1-\sqrt{1+4\frac{A_f\left(\kappa_f+\kappa_m\right)+V\left(k+s\right)}{Q\cdot Pe}}\right)\right], \quad \text{B.18}$$

where the transfer function, F_T, is "1" for

$$c_f(0,t)=\delta(t),$$

or "$1/s$", if

$$c_f(0,t)=H(t).$$

Adsorption in the fracture, f, and matrix, m, is expressed as

$$\kappa_f=\frac{P_f k_{ads}\left(k+s\right)}{k_{ads}+k+s} \quad \text{B.19}$$

and

$$\kappa_m = \phi D_m \sqrt{\frac{s+k+\alpha}{D_m}} \tanh\left[\sqrt{\frac{s+k+\alpha}{D_m}}\left(\frac{L}{2}-\frac{V}{A_f}\right)\right]. \qquad \text{B.20}$$

Note that the fracture surface area, A_f, is the total area which includes both the bottom and top surface of the fracture volume.

An appropriate transfer function, F_T, is introduced to convolute Equation B.1. If F_T is "1" or "$1/s$", c is expressed as a dimensionless value where "0" is the background reservoir concentration and "1" is the concentration of the injected tracer. For efforts to simulate tracer tests under the physical constraints often encountered during field experiments (e.g., reinjected tracer, wellbore storage, time-delay reinjection, etc.)), an alternative transfer function can be used. For example, a transfer function where

$$F_T = \frac{1}{s}\frac{M_{inj}}{V_{inj}}\left(1-\exp\left(-s\frac{V_{inj}}{Q}\right)\right) \qquad \text{B.21}$$

simulates concentration in physical units (e.g., ppm, mg/L, molarity, etc.) for a mass of tracer, M_{inj}, is dissolved in a finite volume, V_{inj}, and injected at a constant volumetric flow rate, Q, which is maintained throughout the duration of the test.

In Reimus et al. (2003), additional transfer functions are provided for circumstances in which tracer concentration at x=0 cannot be modeled as a Dirac Delta function, $\delta(t)$, or a Heaviside function, $H(t)$. Circumstances which are commonly unavoidable during practical field tests include: (1) dilution from wellbore storage; (2) tracer reinjection; and/or (3) time-delays due to surface

piping. In the context of investigating dispersion, these transfer functions are of particular interest, because they can produce a “dispersive-like” effect similar to hydrodynamic dispersion. Therefore, hydrodynamic dispersion, which is based largely on empirical models, can be simulated separately from the influence of non-ideal injection conditions often encountered in practical field tests.

References

Reimus, P., G. Pohll, T. Mihevc, J. Chapman, M. Haga, B. Lyles, S. Kosinski, R. Niswonger, and P. Sanders (2003), Testing and parameterizing a conceptual model for solute transport in a fractured granite using multiple tracers in a forced-gradient test, *Water Resources Research*, 39, doi:10.1029/2002WR001597.

APPENDIX C: CATALYSIS OF PHENYL ACETATE

As was discussed in Chapter 8, the degradation of phenyl acetate exhibited dramatically larger reaction rates compared to the values measured in lab experiments (Nottebohm et al., 2012). A possible explanation for this apparent discrepancy is that the rock surface acted as a reaction catalyst. To quantify this effect, laboratory experiments were conducted in which the reaction rate of phenyl acetate in the absence of clay was measured and compared to the reaction rate when the solution was in contact with clay particles with masses of 1, 2, and 5 g. Experimental design and the analysis presented in this Appendix were carried out by Adam Hawkins. Laboratory experiments were conducted by Xin Zhou, who graduated from Cornell University in the fall of 2016 with a Master's of Engineering in Chemical Engineering.

These particles were collected from the Altona site during drilling activities in 2011 which used a percussion rotary air-blast drill. The drilling process produced these particles as drill cuttings. Particles were suspended in a 100 mL tap water solution which was continuously agitated using a stir bar. Temperature for all experiments was kept at room temperature.

Results of these laboratory experiments are shown in Figure C.1. In 100 mL of a single-phase aqueous solution, the reaction rate was roughly 2.1×10^{-6} s^{-1}, which is equivalent to a half-life of 3.9 d. In contact with 5 g of crushed Potsdam Sandstone, however, the reaction rate is 8.1×10^{-5} which is nearly 40

times faster and results in a half-life of 3.9 h. This effect was found to scale with mass, evident by results of the same experiment conducted with particle masses of 1 and 2 g and resulting in half-lives of 30.7 and 6.6 h, respectively. Because the surface area of the contact between a particles and fluid varies depending on particle mass at constant fluid volume, it is clear that the mineral surfaces are catalyzing the degradation of phenyl acetate into phenol and acetate. This catalytic effect explains the discrepancy between measured and estimated reservoir temperature discussed in Chapter 8.

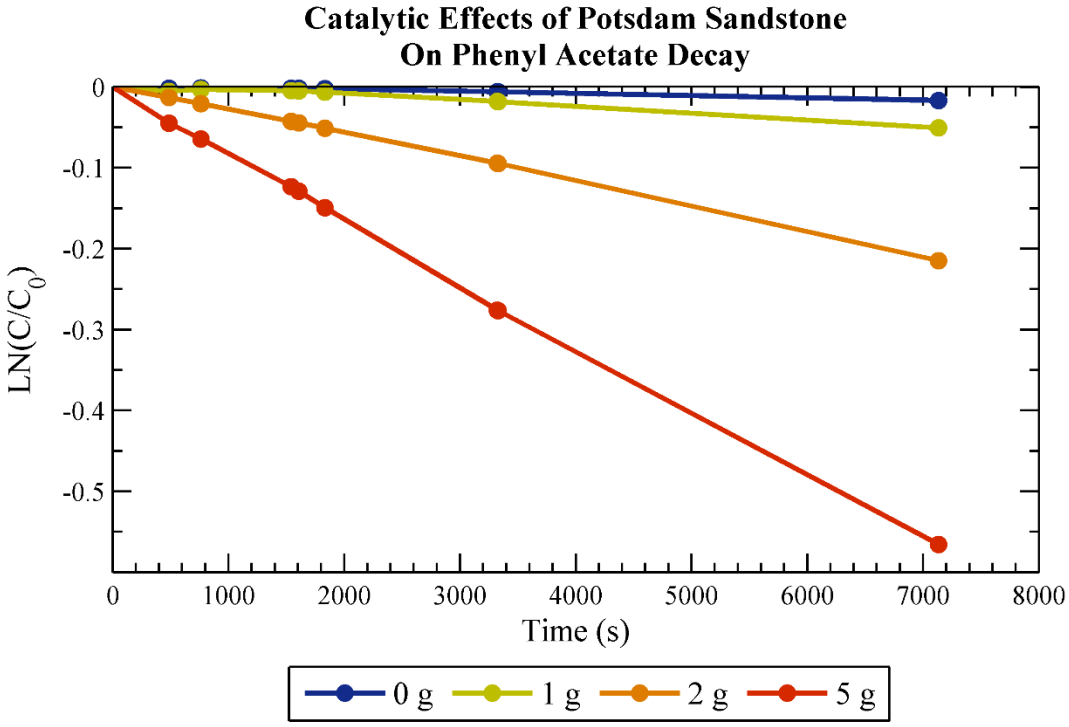

Figure C.1. Catalytic effect of Potsdam Sandstone on phenyl acetate decay for particle masses ranging from 0 to 5 g. "C" is concentration of the reactant, phenyl acetate, and "C_0" is initial phenyl acetate concentration.

During the laboratory experiments, it was discovered that to produce the catalytic effect, the clay particles had to be suspended in aqueous solution for

several weeks. Therefore, five experiments were conducted in which the reaction rate was measured for samples where 1 to 2 g of clay were left in contact with tap water for a range of times from 0 to 28 d. When the reaction is initiated within minutes of introducing clay into the fluid phase, the reaction rate was found to be consistent with the reaction rate measured in the absence of clay, roughly 2 x 10^{-6} s^{-1} (Figure C.2). After 2 and 4 d of contact time, the reaction rate increased by a factor of roughly 1.5 and 3.5, respectively. After 16 and 28 d, the reaction rate increased by a factor of roughly 7 .25 and 12.75, respectively. No further experiments were conducted at larger contact times so it remains uncertain if and when the catalytic effect reaches a maximum.

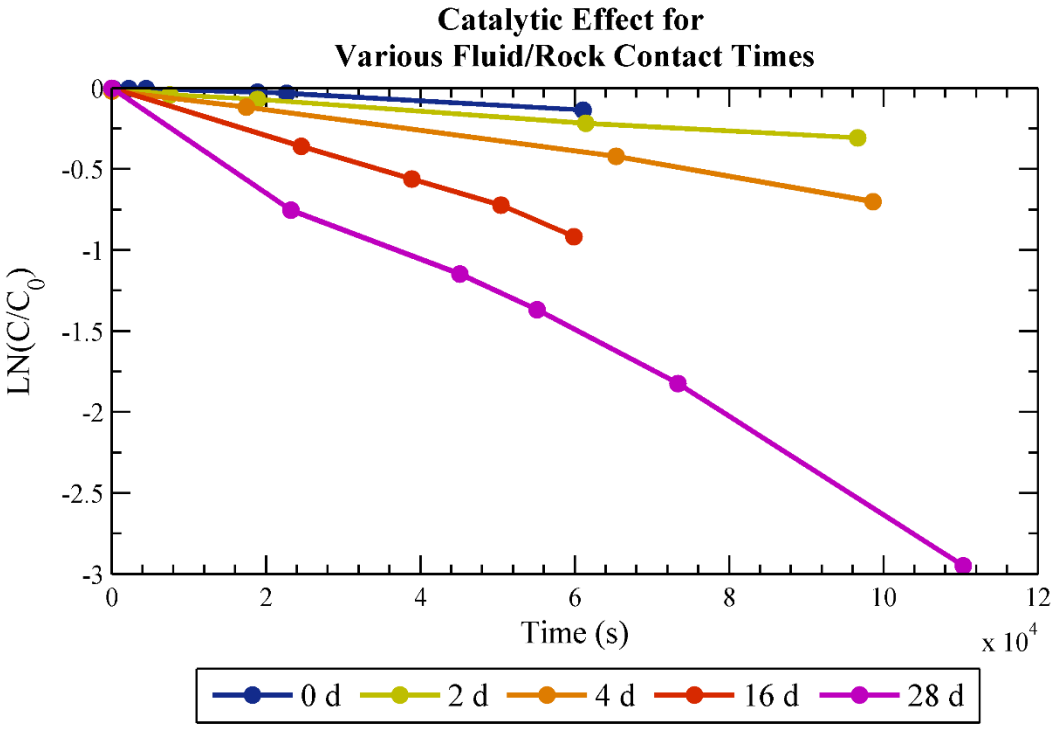

Figure C.2 Reaction rate for phenyl acetate in the presence of clay particles that have been in contact with tap water continuously for 0 to 28 d.

APPENDIX D: POTSDAM SANDSTONE ROCK CORE SAMPLES

In August of 2016, the ten dry boreholes used for temperature monitoring were deepened using a rock core drill bit with an inner diameter of 6.5 cm to a depth of roughly 0.5 m below the target fracture. These cores will eventually be studied to characterize their mineralogy and fracture distribution. In addition to deepening the existing boreholes, two new cores were advanced near well 104. The first, “b11” was advanced from ground surface to 3.3 m and the second “b12” was advanced from ground surface to 8.0 m. After coring b12 to 1.3 m below ground surface, a rotary bit was used to quickly deepen b12 to 3.6 m after which a 5 cm inner diameter core barrel was used to advance b12 to a termination depth of 8.0 m.

A prominent sub-vertical fracture can be seen in several of the core samples. This fracture is partially sealed in some locations and separated in others. When separated, the surface is covered in red-stained minerals that appear to be iron oxides. The strike of this fracture appears to be roughly EW based on their relative positions in the three-dimensional space of the well-field and dips roughly 80°N.

In collaboration with John Christensen and Shaun Brown of the Lawrence Berkeley National Laboratory, A CT-Scan was made of the sub-vertical fracture (Figure D.1). The top of the core sample was roughly 7.4 m below ground surface at b8 and is 13 cm in length. Based on the width of the

fracture represented by green coloration, the aperture of this partially-sealed fracture ranges from roughly 0.2 to 1.2 mm.

In Figure D.2, the same core sample is presented with nine slices revealing the position of the partially-sealed sub-vertical fracture (identified as a white region within the black circle). Aperture was measured based on this unit thickness at 10 locations in each slice. The average of these 90 aperture values is 1.2 mm with a minimum and maximum of 0.6 and 2.4 mm, respectively.

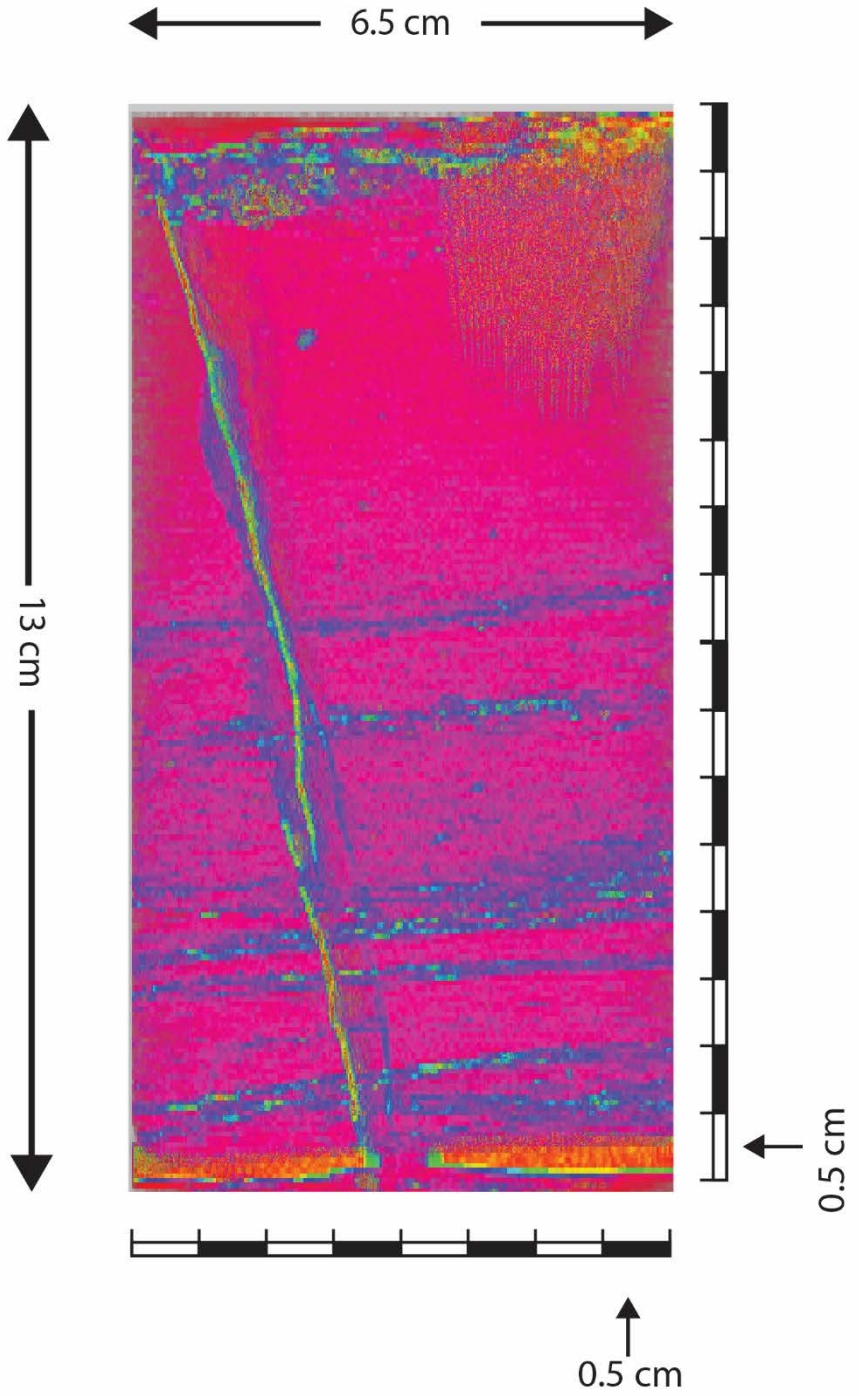

Figure D.1. CT X-Ray image of a vertical cross-section through core sampled from 7.37 to 7.53 m below ground surface at b8. The linear feature extending from the top left to the bottom of the image is the sub-vertical fracture striking roughly EW and dipping 80° N.

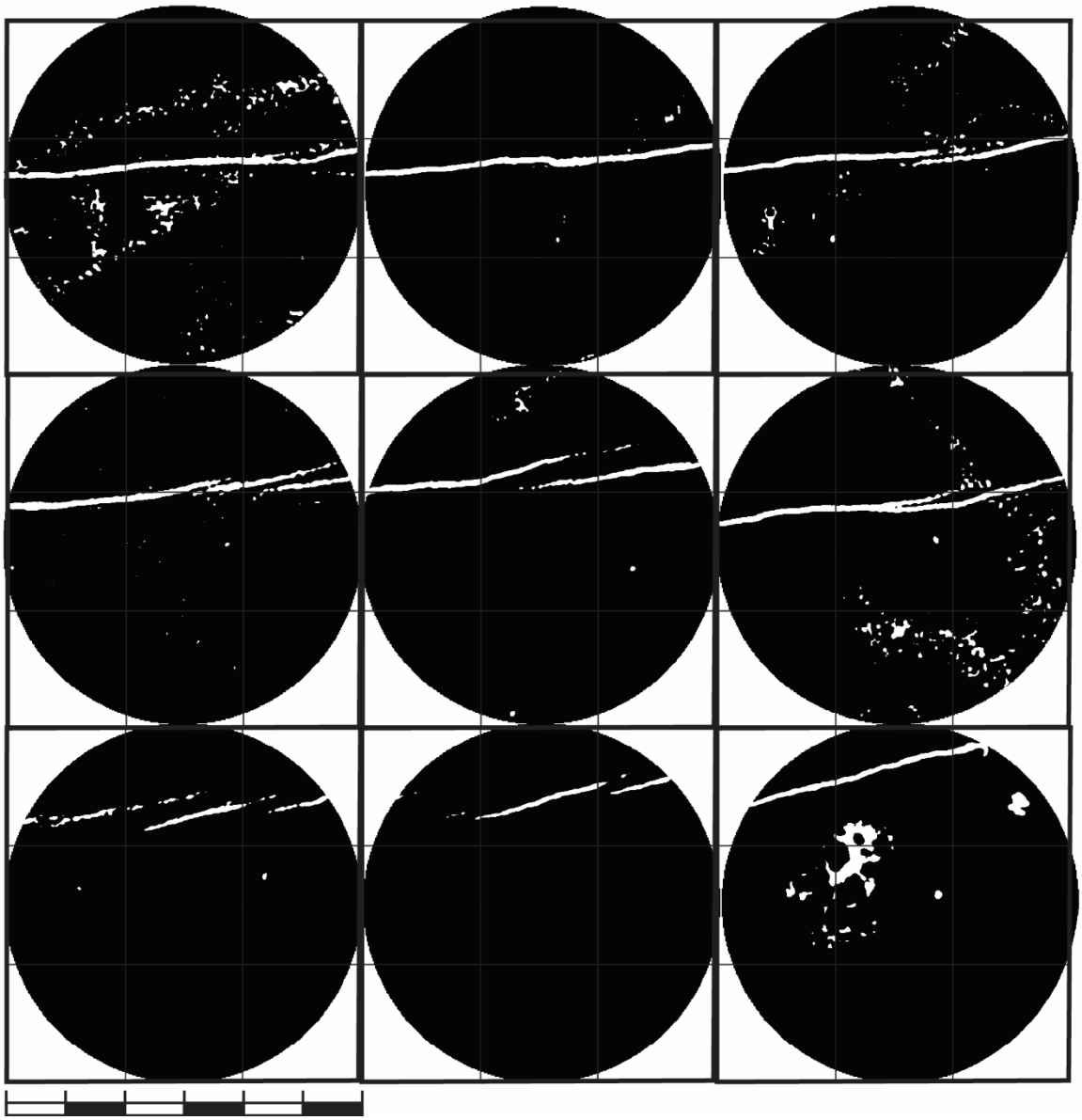

Figure D.2. CT X-Ray scan of b8-01 at various slices along the 13 cm long core. The white geometric form represents the fracture aperture.

APPENDIX E: PHOTOGRAPHS OF PNEUMATIC WELL PACKERS

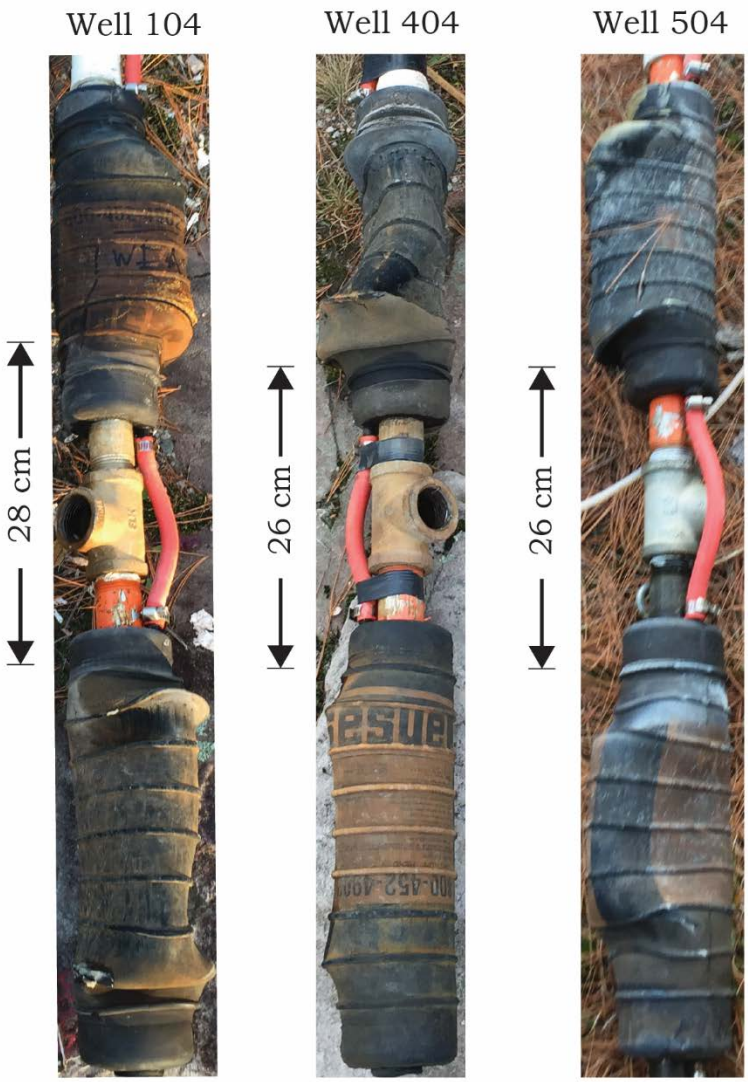

Figure E.1. Photographs of the well packers used to hydraulically isolate the target fracture in three observation wells. Photo were taken in October, 2015 prior to conducting the heat exchange experiment and tracer tests. These pneumatic straddle packers were positioned in observation wells 104, 404, and 504 in alignment with the target fracture. The center of the galvanized “tee” was aligned at a depth of 7.6 m below ground surface.

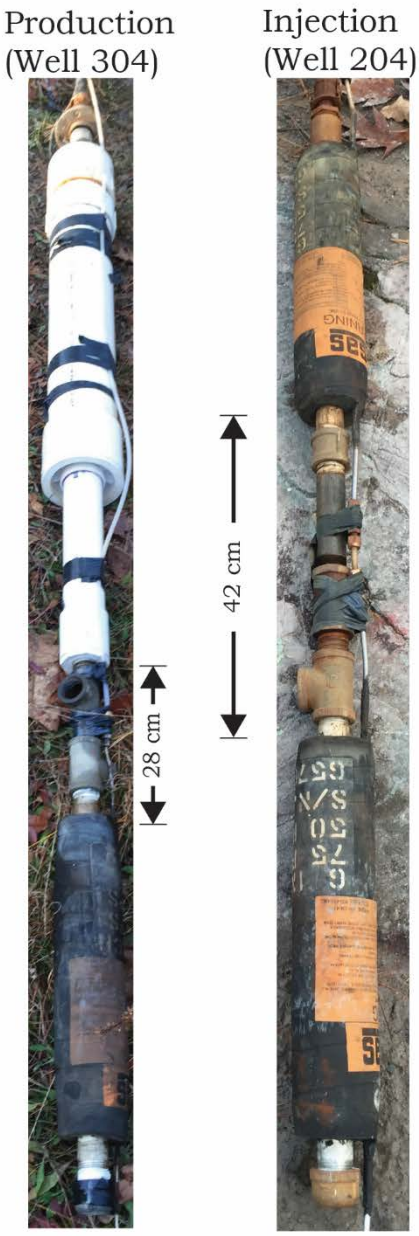

Figure E.2. Photographs of the well packers used to hydraulically isolate the target fracture in the injection (well 204) and production well (well 304). Photos were taken in October, 2015 prior to conducting the heat exchange experiment and tracer tests. The production well packer shown has a Grundfos submersible water pump located within the white Polyvinyl Chloride (PVC) piping above the galvanized “tees”. Both pictured packers were positioned such that the two “tees” of each packer were centered 7.6 m below ground surface, which is the approximate depth of the target fracture.